




Huadong Guo

Big Earth Data in Support of the Sustainable Development Goals (2022)—The Belt and Road

 Science Press
Beijing

OPEN ACCESS

 Springer

Sustainable Development Goals Series

The **Sustainable Development Goals Series** is Springer Nature's inaugural cross-imprint book series that addresses and supports the United Nations' seventeen Sustainable Development Goals. The series fosters comprehensive research focused on these global targets and endeavours to address some of society's greatest grand challenges. The SDGs are inherently multidisciplinary, and they bring people working across different fields together and working towards a common goal. In this spirit, the Sustainable Development Goals series is the first at Springer Nature to publish books under both the Springer and Palgrave Macmillan imprints, bringing the strengths of our imprints together.

The Sustainable Development Goals Series is organized into eighteen subseries: one subseries based around each of the seventeen respective Sustainable Development Goals, and an eighteenth subseries, "Connecting the Goals", which serves as a home for volumes addressing multiple goals or studying the SDGs as a whole. Each subseries is guided by an expert Subseries Advisor with years or decades of experience studying and addressing core components of their respective Goal.

The SDG Series has a remit as broad as the SDGs themselves, and contributions are welcome from scientists, academics, policymakers, and researchers working in fields related to any of the seventeen goals. If you are interested in contributing a monograph or curated volume to the series, please contact the Publishers: Zachary Romano [Springer; zachary.romano@springer.com] and Rachael Ballard [Palgrave Macmillan; rachael.ballard@palgrave.com].

Huadong Guo

Big Earth Data
in Support
of the Sustainable
Development Goals
(2022)—The Belt
and Road

 Science Press
Beijing

 Springer

Huadong Guo
International Research Center
of Big Data for Sustainable
Development Goals (CBAS)
Aerospace Information Research Institute
Chinese Academy of Sciences
Beijing, China



ISSN 2523-3084 ISSN 2523-3092 (electronic)
Sustainable Development Goals Series
ISBN 978-981-97-3277-7 ISBN 978-981-97-3278-4 (eBook)
<https://doi.org/10.1007/978-981-97-3278-4>

Jointly published with Science Press

The print edition is not for sale in China mainland. Customers from China mainland please order the print book from: Science Press.

ISBN of the Co-Publisher's edition: 978-7-03-074646-7

Color wheel and icons: From <https://www.un.org/sustainabledevelopment/>, Copyright © 2020 United Nations. Used with the permission of the United Nations.

The content of this publication has not been approved by the United Nations and does not reflect the views of the United Nations or its officials or Member States.

This project is co-published with Science Press, Beijing, China

© The Editor(s) (if applicable) and The Author(s) 2024. This book is an open access publication.

Open Access This book is licensed under the terms of the Creative Commons Attribution-NonCommercial-NoDerivatives 4.0 International License (<http://creativecommons.org/licenses/by-nc-nd/4.0/>), which permits any noncommercial use, sharing, distribution and reproduction in any medium or format, as long as you give appropriate credit to the original author(s) and the source, provide a link to the Creative Commons license and indicate if you modified the licensed material. You do not have permission under this license to share adapted material derived from this book or parts of it.

The images or other third party material in this book are included in the book's Creative Commons license, unless indicated otherwise in a credit line to the material. If material is not included in the book's Creative Commons license and your intended use is not permitted by statutory regulation or exceeds the permitted use, you will need to obtain permission directly from the copyright holder.

This work is subject to copyright. All commercial rights are reserved by the author(s), whether the whole or part of the material is concerned, specifically the rights of reprinting, reuse of illustrations, recitation, broadcasting, reproduction on microfilms or in any other physical way, and transmission or information storage and retrieval, electronic adaptation, computer software, or by similar or dissimilar methodology now known or hereafter developed. Regarding these commercial rights a non-exclusive license has been granted to the publisher.

The use of general descriptive names, registered names, trademarks, service marks, etc. in this publication does not imply, even in the absence of a specific statement, that such names are exempt from the relevant protective laws and regulations and therefore free for general use.

The publishers, the authors, and the editors are safe to assume that the advice and information in this book are believed to be true and accurate at the date of publication. Neither the publishers nor the authors or the editors give a warranty, express or implied, with respect to the material contained herein or for any errors or omissions that may have been made. The publishers remain neutral with regard to jurisdictional claims in published maps and institutional affiliations.

This Springer imprint is published by the registered company Springer Nature Singapore Pte Ltd. The registered company address is: 152 Beach Road, #21-01/04 Gateway East, Singapore 189721, Singapore

If disposing of this product, please recycle the paper.

Editorial Board

Editor-in-Chief

Huadong Guo

Associate Editors-in-Chief

Fang Chen	Yu Chen	Jinwei Dong	Qunli Han
Chunlin Huang	Lei Huang	Gensuo Jia	Li Jia
Xiaosong Li	Dong Liang	Jie Liu	Shanlong Lu
Zheng Niu	Zhongchang Sun	Futao Wang	Bingfang Wu
Mingquan Wu	Rencheng Yu	Lijun Zuo	

Editorial Board

Jie Bai	Fulong Chen	JinSong Chen	Yaning Chen
Zuoqi Chen	Lijing Cheng	Yun Cheng	Yingying Dong
Shihong Du	Hongtao Duan	Yaya Feng	Danmin Fu
Feng Gao	Xumiao Gao	Haifeng Gu	Jiapaer Guli
Bing He	Yanfang Hou	Kailong Hu	Yonghong Hu
Ni Huang	Wenjiang Huang	Liangliang Jiang	Junsheng Li
Sijia Li	Xuecao Li	Xuegang Li	Zhi Li
Po Teen Lim	Liangyun Liu	Ronggao Liu	Saimiao Liu
Shaochuang Liu	Yang Liu	Yupeng Liu	Lei Luo
Jinge Ma	Shengya Ou	JunQiang Qiao	Jingxiu Qin
Xingli Qin	Liping Shang	Hua Su	Liqun Sun
Shilin Tang	Yunwei Tang	Changjian Wang	Li Wang
Meng Wang	Shenglei Wang	Xuanxuan Wang	Yagang Wang
Xianhu Wei	Xuexin Wei	Lili Xia	Yihan Xie
Dongmei Yan	Nana Yan	Ruixia Yang	Bailang Yu
Hongwei Zeng	Bing Zhang	Miao Zhang	Xiao Zhang
Yuanling Zhang	Chang Zhao	Longlong Zhao	Zhijia Zheng
Guorong Zhong	Jinfeng Zhu	Weiwei Zhu	

Principle Authors

Jie Bai	Fulong Chen	Yaning Chen	Jinsong Chen
Zuoqi Chen	Yu Chen	Lijing Cheng	Yingying Dong
Shihong Du	Hongtao Duan	Xumiao Gao	Feng Gao
Haifeng Gu	Huadong Guo	Bing He	Yanfang Hou
Yonghong Hu	Wenjiang Huang	Lei Huang	Ni Huang
Gensuo Jia	Liangliang Jiang	Guli Jiapaer	Xuegang Li
Zhi Li	Xiaosong Li	Sijia Li	Xuecao Li
Dong Liang	Liangyun Liu	Shaochuang Liu	Ronggao Liu
Saimiao Liu	Yang Liu	Shanlong Lu	Lei Luo
Jinge Ma	Jingxiu Qin	Xingli Qin	Hua Su
Zhongchang Sun	Liqun Sun	Shilin Tang	Yunwei Tang
Futao Wang	Shenglei Wang	Yagang Wang	Li Wang
Xuexin Wei	Mingquan Wu	Bingfang Wu	Yihan Xie
Nana Yan	Ruixia Yang	Bailang Yu	Hongwei Zeng
Bing Zhang	Xiao Zhang	Miao Zhang	Chang Zhao
Longlong Zhao	Zhijia Zheng	Guorong Zhong	Weiwei Zhu
Jinfeng Zhu	Lijun Zuo		

Foreword

The United Nations (UN) 2030 Agenda for Sustainable Development (2030 Agenda) draws a grand blueprint for global sustainable development from the three dimensions of the economy, society, and environment. However, a lack of data, unbalanced development, mutual constraints between goals, and other challenges pose major obstacles to the implementation of the UN Sustainable Development Goals (SDGs) defined in the 2030 Agenda. At the same time, the impact of climate change has intensified, the COVID-19 pandemic has been repeatedly prolonged, and regional tensions have intensified, greatly increasing the difficulty of implementing and realizing the 2030 Agenda. In 2021, President Xi Jinping proposed a global development initiative at the 76th session of the UN General Assembly to accelerate the implementation of the 2030 Agenda and promote stronger, greener, and healthier development.

Also in 2021, the UN Sustainable Development Goals Report clearly pointed out that data is a resource for rebuilding and accelerating the realization of the SDGs, and it is more important than ever to obtain and master timely, high-quality data. To this end, the UN Secretary-General proposed a data strategy to promote the acquisition of more relevant, disaggregated, timely data to track, predict, and accelerate the implementation of the SDGs so that we can transform data and information into insight, and in turn, optimize the decision-making process.

International comparability and availability of data have improved as digitization has accelerated across the globe, but gaps remain in geographic coverage and timeliness of SDG data across sectors, and innovative approaches are urgently needed to fill these gaps. One such innovation is Big Earth Data, a field integrating technologies and methods from Earth science, information science, and space science. Big Earth Data has macroscopic, dynamic monitoring capabilities and can greatly improve data acquisition, providing important support for the realization of the SDGs.

On September 22, 2020, President Xi Jinping announced at the 75th session of the UN General Assembly that China would establish the International Research Center of Big Data for Sustainable Development Goals (CBAS). On September 6, 2021, CBAS was officially established as the world's first international scientific research institution dedicated to using big data to serve the 2030 Agenda. Since its establishment, the center has provided SDG indicators for the world by researching and building a

big data platform for the SDGs, launching and operating a sustainable development science satellite (SDGSAT-1), and carrying out research on technical methods of Big Earth Data for SDG monitoring and evaluation to actively contribute to the implementation of the 2030 Agenda.

From 2019 to 2021, the Chinese Academy of Sciences (CAS) took the lead in compiling the annual “Report on Big Earth Data in Support of the Sustainable Development Goals” for three consecutive years, cumulatively contributing 207 case studies on monitoring and evaluating the SDGs, including 178 data products, 103 methods and models, and 154 decision support guidelines, showing China’s exploration and practice of Big Earth Data technology to support global and regional sustainable development.

This year’s report, *Big Earth Data in Support of the Sustainable Development Goals (2022)—The Belt and Road*, continues to focus on seven SDGs and the multi-indicator intersections of Zero Hunger, Clean Water and Sanitation, Sustainable Cities and Communities, Climate Action, Life Below Water, and Life on Land. This report presents in-depth research on interrelationships, trade-offs, and coordination roles for measuring SDG indicators, including the prospect of expanding the goal of Affordable and Clean Energy (SDG 7) and comprehensive regional research on the SDGs according to regional characteristics. On the basis of the numerous studies presented here, this report concludes with recommendations to heed the changes in the ecological environment, integrate, and innovate on the basis of four-year case results, conduct a comprehensive assessment of 56 environmental indicators, and continue using Big Earth Data to monitor the progress of SDGs.

This report organizes more than 170 scientific research personnel from more than 40 units in scientific research institutes and universities. It brings together the latest research results in the field of big data for sustainable development. The leaders and agencies of CAS have given great support, and the comrades on the writing team have worked hard. I would like to express my heartfelt thanks.



Huadong Guo (Beijing, China)

Director-General of the International
Research Center of Big Data
for Sustainable Development Goals

Member of the 10-Member group
of the United Nations Sustainable
Development Goals Technology Facilitation Mechanism
(2018–2021)

Executive Summary

This report presents 31 case studies where Big Earth Data was used to monitor and evaluate 18 targets under seven SDGs—SDG 2 (Zero Hunger), SDG 6 (Clean Water and Sanitation), SDG 7 (Affordable and Clean Energy), SDG 11 (Sustainable Cities and Communities), SDG 13 (Climate Action), SDG 14 (Life Below Water), and SDG 15 (Life on Land)—as well as a discussion of the interactions among SDG indicators. These cases demonstrate SDG monitoring and assessment outcomes in representative regions involved in China’s Belt and Road (BAR) initiative from three aspects: data products, methods and models, and decision support. They can inform decisions and represent innovative practices using big data to advance the implementation of the SDGs.

Regarding SDG 2, Zero Hunger, the case studies in this report focus on SDG 2.3.1 (production per labor unit) and SDG 2.4.1 (proportion of productive and sustainable agricultural areas), addressing both cropping systems and livestock systems. Seven models were proposed from the aspects of cropland area and cropping intensity (CI), the estimation of production and its impact factors, and grassland carrying capacity (GCC). Datasets include global cropland changes from 1985 to 2020, global CI in 2020, GCC in five Central Asian countries and Mongolia, gridded crop production in Africa, desert locusts in Asia and Africa, and drought distribution in the Mekong River Basin (MRB) of the Indochina Peninsula. Support for decision-making was provided for the development of cropping systems and livestock systems in different regions.

For Clean Water and Sanitation (SDG 6), this report focuses on improving water quality (SDG 6.3) and integrated water resources management (SDG 6.5). The case studies demonstrate research at the global and regional (Central Asia) scales using Big Earth Data. Models were developed for global-scale lake algal bloom extraction and large-scale lake transparency inversion. Datasets were generated for typical global lake algal bloom outbreaks and lake transparency from 2000 to 2021, and decision support guidelines were formed for cooperation-related water events in transboundary rivers in Central Asia. This report exemplifies the feasibility of using water quality indicators obtained by satellite remote sensing to reflect the distribution of water bodies around the world with good water quality, integrating datasets from different sources to solve the problem of data gaps.

In terms of SDG 7, Affordable and Clean Energy, this report utilizes Big Earth Data technology to conduct case studies and generate datasets on the global status of providing electricity, China's international energy cooperation projects (CIECPs), and China's international training on solar energy utilization. These case studies reflect the global energy supply situation and the effectiveness of China's international energy cooperation in recent years from different perspectives.

In the context of SDG 11, Sustainable Cities and Communities, this report details efforts concerning monitoring and evaluating the urbanization process, World Heritage protection, and urban green space. The data products developed by the case studies include, at the global scale, a dataset on the world's major urban built-up area (UBA), a global "NPP-VIIRS-like" nighttime light annual composited dataset, a dataset on global urban land use extents under various shared socioeconomic pathways (SSPs), vector data on World Heritage boundaries, and a dataset on the trend of global greenness. Based on the analysis of the above datasets, the case studies found that global urbanization developed in a more balanced way from 2000 to 2020; the land cover change in World Cultural Heritage sites was generally less than 1% and overall protection was good from 2015 to 2020; China accounts for 19% of the world's UBA, but 28% of the world's significant greening urban areas; and the Chinese population benefiting from significant greening in urban areas accounts for about 47% of the global beneficiary population.

In terms of SDG 13, Climate Action, focusing on the three themes of disaster monitoring and reduction, climate change early warning, and global land/marine carbon sink estimation, the case studies developed a high-temperature heat wave distribution dataset, an ocean heat/salinity dataset, and a series of global land/ocean carbon sink data products. Based on data analysis, it was found that global land continues to heat up, with an increase in the frequency and intensity of heat waves. From 2011 to 2020, the frequency of heat waves in approximately 55% of the global land area showed an upward trend, and the global ocean heat content (OHC) showed a significant increase from 1955 to 2021 at a rate of 5.7×10^{22} J/10a. The warming of the ocean significantly accelerated after the 1990s, and the salinity of the ocean showed a "salty to saltier, light to lighter" change pattern. From 2000 to 2020, the global total terrestrial net ecosystem productivity (NEP) showed a significant increasing trend (0.05 Pg C/a, $p < 0.05$). Overall, the ocean is a strong sink of atmospheric CO₂, especially since 2008, and the intensity of oceanic carbon sequestration has shown a continuous strengthening trend.

Regarding SDG 14, Life Below Water, this report focuses on reducing marine pollution (SDG 14.1) and protecting marine and coastal ecosystems (SDG 14.2). Three case studies were carried out to produce datasets on the spatial distribution characteristics of harmful algal bloom species in the South China Sea and surrounding waters, monitoring and early warning of the thermal environments of coral reef bleaching in China-ASEAN seas, and dynamic changes in phytoplankton size class (PSC) in the North Indian Ocean (NIDO). Corresponding monitoring and analytical methods, models, and decision support guidelines were also produced for supporting

applications. These research results reflect the effectiveness of the implementation of sustainable management of the oceans and seas in recent years from different perspectives.

Regarding SDG 15, Life on Land, the case studies focus on three indicators: specific indicators such as the sustainable management of all types of forests (SDG 15.2), land degradation neutrality (SDG 15.3), and habitat protection of endangered species (SDG 15.5). In the context of the Belt and Road initiative, this report has developed indicator evaluation models and methods supported by Big Earth data. Demonstrative applications have been conducted, resulting in consistent and continuous forest cover data from 2000 to 2020, global 30 m sand dune/land datasets for the years 2000, 2010, and 2020, and spatial distribution products of suitable habitats for wild camels in the years 2050 and 2070 under current and future climate change conditions. This report has also identified key regions of human-induced land degradation in Central Asia, providing robust support for the dynamic monitoring and assessment of SDG 15 indicators.

Regarding interactions among SDGs and integrated evaluations, the sustainable development of the water-energy-food-ecology (WEFE) system in Central Asia was taken as an example. The pressures and transmission processes of water, energy, food, and ecosystems in the five Central Asian countries were studied, and a framework for resolving conflicts between water and energy was proposed. Two mitigation strategies, “same effect trade agreement” (to replace “equivalent trade agreement”) and “power transmission from east to west” (i.e., importing power from China), were put forward to promote the sustainable development of Central Asian countries.

Contents

1	Introduction	1
2	SDG 2, Zero Hunger	5
3	SDG 6, Clean Water and Sanitation	47
4	SDG 7, Affordable and Clean Energy	73
5	SDG 11, Sustainable Cities and Communities	87
6	SDG 13, Climate Action	121
7	SDG 14, Life Below Water	143
8	SDG 15, Life on Land	167
9	Interactions Among SDGs and Integrated Evaluations.	189
10	Summary and Prospects	203
	Index	207

Acronyms

ADI	Agricultural drought index
AEZs	Agro-ecological zones
AGB	Aboveground biomass
AMSR	Advanced microwave scanning radiometer
Argo	Array for Real-time Geostrophic Oceanography
AS-a	Area of artificial surface
AS-B	Spatial combination between artificial surface and bare land
AS-c	Patch count of artificial surface
ASP	Amnesic shellfish poison
AVHRR	Advanced Very High Resolution Radiometer
B-a	Area of bare land
BA-HID	Boundary areas-human intervention degree
BAR	Belt and Road
BEPS	Boreal ecosystem productivity simulator
BGC-Argo	Biogeochemical-Argo
CA	Cellular automata
CAMA	China Association of Marine Affairs
CCA	Canonical correspondence analysis
CFS	Climate forecast system
CHIRPS	Climate Hazards Group InfraRed Precipitation with Station data
Chla	Chlorophyll a
CI	Cropping intensity
CITES	Convention on International Trade in Endangered Species of Wild Fauna and Flora
CL-a	Area of cultivated land
CL-AS	Spatial combination between cultivated land and bare land
CL-c	Patch count of cultivated land
CL-F	Spatial combination between cultivated land and forest
CL-G	Spatial combination between cultivated land and grassland
CMI	Cyanobacteria and macrophytes index
CR	Critically endangered
CRU	Climatic Research Unit
DEM	Digital elevation model
DIC	Dissolved inorganic carbon
DMSP-OLS	Defense Meteorological Satellite Program-Operational Linescan System

DNA	Deoxyribonucleic acid
DORS	Deep ocean remote sensing
DOY	Day of year
DSP	Diarrhetic shellfish poison
DSR	Dynamic sediment ratio
ECMWF	European Centre for Medium-Range Weather Forecasts
EMLS	European Multi Lake Survey
ENSO	El Niño and Southern Oscillation
ESA CCI	European Space Agency Climate Change Initiative
EVI	Enhanced vegetation index
F-a	Area of forest
FAI	Floating algae index
FAO	Food and Agriculture Organization of the United Nations
F-AS	Spatial combination between forest and artificial surface
F-B	Spatial combination between forest and bare land
F-c	Patch count of forest
GAEZ4.0	Global Agro-Ecological Zones V4
G-AS	Spatial combination between grassland and artificial surface
GBIF	Global Biodiversity Information Facility
GCBD	Global Coral Bleaching Database
GCBI	Grassland capacity balance index
GCC	Grassland carrying capacity
GCSI	Grassland carrying status index
GDP	Gross domestic product
GEE	Google Earth Engine
GEO	Group on Earth Observations
GFS	Global Forecast System
GHCN	Global Historical Climatology Network
GHSL	Global Human Settlement Layer
GIS	Geographic information system
GLASS	Global Land Surface Satellite
GLWD	Global Lakes and Wetlands Database
GPWv4	Gridded Population of the World, v.4
HID	Human intervention degree
HSI	Habitat suitability index
IAP	Institute of atmospheric physics
I-c	Patch count of ice
IEA	International Energy Agency
IGBP	International Geosphere-Biosphere Programme
IIASA	International Institute for Applied Systems Analysis
IRENA	International Renewable Energy Agency
IUCN	International Union for Conservation of Nature
LAI	Leaf area index
LC	Ratio of land-cover change
LCRPGR	Ratio of land consumption rate to population growth rate
LC _x	Ratio of land-cover change of certain type
LDN	Land degradation neutrality
LP DAAC	Land Processes Distributed Active Archive Center
LST	Land surface temperature

MAE	Mean absolute error
MBT	Mechanical bathythermographs
MERRA	Modern era retrospective analysis for research and applications from NASA
MODIS	Moderate Resolution Imaging Spectroradiometer
MRB	Mekong River Basin
MRC	Mekong River Commission
NASA	National Aeronautics and Space Administration
NCEI	National Centers for Environmental Information
NCEP	National Centers for Environmental Prediction
NDSI	Normalized difference snow index
NDVI	Normalized difference vegetation index
NEP	Net ecosystem production
NOAA	National Oceanic and Atmospheric Administration
NODC	National Oceanographic Data Center
NPP	Net primary productivity
NPP-VIIRS	National Polar-orbiting Partnership—Visible Infrared Imaging Radiometer Suite
NSP	Neurotoxic shellfish poison
OBIA	Object-based image analysis
OHC	Ocean heat content
OISST	Optimum interpolation sea surface temperature
OLDI	Optimal land degradation index
PAR	Photosynthetically active radiation
$p\text{CO}_2$	Partial pressure of the CO_2
PET	Potential evapotranspiration
PSO-PEE	Projection pursuit model based on particle swarm optimization
PSP	Paralytic shellfish poison
RCP	Representative concentration pathway
RMSE	Root mean square error
SD	Secchi disk
SDGs	Sustainable Development Goals
SDSN	Sustainable Development Solutions Network
SHAP	Sharpley Additive exPlanations
SNA	Social network analysis
SOM	Self-organizing map
SPEI	Standardized precipitation evapotranspiration index
SRTM	Shuttle Radar Topography Mission
SSPs	Shared socioeconomic pathways
TEOW	Terrestrial ecoregions of the world
TFDD	Transboundary Freshwater Dispute Database
TOA	Top-of-atmosphere
TVDI	Temperature vegetation dryness index
TWI	Turbid water index
UCSB/CHC	Climate Hazards Center of the University of California, Santa Barbara
UNCCD	United Nations Convention to Combat Desertification

UNEP	United Nations Environment Programme
UNESCO	United Nations Educational, Scientific and Cultural Organization
USDA	United States Department of Agriculture
VCHP	Vietnam Central High Plain
WB-a	Area of water body
WB-AS	Spatial combination between water body and artificial surface
WDPA	World Database on Protected Areas
WEFE	Water-energy-food-ecology
WHO	World Health Organization
WSI	Water stress index
XBT	Expendable bathythermograph
XGBoost	eXtreme Gradient Boosting
ZOTU	Zero-radius operational taxonomic unit
Z_{SD}	Secchi disk depth



Introduction

1

The 17 SDGs adopted by the UN as part of the 2030 Agenda constitute a global framework for achieving sustainable development. They have become a strategic priority and focus of action for countries worldwide. However, almost half-way into the 2030 Agenda process, its implementation has been seriously hindered by climate change and the COVID-19 pandemic, with global progress in individual goals even facing setbacks. The goals will not be achieved by 2030 unless implementation is accelerated. In 2021, about one-tenth of the world's population went hungry; more than three billion people were at health risk due to scarce data on the water quality of rivers, lakes, and groundwater; globally, 733 million people still lacked access to electricity; cities were hard hit by the COVID-19 pandemic; four key climate change indicators—global greenhouse gas concentration, sea-level rise, ocean heat, and ocean acidification—hit record highs; increasing ocean acidification, eutrophication, and plastic pollution put the livelihoods of billions of people at risk; and continued global deforestation, land and ecosystem degradation, and loss of biodiversity posed major threats to human survival and sustainable development (UN 2022; Sachs et al. 2022).

Science, technology, and innovation can help address these major challenges, primarily to support assessments at national and local scales and inform policy-making by enhancing data capacity for SDG monitoring and evaluation. The UN Sustainable Development Goals Report 2022 pointed out that the pandemic has delayed the development of new national statistical plans worldwide, and there are still considerable gaps in the geographical coverage and timeliness of global data on indicators (UN 2022). Meanwhile, the current indicator data are primarily of coarse-grained statistical values, with the time resolution mostly being “annual” and the spatial resolution mostly “national,” incapable of disaggregation by geographical locations, population distributions, and environmental differences, which are crucial to thoroughly assessing regional differences in SDG progress and identifying those lagging behind. Thus, there is not enough data to effectively inform sub-national governments' decision-making. According to estimates from the Organisation for Economic Co-operation and Development (OECD), 105 out of the 169 SDG targets will be challenging to achieve without sufficiently engaging sub-national governments (OECD 2020). Many are environmental targets sensitive to spatial and temporal changes.

As the core of digital technology, big data has become an important engine of digital transformation across societies. Big Earth Data, a key part of big data, mainly composed of Earth observation and geospatial data, has the advantages of easy acquisition, timely updates, objective results, and higher resolution. Moreover, it covers different spatial scales and geographical locations free from administrative fragmentation, allowing a more accurate assessment of SDG indicator progress and prompt detection of problems. Its role in analyzing the complex interactions and co-evolution between nature and social systems will contribute to the overall understanding and realization of the SDGs.

The seven SDGs of Zero Hunger (SDG 2), Clean Water and Sanitation (SDG 6), Affordable and Clean Energy (SDG 7), Sustainable Cities and Communities (SDG 11), Climate Action (SDG 14), Life Below Water (SDG 14), and Life on Land (SDG 15) are closely related to Earth's surface environment and human activity and can be directly measured and evaluated using Big Earth Data. The Chinese Academy of Sciences (CAS) has used its interdisciplinary strengths to gather a wide variety of Big Earth Data, including satellite remote sensing images, geospatial data, social media data, and statistical data, for these seven SDGs. CAS has developed innovative technologies and methods for big data processing and analysis based on cloud computing, such as the production of global public data products, the monitoring and evaluation of SDG indicators at multiple scales, and multi-indicator trade-off-and-synergy analysis, to provide data, methods, and information for SDG-related progress assessments, multi-disciplinary research, and multi-level decision-making (Fig. 1.1).

The reports on Big Earth Data in Support of the Sustainable Development Goals have been released annually since 2019. In terms of filling the data gaps, the reports provide high-quality data products previously lacking for monitoring SDG indicators, such as the dataset on the prevalence of stunting among children under five in China. They also provide additional background and analytical data for a deeper understanding of the progress and drivers of indicators, such

as long-term time-series data products on global land use classification. In terms of methods and models, the reports offer new ways for more timely and detailed assessment and prediction of SDG indicators, such as a high-precision inversion model of global crop intensity and rapid extraction method of global urban impervious surfaces. The reports also present scientific evidence for decision support, including the tracking and assessment of China's land degradation neutrality (LDN) and its contribution to the world, and the assessment of dynamic changes of water bodies in Ramsar sites, which can inform policy-making on improving the global synergy and comparability of indicators and addressing cross-border sustainable development issues. In 2022, in the context of climate change, the report added a chapter that looks at SDG 7 and its monitoring and evaluation based on Big Earth Data and explored the interactions between climate change and food systems, the carbon sequestration effect of desertification control, and changes in the physical marine environment under global warming.

Based on the datasets from the 2019–2022 reports, and with reference to the explicit thresholds in SDGs and targets, and quantitative targets defined by UN agencies and international organizations, the 2022 report assesses China's progress on 56 environmental SDG indicators between 2010 and 2021 (UNEP 2021). Some quantitative findings on the progress include the exploratory results of applying critical big data processing, analytics, and other innovative methods.

The BAR is an abbreviation of the “Silk Road Economic Belt” and the “21st Century Maritime Silk Road,” or the Belt and Road. The regions along the BAR are the most obvious areas with unbalanced and inadequate development and are crucial to the implementation of the 2030 Agenda. The 2022 report focuses on updates and extensions, new methodologies and indicators, the tracking and evaluation of SDG implementation, the study of interactions among multiple SDGs, and coordinated development in light of those interactions. It presents 47 case studies on 19 targets relevant to countries and

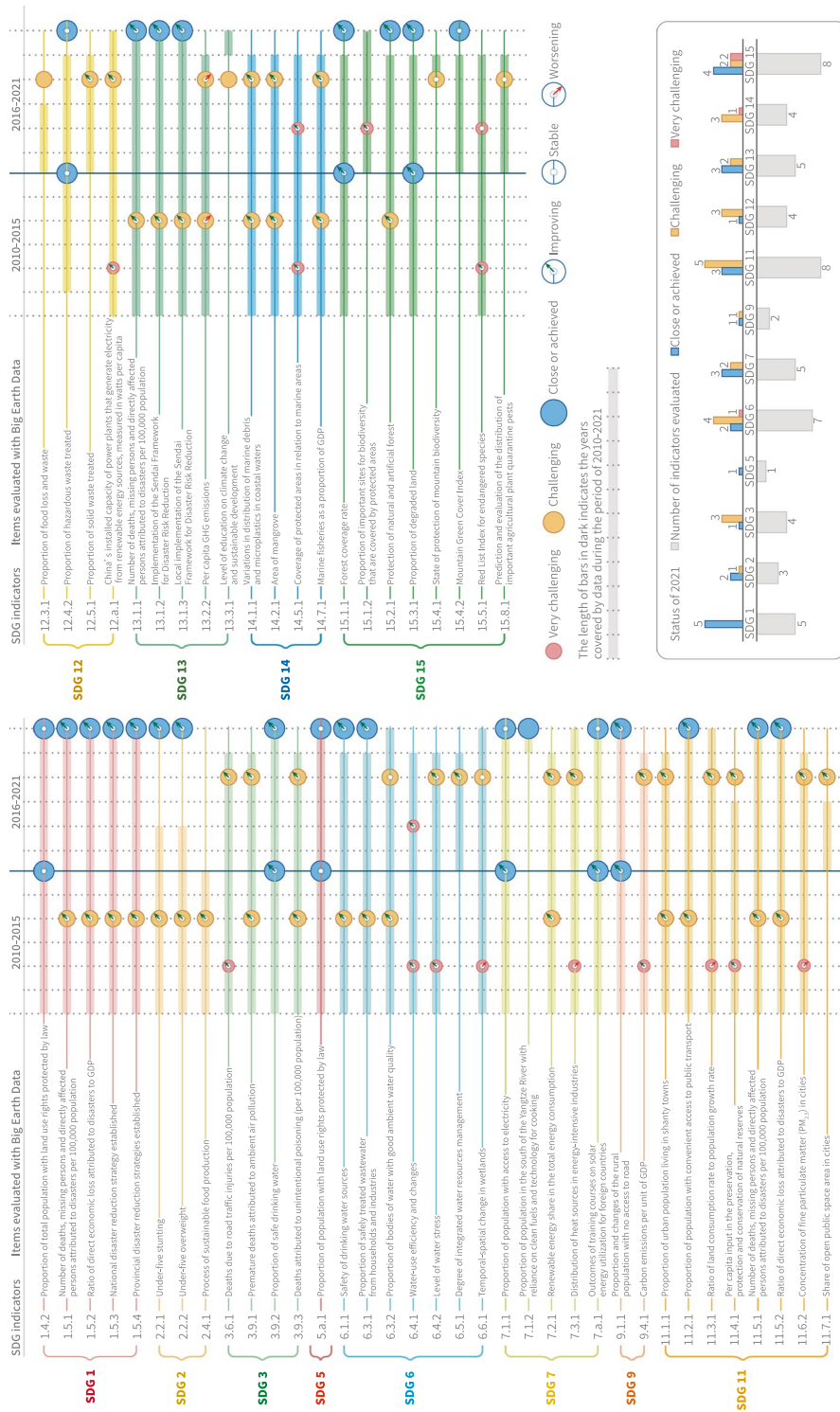


Fig. 1.1 Examples of how big earth data supports SDGs

regions involved in the BAR initiative. The 2022 report showcases the results of research, monitoring, and evaluation of SDGs and their indicators at four scales—local, national, regional, and global—totaling 31 data products, 21 methods and models, and 33 decision-support recommendations.

With a deep commitment to sustainable development and experience-sharing, China has been promoting a balanced, coordinated, open, and inclusive new stage of global development. In September 2021, President Xi Jinping proposed a Global Development Initiative, calling for all-round cooperation in priority areas, including poverty alleviation, food security, climate change, green development, and connectivity, to ensure that no one is left behind in these areas aligned with the 2030 Agenda. According to the list of deliverables attached to the Chair's Statement of the High-level Dialogue on Global Development held in June 2022, China will launch a Sustainable Development Satellite Constellation Plan, and develop and share data and information for SDG monitoring, which will be an important contribution to advancing global SDG cooperation in coordinated Earth observation, data sharing and application, and accelerating the implementation of the 2030 Agenda.

As the mid-term evaluation of the 2030 Agenda approaches, the UN will comprehensively review and adjust its SDG indicator framework globally. In the context of lacking

enough indicator monitoring data, properly adding easily accessible and internationally comparable big data indicators will effectively improve the existing condition of SDG monitoring and evaluation, and effectively support decision-making for sustainable development both globally and along the Belt and Road.

The book is divided into chapters. This chapter has introduced the topics of the case studies and the purpose of compiling them in this report. Chapters 2–8 provide examples of using Big Earth Data to measure and monitor the progress of seven SDGs. Chapter 9 provides new insights into the interactions among the SDGs and integrated evaluations. Chapter 10 summarizes the studies and reflects on future prospects.

References

- OECD (2020) A territorial approach to the sustainable development goals: synthesis report (2020). <https://doi.org/10.1787/e86fa715-en>
- Sachs JD, Lafortune G, Kroll C et al (2022) From crisis to sustainable development: the SDGs as roadmap to 2030 and beyond. In: Sustainable development report 2022. Cambridge University Press, Cambridge. <https://www.sustainabledevelopment.report/reports/sustainable-development-report-2022/>
- UN (2022) The sustainable development goals report 2022. UN, New York. <https://unstats.un.org/sdgs/report/2022>
- UNEP (2021) Measuring progress: environment and the SDGs. <https://wedocs.unep.org/bitstream/handle/20.500.11822/35968/SDGMP.pdf>. 15 June 2022

Open Access This chapter is licensed under the terms of the Creative Commons Attribution-NonCommercial-NoDerivatives 4.0 International License (<http://creativecommons.org/licenses/by-nc-nd/4.0/>), which permits any noncommercial use, sharing, distribution and reproduction in any medium or format, as long as you give appropriate credit to the original author(s) and the source, provide a link to the Creative Commons license and indicate if you modified the licensed material. You do not have permission under this license to share adapted material derived from this chapter or parts of it.

The images or other third party material in this chapter are included in the chapter's Creative Commons license, unless indicated otherwise in a credit line to the material. If material is not included in the chapter's Creative Commons license and your intended use is not permitted by statutory regulation or exceeds the permitted use, you will need to obtain permission directly from the copyright holder.





2.1 Background

As we approach the midpoint in the implementation of the 2030 Agenda, the achievement of Zero Hunger remains a challenge. In 2021, nearly one-third of the global population (approximately 2.3 billion people) were moderately or severely food insecure, with an increase of nearly 350 million in just one year (FAO, IFAD et al. 2022). Sub-Saharan Africa and South Asia, where small-scale peasant households are predominant, have seen the largest increase in food-insecure people. The outbreak of wars in the Russia–Ukraine region—the source of 30% of global exports of wheat, 20% of maize and 80% of sunflower seed products—has added to global food insecurity. This, along with climate change, extreme weather, conflicts, economic shocks, and rising inequalities, has steered the world away from the goal of achieving Zero Hunger by 2030 (UN 2022).

There is a global consensus on initiating and accelerating the transformation of the agro-food system. In 2021, the UN convened a Food Systems Summit that highlighted how the transformation of food systems would help achieve the SDGs by promoting human health and improving the planet's environment. However,

data, a key driver of the agro-food system and related trends, are far from complete for monitoring progress toward the goal of Zero Hunger, with large deficiencies in geographic coverage, timeliness, and level of classification. More than half of the countries or regions in the world do not have access to valid data for monitoring progress toward Zero Hunger. Big Earth Data with macro-level, dynamic, and rapid monitoring capabilities, can enable regional assessments of food production, environmental changes, and more, realizing a holistic understanding of macro-scale progress and a detailed grasp of regional differences. The effective combination of Big Earth Data and statistical data can greatly improve the current situation of measuring SDG indicators where only assessment methods but no data are available, and can provide new impetus for monitoring the implementation of the SDGs.

Based on our reports over the past three years, we have laid emphasis on SDG 2.3 and SDG 2.4. Focusing on the plant industry in the agricultural production system, we carried out a series of studies ranging from cropland extent distribution, cropping pattern monitoring, and desert locust plague assessment to cropland productivity monitoring, productivity potential assessment, and food security early warning.

In the 2022 report, we will further strengthen the research and development of global public data products that support the monitoring of progress toward Zero Hunger, while continuing to explore the possibilities of using Big Earth Data to monitor sustainable agricultural development in food security hotspots and sensitive regions, with a view to providing support in terms of data, technology, and decision-making for global food security and regional sustainable agricultural development.

2.2 Main Contributions

This chapter illustrates seven case studies that monitored and evaluated indicators of progress toward SDG 2 based on two specific targets, demonstrating China's contributions to the global monitoring of SDG 2 indicators in three aspects; that is, data products, methods and models, and decision support (Table 2.1).

2.3 Case Studies

2.3.1 Dynamic Global Cropland Analysis, 1985–2020

Target: SDG 2.3: By 2030, double the agricultural productivity and incomes of small-scale food producers, in particular women, indigenous peoples, family farmers, pastoralists and fishers, including through secure and equal access to land, other productive resources and inputs, knowledge, financial services, markets, and opportunities for value addition and non-farm employment.

2.3.1.1 Background

SDG 2.4.1, “proportion of agricultural area under productive and sustainable agriculture”, is an important indicator directly related to global food security and sustainable development. In recent decades, with the rapid growth of the global population and the acceleration of industrialization and urbanization, the per capita

cropland area and the amount of food are facing great challenges. According to statistics of the Food and Agriculture Organization of the UN (FAO), the total number of hungry people in the world showed an improving trend of gradual reduction in the early twenty-first century, but this trend has reversed in recent years, and the number of hungry people increased from 604 million in 2014 to 768 million in 2020 (FAO 2020). In order to cope with global food insecurity, the global cropland area is showing a significant increase. Specifically, since the beginning of the twenty-first century, the increase in agricultural cropland area accounted for about 9% of the total cropland area in 2000 (Potapov et al. 2022). Thus, the use of remote sensing data to monitor the change in cropland area is of great significance for assessing global food security.

2.3.1.2 Data

- All available Landsat observations over the globe from 1985 to 2020.
- Three global 30 m land-cover products, including global land-cover with fine classification at 30 m in 2020 (GLC_FCS30-2020), GlobaLand30 in 2020 from the National Geomatics Center of China, and the Global Food Security Analysis Data at 30 m (GFSAD30) cropland product from the United States Geological Survey.
- Global and national population statistics from 1985 to 2020 from the Population Division of the Department of Economic and Social Affairs of the UN.

2.3.1.3 Methods

With time-series cropland dynamic monitoring, the traditional supervised classification strategy usually causes great uncertainties due to the transmission and accumulation of classification errors. In this case, based on full time-series remote sensing observations, we first used the continuous change detection model to fit the time-series reflectance spectra ($\rho_{i,t}^*$). Then, the change time and change frequency were captured according to the difference ($\Delta\rho$) between

Table 2.1 Cases and their main contributions

Targets	Cases	Contributions
SDG 2.3 By 2030, double the agricultural productivity and incomes of small-scale food producers, in particular women, indigenous peoples, family farmers, pastoralists and fishers, including through secure and equal access to land, other productive resources and inputs, knowledge, financial services, markets and opportunities for value addition and non-farm employment	Dynamic global cropland analysis, 1985–2020	Data product: Global 30 m cropland dynamic monitoring dataset from 1985 to 2020 Method and model: A novel cropland dynamic monitoring model by coupling with continuous change detection and dynamic updating algorithm Decision support: Analyzing the gain and loss of cropland and the per capita cropland of major countries from the national and continental scales, providing data support for global food security assessment
	Spatial pattern of cropping intensity and gaps at the global scale	Data product: Global 30 m resolution CI in 2020 Method and model: Global high-resolution remote sensing extraction model for CI Decision support: Identifying areas with large CI gaps in the world to inform decisions on global grain output increase
	Assessment of grassland carrying capacity in five Central Asian countries	Data product: Datasets on GCC in five Central Asian countries in 2010, 2015, and 2020 Method and model: Grassland carrying capacity for ecological conservation objectives in arid areas Decision support: Information for evaluating the productivity of herdsmen in arid areas
	Spatial and temporal variation in grassland carrying capacity in Mongolia and its causes	Data product: Aboveground biomass (AGB) data and GCC data, 2010–2020 Method and model: Evaluation method for GCC in Mongolia Decision support: Data for research and management of the sustainable development of livestock farming in Mongolia
	Identification of areas of stability and vulnerability in crop production in Africa	Data product: Gridded production of maize, rice, wheat, and soybean across African countries, 2010–2020 Method and model: Data-driven gridded crop production model Decision support: Key scientific data to support the identification of vulnerable, stable, and highly productive areas of maize, rice, wheat, and soybean in Africa, as well as the analysis of drivers affecting the spatial distribution of production
SDG 2.4 By 2030, ensure sustainable food production systems and implement resilient agricultural practices that increase productivity and production, that help maintain ecosystems, that strengthen capacity for adaptation to climate change, extreme weather, drought, flooding and other disasters and that progressively improve land and soil quality	Monitoring desert locusts in Asia and Africa	Data product: 500 m remote sensing monitoring dataset of desert locusts in Asia and Africa, 2018–2022 Method and model: Monitoring and forecasting models for desert locust plague Decision support: Results contribute to the protection of agricultural production and food security, and provide important information for locust plague emergency response
	Impacts of extreme drought on agricultural production in the Mekong River Basin of the Indochina Peninsula	Data product: Meteorological drought monitoring datasets for the MRB, 2010–2020 Method and model: Models for meteorological drought and agricultural drought monitoring Decision support: Theoretical basis for identifying areas vulnerable to stable food production and decision-making reference for disaster prevention, loss reduction, and prompt response to potential food crises for management authorities

the model fitting value and the real observation value ($\rho_{i,t}$):

$$\rho_{i,t}^* = a_{0,i} + \sum_{k=1}^n \left(a_{k,i} \cos \left(\frac{2\pi t}{kT} \right) + b_{k,i} \sin \left(\frac{2\pi t}{kT} \right) \right) + c_{0,i} \times t$$

$$\Delta\rho = \rho_{i,t}^* - \rho_{i,t},$$

where $a_{0,i}$ denotes the mean value of the fitted model at the i th band, $a_{k,i}$ and $b_{k,i}$ are the regression coefficients of cosine and sine terms, the $c_{0,i}$ represents the slope of the trend change of the model under full time-series observations, t is the t th Julian day, and n and T are the order and period of the Fourier terms in the fitted model.

On this basis, in order to clarify the dynamic changes of croplands from the full-time satellite observations, this case study first extracted high-confidence, stable time-series cropland samples from three sets of global 30 m land-cover products. Then, combining multi-temporal phenological characteristics and the locally adaptive random forest classification model, we updated cropland-related land-cover changes in real time to achieve the dynamic monitoring target of global 30 m cropland from 1985 to 2020. Lastly, we further combined the statistics of the global population and grain production to quantitatively analyze the per capita cropland at the national scale, which provides scientific understanding and data support for the assessment of food security in various countries.

2.3.1.4 Results and Analysis

Figure 2.1 illustrates the spatial distribution intensity of global 30 m cropland dynamics from 1985 to 2020. In terms of the overall spatial distribution pattern, global croplands are mainly concentrated in areas with flat terrain and relatively abundant rainfall, such as South Asia, Europe, the Great Plains of North America, and the La Plata Plain in South America.

Using eight periods of the global 30 m cropland dynamic monitoring dataset from 1985 to 2020, we quantified the cropland change areas in various countries, and the results indicate

that the cropland dynamics show great differentiation at the national scale. For example, in the populous countries represented by China and India, due to economic growth and urban development needs from 1985 to 2020, some croplands were transformed into impervious surfaces. Correspondingly, due to further development of the agricultural economy in some South American and Southeast Asian countries represented by Brazil, Argentina, and Indonesia, some forests have been reclaimed as newly added croplands. Among them, the increased croplands in Brazil reached about 134,800 km² from 1985 to 2020.

Figure 2.2 illustrates the quantitative statistics of the changed cropland areas over the six continents from 1985 to 2020 (5-year interval). The results indicate that the global total cropland area shows a steady increase over time, with a total increase of about 4.23×10^5 km². Specifically, the increased croplands are mainly concentrated in Africa and South America, because a large amount of wasteland in Africa has been reclaimed as croplands in recent decades, while some forests in South America have been logged and then transformed into croplands, which has led to the growth of croplands in Africa and South America with 454,900 and 266,300 km², respectively.

In addition, we combined the dynamic global cropland data and population statistics to analyze the per capita cropland of the top 20 countries in the world from 1985 to 2020, as shown in Fig. 2.3. The results indicate that there is a significant phenomenon of more people and less land in Asian countries (such as Japan, Bangladesh, India, and China, where the per capita cropland is less than 2.00 km² per thousand people), especially the per capita cropland in Japan at about 0.438 km² per thousand people, and with the increasing population, the per capita cropland in Asian countries is showing an increasingly tense trend. Relatively speaking, countries such as the United States, Russia, and Brazil have high proportions of per capita cropland. Although the population has increased. Significantly increased from 1985 to 2020, the proportion of per capita cropland is still significantly higher than that of Asian countries.

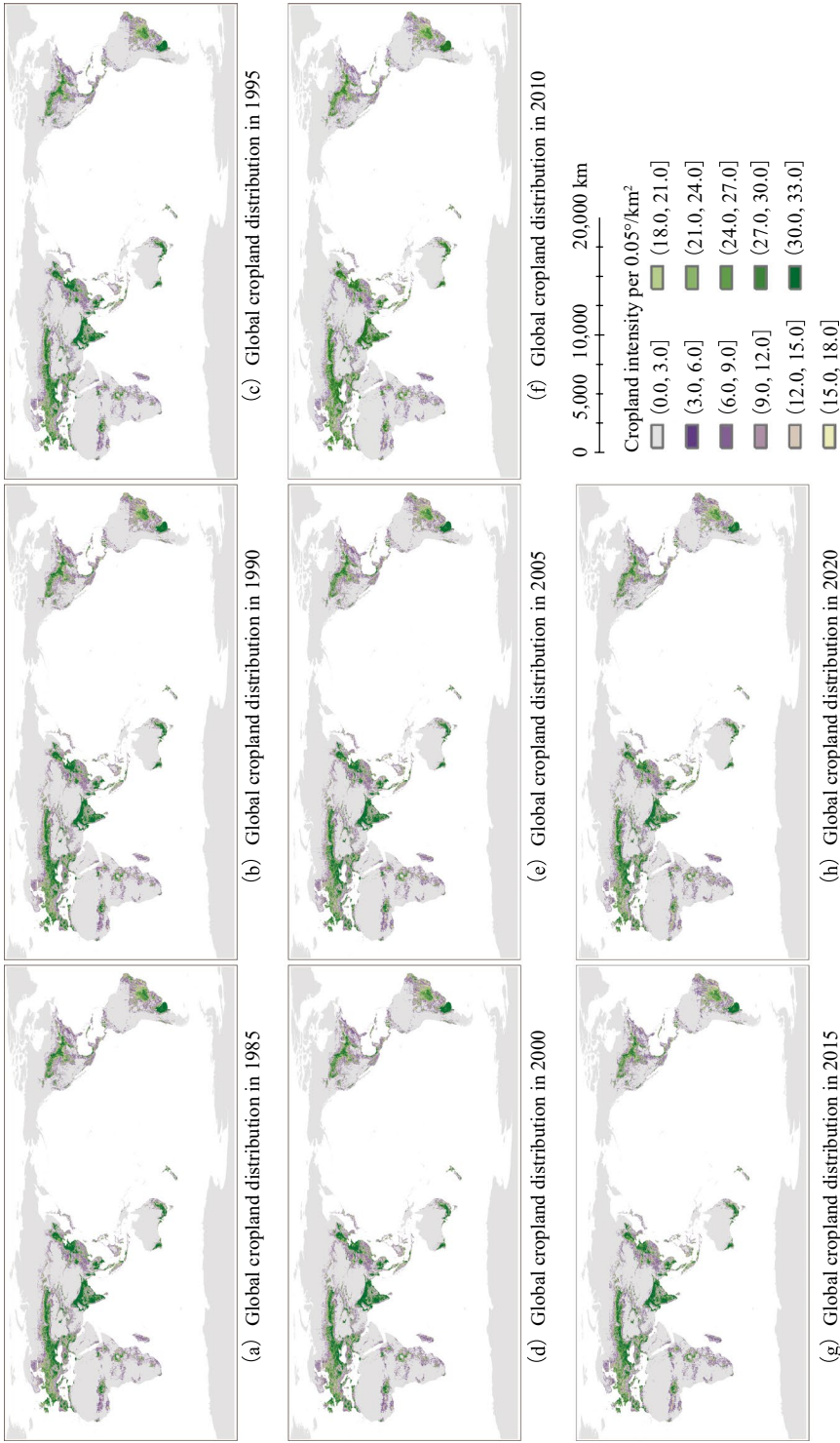


Fig. 2.1 Spatial distribution intensity of global 30 m cropland from 1985 to 2020 under a 0.05° geographic grid

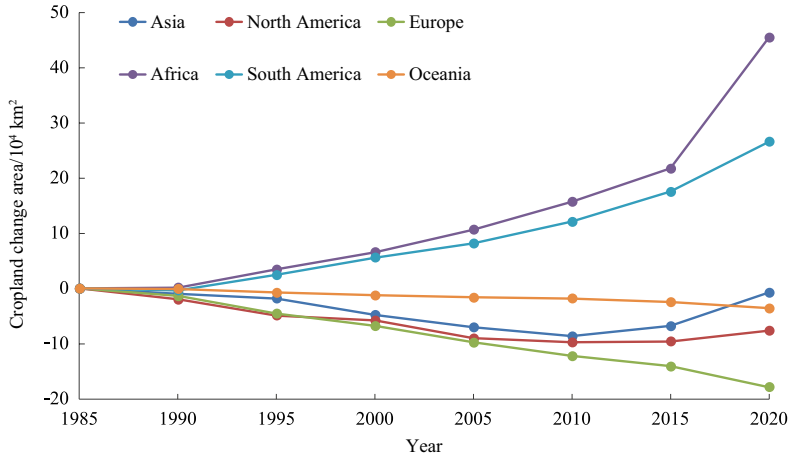


Fig. 2.2 Cropland change area over the six continents from 1985 to 2020

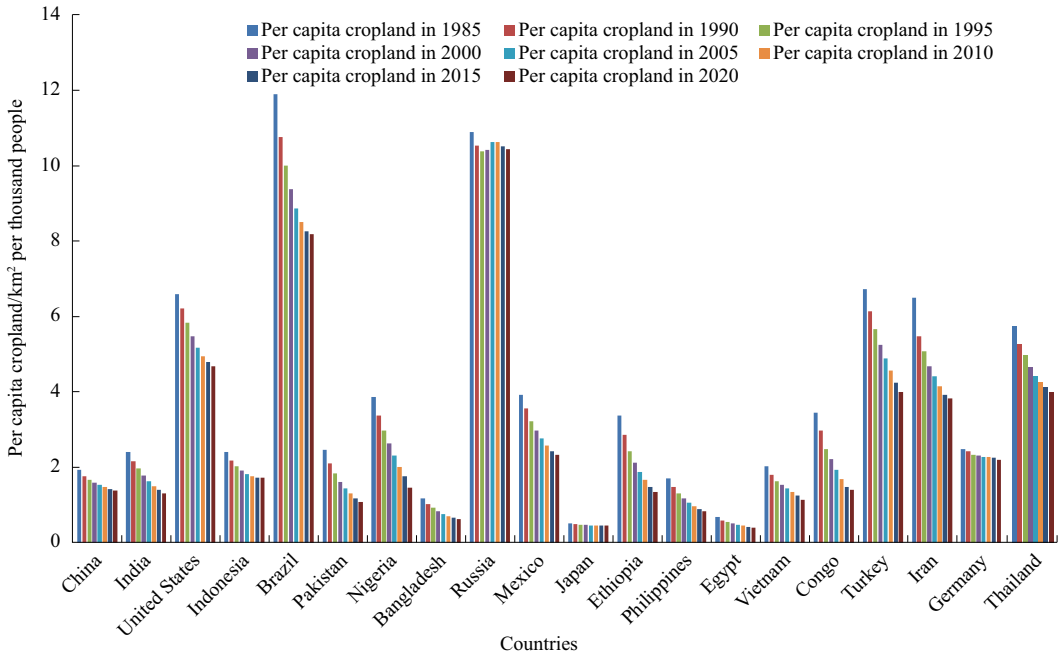


Fig. 2.3 Statistics on the per capita cropland of the 20 most populous countries from 1985 to 2020 (demographic data came from the department of economic and social affairs of the UN)

2.3.1.5 Highlights

- A novel global 30 m cropland dynamic monitoring dataset from 1985 to 2020 was developed.
- The total area of cropland has shown a steady growth trend over the globe from 1985 to 2020, and the net increase of global cropland from 1985 to 2020 was 4.23×10^5 km².
- The cropland dynamics show great differentiation at the national scale. For example, some tropical countries such as Brazil and Indonesia have experienced significant deforestation and reclamation, while developing countries such as China and India have shown the obvious phenomenon of transforming croplands into impervious surfaces.

2.3.1.6 Discussion and Outlook

In this case study, based on the long-term Landsat satellite remote sensing data from 1985 to 2020, a cropland dynamic monitoring model coupled with continuous change detection and a dynamic updating method was proposed, which can improve the continuity and reliability of dynamic cropland monitoring spatially and temporally. Then, we used time-series observations and the proposed methods to develop a global 30 m dynamic cropland monitoring product from 1985 to 2020. Next, we analyzed the gain and loss of cropland on the national and continental scales, and further combined global demographic data to reveal that the global per capita cropland is showing an increasingly tense trend. In future, the monitoring model will be further optimized to realize dynamic cropland monitoring that can distinguish major crop types, and quantitatively analyze global and national food security in combination with multi-source statistical data such as global grain production, so as to provide a more scientific understanding for the realization of sustainable development and accurate data support.

2.3.2 Spatial Pattern of Cropping Intensity and H Gaps at the Global Scale

Target: SDG 2.3: By 2030, double the agricultural productivity and incomes of small-scale food producers, in particular women, indigenous peoples, family farmers, pastoralists and fishers, including through secure and equal access to land, other productive resources and inputs, knowledge, financial services, markets, and opportunities for value addition and non-farm employment.

2.3.2.1 Background

Cropland provides food that supports the very existence and development of humans. Its sustainable use plays an important role in achieving the goal of Zero Hunger. China is a largely agricultural country, but it has a low level of per capita cropland and faces pressure on its food production system brought by industrialization and urbanization (Zuo et al. 2018). Cropping Intensity (CI), defined as the number of crop planting and harvesting cycle(s) within a full year (Liu et al. 2020), is an important indicator that offers a measure of cropland utilization and has profound implications for closing food production gaps and agricultural intensification (Zhang et al. 2021). Its sustained stability is directly linked to the national food security strategy.

Due to diverse cropping practices and various agricultural landscapes across the globe, the retrieval of CI at high resolution with satisfactory accuracy is a great challenge. Previous studies have mainly focused on investigating the spatiotemporal patterns of CI ranging from regions to the entire globe with the use of coarse-resolution data, which are inadequate for characterizing farming practices within heterogeneous landscapes. Thanks to more advanced remote sensing technology, the popularization of high spatiotemporal resolution data has greatly contributed to the accuracy of CI mapping.

This study integrated multi-source remote sensing data and cloud computing technology, to map and analyze CI at the global scale in 2020. Cropping intensity gaps were also analyzed and compared between China and other major agricultural countries.

2.3.2.2 Data

- **Satellite Data:** Sentinel-2, Landsat-5, Landsat-7, Landsat-8, and Gaofen-1 data from 2019 to 2021; moderate resolution imaging spectroradiometer (MODIS) normalized difference vegetation index (NDVI) data at 250 m resolution from 2019 to 2021.
- **Global cropland and CI products** at 30 m resolution from 2016 to 2018 (Zhang et al. 2021), cropland layer (2017) from ChinaCover 30 m resolution land-cover data, GFSAD30 cropland dataset from the United States Geological Survey, and global cropland dynamics 2000–2019 at 30 m resolution (Potapov et al. 2022).
- **Auxiliary Data:** global agro-ecological zones (AEZs) (Gommes et al. 2016), potential multiple-cropping zones from Global Agro-Ecological Zones V4 (GAEZ4.0), and ground-based CI samples.

2.3.2.3 Methods

Globally, 110 AEZs were identified, taking into account differences in climatic zones, topographic conditions, cropping systems, and cropland distributions. According to the phenological information of the AEZs, the starting dates and ending dates of monitoring were determined based on time series MODIS NDVI data at 250 m. The mode of the vegetation index through time for each ecological zone was calculated within the cropland mask area and was used as the start time for monitoring CI for each zone. Within each monitoring unit, all available images of top-of-atmosphere (TOA) reflectance from Landsat, Sentinel-2 (global), and GaoFen (GF-1, China) satellites during the monitoring period were used for CI mapping. These images were used to compose the 16-day TOA reflectance time series based on the maximum

composition method. In order to ensure data continuity, this study used MODIS NDVI data at 250 m to fill temporal gaps with the following steps. First, the MODIS NDVI data at 250 m were re-sized to 30 m using the bicubic algorithm. Second, the Whittaker smoothing algorithm was applied to the gap filled with the NDVI time series to smooth the NDVI time series. We included two phenology metrics, mid-greenup and mid-greendown, which were derived as the day of year (DOY) at the transition points in the greenup and greendown periods when the smoothed NDVI time series passes 50% of the NDVI amplitude. An interval starting from mid-greenup and ending at mid-greendown was defined as a growing phenophase, and an interval moving from mid-greendown to mid-greenup was defined as a non-growing phenophase (Liu et al. 2020; Zhang et al. 2021). We set a lower limit of the growing-harvesting cycle length to 48 days for removing the false cycles. Finally, global CI was mapped at 30 m resolution for 2020. The results were validated based on a large number of ground-based samples obtained worldwide.

Based on the zonal statistical method, the average of CI for each country and the AEZs were calculated and compared with the potential multiple-cropping zones to analyze and identify the CI gaps.

2.3.2.4 Results and Analysis

According to the global CI map at 30 m resolution, the CI index averaged 115% globally in 2020, with 85.2% of cropland in single cropping, 14.4% in double cropping, mainly in East Asia, Southeast Asia, South Asia, and South America (Fig. 2.4). Globally, only 0.4% of the cropland presents triple cropping or above, scattered in tropical and subtropical regions. The cropping pattern is closely related to the water and heat conditions required for crop development. The high average annual temperature and abundant precipitation in the tropical climate zone can meet the heat and water demands of crops with multiple-cropping patterns. The proportion of cropland with multiple-cropping patterns to the total cropland area in regions such

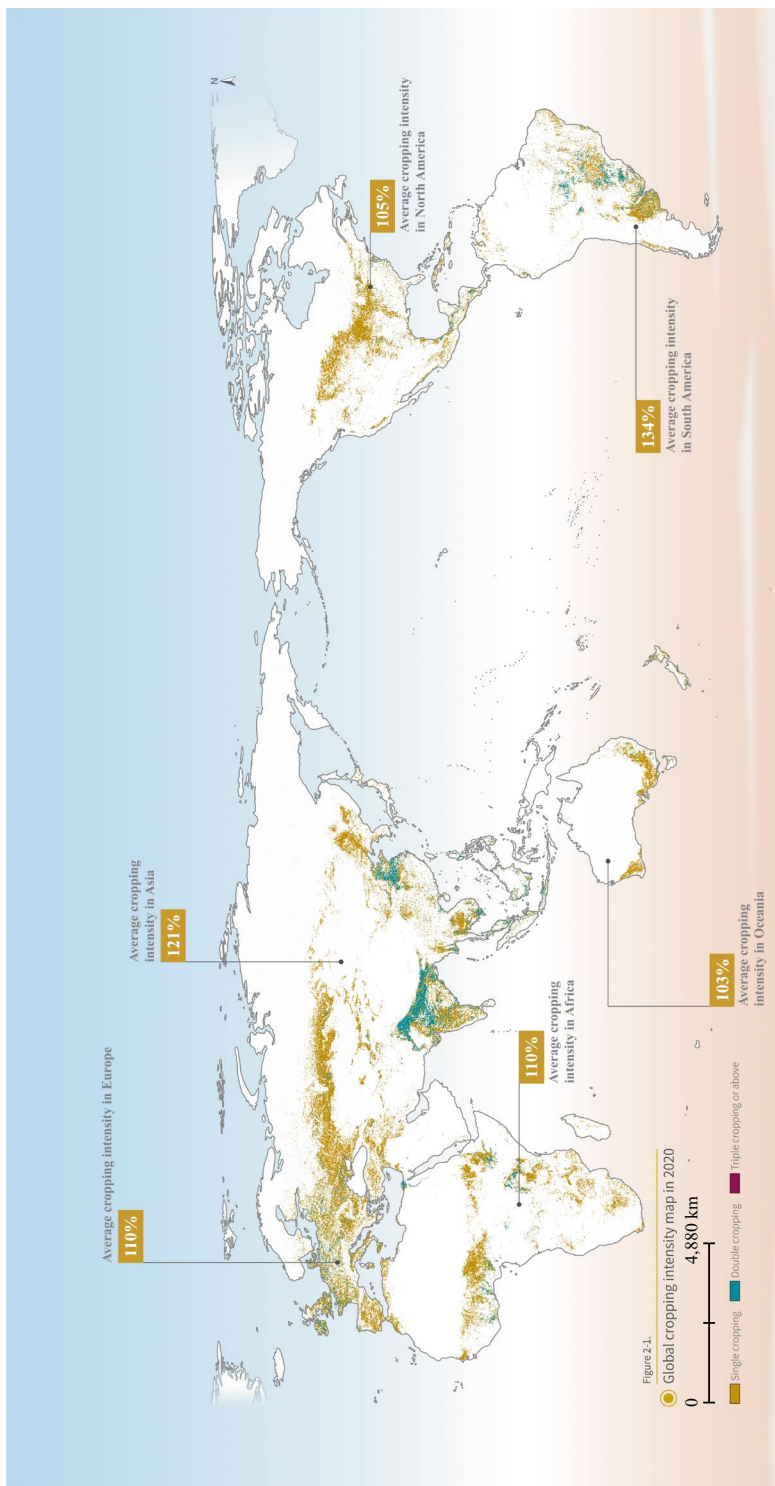
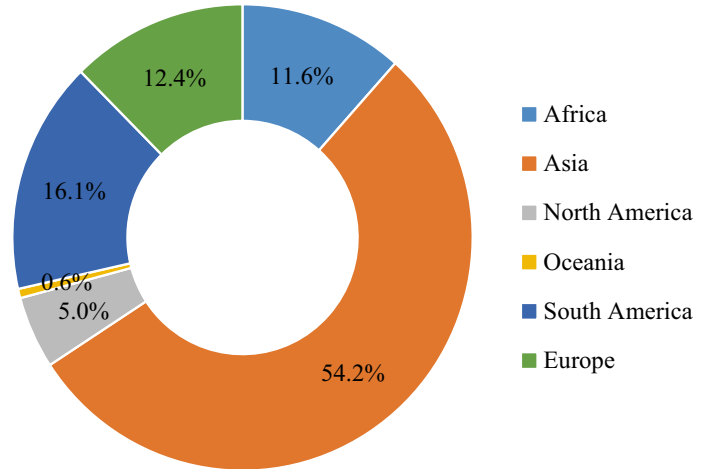


Fig. 2.4 Spatial distribution of global CI

Fig. 2.5 Proportions of multiple-cropping land to the global multiple-cropping land area for six continents



as the Amazon, Gulf of Guinea in West Africa and Congo Basin exceeds 30%. Regions such as the Indo-Gangetic Plain, Huang-Huai-Hai Plain, and the Nile River Delta are benefiting from agricultural infrastructure inputs, where CI is higher than that in other areas at the same latitude. Southern Africa and Australia have high irregularity in precipitation and less irrigation infrastructure as well. Agricultural practices mostly happen in the rainy season, with limited cropland in multiple-cropping patterns. Regions from southeastern Brazil to the Argentine Pampas in the Southern Hemisphere at the same latitude have a predominantly subtropical monsoon climate with mild temperature and high precipitation. The proportion of the multiple-cropping patterns in regions from southeastern Brazil to the Argentine Pampas is greatly higher than that of Southern Africa and Australia. There are significant differences in CI among continents, with the highest average CI in South America at 134%. The average CI in Asia is 121%, slightly lower than that in South America. Europe and Africa were observed with an average CI of 110%, higher than those in North America and Oceania, which have the lowest CI at 105% and 103%, respectively.

The global distribution of multiple-cropping cropland is uneven across different continents. Asia accounts for 38.0% of the world's cropland area, but its share of multiple-cropping cropland to the global share is much higher at 54.2%

(Fig. 2.5). South America accounts for 7.1% of the world's cropland area, but its multiple-cropping cropland accounts for a significant proportion of 16.1% of the world's multiple-cropping cropland. Africa's multiple-cropping cropland accounts for 11.6% of the global share, which is lower than its proportion of cropland area in the world. However, considering its lagging agricultural infrastructure, resources, and investments, Africa already has a commendable achievement in its more than 10% of cropland with multiple-cropping patterns. In contrast, the proportion of cropland with multiple-cropping patterns in Europe, North America, and Oceania is significantly smaller than their proportion of cropland areas.

The regions with great potential for increasing CI are mainly concentrated in countries of Southeast Asia, central South America, southern North America, and central Africa. The climate conditions are favorable to multiple cropping in Central America, Southeast Asia and Africa's equatorial region, where the CI gaps are larger than those in other regions. The CI gaps of most countries in the above-mentioned regions exceed 0.75 when climate conditions are fully utilized. Actual CI in South Asian and Arabian Peninsula countries, Egypt, and some countries in Central Asia has surpassed its potential levels under rain-fed conditions. This is mainly due to investment in infrastructure and management, such as irrigation activities in dry seasons or prolonged

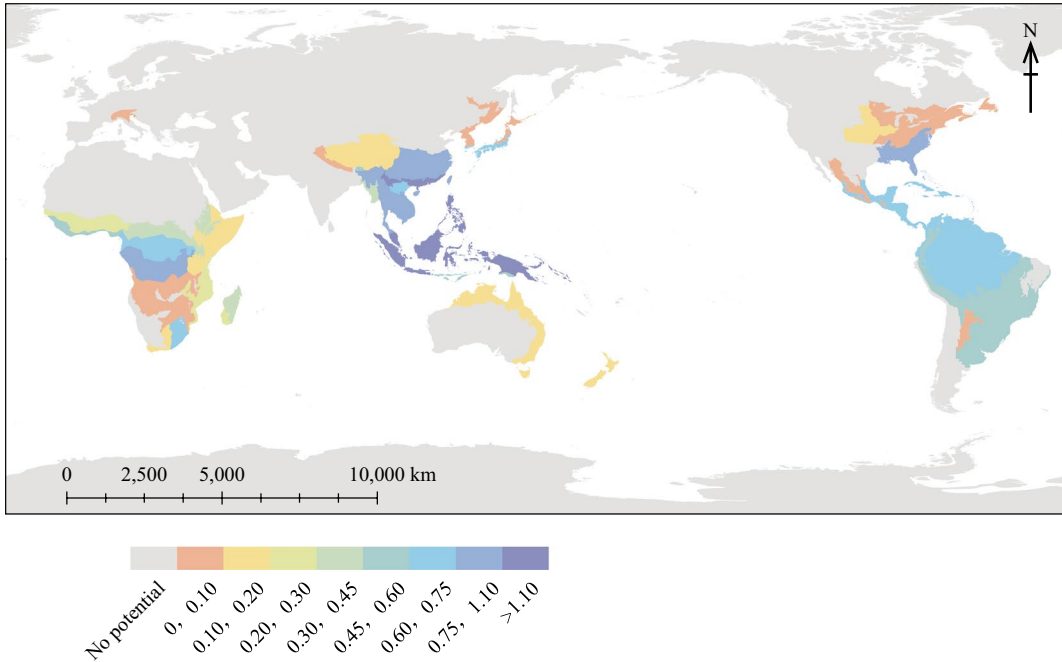


Fig. 2.6 CI gaps at the sub-national scale

drought periods (Fig. 2.6). In China, larger CI gaps are observed in the southern Yangtze River areas, where economic development is robust and there is significant labor migration from rural to urban areas. Land use intensification can be further improved in the south through better coordination between economic and agricultural development and through innovation and technology. Globally, grain production is expected to increase by 230 million tons, or 6.4% of the current global total grain production, by closing the CI gaps.

2.3.2.5 Highlights

- Based on Big Earth Data and cloud computing techniques, this study produced global 30 m cropping intensity in 2020 (GCI30_2020), providing a quantitative assessment of the current state and potential for the improvement of multiple cropping worldwide.
- In 2020, about 85.2% of global cropland was in the single cropping pattern, and multiple cropping was limited by various

environmental factors such as radiation, temperature, water, and soil, and showed an overall latitudinal distribution. Multiple-cropping patterns are mainly concentrated in the Indo-Gangetic Plain, Huang-Huai-Hai Plain, and Nile River Delta.

- There is still huge untapped potential for multiple cropping in Central America, Africa's equatorial region, and Southeast Asia, where natural agricultural resources are not fully exploited. The average potential for multiple cropping in these regions is greater than 0.75. In China, the potential mainly exists in the southern areas of the Yangtze River. Crop production is expected to increase by 230 million tons, or 6.4% of the current global production, if the CI gaps at rain-fed conditions are achieved.

2.3.2.6 Discussion and Outlook

GCI30_2020 can provide scientific data support for the quantitative analysis of intensity and the sustainability of cropland use. GCI30_2020 quantitatively reflects the spatial differences

in actual CI in different countries and regions around the world. It was found that the greatest potential for improving CI is in tropical regions. These areas could further improve their CI to fully utilize their natural conditions, such as radiation, temperature, and available water, to make greater contributions to the achievement of Zero Hunger. The potential to increase CI in southern China is significantly higher than that in the north. In future, regional economic sustainable development and high-standard farmland construction could be considered, and the utilization of regional agricultural resources could be strengthened to stabilize the regional food production level.

However, the uncertainty of the CI map in tropical regions or other cloud-prone regions is higher than that in other regions due to the data quality of optical remote sensing data, which are commonly used currently. In future, synthetic aperture radar (SAR) data can be used to tackle the difficulty in obtaining optical images in frequently cloudy and rainy regions, and to improve the accuracy and reliability of CI products.

2.3.3 Assessment of Grassland Carrying Capacity in Five Central Asian Countries

Target: SDG 2.3: By 2030, double the agricultural productivity and incomes of small-scale food producers, in particular women, indigenous peoples, family farmers, pastoralists and fishers, including through secure and equal access to land, other productive resources and inputs, knowledge, financial services, markets, and opportunities for value addition and non-farm employment.

2.3.3.1 Background

Doubling the income of pastoralists in particular is one of the key objectives of SDG 2.3, and carrying out research on livestock carrying capacity is one of the ways to objectively assess the production and income of herdsmen. The dominant methods of breeding are family, small-scale,

and scattered breeding. Meat and dairy products account for a high proportion of local people's diets. Recently, overgrazing and drought have resulted in serious degradation of desert/semi-desert grassland in Central Asia. This has a huge impact on the local livestock industry, so the proportion of meat imports has soared. Therefore, it is essential to divide the type composition, distributions, and area changes of the main grassland resources, identify the temporal and spatial characteristics of grassland degradation, and quantify GCC in the five Central Asian countries. This can provide a scientific reference for the sustainable development of livestock, and also provide technical support for China-led solutions to eliminate Zero Hunger in Central Asia.

In previous studies, the main research objects of GCC have been grasslands (meadows) in mountains or the river valleys, but rarely have they included sparse vegetation areas such as deserts and shrubland. In the central and southern parts of the five Central Asian countries, the vast desert areas with an average vegetation fraction of 30% are winter pasture and camel breeding areas, so they are also an important component of the assessment of GCC. The vegetation of the desert/semi-desert of Central Asia is sparse and unevenly distributed. At present, many large-scale and long-term time-series remote sensing vegetation products have missing values and also lack ground observation data (such as forage yield, AGB, and vegetation coverage) in this region. The assessment of GCC mainly focuses on the calculation of AGB or forage yield in domestic and foreign research. However, the ecological environment in the desert/semi-desert of Central Asia is extremely fragile, and it is difficult to recover in a short time once damaged. Therefore, the ecological protection objectives (such as grassland, soil, and water) should also be considered in the assessment of GCC to ensure the sustainable development of animal husbandry. This case focuses on desert/semi-desert grassland, identifies the classification of grassland types (including desert and shrubland), establishes an assessment method of GCC based on ecological

protection objectives, and evaluates the development potential of grassland in the five Central Asian countries.

2.3.3.2 Data

- Raster datasets of land use/land cover (LULC), fraction of vegetation coverage (FVC) and net primary productivity (NPP) from the CAS “Big Earth Data Science Engineering Project” (CASEarth) in 2010, 2015, and 2020 with a spatial resolution of 500 m.
- Raster datasets of livestock production from the Gridded Livestock of the World database (GLW 3) (Gilbert et al. 2018) in 2010 with a spatial resolution of 0.083333°.
- Monthly raster datasets for temperature and precipitation from the University of East Anglia’s Climatic Research Unit gridded Time Series (CRU TS 4.0) during 2010–2020 with a spatial resolution of 0.5°.
- Main livestock production statistics of the five Central Asian countries in 2010, 2015, and 2020 from the Food and Agriculture Organization Statistics (FAOSTAT) Database.
- Observed data of grassland AGB in the five Central Asian countries in 2018 and 2019 (CAS Research Center for Ecology and Environment of Central Asia).
- Other Data: vector dataset of terrestrial ecoregions of the world (TEOW) (Olson et al. 2001), Harmonized World Soil Database Version 1.2 (Nachtergaele et al. 2012), and Shuttle Radar Topography Mission (SRTM) digital elevation model (DEM).

2.3.3.3 Methods

This case identifies the distribution and extent of grassland (including desert and shrubland) using LULC and GLW datasets. Grassland types were distinguished by the comprehensive index method based on terrain, climate, soil, and TEOW data. Vegetation growth and vegetation coverage were used with the entropy weight method (EWM) to evaluate the spatiotemporal variations of grassland degradation in the five Central Asian countries. Based

on the NPP simulated by the boreal ecosystem productivity simulator (BEPS) model, the method of AGB allocation proposed by Hui and Jackson (2006) was used to calculate the AGB of grassland. Combined with the observed AGB of grassland in 2018 and 2019, the forage yield in Central Asia was estimated and verified. A comprehensive evaluation system was established to calculate a reasonable GCC from four factors: ecology, topography, human activity, and soil and water. Then, the spatiotemporal change analysis of GCC was carried out for Central Asia based on ecological protection objectives. Finally, the grassland capacity balance index (GCBI) was used to evaluate the grassland development potential and grassland overgrazing:

$$\text{GCBI} = \frac{C_a - C_r}{C_r} \times 100\%,$$

where C_a is the actual GCC, and C_r is the reasonable GCC. The actual GCC came from the statistics of livestock production published by FAOSTAT, and the reasonable GCC was estimated by the above evaluation system of GCC. If the value of GCBI is positive, it means that the actual grazing quantity of grassland is greater than the reasonable GCC, that is, overgrazing exists. If the value of GCBI is negative, it indicates that the actual grazing quantity of grassland is less than the reasonable GCC, that is, it has grazing potential and can accommodate a certain amount of livestock grazing.

2.3.3.4 Results and Analysis

The types and distributions of grassland in the five Central Asian countries are shown in Fig. 2.7. According to the statistical analysis, the grassland area in the five Central Asian countries was 252.48×10^4 – 251.98×10^4 km² during 2010–2020. Desert grassland accounted for 44.63% of the grassland area, which was mainly distributed in Turkmenistan, Uzbekistan, and southern Kazakhstan, while 33.38% of the grassland area was semi-desert grassland, which was mainly distributed in central Kazakhstan, and 14.83% of that was Kazakh steppe, which was in northern Kazakhstan. The grassland

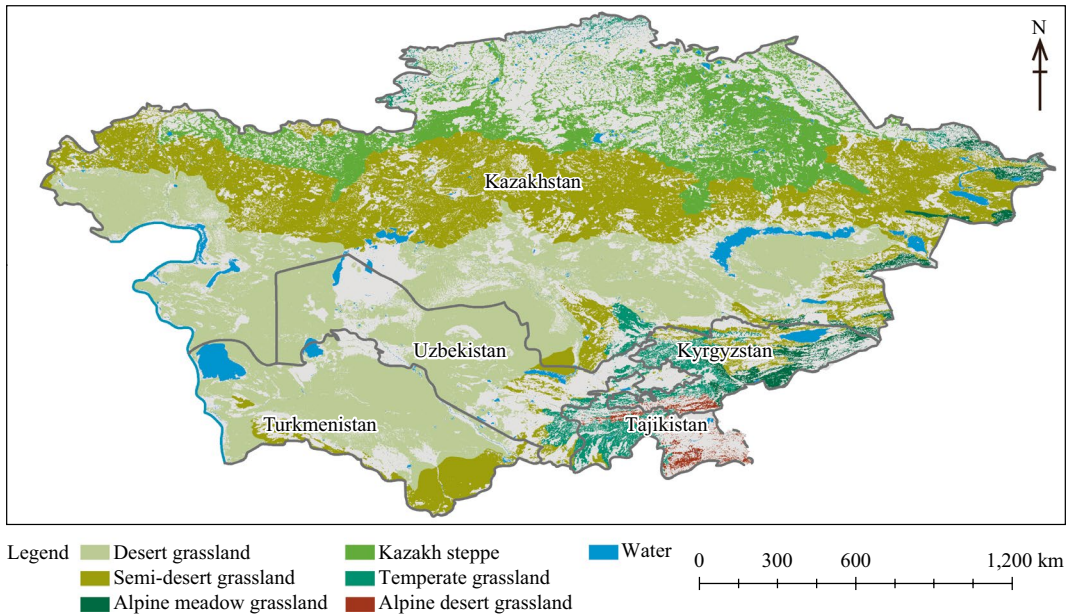


Fig. 2.7 Grassland types in the five Central Asian countries (2020)

areas of temperate grassland and alpine meadow grassland were relatively small, accounting for 4.07% and 2.24% of the grassland area, respectively. They were mainly distributed in Kyrgyzstan, Tajikistan, and mountainous eastern areas of Kazakhstan. The smallest area of alpine desert grassland (0.85%) was concentrated in the Pamir Mountains of Tajikistan. Kazakhstan had the largest grassland area (70%), followed by Turkmenistan and Uzbekistan (13.92% and 10.34%, respectively), and the mountainous countries of Kyrgyzstan and Tajikistan had the smallest grassland areas (9.14% and 4.93%, respectively).

The grassland in the five Central Asian countries was mainly moderately degraded, accounting for 47.92% of the total grassland area (Fig. 2.8). The moderate degradation of grassland was mainly distributed in semi-desert grassland in southern Kazakhstan and the Kazakh steppe in northern Kazakhstan, accounting for 53%–58% of the areas of these two grassland types. The proportion of severe degradation of the grassland area was 22.99%, which was concentrated in the desert grassland of Uzbekistan and Turkmenistan, and the

alpine desert grassland in the Pamir Mountains, accounting for 37%–45% of the areas of these two grassland types. Temperate grassland and alpine meadow grassland had mainly no degradation and light degradation. Especially in alpine meadow grassland, the undegraded area accounted for 55% of the grassland type. The spatiotemporal changes of grassland degradation in the five Central Asian countries from 2010 to 2020 showed that grassland degradation first decreased and then increased. The proportion of severe and moderate degradation of grassland areas decreased from 76.36% in 2010 to 65.79% in 2015, and then increased to 76.85% in 2020. Grassland degradation was concentrated in the western coastal lowlands of the Caspian Sea, near the Aral Sea, the western Tianshan Mountains, and eastern Kazakhstan. The grassland restoration area was distributed discontinuously in semi-desert grassland in southern Kazakhstan, central Kazakh steppe, and desert grassland in central Turkmenistan.

The available forage yield in the five Central Asian countries (Fig. 2.9) is related to grassland types. In 2020, alpine meadow grassland and temperate grassland had the highest yield (2531

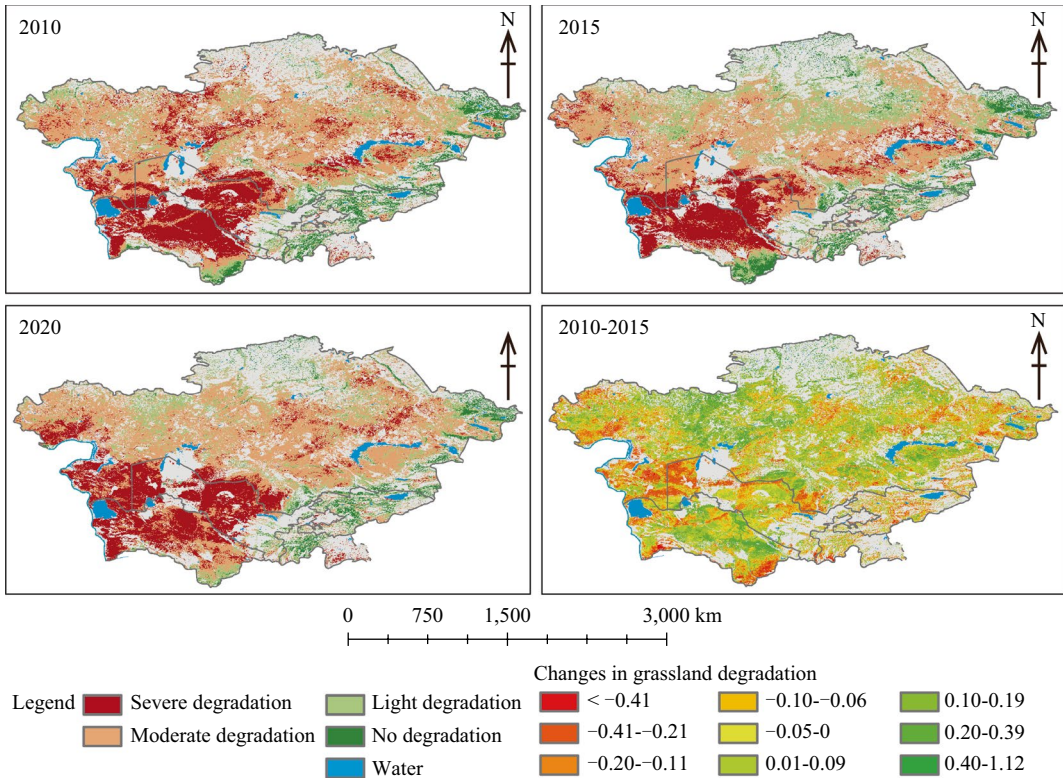


Fig. 2.8 Distribution and variation of grassland degradation in the five Central Asian countries

kg/hm² and 2406 kg/hm²). It was followed by Kazakh steppe and semi-desert grassland (2247 kg/hm² and 1372 kg/hm²), while desert grassland and alpine desert grassland had the lowest yield (484 kg/hm² and 512 kg/hm²). The forage yield in Kyrgyzstan and Tajikistan was the highest, while that in Uzbekistan and Turkmenistan was the lowest. From 2010 to 2020, the forage yield of Kazakh steppe and semi-desert grassland in Kazakhstan increased significantly, while that of the desert grassland of the Aral Sea Basin, eastern alpine meadow and alpine desert grasslands obviously decreased in Turkmenistan and Uzbekistan.

In 2020, desert grassland and alpine desert grassland had the lowest carrying capacity (10–15 SU/hm²), semi-desert grassland and Kazakh steppe had a medium carrying capacity (30–60 SU/hm²), while temperate grassland and alpine meadow grassland had the highest (120–300

SU/hm²) (Fig. 2.10). From 2010 to 2020, the reduction of GCC was mainly distributed in the desert grassland in central Turkmenistan and Uzbekistan, the alpine meadow grassland in eastern Kazakhstan, and the alpine desert grassland in the Pamir Mountains. The increased GCC was found in the middle areas of semi-desert grassland, Kazakh steppe, and partial temperate grassland.

Kazakhstan had great potential for livestock development (Fig. 2.11) with the value of GCBI being -158%–190%, and it was mainly located in the country's southcentral semi-desert grassland and the northern Kazakh steppe. The GCBI of grassland in Kyrgyzstan increased from -8.19% in 2010 to 19.64% in 2020, indicating that the development potential of grassland was gradually decreasing and the development of animal husbandry was becoming saturated. The grassland in Uzbekistan had

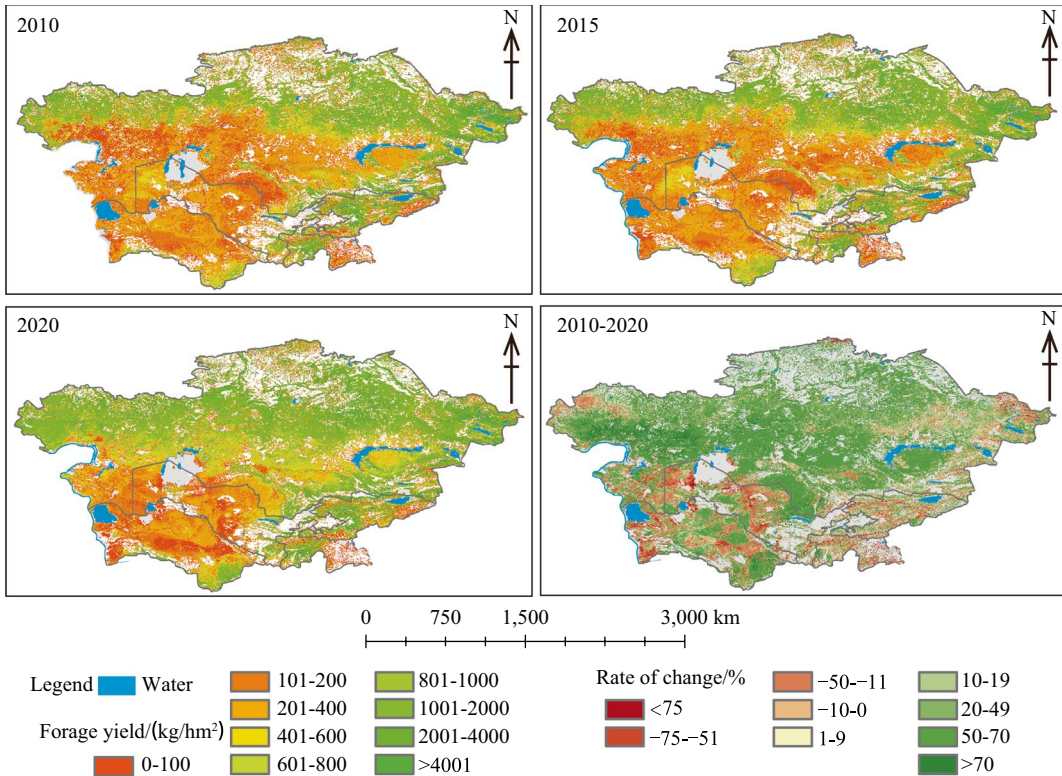


Fig. 2.9 Distribution and variation of available forage yield in the five Central Asian countries (2010, 2015, 2020)

the most overgrazing with the value of GCBI being 88.22%. Next came Turkmenistan and Tajikistan, with a GCBI of 67.13% and 59.19%, respectively.

2.3.3.5 Highlights

- A scheme was proposed for grassland classification types including desert grassland and semi-desert grassland in arid areas of Central Asia, establishing an assessment method of GCC for ecological protection, and also a new dataset for an SDG 2.3 index in arid regions.
- Desert grassland and semi-desert grassland, which are the main grassland types, were moderately degraded during the study period, while temperate grassland and alpine meadow grassland, accounting for a few areas, were lightly degraded in the five Central Asian countries.

- Among the five Central Asian countries, Kazakhstan has the greatest development potential for grassland. The development potential of grassland in Kyrgyzstan gradually decreased and tended toward saturation. Meanwhile, the grassland of Uzbekistan was heavily overgrazed, followed by Turkmenistan and Tajikistan.

2.3.3.6 Discussion and Outlook

Based on new technologies and products of Big Earth Data, combined with internationally shared datasets, grassland characteristics, field observations and expert knowledge in Central Asia, an evaluation index system of GCC was constructed, including sparse desert vegetation that can meet the ecological conservation objectives in arid areas. On this basis, an assessment of GCC was carried out in the five Central Asian countries, and spatial distribution maps of different GCC in Central Asia

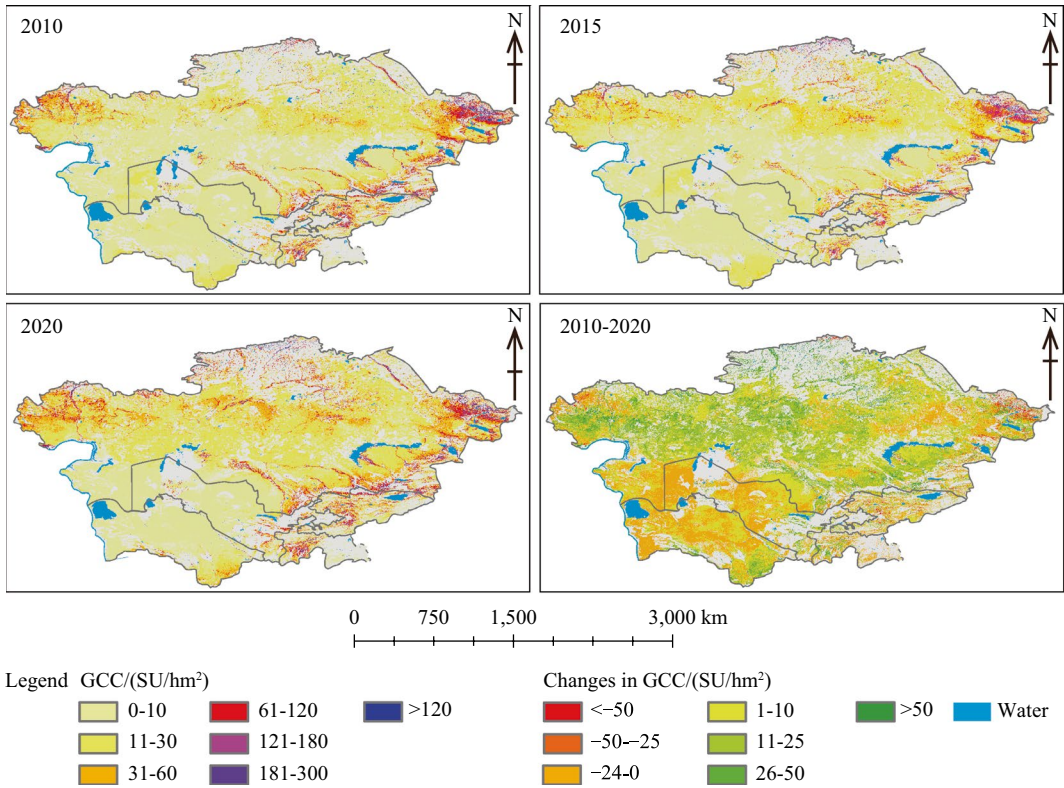


Fig. 2.10 Distribution and variation of GCC in the five Central Asian countries (2010, 2015, 2020)

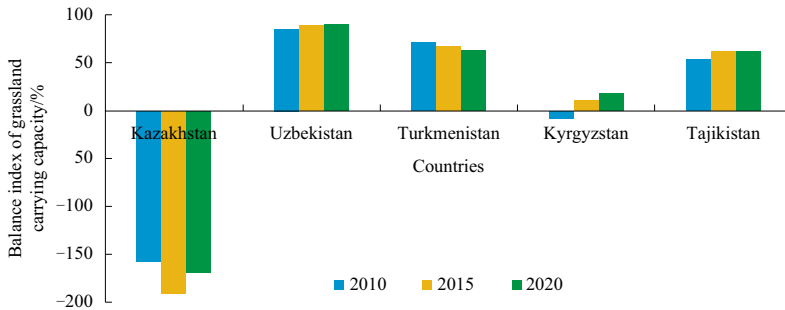


Fig. 2.11 GICBI in the five Central Asian countries (2010, 2015, 2020)

were produced, which could provide information support for an SDG 2.3 index—evaluation of herdsmen’s productive capacity in typical arid areas. In future, other biological

factors affecting GCC should be considered, and the evaluation system should be gradually improved to enhance the accuracy and applicability of evaluations.

Desert and semi-desert grassland areas in Central Asia account for 78% of the grassland area, most of which are seriously degraded. Meanwhile, disorderly and excessive grazing activities aggravate grassland degradation here. Moreover, scattered and small-scale livestock farming, which is dominated by families, cannot resist the losses caused by natural disasters. All of these issues intensify the challenges to eliminating local Zero Hunger. In future, it is suggested to pay more attention to grassland resource restoration and protection under harsh conditions in desert and semi-desert grassland areas, and also strengthen the construction of modern centralized animal husbandry bases, so as to ensure the efficient and sustainable development of animal husbandry in Central Asia.

2.3.4 Spatial and Temporal Variation in Grassland Carrying Capacity in Mongolia and Its Causes

Target: SDG 2.3: By 2030, double the agricultural productivity and incomes of small-scale food producers, in particular women, indigenous peoples, family farmers, pastoralists and fishers, including through secure and equal access to land, other productive resources and inputs, knowledge, financial services, markets, and opportunities for value addition and non-farm employment.

2.3.4.1 Background

Grasslands in Mongolia cover more than 80% of the country's land area, and are the most dominant ecosystem type in the country. Livestock farming is the basis of Mongolia's national economy and the livelihoods of local herdsmen (Angerer et al. 2008). Grassland ecosystems are one of the most sensitive systems to global climate change, and the degradation of grasslands in Mongolia is becoming increasingly significant due to climate change and human activity. With varying extents of desertification occurring in some areas, concerns have been raised about grassland ecology. The study of GCC and its

driving factors has important research implications and applications for the sustainable development of grassland ecosystems and livestock husbandry, as well as for the livelihoods of herdsmen.

“Volume of production per labor unit by classes of farming/pastoral/forestry enterprise size” is an important indicator of SDG 2.3. However, the monitoring of this indicator is still at the stage of no data and no methodology. A dilemma is also faced by Mongolia when the evaluation indicators are applied to animal husbandry management. Therefore, this study combines remote sensing, ground observations and survey statistics to carry out the monitoring of AGB changes in Mongolian grasslands from 2010 to 2020, investigating the characteristics of spatial and temporal changes in AGB for grasslands, and quantitatively analyzing the spatial and temporal variability in GCC. This study will help to understand the impacts of livestock production activities on grassland ecosystems and provide support for research and management of sustainable development of livestock farming in Mongolia. It also provides a technical approach and information reference for the application of Earth observation technology in grassland and livestock farming to achieve SDG 2.3 in Mongolia.

2.3.4.2 Data

MODIS Terra Surface Reflectance Daily Global 250 m (MOD09GQ) and MODIS Terra Surface Reflectance Daily Global 500 m (MOD09GA) datasets from 2010 to 2020 from the Land Processes Distributed Active Archive Center (LP DAAC) of NASA. Band reflectance data at a spatial resolution of 250 m for the former and 500 m for the latter were selected.

Solar radiation dataset from 2010 to 2020 from the National Centers for Environmental Prediction (NCEP) Climate Forecast System (CFS) at 250 m and 500 m spatial resolution.

Statistical data for livestock populations from 2010 to 2020 from the Mongolian Statistical Yearbook.

Mongolian grassland type data, province boundary, and ground-based AGB observation

data during 2016–2019 from the National Remote Sensing Centre, Information and Research Institute of Meteorology, Hydrology and Environment, Mongolia.

2.3.4.3 Methods

Grassland AGB is a key indicator in the calculation of GCC. In this study, a combination of the Carnegie–Ames–Stanford Approach (CASA) model and root–shoot ratio method was used to estimate grassland AGB during the growing season (April–October), and validated using ground-based observations. The CASA model was used to estimate the NPP of grassland during the growing season (Field et al. 1995; Bao et al. 2019); the root–shoot ratio method proposed by Gill et al. (2002) was used to estimate AGB combined with the root–shoot ratio coefficients of the three main grassland types in Mongolia (forest steppe, typical steppe, and desert steppe).

GCC refers to the capacity of a unit area of grassland resource to sustainably carry livestock (Roe 1997; Hobbs and Swift 1985). According to the actual situation in Mongolia, grassland AGB during the growing season by remote sensing data, the daily intake of one standard sheep unit in Mongolia, grazing days, and grassland utilization levels for different grassland types were used to calculate GCC (Nandintsetseg et al. 2018). The grassland carrying status index (GCSI), proposed based on the balance of supply and consumption, is calculated by the ratio of the actual livestock data to GCC. This index can directly reflect the status of GCC. A GCSI value greater than 1.0 indicates that the actual amount of grassland grazing exceeds the carrying capacity, implying overload. A GCSI value less than 1.0 indicates that grassland resources are sustainable and have the potential to carry more livestock.

Based on the AGB and GCSI monitoring data from 2010 to 2020, a linear trend analysis was used to analyze their change trends, and a linear regression model was used to determine the main influencing factors.

2.3.4.4 Results and Analysis

1. Spatial and Temporal Variation in Grassland AGB

The model was validated using ground-based AGB observation data. The data estimated by the model was in good agreement with the observed data, with R^2 varying between 0.59 and 0.79 and root mean square error (RMSE) ranging from 13.91 g/m² to 26.57 g/m², which can meet the analysis of grassland AGB and carrying capacity at a large scale. The spatial distribution map of the multi-year average AGB of Mongolia grasslands showed a general decreasing trend from north to south (Fig. 2.12), with the highest AGB in the forest steppe region at 160.0 g/m² and the lowest AGB in the desert steppe region at 12.2 g/m². The inter-annual variation in the average AGB of Mongolian grasslands from 2010 to 2020 was not significant, with a general trend of fluctuation and decline. AGB in typical steppe regions decreased at an annual rate of 0.077 g/m², while AGB of forest steppe and desert steppe regions increased at an annual rate of 0.158 g/m² and 0.160 g/m², respectively. Since typical steppe regions occupy half of the total grassland area, the decreasing trend of AGB in typical steppe regions also led to a decreasing trend in the whole grassland region.

2. Spatial and Temporal Variation in GCC

The average GCC for the period 2010–2020 was $99,883 \times 10^3$ SU. The highest GCC value of $14,262 \times 10^3$ SU was recorded in Khövsgöl Province, while the lowest GCC value of 108×10^3 SU was recorded in Orkhon Province. Due to the direct influence of AGB, the average GCC value in the whole grassland region decreased by 185.5×10^3 SU per year between 2010 and 2020 (Fig. 2.13). The downward trends in GCC values occurred mainly in most of the central and eastern provinces. Some western provinces (e.g., Uvs, Bayan-Ölgii, Khovd, Usu, and Zavkhan) showed an increasing trend in GCC values.

According to the stock and slaughter data for five livestock species (sheep, goats, cattle,

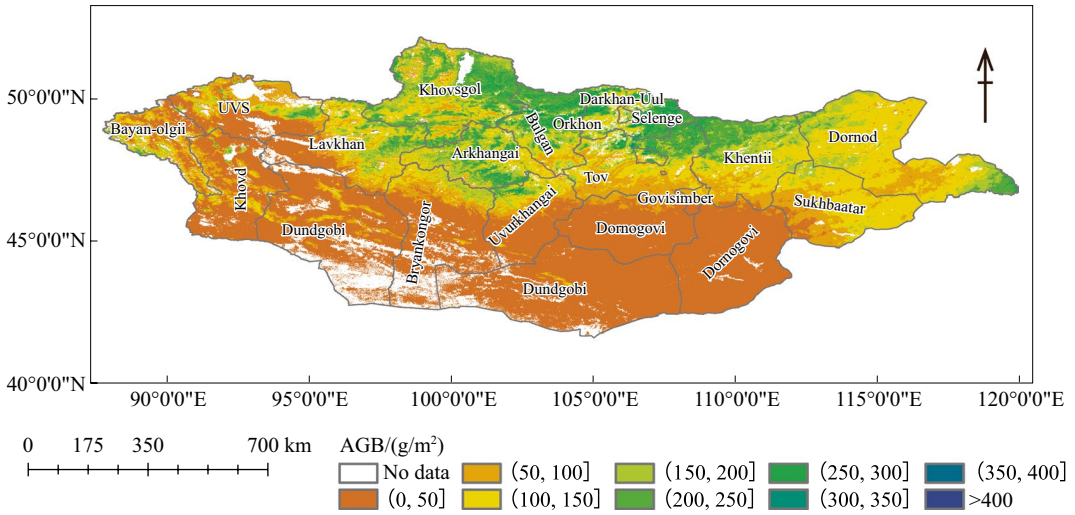


Fig. 2.12 Multi-year average AGB of Mongolian grasslands during the growing season from 2010 to 2020

horses, and camels) in Mongolia, there was an overall significant increasing trend in the number of major livestock in Mongolia from 2010 to 2020, with an annual growth rate of 8182×10^3 SU. The total number of livestock in 2020 was 2.27 times higher than that in 2010. The rapid growth period occurred in the period of 2010–2016 with an annual growth rate of 9311×10^3 SU, after which the growth rate of livestock

numbers slowed down and decreased by approximately 40.7%.

The average GCSI for Mongolia as a whole for the period 2010–2020 was 0.92. This indicated that the livestock carrying conditions were close to equilibrium. The average GCSI for Mongolia increased significantly from 2010 to 2020, with an annual rate of change of 0.08 (Fig. 2.13). The average GCSI value increased

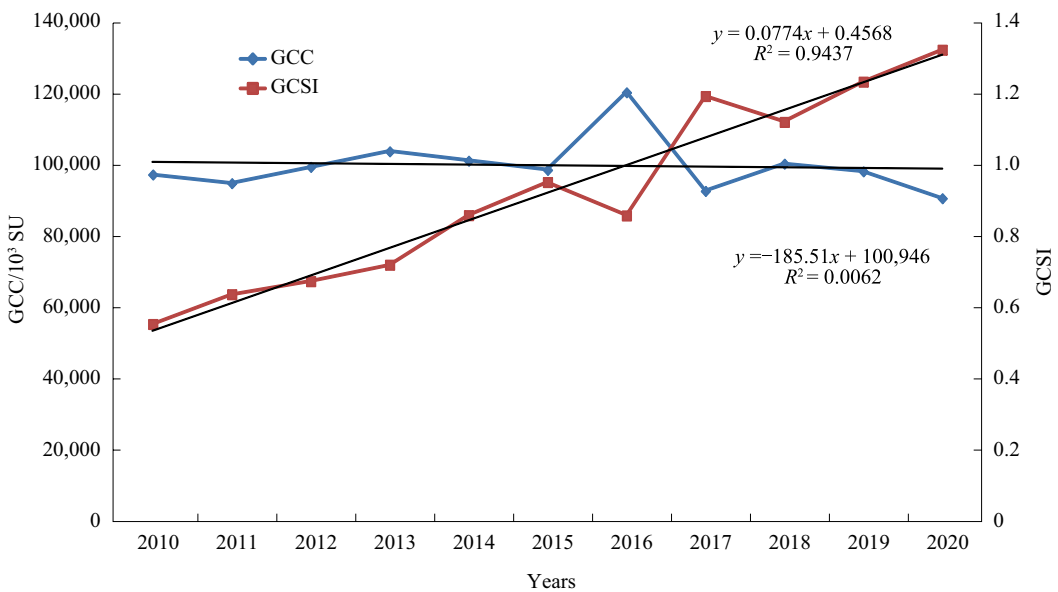


Fig. 2.13 GCC and GCSI in Mongolian grasslands from 2010 to 2020

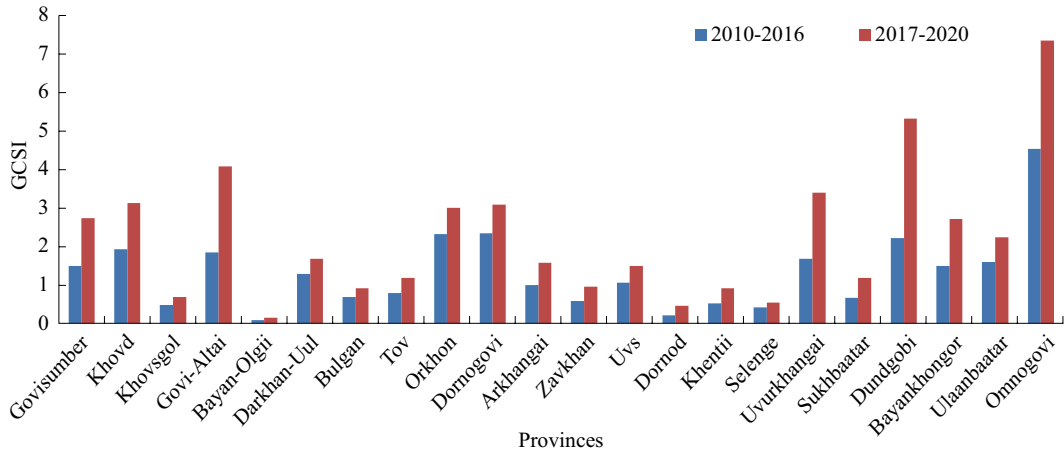


Fig. 2.14 Average GCSI of provinces in Mongolia during two periods, 2000–2016 and 2017–2020

from 0.55 in 2010 to 0.86 in 2016, and sharply increased to 1.19 in 2017, then gradually increased until 2020. Although the GCSI value in 2020 increased by 1.4 times since 2010, a clear phase change was shown in two periods, 2010–2016 and 2017–2020. From 2017 to 2020, the GCSI values were all greater than 1.0 due to a significant increase in the number of livestock, indicating a significant overgrazing condition of Mongolian grasslands in general. The multiple regression analysis between the impact factors (precipitation, temperature, AGB, and livestock numbers) and GCSI was made for the years 2010–2020. The results show that the changes in livestock numbers were the main impact factor to the changes in GCSI, with a contribution of 89.2%.

The average GCSI values varied considerably among provinces during the periods of 2010–2016 and 2017–2020. The provinces in the southern region, extending from Khovd Province eastwards to Dornogovi Province, showed a significant overgrazing status in the two periods. As desert steppe covers more than 60% of the total grassland area, the eight provinces (Khovd, Govi-Altai, Bayankhongor, Ömnogovi, Orkhon, Dundgobi, Govisumber, and Dornogovi) were more vulnerable to environmental and climate change impacts.

In the northern provinces of Bayan-Ölgii, Zavkhan, Khövsgöl, Bulgan, Selenge, Khentii,

and Dornod, the average GCSI values were below 1.0 for the two periods, implying that there is still room for grasslands to carry more livestock. In Uvs Province, Arkhangai Province, Orkhon Province, Darkhan-Uul Province, and Ulaanbaatar City, grasslands were overgrazed in both periods. The GCC situation was more severe in 2017–2020 than that in 2010–2016. The grasslands in Töv Province and Sükhbaatar Province became overgrazed in 2017–2020. It is important to keep track of the provinces where overgrazing occurred for the purpose of livestock management. The increases in GCSI in these regions will have a significant negative effect on ecology and will threaten the sustainability of grassland ecosystems (Fig. 2.14).

2.3.4.5 Highlights

- Based on remote sensing, ground observations and survey statistics, a method for monitoring and evaluating the carrying capacity of Mongolian grasslands was constructed by combining the CASA model, root–shoot ratio method, grassland availability, and livestock information. It provides a new way to monitor the grassland productivity and evaluate the grassland utilization in Mongolia, and serves the sustainable development of livestock farming.

- The situation of the carrying capacity of Mongolian grasslands deteriorated over the period 2010–2020, especially from 2017 to 2020, with a significant imbalance in grassland supply and consumption. The grasslands in more than half of the country's provinces were overgrazed. The significant increase in the number of livestock is the main impact factor to explain the grassland overgrazing.

2.3.4.6 Discussion and Outlook

The analysis and evaluation of GCC in Mongolia has long relied on extensive ground-based biomass observations, especially in years of droughts and snowstorms, which directly result in livestock losses and threaten the livelihoods of herdsman. Effective and timely analysis and evaluation of GCC are essential for the orderly management of livestock grazing and the sustainable development of livestock farming. This study presents a method to monitor AGB and evaluate GCC in Mongolia using Big Earth Data to support the evaluation of SDG 2.3.1.

From the perspective of grassland supply and consumption, the CASA model and root–shoot ratio method were integrated to better estimate the AGB and GCSI of Mongolian grasslands by fully using the Big Earth Data products. The current situation of Mongolian grassland productivity was investigated by using AGB data during 2010–2020. By using the information on the grassland utilization level, intake, and actual livestock, the carrying capacity was analyzed, and the state of GCC was evaluated. It was found that the GCSI index of Mongolian grasslands showed a significant increase in general, among which the increase in livestock was the main impact factor with a contribution rate of 89.2%. The state of GCC varied significantly across the country, especially in the eight provinces in the south and five central provinces. The grassland in these provinces has generally been overgrazed, especially in the years from 2017 to 2020. Therefore, effective measures are urgently needed to mitigate the impacts on grassland ecosystems. Additionally, it is noticeable that the empirical coefficients of grassland availability used in this study for forest steppe, typical

steppe, and desert steppe do not fully take into account the effects of factors such as grassland palatability, grassland nutrients, water sources, and topographic conditions, and the effects of human activity such as fodder supplementation and nomadic grazing on the regional GCC are not taken into account in the evaluation of the state of GCC. These factors need to be further explored in subsequent studies.

2.3.5 Identification of Areas of Stability and Vulnerability in Crop Production in Africa

Target: SDG 2.3: By 2030, double the agricultural productivity and incomes of small-scale food producers, in particular women, indigenous peoples, family farmers, pastoralists and fishers, including through secure and equal access to land, other productive resources and inputs, knowledge, financial services, markets, and opportunities for value addition and non-farm employment.

2.3.5.1 Background

The African continent, particularly sub-Saharan Africa, faces the greatest challenge in achieving Zero Hunger. According to the UN FAO SDG indicators Data Portal, Africa is the continent with the highest proportion of moderate or severe food insecurity and severely food-insecure people. According to the Sustainable Development Goals Report 2021 (UN 2021), even after the introduction of the SDGs in 2015, the proportion of people suffering from food insecurity in Africa will remain high, and the goal of Zero Hunger will remain difficult to achieve.

2.3.5.2 Data

- UN FAO statistics on crop production quantities and harvested areas of maize, rice, wheat, and soybean for the period 2010–2020 (FAO 2024).
- Precipitation, temperature, radiation, and potential biomass data from the CropWatch

global agricultural monitoring platform (accessed: cloud.croptwatch.com.cn).

- MODIS vegetation NPP (Running and Zhao 2021) and leaf area index (LAI) (Myneni et al. 2021).

2.3.5.3 Methods

This study identified the spatial and temporal patterns of crop production in Africa from 2010 to 2020 at both national and pixel levels. At the national level, linear trend fitting was used to analyze the trends in gross crop production and per capita crop production in African countries and to quantify the spatial distribution of increasing, decreasing, and unchanged areas. At the pixel level, a data-driven model of gridded crop production for maize, rice, wheat, and soybean from 2010 to 2020 was developed using the random forest by analyzing the linkage of the gross production of maize, rice, wheat, and soybean with the NPP, LAI, and CropWatch agro-climatic data. The change trend of the gridded production of maize, rice, wheat, and soybean in Africa from 2010 to 2020 was determined using a linear trend fitting grid by grid.

2.3.5.4 Results and Analysis

1. Trends in gross crop production and per capita crop production by countries in Africa from 2010 to 2020

Crop production in West Africa, East Africa, and Central Africa showed a steady growth trend from 2010 to 2020, with trend annual growth rates of 4.0%, 4.8%, and 5.3%, respectively. Many countries in West Africa, Central Africa and East Africa showed an upward trend in crop production from 2010 to 2020, while a few countries showed a downward trend, such as Libya, Madagascar and Central African Republic (Fig. 2.15a). Many countries in West Africa, as well as the Democratic Republic of the Congo and Ethiopia, showed significant growth in annual per capita crop production, while some countries show a downward trend, such as Libya, Madagascar, Mozambique, and Uganda (Fig. 2.15b). Regionally, the trend annual growth rate in annual per capita crop production for West African countries from 2010 to 2020 is 1.2%. Both East Africa and Central Africa have experienced rapid growth in

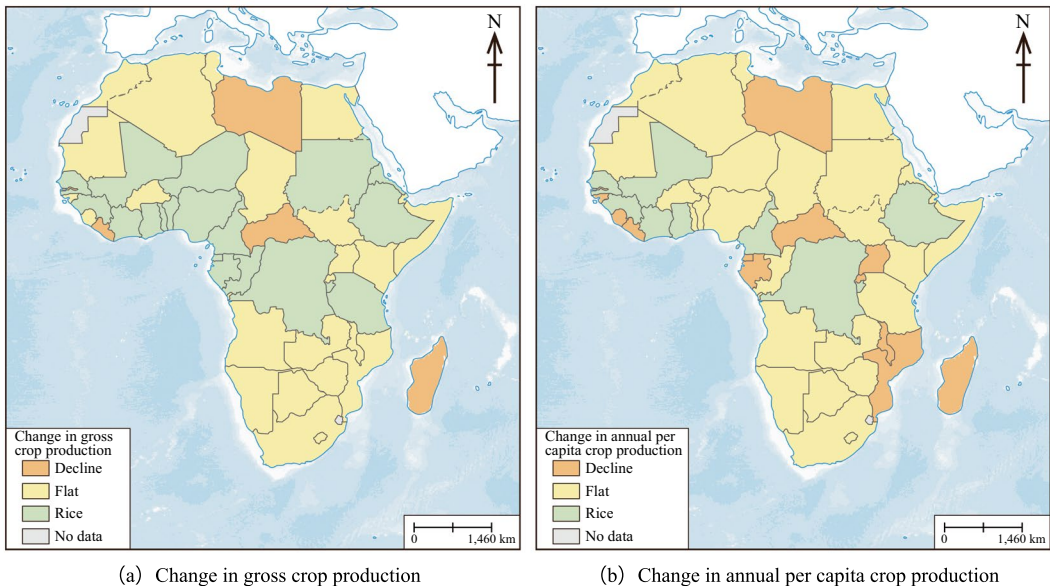


Fig. 2.15 Changes in gross crop production and annual per capita crop production by countries in Africa from 2010 to 2020

annual per capita crop production, with annual growth rates of 2.0% and 2.1%, respectively. In Southern Africa, annual per capita crop production has declined significantly, with an annual growth rate of -2.0% .

By 2020, annual per capita crop production in Africa was still not promising, with most countries still producing less than the crop security baseline of 400 kg per capita per year (Fig. 2.16a). In West Africa, annual per capita crop production remained above 300 kg from 2015 to 2020, while in East, Central, Southern, and North Africa, it was still below 300 kg per capita per year. The combination of per capita crop production and its trend indicated that most African countries are still far from achieving the goal of Zero Hunger (Fig. 2.16b).

2. Changing spatial and temporal patterns of gross crop production from 2010 to 2020

Coupling the agro-climatic and agronomic information from CropWatch with the LAI and NPP data from global land surface satellite (GLASS), a data-driven gridded crop production model was constructed to generate gridded

FAO statistical production of maize, wheat, rice, and soybean for African countries from 2010 to 2020. On this basis, spatial statistics and trend analysis were used to quantify the distributions (Fig. 2.17) and trends (Fig. 2.18) of the gross production of maize, wheat, rice, and soybean in Africa. African maize, wheat, rice, and soybean production were classified into 12 classes (Fig. 2.19) based on the percentiles (25%, 50%, 75%) and trends (decline, flat, rise) of crop production.

The production of maize, wheat, rice, and soybean varies widely due to differences in geography, climate, irrigation, nutrition, and management. South Africa, the Lake Victoria region, the Nile Delta, the Lake Malawi region, and some areas of West Africa are major maize-producing areas. The Nile River Delta, Nigeria, Tanzania, and Madagascar are major rice-producing areas. The coastal areas of North Africa and central Ethiopia are major producers of wheat, and South Africa and Nigeria are major producers of soybean.

Linear analysis was used to determine trends in maize, wheat, rice, and soybean production from 2010 to 2020 at the pixel level, with 50.0%

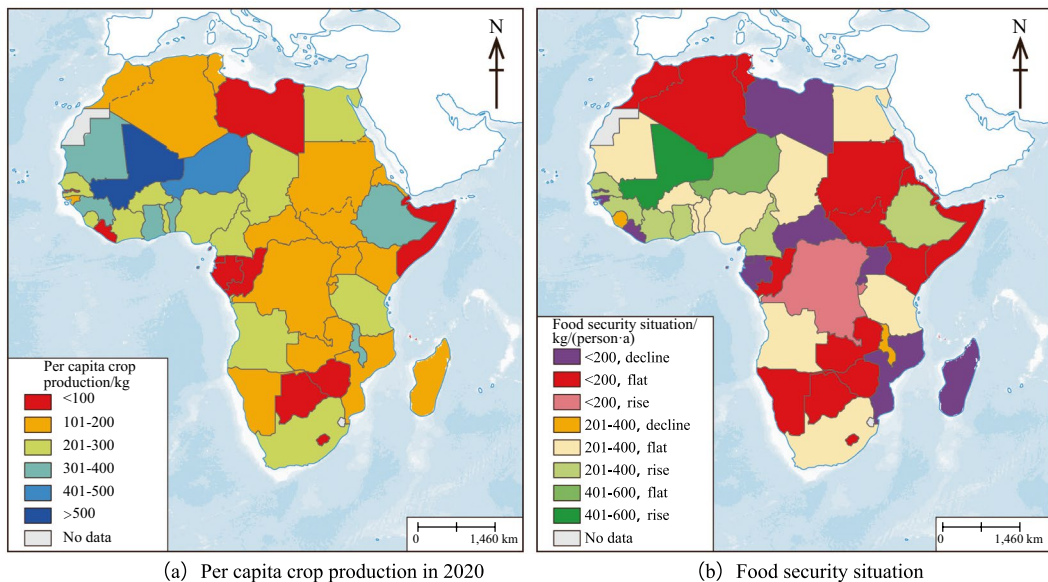


Fig. 2.16 Per capita crop production and food security situation in African countries in 2020

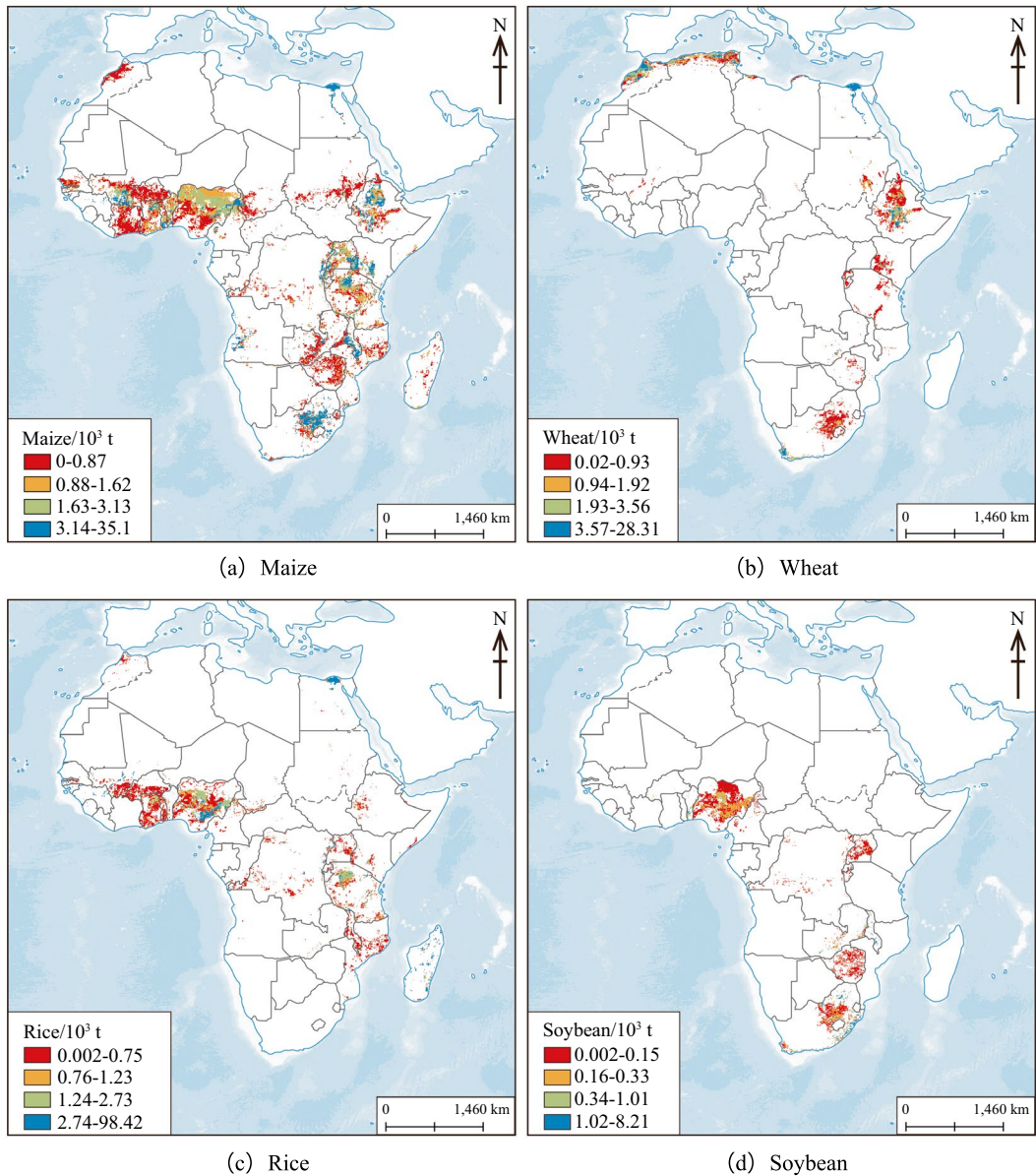


Fig. 2.17 Spatial distribution of gross production of maize, wheat, rice, and soybean in Africa

of maize, 61.5% of rice, and 60.2% of soybean areas showing significant increasing trends, and 28.6% of wheat areas showing a significant increasing trend.

Combining the spatial distributions and changing trends of maize, wheat, rice, and soybean production, 15.57%, 13.90%, 11.89%,

and 4.14% of the maize, wheat, rice, and soybean areas respectively were highly productive areas based on the 25% production percentile, while 49.10%, 58.08%, 63.43%, and 65.83% of the maize, wheat, rice, and soybean areas were low-productivity and vulnerable areas, but with a clear upward trend of improvement.

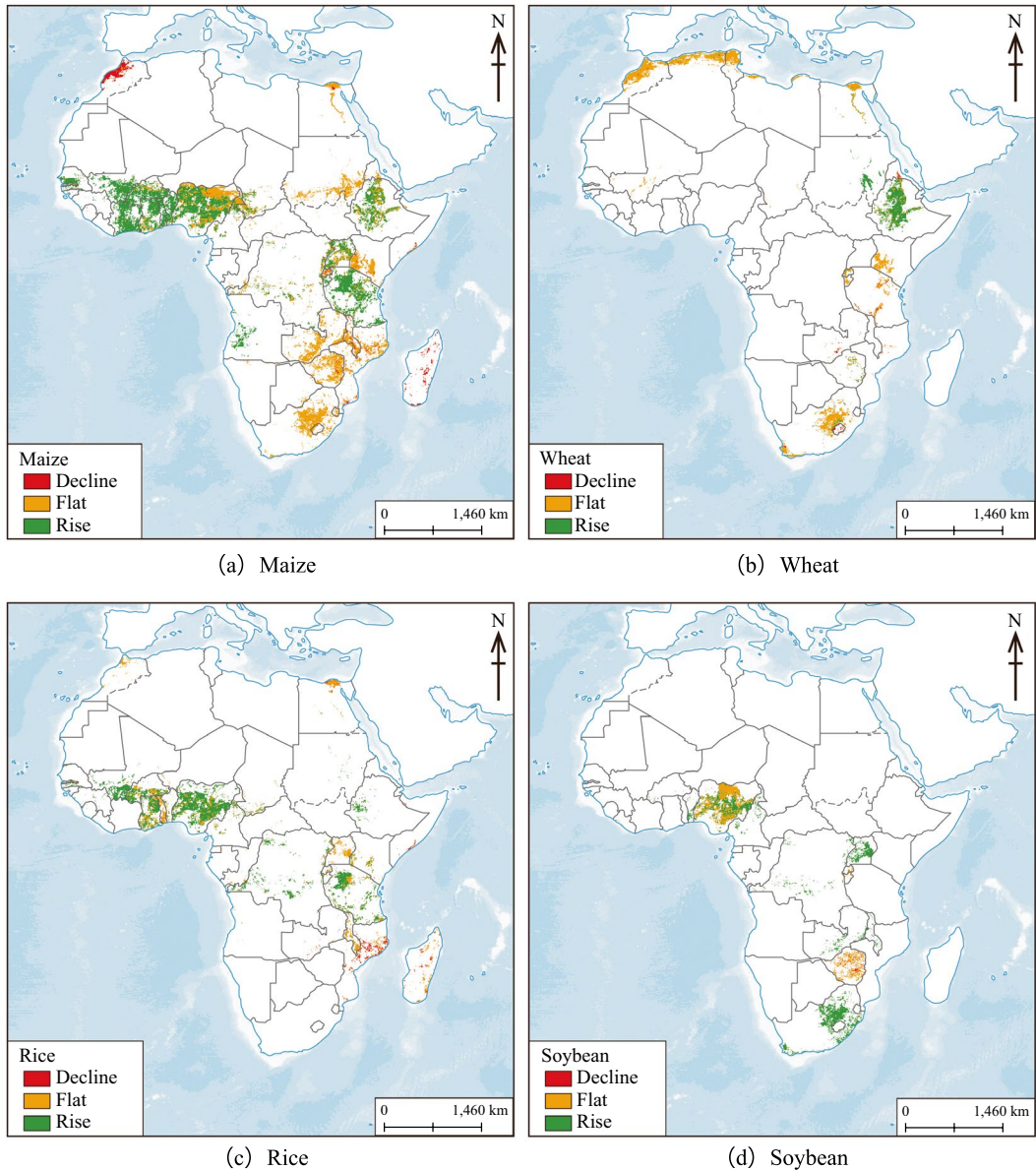


Fig. 2.18 Trends in the gross production of maize, wheat, rice, and soybean in Africa

2.3.5.5 Highlights

- The spatial and temporal patterns of Africa's crop production between 2010 and 2020 were analyzed, and trends in gross crop production and per capita crop production in Africa between 2010 and 2020 were identified. The results show that gross crop production and per capita crop production have increased significantly in West Africa, Central Africa, and East Africa. However, there is still a long way to go to achieve food self-sufficiency and Zero Hunger.
- A data-driven gridded crop production model was designed to generate gridded production of maize, wheat, rice, and soybean across African countries for the period 2010–2020. The results show that the South Africa, Lake

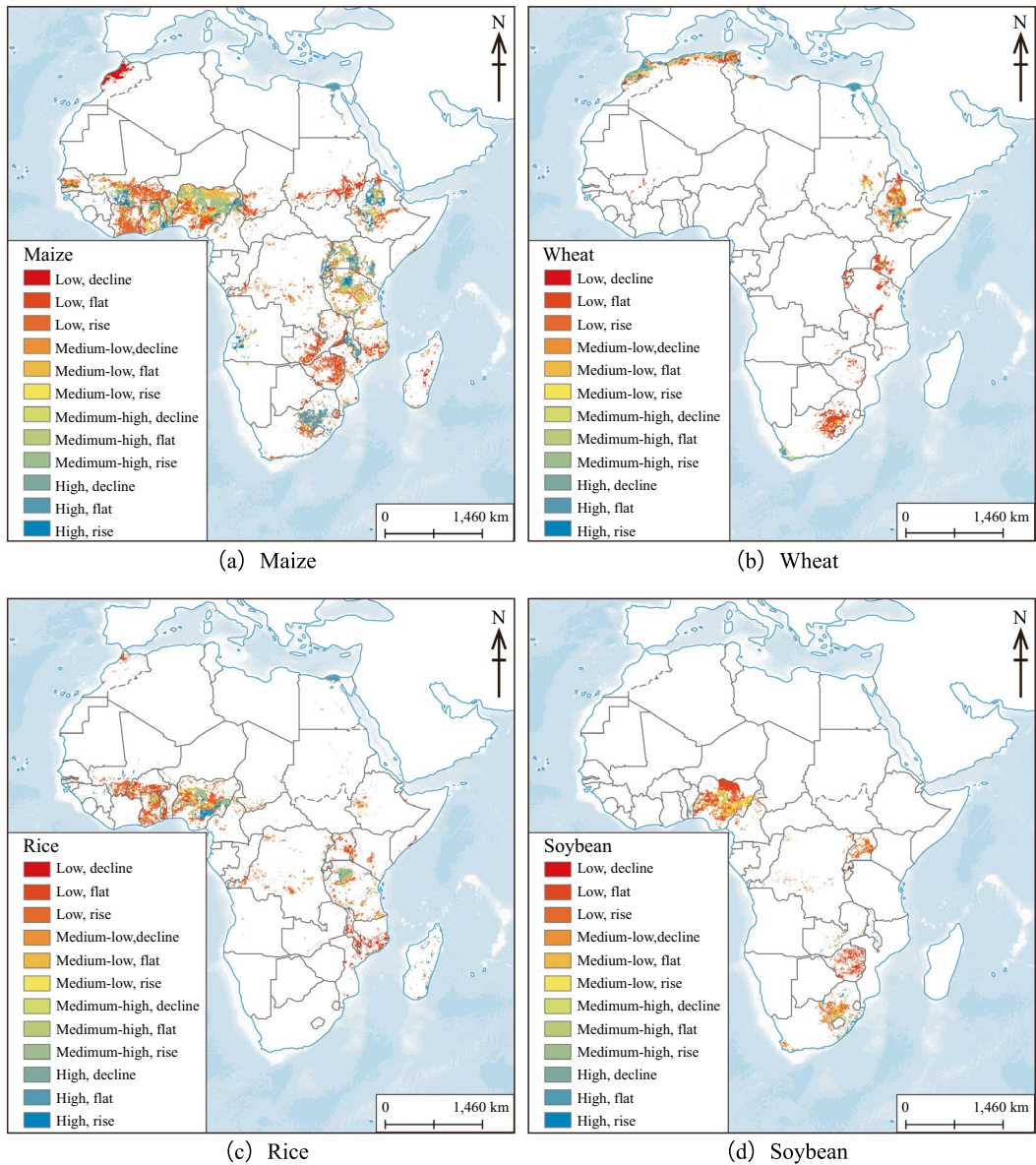


Fig. 2.19 Patterns of maize, wheat, rice, and soybean production in Africa

Victoria, Nile River Delta, and Lake Malawi regions were the most productive growing areas for maize in Africa; the North African coastal region was a high and stable productive area for wheat in Africa; Nigeria and South Africa were highly productive and stable for rice in Africa; and South Africa was highly productive for soybean in Africa.

2.3.5.6 Discussion and Outlook

This study quantifies the spatial and temporal trends of crop production in Africa from 2010 to 2020 at the national and pixel levels. A data-driven gridded crop production model was developed to generate gridded data of maize, wheat, rice, and soybean production in Africa from 2010 to 2020, providing key scientific

data to support the identification of vulnerable, stable, and highly productive areas of maize, wheat, rice, and soybean in Africa, as well as the analysis of drivers affecting the spatial distributions of production.

This study found that: (1) Africa's gross crop production and annual per capita crop production show significant regional disparities, with West Africa, East Africa, and Central Africa showing significantly increasing trends in crop production from 2010 to 2020, while Southern Africa and North Africa are in a state of stagnation. (2) Africa's annual per capita crop production is far below the international food security benchmark, and there is increasing pressure to meet the goal of SDG 2, Zero Hunger. (3) While wheat production on the continent is stagnating, Africa's maize, rice, and soybean production as a whole shows significant increasing trends, though nearly 50% of maize, wheat, rice, and soybean cropland is in vulnerable, low-productivity areas.

2.3.6 Monitoring Desert Locusts in Asia and Africa

Target: SDG 2.4: By 2030, ensure sustainable food production systems and implement resilient agricultural practices that increase productivity and production, that help maintain ecosystems, that strengthen capacity for adaptation to climate change, extreme weather, drought, flooding, and other disasters and that progressively improve land and soil quality.

2.3.6.1 Background

Food security is the cornerstone of human survival, social stability, and global sustainable development. In the context of climate change, the scope and prevalence of pests have obviously expanded and increased. Among them, the desert locust is one of the most destructive migratory pests in the world, and it is also a major agricultural pest. It has a strong flight capability and large food intake, and can gather to form huge swarms and migrate long distances. Monitoring desert locusts is of great

strategic significance for reducing the application of chemical pesticides, ensuring food security and ecological security, and establishing a sustainable food production system.

In 2018, heavy rainfall in the southern Arabian Peninsula provided favorable conditions for the breeding and multiplication of desert locusts, leading to their continuous multiplication and gradual sweeping of the Horn of Africa and countries in Southwest Asia. In 2020, desert locusts continued to multiply and spread in the Horn of Africa, the southern Arabian Peninsula, and the coasts of the Red Sea. The desert locust infestations in Somalia, Ethiopia, and Kenya were still serious, and many areas became new breeding areas of desert locusts. As of 2021, although the insect swarms declined, they were still active in the Horn of Africa, and some spread to northeastern Tanzania. In 2022, the scale and number of swarms in Asia and Africa significantly decreased, but they were still present in some areas. As desert locust outbreaks can cause serious damage, there is a continuing need for dynamic monitoring and early warning, prevention, and control of locust disasters. FAO has issued an early warning to the world, hoping that countries will be highly alert to locust plagues and adopt multi-country joint prevention and control measures to prevent pests from invading countries and creating serious food crises. Traditional visual hand-check single-point monitoring methods and limited-site meteorological prediction methods can only obtain information on the occurrence and development of pests at "points" and cannot meet the needs of large-area "surface" monitoring for the timely prevention and control of pests. Remote sensing, as a technology that can quickly obtain continuous surface information, provides a possibility for monitoring the occurrence and development of pests on a large scale. Scientific prevention and control and ensuring food security are of great significance. In addition, continuously updated encrypted meteorological station data and regional meteorological parameter products formed by the coupling of remote sensing and meteorological data provide a source of information for the dynamic monitoring of locust occurrences.

This case study used multi-source data, combined with meteorological data, basic geographic data, ecological data, ground survey data, plant protection information, and the biological characteristics, migration, and diffusion conditions of desert locusts to build a pest monitoring and forecasting model. Big data analysis and processing on the Digital Earth Science Platform were carried out for the temporal and spatial distribution of desert locust reproduction and migration in the Horn of Africa and countries in Southwest Asia and locust plague monitoring in key countries. Intercontinental locust plague monitoring and risk prediction were carried out, and the relevant results were provided to FAO to support joint prevention and control in multiple countries and ensure the safety of agricultural production in invaded countries.

2.3.6.2 Data

- Remote sensing Data: MODIS data in Asia and Africa from 2018 to 2022 (resolution: 500 m, <https://ladsweb.modaps.eosdis.nasa.gov/search/>), Landsat data (resolution: 30 m, <https://earthexplorer.usgs.gov/>), Sentinel data (resolution: 10 m, <https://scihub.copernicus.eu/>), Planet data (resolution: 3 m) in a representative area of key countries, Worldview data (resolution: 0.5 m), SMAP soil moisture data from 2018 to 2020 (resolution: 0.25°, <https://earthdata.nasa.gov/>), G-Portal soil moisture data from 2021 to 2022 (resolution: 50 km, <https://gportal.jaxa.jp/gpr/>), greenness data from 2018 to 2020 (http://iridl.ldeo.columbia.edu/maproom/Food_Security/Locusts/Regional/greenness.html) and GSMaP rainfall data from 2018 to 2022 (<https://sharaku.eorc.jaxa.jp/GSMaP>).
- Meteorological Data: complete long-term time-series meteorological data of international meteorological stations from 2018 to 2022, tropical cyclone data and numerical meteorological forecast products for the Indian Ocean and Arabian Sea region from 2018 to 2022 (<http://www.nmc.cn/publish/typhoon/totalcyclone.htm>), and European Centre for Medium-Range Weather Forecasts (ECMWF) climate assimilation data for Asia–Africa (<https://www.ecmwf.int/en/forecasts/datasets>).
- Basic Geographic Information: global land use data (resolution: 10 m and 30 m) (<https://www.geodata.cn>), global DEM data, main crop planting areas in Asia and Africa (wheat, rice, maize, etc.) (<https://ipad.fas.usda.gov/ogamaps/cropcalendar.aspx>), and administrative division data (<https://www.tianditu.cn/>).
- Other Data: ground survey data released by FAO (<https://locust-hub-hqfao.hub.arcgis.com/>).

2.3.6.3 Methods

This case study takes desert locusts as the research object. First, the habitat factors affecting the reproduction and development of desert locusts were extracted, and the time lag pattern of the long-term time-series habitat factors was analyzed. Locust breeding areas were monitored at a large scale with the assistance of spatial analysis, geostatistics, spatiotemporal data fusion, and other techniques of geographic information systems (GIS). Second, graph convolutional neural networks were introduced to represent the migration of desert locusts, achieving spatial correlation analysis of desert locusts' breeding areas. The long short-term memory (LSTM) network was used to analyze the linkage in the time series. The forecasting of the migratory paths of desert locusts was achieved by multiple spatiotemporal module operations. Third, combined with the locust monitoring model, the vegetation growth curve was analyzed for each key damaged country from 2018 to 2022, and the information on the locust damage was extracted to delineate the spatial range and area of the locust plague. Fourth, fine-scale remote sensing monitoring was carried out for the hotspot countries and regions with locust damage, including damaged vegetation types (cropland, grassland, and shrubland), the spatial distribution of damage, and total damage areas.

2.3.6.4 Results and Analysis

In 2022, due to the influence of drought and control measures, the scale and number of locust swarms in Asia and Africa were significantly

reduced compared with the previous two years. Desert locusts were mainly distributed in southeastern Egypt, Sudan, Yemen, Somalia, Ethiopia, southeastern Iran, and southwestern Pakistan. From January to February, the vegetation in Somalia and Ethiopia gradually dried up due to insufficient precipitation, affecting locust breeding, while in southeastern Egypt, the Red Sea coast of Sudan, and Yemen, the soil moisture and vegetation conditions were favorable for the breeding and maturation of locusts. In Iran and Pakistan, vegetation greened up gradually after precipitation, providing suitable conditions for the reproduction of local locusts. In March, locusts continued to breed and mature in southeastern Iran and southwestern Pakistan, while in southeastern Egypt, the Red Sea coast of Sudan, and Yemen, locust breeding was limited due to gradually drying weather. In April, due to the drought climate along the Red Sea coast of Yemen being unfavorable for desert locust breeding, locusts migrated northeast to the central Arabian Peninsula, where conditions were suitable for reproduction. From April to June, as temperatures continued to rise, locusts bred and matured in the central Arabian Peninsula, and migrated eastward along the southern border of Iran to the Iran-Pakistan border and southwestern Pakistan. A small number of adults and locusts were present near Jiwani, along the southern coast of Baluchistan Province, Pakistan. In addition, during this period, as temperatures increased in southeastern Iran and southwestern Pakistan, local locusts continued to mature and reproduce, combined with the arrival of migrating locusts, which further migrated to the summer breeding areas in southeastern Pakistan. The meteorological conditions of drought in June 2022 would, to some extent, limit the large-scale reproduction of locusts (Fig. 2.20).

Since June 2021, Ethiopia and Somalia in the Horn of Africa have been severely affected by locust plagues. As of June 2022, the area of vegetation loss in Ethiopia was approximately 3.9858 million hm^2 , accounting for 3.5% of the total vegetation area, including 433.7 thousand hm^2 of cropland, 523.1 thousand hm^2 of

grassland, and 3029.0 thousand hm^2 of shrubland, accounting for 1.8%, 3.0% and 4.1% of the total areas of cropland, grassland, and shrubland, respectively. The areas along the Great Rift Valley in East Africa and its northern region suffered the most severe damage. The vegetation in the areas along the eastern border with Somalia and the southern border with Somalia and Kenya was also significantly affected. The area of vegetation loss in Somalia was approximately 1.4754 million hm^2 , accounting for 3.0% of the total vegetation area, including 0.6 thousand hm^2 of cropland, 94.6 thousand hm^2 of grassland, and 1,380.2 thousand hm^2 of shrubland, accounting for 0.6%, 2.4% and 3.1% of the total areas of cropland, grassland, and shrubland, respectively. The affected area was mainly located in the northern desert region bordering Ethiopia, where desert locusts have undergone multi-generational breeding. Iran and Pakistan were also affected by locust infestations. The area of vegetation loss in Pakistan was approximately 1,966.26 hm^2 , mainly in southern and southeastern Pakistan. The area of vegetation loss in Iran was approximately 632.88 hm^2 , mainly in southern Iran (Fig. 2.21).

2.3.6.5 Highlights

- From June 2021 to June 2022, the area of vegetation loss in Ethiopia was approximately 3.98 million hm^2 , accounting for 3.5% of the total vegetation area; the area of vegetation loss in Somalia was approximately 1.47 million hm^2 , accounting for 3.0% of the total vegetation area; and the areas of vegetation loss in Pakistan and Iran were approximately 1966.26 hm^2 and 632.88 hm^2 , respectively.
- The desert locust monitoring products have been integrated into the FAO HIH platform and have been adopted by international organizations such as the Global Biodiversity Information Facility (GBIF) and Group on Earth Observations (GEO), supporting collaborative pest control efforts among multiple countries and ensuring food security and sustainable development.

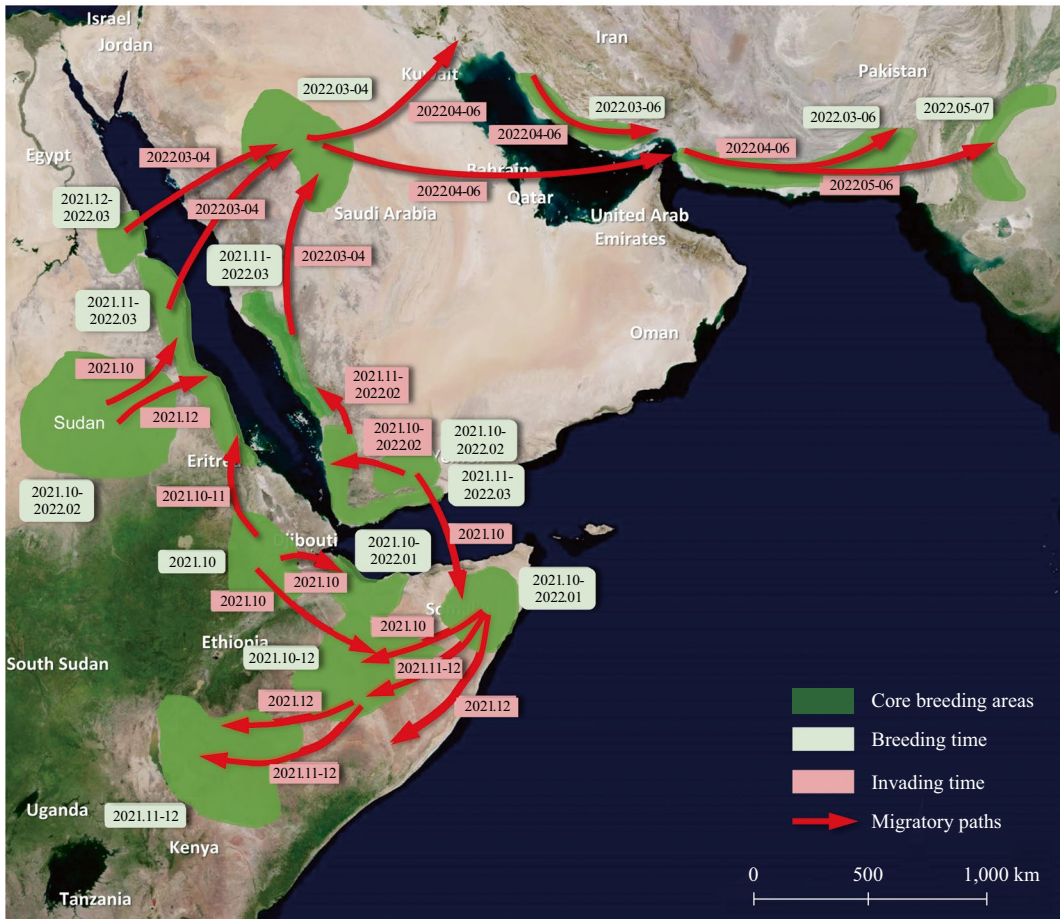


Fig. 2.20 Core breeding areas and migratory paths of desert locusts from October 2021 to July 2022

2.3.6.6 Discussion and Outlook

In terms of technological innovation, this case study used international shared remote sensing data to conduct systematic research on the extraction of large-scale desert locust breeding areas, long-term time-series quantitative monitoring of locust migration paths, and quantitative monitoring of locust plagues through big data analysis and processing on the Digital Earth Science Platform. The desert locust plagues in Asia and Africa were monitored by remote sensing to gather updates on damage dynamics. The research results could contribute to the

protection of agricultural production and food security, and provide important information support for locust plague emergency response.

In terms of application and promotion, FAO and GBIF adopted the monitoring results on the core breeding areas and migratory paths of desert locusts in Asia and Africa from 2021 to 2022, as well as the locust monitoring results in key countries (Ethiopia, Somalia, Pakistan, and Iran). The products of this case study provide information support for multi-country joint prevention and control of pests to ensure agricultural production.

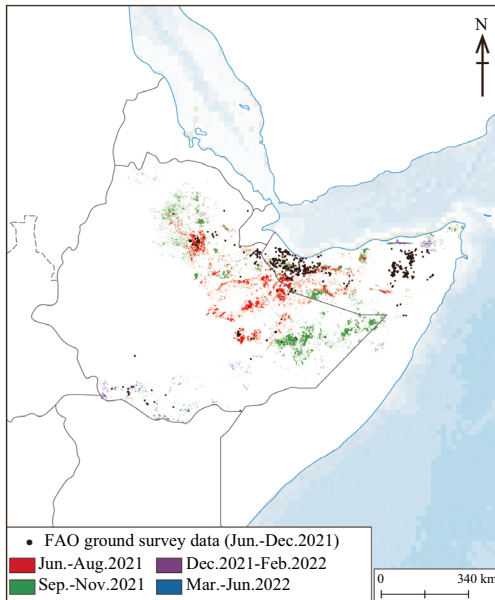


Fig. 2.21 Desert locust plague monitoring in Somalia and Ethiopia from June 2021 to June 2022

2.3.7 Impacts of Extreme Drought on Agricultural Production in the Mekong River Basin of the Indochina Peninsula

Target: SDG 2.4: By 2030, ensure sustainable food production systems and implement resilient agricultural practices that increase productivity and production, that help maintain ecosystems, that strengthen capacity for adaptation to climate change, extreme weather, drought, flooding, and other disasters and that progressively improve land and soil quality.

2.3.7.1 Background

Due to climate change and global warming, extreme weather events are becoming more frequent, intensifying the impacts of drought in some areas of the world. Droughts are expanding in scope, severity, and duration, while the fragility of agricultural ecosystems continues to increase. As a result, global food security is facing a severe challenge (Allen and Ingram 2002; Alexander et al. 2006; Baudoin et al. 2017). Rice is one of the three principal cereal

crops worldwide, and the Mekong River Basin (MRB) in Southeast Asia is a significant global producer of rice. Each country in the Basin plays a crucial role in global rice production and exports. However, the region is characterized by distinct dry and rainy seasons, and is sensitive to climate change. The increasing frequency of extreme weather events has further intensified the region's drought risks, posing a severe threat to rice yields and quality (Ho and Shimada 2021).

This case focuses on SDG 2.4, which aims to establish sustainable food production systems to strengthen the ability to cope with climate change, extreme weather, droughts, floods, and other disasters. Using the MRB, a typical area vulnerable to stable food production, as the study area, this case monitored and analyzed the spatiotemporal distribution patterns of meteorological and agricultural droughts, and clarified the impacts of meteorological droughts on agricultural production in different regions. The results can provide references for drought prevention and response to food crises in areas vulnerable to food production under extreme climate conditions, thereby facilitating the achievement of SDG 2, Zero Hunger.

2.3.7.2 Data

- 1982–2020 global daily precipitation data from the Climate Hazards Group InfraRed Precipitation with Station data (CHIRPS) provided by the Climate Hazards Center of the University of California, Santa Barbara (UCSB/CHC) at a resolution of 5566 m.
- 1982–2020 global monthly potential evapotranspiration (PET) data averaged by hour of day provided by the ECMWF at a resolution of 11,132 m.
- 2010–2020 global land-cover products provided by the European Space Agency Climate Change Initiative (ESA CCI) at a resolution of 300 m.
- 2010–2020 MODIS surface reflectance products (MOD09), one scene per day, at a resolution of 250 m.

- Administrative division data of countries in the Indochina Peninsula and vector data of the MRB provided by the Mekong River Commission (MRC).

2.3.7.3 Methods

1. Method for Meteorological Drought Monitoring

The standardized precipitation evapotranspiration index (SPEI) (Vicente-Serrano et al. 2010) is a method for monitoring meteorological droughts. It considers the combined impacts of precipitation and evapotranspiration. It has the advantages of monitoring multiple time scales and long-term spatial comparisons, making it particularly suitable for analyzing meteorological droughts in the context of global warming. A smaller SPEI value indicates more severe droughts, while a larger value indicates more humid conditions. In this case study, the Google Earth Engine cloud platform was used to calculate the total monthly precipitation and evapotranspiration from 1982 to 2020 in the study area. Based on this, the monthly SPEI was calculated at scales from 1 to 12 months from 2010 to 2020. SPEI at the 3-month scale in May (for the dry season) and at the 4-month scale in October (for the rainy season) were respectively selected to represent the meteorological drought conditions during each season, considering the impacts of the wet and dry season climate characteristics on rice cropping systems and rice growth cycles (rain-fed croplands are typically single-season rice, usually planted during the rainy season; irrigated croplands are typically multi-season rice, planted during both the wet and dry seasons). Furthermore, considering the significant variation in terrain features from north to south in the MRB, the study area was divided into five regions based on administrative division and topographical characteristics: Laos, Thailand, Cambodia, the Mekong Delta, and the Vietnam Central High Plain (VCHP). The spatial and temporal distribution patterns of meteorological droughts were

analyzed for each region. The standard for dry and wet grades of meteorological droughts can be found in the monitoring results.

2. Method for Agricultural Drought Monitoring

The wide north–south span and variation in terrain features in the study area make rice planting periods complex. The difference between the maximum NDVI values for droughts and normal years during a growth cycle was calculated to monitor agricultural drought conditions. Since rice is only planted in irrigated croplands during the dry season, irrigated fields were selected while monitoring agricultural drought in the dry season, whereas all croplands were selected during monitoring in the rainy season. Cropland data were obtained from the ESA CCI land-cover products. Based on the results of meteorological drought monitoring, drought and non-drought years during the dry and rainy seasons from 2010 to 2020 were determined, and agricultural droughts during drought years in the dry and rainy seasons were monitored to construct an agriculture drought index (ADI), using the following formula:

$$ADI = NDVI_{\max\text{-year}} - NDVI_{\max\text{-mean}}$$

where $NDVI_{\max\text{-year}}$ represents the maximum NDVI value during a rice growth cycle in a given year under meteorological drought conditions, while $NDVI_{\max\text{-mean}}$ represents the mean value of maximum NDVI values for corresponding planting seasons during non-meteorological drought years. In this case, the occurrence month of $NDVI_{\max}$ for rice in the dry season was restricted to occur between January and June, while that for rice in the rainy season was limited to July to December. Based on the ADI, the agricultural droughts were classified into five categories: extreme drought, severe drought, moderate drought, slight drought, and near normal, corresponding to ADI values of ≤ -0.20 , $(-0.20, -0.15]$, $(-0.15, -0.10]$, $(-0.10, -0.05]$, and > -0.05 , respectively.

2.3.7.4 Results and Analysis

1. Spatiotemporal distribution patterns of meteorological droughts in MRB from 2010 to 2020

This case study found that the lower reaches of the MRB experienced a weak drying trend from 2010 to 2020. The climate conditions in the Basin were notably wet in 2011–2012 and 2017–2018, and dry in 2010, 2015–2016, and 2019–2020 (Fig. 2.22). Through the monitoring of meteorological droughts during the dry and rainy seasons on an annual basis (Fig. 2.23), it was found that the dry seasons in 2011, 2012, and 2017 and the rainy seasons in 2011, 2013, and 2017 had significantly wet conditions, while the dry seasons in 2010, 2015, 2016, 2019, and 2020 and the rainy seasons in 2012, 2015, 2018, and 2019 were under significantly dry conditions. However, due to uneven rainfall distribution, there were significant differences in the drought and wetness distribution patterns among different regions at different time periods and spatial scales. Laos experienced varying degrees of extreme droughts during the dry seasons in 2015, 2016, and 2019, and during the rainy season in 2019; Thailand experienced similar conditions during the dry and rainy seasons in 2019; Cambodia experienced severe droughts during the dry season in 2016 and the rainy seasons in 2015 and 2019; the Mekong Delta experienced extreme droughts during the rainy seasons in 2015 and 2019 and the dry season in 2016; and the VCHP experienced extreme droughts during the rainy seasons in 2015 and 2019. Cambodia, the Mekong Delta, and the VCHP experienced continuous severe droughts from the dry season in 2015 to the dry season in 2016. Laos suffered from extensive extreme droughts during both the dry and rainy seasons in 2019 (34.40% and 24.46% of the total area of Laos, respectively). Additionally, Cambodia and the Mekong Delta went through moderate to extreme meteorological droughts from the rainy season in 2019 to the dry season in 2020.

2. Spatiotemporal distribution patterns of agricultural droughts and their causes

This case study found that although the MRB experienced varying degrees of meteorological droughts during both the dry and rainy seasons, the occurrence and proportion of agricultural droughts during the dry season were higher overall than those during the rainy season (Fig. 2.24). Due to consecutive years of meteorological droughts in 2015–2016 and 2019–2020, a significant agricultural extreme drought occurred in various regions during the dry seasons of 2016 and 2020 compared to other years. Agricultural droughts during the rainy seasons were generally weaker, mostly slight drought, with only a small proportion of regions in the Mekong Delta experiencing extreme droughts. These results indicate that meteorological droughts during the rainy seasons have less impact on agricultural production in the upstream countries. However, due to the combined impacts of meteorological droughts and the considerable river water consumption by the upstream countries, agricultural production in the downstream Mekong Delta region was significantly impacted even during the rainy seasons in severe meteorological drought years. Therefore, it can be seen that the Mekong Delta is sensitive to climate change and is a typical fragile area for stabilizing agricultural production.

To further explore the impacts of meteorological droughts during the dry season on the distribution patterns of agricultural droughts, we analyzed severe agricultural drought years, 2016 and 2020, at a provincial level (Fig. 2.25). In general, regions with significant differences in terrain, such as northern Laos and the VCHP, have a stronger agricultural production adaptation to meteorological droughts compared to flat areas such as Thailand and Cambodia. Conversely, the flat and low-lying coastal areas of the Mekong Delta, which are susceptible to multiple impacts from meteorological and hydrological droughts and seawater intrusion, have weaker adaptation abilities. In both years,

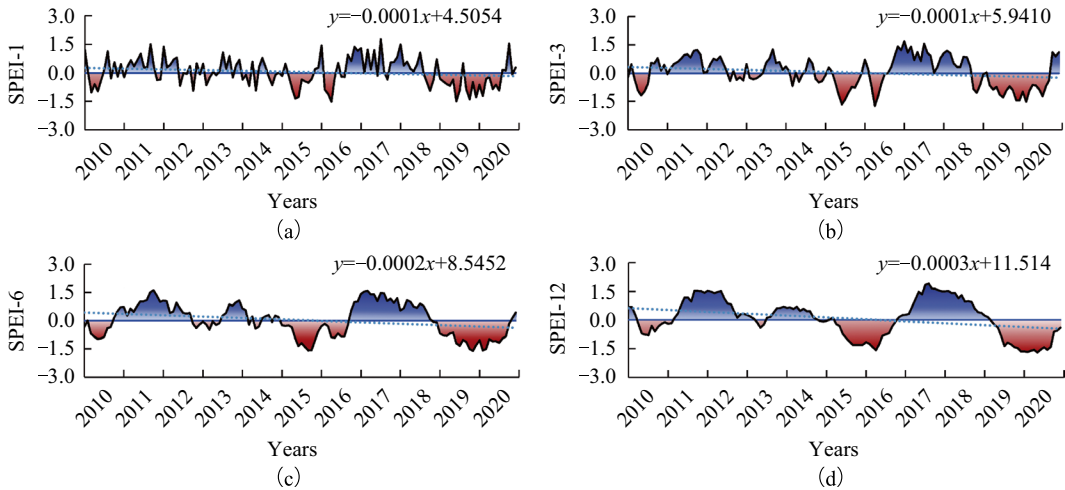


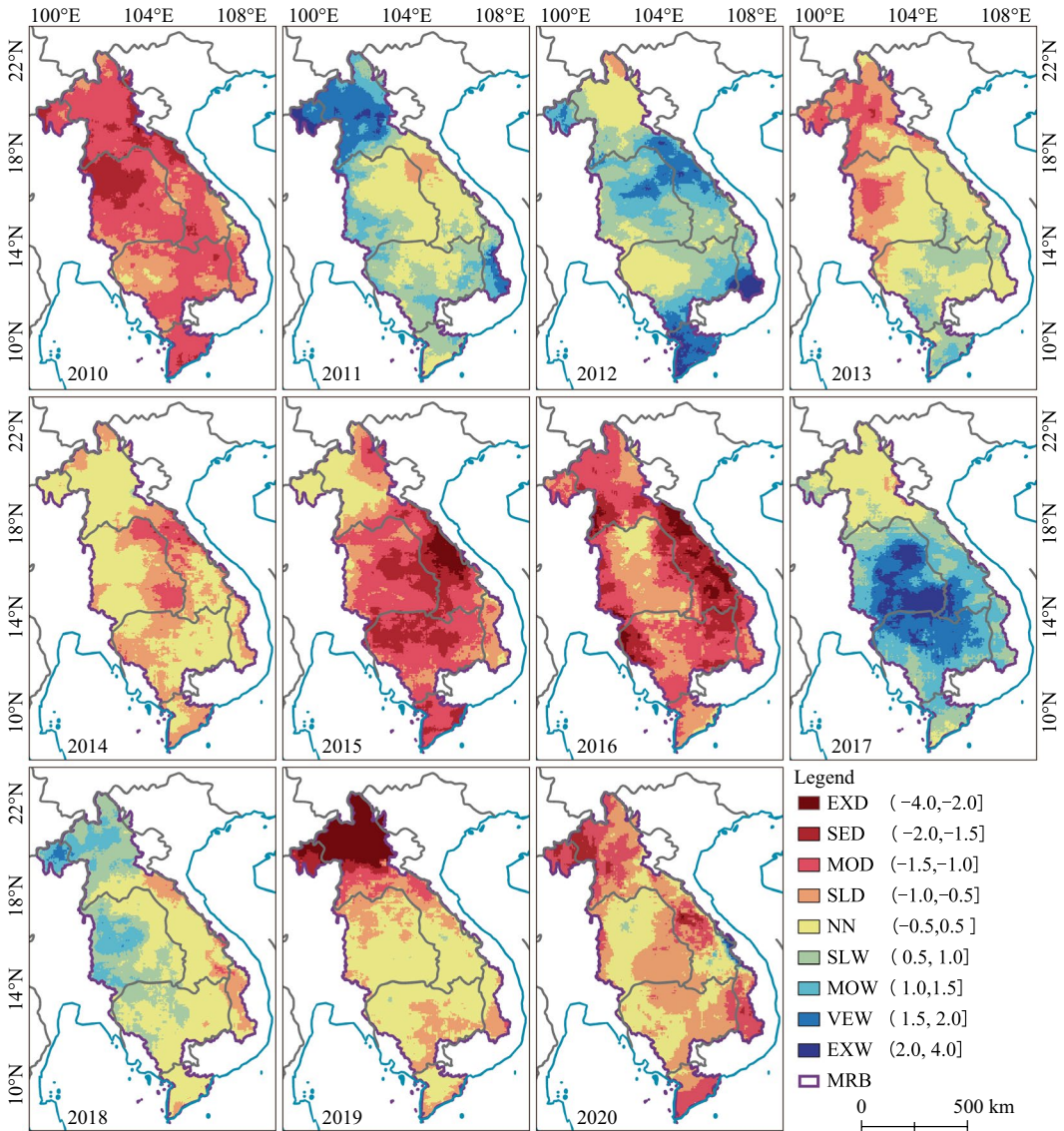
Fig. 2.22 Dry/wet change trends in the MRB at different time scales from 2010 to 2020. *Note* The SPEI value is the average value of the entire study area and reflects overall dry/wet conditions. The blue areas represent positive values of SPEI, indicating wet conditions; while the red areas represent negative values of SPEI, indicating dry conditions

each region had a similar distribution pattern of agricultural droughts. The severity of agricultural droughts in northern Laos was generally lower than that in the southern provinces, mainly due to the larger terrain differences in the north, where low-lying croplands received irrigation water from upstream rivers and saw a convergence of rainwater from higher elevations. In contrast, the south had lower terrain differences and suffered from reduced river flow caused by meteorological droughts. Agricultural droughts in Thailand showed a clear trend of decreasing severity from northwest to southeast due to severe meteorological droughts and the northwest's higher elevation, leading to higher river flow downstream. Cambodia exhibited a characteristic where the severity of agricultural droughts was higher in the north than that in the south. The northern region's higher elevation leads to water convergence in the south from both the Mekong River and Tonle Sap Lake for irrigation purposes. However, in the Mekong Delta region, a significant loss in agricultural production occurred in coastal provinces due to extremely low river flow at the river mouth caused by meteorological droughts and upstream water consumption, combined with

seawater intrusion. These resulted in higher agricultural drought severity in the southern areas compared to the northern areas.

2.3.7.5 Highlights

- Datasets of meteorological drought monitoring for the MRB from 2010 to 2020 were obtained at a spatial resolution of 5566 m.
- From 2010 to 2020, the MRB showed a weak trend toward increased aridity. Severe meteorological droughts occurred in 2010, 2015–2016, and 2019–2020. Cambodia and the Mekong Delta experienced severe droughts in 2015–2016, while Laos and Cambodia experienced severe droughts in 2019–2020, with some areas reaching extreme droughts.
- The impacts of meteorological droughts on agricultural production during the dry season are more severe than those during the rainy season. The Mekong Delta is a typical area vulnerable to stable food production. Influenced by meteorology, hydrology, and topography, the severity of agricultural droughts during the dry season in the Basin is characterized by southern Laos being higher than northern Laos, northwestern Thailand being higher than



(a) Spatial and temporal distribution patterns of meteorological droughts in the dry season of the MRB

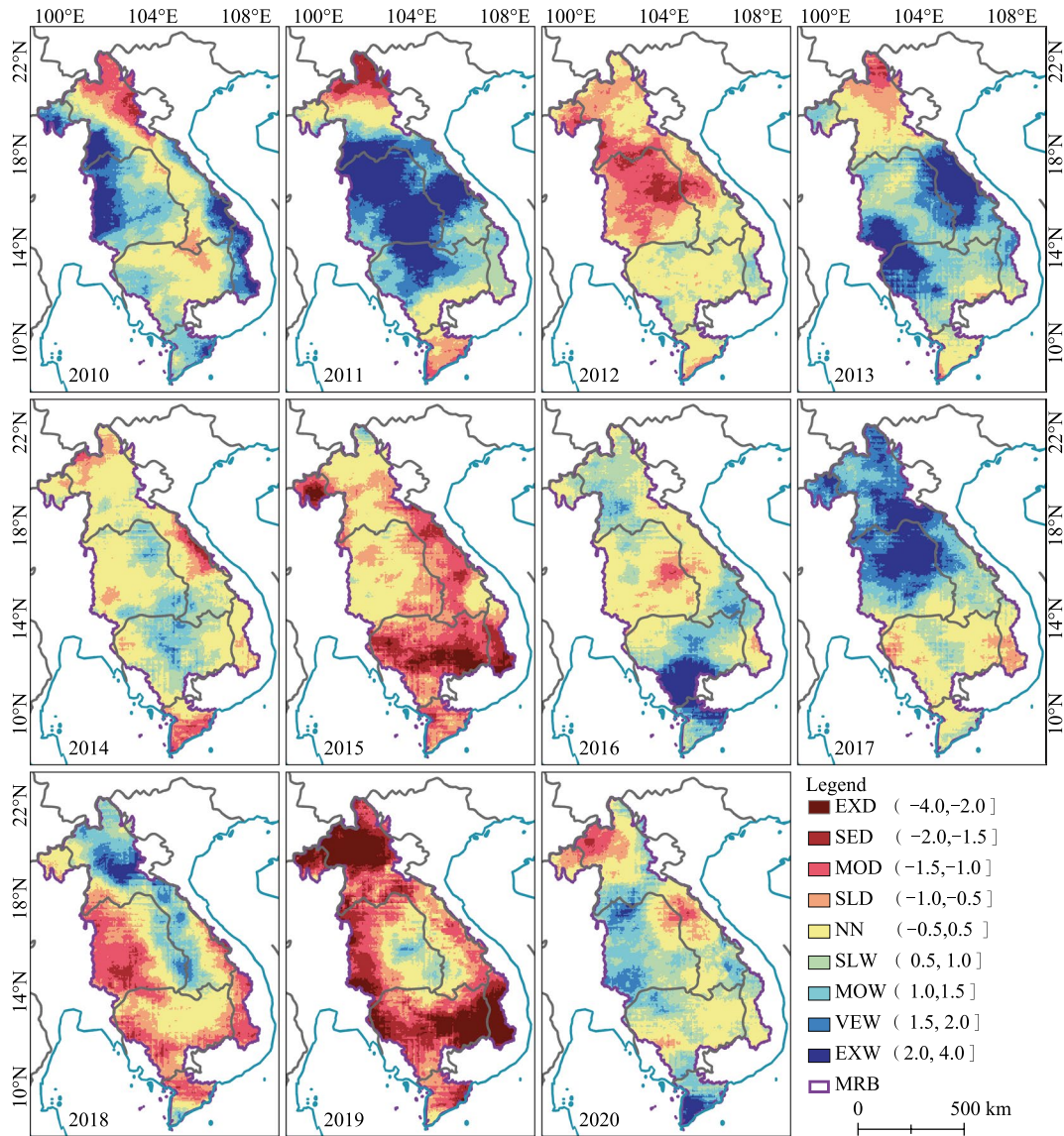
Fig. 2.23 Spatial and temporal distribution patterns of meteorological droughts during the dry season (a) and the rainy season (b) in the MRB from 2010 to 2020. *Note* for this and subsequent figures: EXD: extreme drought. SED: severe drought. MOD: moderate drought.

SLD: slight drought. NN: near normal. SLW: slightly wet. MOW: moderate wet. VEW: very wet. EXW: extremely wet. The number ranges in the legend are the SPEI ranges corresponding to different wet and dry grades

southeastern Thailand, northern Cambodia being higher than southern Cambodia, and the southern part of the Mekong Delta being higher than the northern part.

2.3.7.6 Discussion and Outlook

Based on Big Earth Data such as meteorological and multi-source remote sensing, this case monitored meteorological droughts in the MRB



(b) Spatial and temporal distribution patterns of meteorological droughts in the rainy season of the MRB

Fig. 2.23 (continued)

from 2010 to 2020, and explored the spatiotemporal distribution patterns of meteorological droughts during the dry and rainy seasons in five regions, including Laos, Thailand, Cambodia, the Mekong Delta, and the VCHP. Agricultural droughts during meteorological drought years in the dry and rainy seasons were monitored, and the adaptability of different regions in the MRB to meteorological droughts was analyzed

to identify areas vulnerable to stable food production. Based on the distribution patterns of agricultural droughts in each province, the distribution characteristics and causes of agricultural drought severity in different regions were analyzed. The research results can provide a theoretical basis for identifying areas vulnerable to stable food production and a decision-making reference to management authorities for disaster

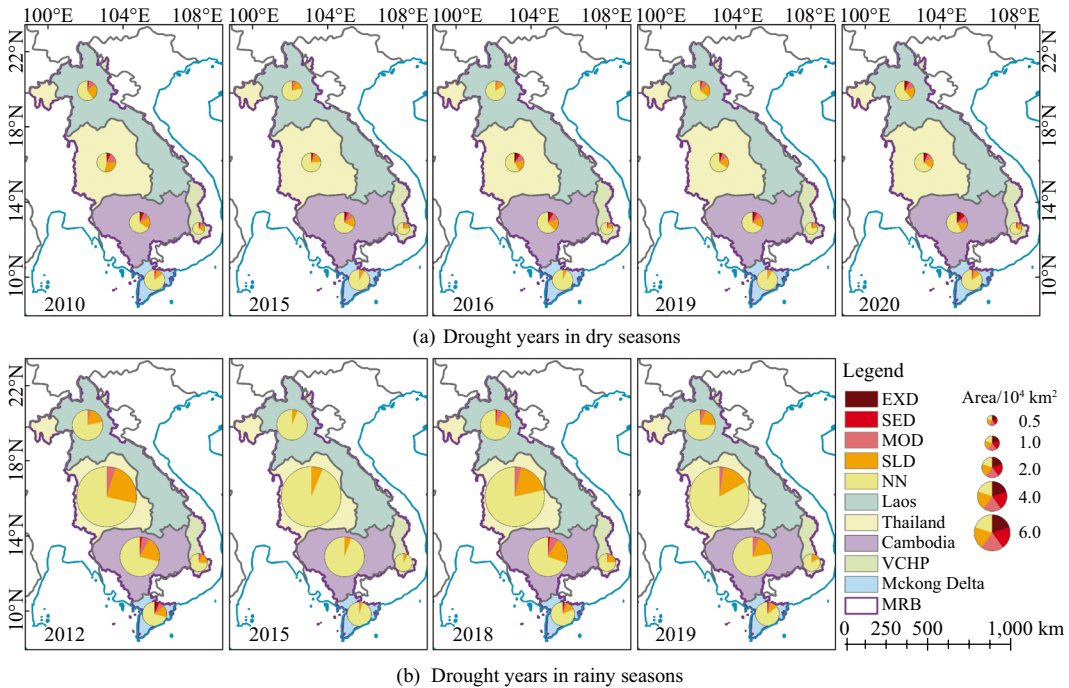


Fig. 2.24 Areas and proportion of agricultural droughts in the five regions during meteorological drought years in dry seasons (a) and rainy seasons (b). Note The size of the pie chart represents the total area of croplands in the

corresponding region during dry and rainy seasons, with the irrigated cropland for the dry season and all croplands for the rainy season

prevention and mitigation in response to potential food crises.

Meteorological droughts are just one manifestation of drought risk, presenting climate risk events that exist under the background of global climate change. However, agricultural production involves highly participatory socioeconomic activities that are subject to human intervention. Adequate human intervention, such as timely water conservation measures, can alleviate agricultural droughts and prevent them from developing into actual droughts. As a result, the future plan is to integrate the monitoring of meteorological, hydrological, and soil conditions for comprehensive agricultural drought monitoring based on the methods and analysis approaches proposed in this case study. In addition, the study area will expand to conduct larger-scale monitoring of meteorological and agricultural droughts, providing scientific guidance to decision-making authorities to enhance the ability of

regions vulnerable to stable food production to adapt to extreme weather and drought disasters.

2.4 Summary

On the global scale and regional scale (countries of the BAR initiative), we developed and analyzed public datasets that support indicator monitoring for SDG 2.3.1 (“volume of production per labor unit by classes of farming/pastoral/forestry enterprise size”) and SDG 2.4.1 (“proportion of agricultural area under productive and sustainable agriculture”), and released a dynamic monitoring dataset for global 30 m cropland from 1985 to 2020 and global 30 m resolution CI spatial distribution for 2020, which provided the basis for carrying out global food production monitoring. At the same time, we analyzed key issues in hotspot regions to provide decision support for the sustainable

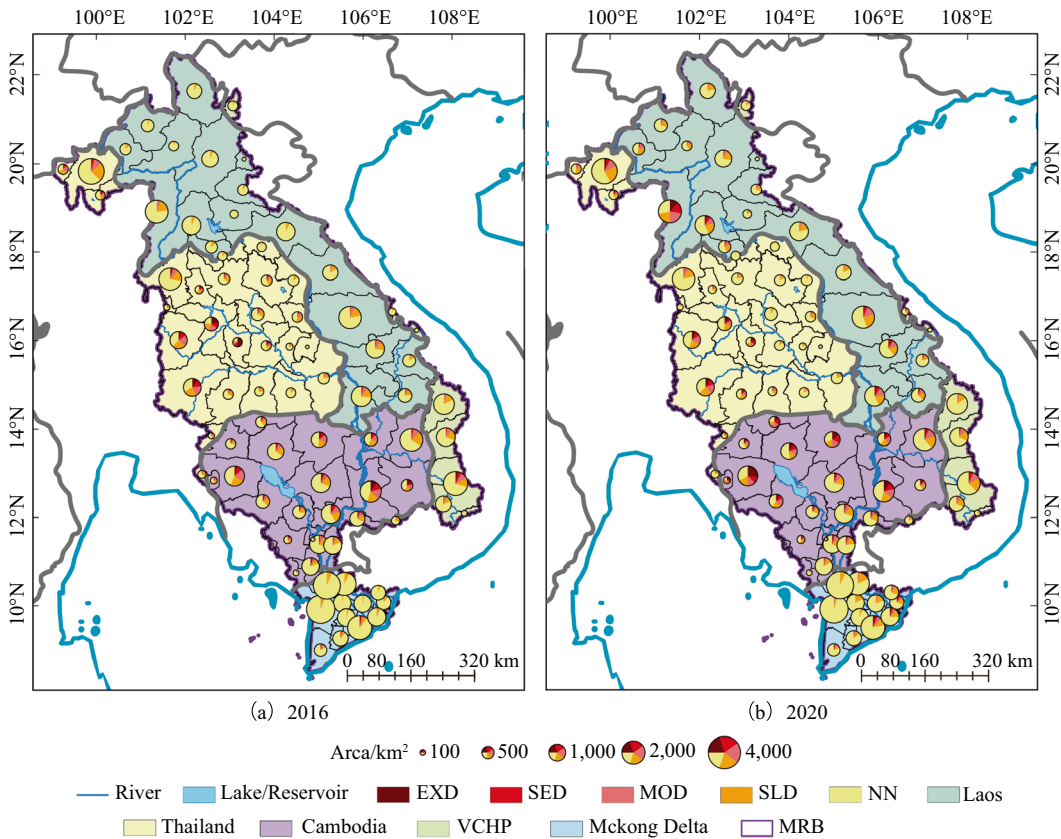


Fig. 2.25 Spatial distribution patterns and area proportion of agricultural droughts by province during the dry season in the MRB for 2016 and 2020. *Note*

The size of the pie chart in the figure represents the irrigated cropland area during the dry season for each province

development of regional agriculture and the realization of Zero Hunger. The main research findings are as follows.

- (1) From 1985 to 2020, the total area of cropland in the world showed steady growth, which was mainly attributed to significant deforestation and land reclamation in tropical countries such as Brazil and Indonesia. In 2020, about 14.8% of global cropland experienced multiple cropping, with Indo-Gangetic Plain, Huang-Huai-Hai Plain, and Nile River Delta being the regions with the highest concentrations of multiple-cropping in the world. If the actual level of multiple cropping can be improved to the potential level under rain-fed conditions on a global scale, it is expected to increase grain yield

- by 230 million tons, equivalent to 6.4% of the current global grain yield.
- (2) In the five Central Asian countries where animal husbandry is relatively predominant, the grassland is mainly desert and semi-desert, and is moderately degraded in general. Grassland overgrazing is serious in Uzbekistan, Turkmenistan, and Tajikistan, and GCC is tending to decrease.
- (3) Africa is a food security-sensitive region. The gross crop production and per capita crop production in West Africa, Central Africa, and East Africa increased significantly from 2010 to 2020, but are still far from the goal of food self-sufficiency. The desert locust plague that has ravaged Asia and Africa since 2018 is still spreading, with some 3–3.5% of the total vegetation

area lost in Somalia and Ethiopia between June 2021 and April 2022. The MRB in Southeast Asia showed a weak drying trend from 2010 to 2020 and the impact of meteorological drought on agricultural production in the dry season was more serious than that in the rainy season.

References

- Alexander LV, Zhang XB, Peterson TC et al (2006) Global observed changes in daily climate extremes of temperature and precipitation. *J Geophys Res* 111(D5):1–22
- Allen MR, Ingram WJ (2002) Constraints on future changes in climate and the hydrologic cycle. *Nature* 419(6903):224–232
- Angerer J, Han G, Fujisaki I et al (2008) Climate change and ecosystems of Asia with emphasis on Inner Mongolia and Mongolia. *Rangelands* 30(3):46–51. [https://doi.org/10.2111/1551-501X\(2008\)3046:CCAE OA2.0.CO2](https://doi.org/10.2111/1551-501X(2008)3046:CCAE OA2.0.CO2)
- Bao G, Chen J, Chopping M et al (2019) Dynamics of net primary productivity on the Mongolian Plateau: joint regulations of phenology and drought. *Int J Appl Earth Obs Geoinf* 81:85–97. <https://doi.org/10.1016/j.jag.2019.05.009>
- Baudoin MA, Vogel C, Nortje K et al (2017) Living with drought in South Africa: lessons learnt from the recent El Niño drought period. *Int J Disaster Risk Reduction* 23:128–137
- FAO et al (2022) The State of Food Security and Nutrition in the World 2022: repurposing food and agricultural policies to make healthy diets more affordable. Rome, FAO
- FAO (2020) The state of food and agriculture 2020. <https://www.fao.org/3/cb1447en/cb1447en.pdf>
- FAO (2024) Food and agriculture data. Rome. <https://www.fao.org/faostat/en/#home>
- Field CB, Randerson JT, Malmstrom CM (1995) Global net primary production: combining ecology and remote sensing. *Remote Sens Environ* 51(1):74–88
- Gilbert M, Nicolas G, Cinardi G et al (2018) Global distribution data for cattle, buffaloes, horses, sheep, goats, pigs, chickens and ducks in 2010. *Sci Data* 5:180227
- Gill RA, Kelly RH, Parton WJ et al (2002) Using simple environmental variables to estimate below-ground productivity in grasslands. *Glob Ecol Biogeogr* 11(1):79–86
- Gommes R, Wu B, Li Z et al (2016) Design and characterization of spatial units for monitoring global impacts of environmental factors on major crops and food security. *Food Energy Secur* 5(1):40–55
- Ho TT, Shimada K (2021) The effects of multiple climate change responses on economic performance of rice farms: evidence from the Mekong Delta of Vietnam. *J Clean Prod* 315:128129
- Hobbs NT, Swift DM (1985) Estimates of habitat carrying capacity incorporating explicit nutritional constraints. *J Wildl Manage* 49(3):814–822
- Hui D, Jackson RB (2006) Geographical and interannual variability in biomass partitioning in grassland ecosystems: a synthesis of field data. *New Phytol* 169:85–93
- Liu C, Zhang Q, Tao S et al (2020) A new framework to map fine resolution cropping intensity across the globe: algorithm, validation, and implication. *Remote Sens Environ* 251:112095
- Myneni R, Knyazikhin Y, Park T (2021) MODIS/terra leaf area index/FPAR2.8-Day L4 global 500 m SIN grid V061. 2021, distributed by NASA EOSDIS Land Processes Distributed Active Archive Center, <https://doi.org/10.5067/MODIS/MOD15A2H.061>. Accessed 07 Jan 2024
- Nachtergaele F, van Velthuizen H, Verelst L (2012) Harmonized World Soil Database v 1.2. Rome, Italy and IIASA, Laxenburg, Austria. Food and Agriculture Organization of the United Nations, International Institute for Applied Systems Analysis, ISRIC-World Soil Information, Institute of Soil Science-Chinese Academy of Sciences, Joint Research Centre of the European Commission
- Nandintsetseg B, Shinoda M, Erdenetsetseg B (2018) Contributions of multiple climate hazards and overgrazing to the 2009/2010 winter disaster in Mongolia. *Nat Hazards* 92(S1):109–126
- Olson DM, Dinerstein E, Wikramanayake ED et al (2001) Terrestrial ecoregions of the world: a new map of life on Earth. *Bioscience* 51:933–938
- Potapov P, Turubanova S, Hansen MC et al (2022) Global maps of cropland extent and change show accelerated cropland expansion in the twenty-first century. *Nature Food* 3(1):19–28
- Roe EM (1997) Viewpoint: on rangeland carrying capacity. *J Range Manag* 50(5):467–472
- Running S, Zhao M (2021) MODIS/terra net primary production gap-filled yearly L4 global 500 m SIN grid V061. NASA EOSDIS Land Processes Distributed Active Archive Center. Accessed 07 Jan 2024 from <https://doi.org/10.5067/MODIS/MOD17A3HGF.061>
- UN (2021) The sustainable development goals report 2021. New York. <https://unstats.un.org/sdgs/report/2021/>
- UN (2022) The sustainable development goals report 2022. UN, New York. <https://unstats.un.org/sdgs/report/2022>
- Vicente-Serrano SM, Beguería S, López-Moreno JJ (2010) A multiscalar drought index sensitive to global warming: the standardized precipitation evapotranspiration index. *J Clim* 23(7):1696–1718

- Zhang M, Wu B, Zeng H et al (2021) GCI30: a global dataset of 30 m cropping intensity using multisource remote sensing imagery. *Earth System Science Data* 13(10):4799–4817
- Zuo L, Zhang Z, Carlson KM et al (2018) Progress towards sustainable intensification in China challenged by land-use change. *Nature Sustainability* 1(6):304–313

Open Access This chapter is licensed under the terms of the Creative Commons Attribution-NonCommercial-NoDerivatives 4.0 International License (<http://creativecommons.org/licenses/by-nc-nd/4.0/>), which permits any noncommercial use, sharing, distribution and reproduction in any medium or format, as long as you give appropriate credit to the original author(s) and the source, provide a link to the Creative Commons license and indicate if you modified the licensed material. You do not have permission under this license to share adapted material derived from this chapter or parts of it.

The images or other third party material in this chapter are included in the chapter's Creative Commons license, unless indicated otherwise in a credit line to the material. If material is not included in the chapter's Creative Commons license and your intended use is not permitted by statutory regulation or exceeds the permitted use, you will need to obtain permission directly from the copyright holder.





SDG 6, Clean Water and Sanitation

3

3.1 Background

According to the comprehensive assessment report issued in 2021 by UN-Water, the world was already off track on SDG 6 even before the outbreak of the COVID-19 pandemic (UN-Water 2021). There are still 2 billion people worldwide without access to safely managed drinking water and 3.6 billion without safe sanitation facilities. In addition, 2.3 billion people lack soap and basic hand-washing facilities at home. Most wastewater is untreated before being discharged. One-fifth of the world's river basins are experiencing rapid changes. In the next nine years, we need to move four times faster in some fields to meet SDG 6 on time (Harlin et al. 2021).

Rivers, lakes, and groundwater are the main sources of freshwater and are therefore closely linked to the health and safety of life on Earth. Globally, however, polluted rivers, lakes, and groundwater are endangering the health of vital freshwater ecosystems. Accurate monitoring and assessment of the water quality in these bodies will help detect problems in time and take effective countermeasures to solve them. SDG 6.3.2 measures the proportion of bodies of water with good ambient water quality. It is an important indicator reflecting the health of freshwater ecosystems and relies mainly on the water

quality data of rivers, lakes, and groundwater obtained from field measurements and laboratory tests. At present, many developed countries have established long-term water quality-monitoring projects, but most countries still have not formed a regular water quality data monitoring network (WHO and UN-Habitat 2018), which affects regular monitoring and evaluation at the national scale, and new technologies are urgently needed to solve this problem. Most of the global freshwater ecosystems consisting of rivers, lakes, and groundwater are shared by different countries. Globally, 153 countries share transboundary basins, which account for more than 60% of the world's freshwater flows (UN and UNESCO 2021), so cooperation in these transboundary basins is crucial for equitable sharing and sustainable water management. SDG 6.5.2 reflects the “proportion of transboundary basin area with an operational arrangement for water cooperation”, and its evaluation depends entirely on the statistical data reported by UN member states. Affected by national economic development and international political situations and events, the global monitoring and evaluation of this indicator at a national resolution are not sufficient.

This chapter exemplifies the feasibility of using water quality indicators obtained from satellite remote sensing to reflect the global

progress of SDG 6.3.2 through two global-scale cases. In addition, the case of assessing the progress of SDG 6.5.2 on transboundary rivers in Central Asia demonstrates the feasibility of integrating datasets from different sources to solve the problem of missing data.

3.2 Main Contributions

The main contributions of the three cases in this chapter include global-scale lake algal bloom extraction and large-scale lake and reservoir transparency inversion models, worldwide algal bloom outbreaks in a sample of representative lakes and lake and reservoir transparency datasets from 2000 to 2021, and water cooperation decision-making support for transboundary rivers in Central Asia (Table 3.1).

3.3 Case Studies

3.3.1 Global Spatial and Temporal Distribution of Algal Blooms in Representative Lakes

Target: SDG 6.3: By 2030, improve water quality by reducing pollution, eliminating dumping and minimizing release of hazardous chemicals

and materials, halving the proportion of untreated wastewater and substantially increasing recycling and safe reuse globally.

Indicator: SDG 6.3.2: Proportion of bodies of water with good ambient water quality.

3.3.1.1 Background

Lakes are an important component of the terrestrial water cycle, but the eutrophication of lakes is deepening, leading to the massive growth of algae and the appearance of algal blooms, which seriously threaten the sustainable development of both the lake ecosystem and human society (Hou et al. 2022; Paerl and Huisman 2008). Under sustained global warming and escalating human activity, it is expected that the intensity of algal blooms will increase globally in the coming decades (Paerl et al. 2016). In order to achieve the SDGs and formulate effective management measures to respond to future threats from algal blooms, it is necessary to understand their spatial and temporal distribution. Therefore, based on MODIS images, we propose to construct a framework of algal blooms in lakes through remote sensing methods. The algal bloom dataset for representative lakes globally, from 2000 to 2020, was retrieved on Google Earth Engine. Based on the classification of temporal patterns of algal blooms, the spatiotemporal patterns and historical trends of algal blooms in a sample of representative lakes

Table 3.1 Cases and their main contributions

Indicators	Cases	Contributions
SDG 6.3.2 Proportion of bodies of water with good ambient water quality	Global spatial and temporal distribution of algal blooms in representative lakes	Method and model: Global algal bloom extraction method for representative lakes based on Google Earth Engine and MODIS data Data product: Dataset of algal bloom outbreaks in representative lakes around the world, 2000–2020
	Global temporal and spatial changes in water transparency in large lakes	Method: Global transparency inversion model for large lakes based on satellite remote sensing Data product: Dataset of the spatial distribution of water transparency in large lakes around the world, 2000–2021
SDG 6.5.2 Proportion of transboundary basin area with an operational arrangement for water cooperation	Dynamic changes in water events in transboundary rivers in Central Asia	Data product: Dataset of water conflict/cooperation events in transboundary rivers of Central Asia, 1951–2021 Decision support: Data for Central Asian countries to carry out transboundary cooperation

were analyzed. Finally, the driving forces of algal blooms were revealed, promoting the progress of SDG 6.3.2, and providing decision support for the scientific assessment of lake water quality and management.

3.3.1.2 Data

- Satellite Data: MOD09GQ (daily/250 m) and MOD09GA (daily/500 m resampled to 250 m) reflectance products from 2000 to 2020, MOD11A1 (daily, 1000 m resampled to 250 m) land surface temperature (LST) product, and MOD10A1 (daily, 1000 m resampled to 250 m) normalized difference snow index (NDSI) product.
- Global Lake Boundary Dataset: HydroLAKES dataset (Messager et al. 2016).
- Climate Zone Data: Köppen climate zone (Rubel and Kottek 2010).
- Meteorological Data: ERA5-Land (2000–2020) (Muñoz-Sabater et al. 2019).
- Land Use Data: MCD12Q1 (2000–2020) (Friedl and Sulla-Menashe 2019).
- Population Density Data: LandScan (2000–2020) (Dobson et al. 2000).
- Human footprint data (2000–2018) (Mu et al. 2022).
- Nighttime light (NTL) intensity data (2000–2020) (Chen et al. 2021).

3.3.1.3 Methods

In this case study, MODIS images were used to extract the algal bloom area using the floating algae index (FAI) and maximum gradient method. The MODIS NDSI (MOD10A1) and LST (MOD11A1) were used to eliminate the influence of non-algal bloom pixels. The FAI is an index based on MODIS Rrc data (reflectance after removing Rayleigh scattering) and is calculated using three bands: red (645 nm), near-infrared (NIR) (859 nm), and short-wave infrared (SWIR) (1240 nm) to extract algal blooms (Hu 2009). The calculation formula is as follows:

$$\begin{aligned} \text{FAI} &= R_{\text{NIR}} - R'_{\text{NIR}} \\ R'_{\text{NIR}} &= R_{\text{RED}} + [R_{\text{SWIR}} - R_{\text{RED}}] \\ &\quad \times [(\lambda_{\text{NIR}} - \lambda_{\text{RED}})/(\lambda_{\text{SWIR}} - \lambda_{\text{RED}})], \end{aligned}$$

where R_{NIR} is the baseline reflectance at the NIR band, and R_{Red} , R_{NIR} , and R_{SWIR} are the reflectance in the red, NIR, and SWIR bands, respectively. In this case, the NDSI, turbid water index (TWI), and the cyanobacteria and macrophytes index (CMI) were used to remove the effects of ice, turbid water areas, and aquatic vegetation areas (Liang et al. 2017), respectively.

Based on the literature review, 20 lakes with algal blooms in North America, Africa, and Asia were selected as the objects for threshold statistics. In order to cover more types of lakes, these lakes are located on four continents in three climatic zones, and the land use types of their basins vary from urban, forest, grassland, and cropland. The corresponding gradient image was calculated, and a histogram of the remaining pixels was constructed. Notably, the histogram was constructed based on the FAI gradient values to locate pixels at the maximum gradient value, and the average FAI value corresponding to these pixels with the maximum gradient was used as the threshold for differentiating algal bloom-infested and algae-free waters. The threshold values for all images were statistically analyzed together to ensure a consistent threshold for all data over the whole period (Hu et al. 2010; Ma et al. 2020), while the total FAI accumulation value of each FAI image of each lake was counted to eliminate the interference of the images without algal blooms on the threshold determination (the first 50% of the FAI images were used to determine the initial threshold). Then the initial threshold was used to extract the algal bloom coverage, and the pixels with a bloom coverage greater than 10% were re-calculated by the maximum gradient method to obtain a new threshold. After the loop iteration, the threshold stabilized to the final threshold.

This case study selected background data in four aspects of the lake: (1) background factors, including average lake depth, surface area, and dynamic sediment ratio [DSR, calculated by the surface area and lake depth to estimate the sensitivity of the lake to sediment resuspension caused by wind-driven waves (Håkanson and Jansson 1983)]; (2) climatic factors, including annual mean temperature, annual mean winter temperature (Northern Hemisphere: the average temperature of December of the previous year to February of the current year; Southern Hemisphere: the average temperature of June to August), annual mean precipitation, annual mean air pressure, and annual mean wind speed; (3) human activity factors, including population density, NTL intensity, human footprint; and (4) land use, including the calculated proportion of urban land, cropland, forest, grassland, and permanent wetland in the watershed. The data statistics were determined per lake basin using the basin boundary data from HydroBASINS (Lehner and Grill 2014). The correlations between bloom parameters and bloom-driving factors at the global scale were calculated. Random forest regression was used to calculate the contribution of each driving factor to the spatial distribution of algal blooms (Leach et al. 2018). For parameters that remained unchanged during the study period, such as lake area, lake depth, and DSR, the contribution was calculated using the mean value of the algal bloom parameters within the time range.

3.3.1.4 Results and Analysis

1. Spatial Distribution of Algal Blooms

Of the 161 large lakes studied, 70 were identified as having algal blooms (including 20 lakes for FAI threshold statistics), accounting for 43% of those studied (Fig. 3.1). North America had the highest number of lakes with algal blooms ($N=21$ lakes, 38% of North American lakes studied), followed by Asia ($N=19$ lakes, 34% of Asian lakes). The highest percentages of lakes with algal blooms occurred in Europe ($N=10$ lakes, 71% of European lakes) and Africa

($N=14$ lakes, 58% of African lakes). Only four lakes in South America and two in Oceania were recorded with algal blooms (Fig. 3.1).

There were 22 representative lakes worldwide that experienced significant algal blooms (i.e., a surface extension of algal blooms greater than 25% of the lake was observed from 2000 to 2020). These lakes are distributed in Asia, North America, Europe, and Africa. Asia has nine lakes with significant algal blooms, including China's Taihu Lake, Chaohu Lake, and Hulun Lake; Buir Lake on the China–Mongolia border; Xingkai Lake on the China–Russia border; Zaysan Lake in Kazakhstan; Lake Beysehir in Turkey; Lake Sevan in Armenia; and Lake Bay in the Philippines. North America has seven lakes with significant algal blooms, including Lake Churchill, Lake Winnipeg, Lake Dauphin, Lake Peter Pond, and Lake Lesser Slave in Canada and Lake Winnebago and Lake Okeechobee in the United States. Europe and Africa each have three lakes with significant algal blooms, including Lake Belye and Lake Ilmen in Russia, Lake Peipsi shared by Russia and Estonia, Lake Manyara in Tanzania, Lake Chilwa on the Malawi–Mozambique border, and Lake Toshka in Egypt. Among these lakes, Lake Manyara in Tanzania and Taihu Lake and Chaohu Lake in China were observed to experience the most significant algal blooms and most severe algal phenomena.

2. Temporal Patterns of Algal Blooms

According to the temporal patterns of algal blooms, the lakes were classified into lakes without algal blooms, lakes with sporadic blooms (no more than three consecutive years of algal blooms), lakes with seasonal blooms (no more than one season of algal blooms per year), and lakes with perennial blooms (multi-seasonal blooms over many years).

There are five lakes with perennial blooms, seven with seasonal blooms, 58 with sporadic blooms, and 91 with no bloom worldwide (Fig. 3.2). Lakes with perennial blooms were concentrated in the tropical and subtropical regions of Asia and Africa, namely: Lake

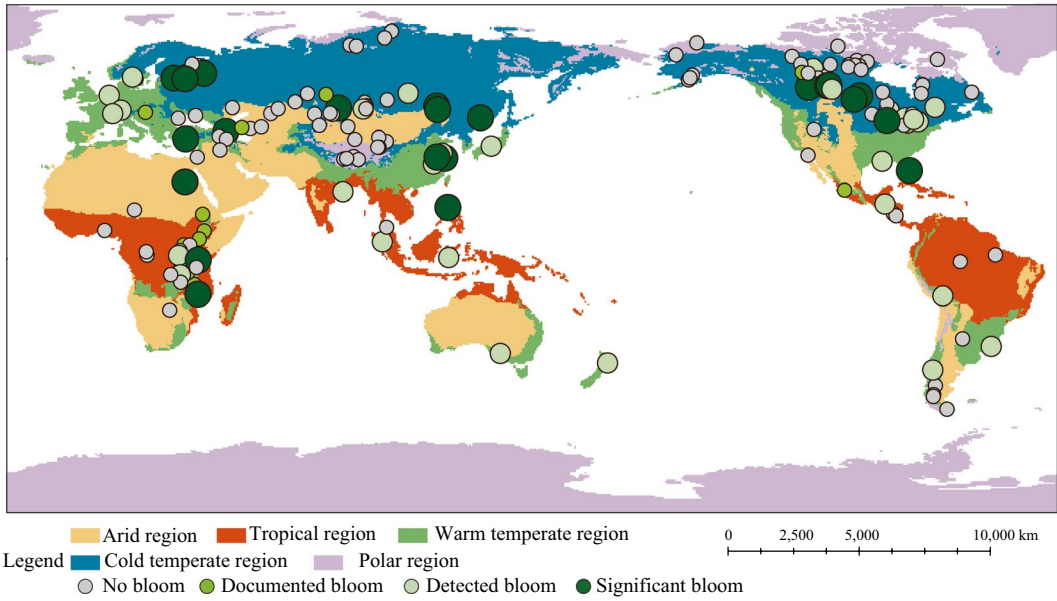


Fig. 3.1 Classification and distribution of large lakes with algal blooms worldwide from 2000 to 2020. *Note* The size of the dots is the max percent of algal blooms from 2000 to 2020

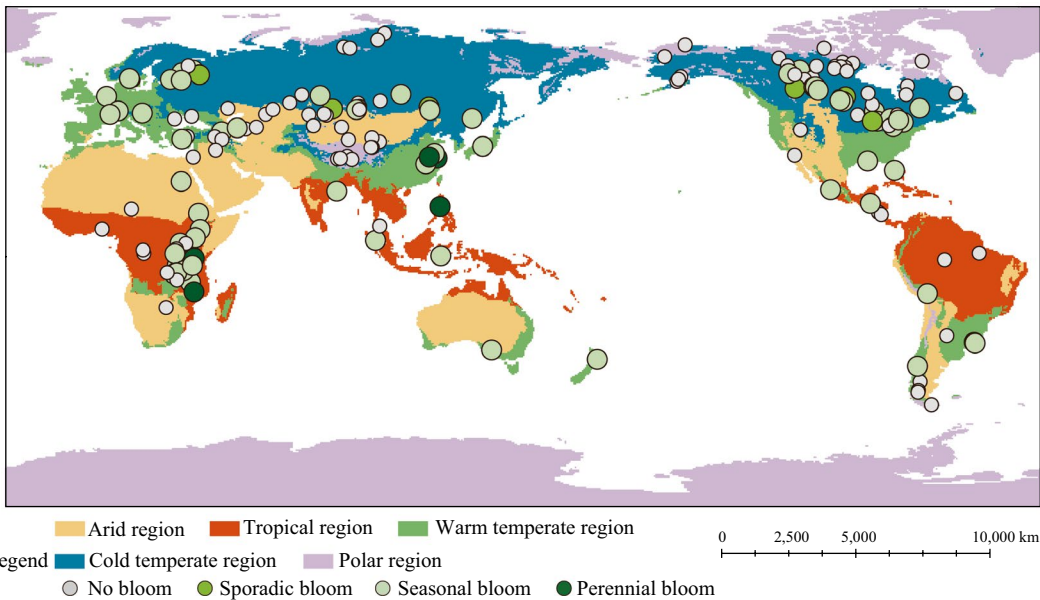


Fig. 3.2 Classification and distribution of lakes with algal blooms from 2000 to 2020. *Note* The lakes that recorded the existence of algal blooms from the literature review were also identified as lakes with sporadic blooms

Taihu, Lake Chaohu, and Lake Bay in Asia and Lake Chilwa and Lake Manyara in Africa. Lakes with seasonal blooms were concentrated in Asia,

Europe, and North America, including Lake Hulun in China; Lake Zaysan in Kazakhstan; Lake Belye in Russia; Lake Lesser Slave, Peter

Pond Lake, and Lake Winnipeg in Canada; and Lake Winnipeg and Lake Winnebago in the United States. The 58 lakes with sporadic blooms were distributed worldwide, including 12 in Africa, 14 in Asia, 9 in Europe, 17 in North America, 4 in South America, and 2 in Oceania. Overall, 9% of lakes in Asia were characterized as lakes with perennial and seasonal blooms, which showed the highest proportion. Lakes in South America and Oceania experienced only sporadic blooms.

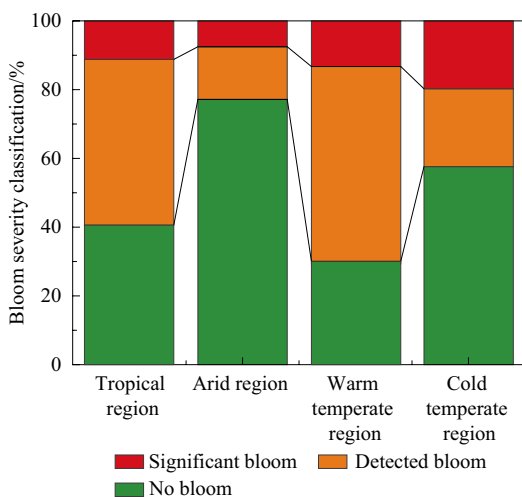
3. Characteristics Across Climate Zones

The patterns of algal blooms in lakes vary significantly in different climate zones (Fig. 3.3), based on the Köppen climate classification system (Rubel and Kottek 2010). The proportion of lakes with algal blooms in warm temperate and tropic zones exceeded 50%, with warm temperate lakes having the highest proportion (59%). The proportion of lakes experiencing algal blooms was lower in cold temperate and arid zones, with the lowest proportion (12%) in arid zones. The highest proportion of lakes with significant algal blooms was in cold temperate zones, followed by warm temperate, tropical, and arid zones. In terms of seasonal characteristics of algal blooms, perennial blooms occurred

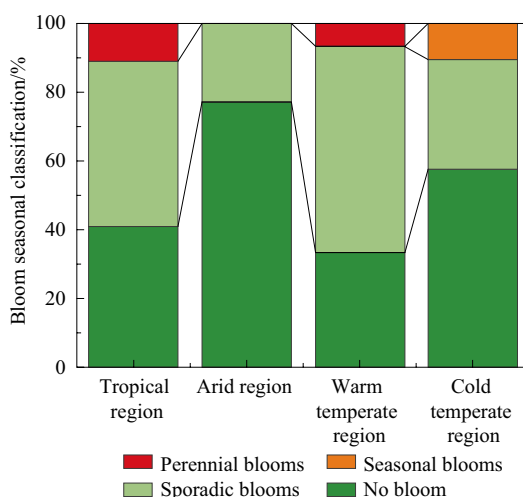
only in tropical and warm temperate lakes, seasonal blooms occurred only in cold temperate lakes, and arid lakes were characterized by sporadic blooms.

4. Global Driving Factors of Algal Blooms in Lakes

Climate factors contributed the most (Contribution: 44%, similarly hereinafter) to the initial bloom time, followed by human activity factors (33%) (Table 3.2). Winter temperature (27%) was negatively correlated with the initial bloom time ($r = -0.68$, $p < 0.01$) (Fig. 3.4). The duration of algal blooms (49%) and their frequency (46%) were mainly dominated by human activity factors. The dominant factors of the duration of algal blooms were NTL intensity (17%), lake depth (15%), and winter temperature (10%). The primary factors affecting the algal bloom frequency were lake depth (15%), NTL intensity (15%), winter temperature (12%), and wind speed (10%). Human activity factors were the dominant factors for both the max bloom area (53%) and the mean bloom area (45%). The analysis showed that the contributions of factors affecting the max bloom area were dispersed, with the proportion of grassland in the basins contributing the most, accounting for only 10%, and the contributions



(a) Proportion of different bloom severity classifications



(b) Proportion of seasonal characteristics of algal blooms

Fig. 3.3 Algal blooms in different climate zones

Table 3.2 Contribution ratio of each algal bloom parameter to spatial variations of driving factors ($N=14$) after excluding urban coverage and annual temperature in lakes with significant blooms ($N=22$) from a random forest regression model (Unit: %)

Driving factors	Initial bloom time	Duration time	Max bloom percent	Mean bloom percent	Bloom frequency	
Climate factors	43.55	29.55	29.94	30.97	32.87	
Winter temperature	26.74	10.27	5.07	12.96	12.45	
Wind speed	7.75	8.27	8.35	6.91	10.48	
Air pressure	4.52	5.69	9.21	7.44	6.41	
Precipitation	4.54	5.33	7.31	3.67	3.53	
Lake morphological factors	23.73	21.54	17.06	23.89	20.68	
Lake depth	16.28	15.05	6.10	14.21	15.12	
Surface area	3.55	3.04	6.73	6.74	2.79	
DSR	3.91	3.45	4.23	2.93	2.77	
Human activity factors	32.73	48.90	53.00	45.14	46.46	
Human activity indicators	NTL intensity	8.83	17.25	8.12	16.62	14.81
	Population density	5.95	8.13	6.79	6.58	8.86
	Human footprint	2.90	6.68	6.50	5.14	6.46
Land use indicators	Grassland coverage	3.24	7.19	10.47	7.70	6.20
	Forest coverage	4.90	4.01	7.68	3.06	3.80
	Wetland coverage	2.63	2.93	7.43	3.27	3.28
	Cropland coverage	4.28	2.71	6.01	2.77	3.05

of other factors being minor. The dominant factors affecting the mean bloom area were NTL intensity (17%), lake depth (14%), and winter temperature (13%). Overall, climate warming caused algal blooms to occur earlier, while human activity increased the frequency and area of algal blooms.

3.3.1.5 Highlights

- A global algal bloom extraction process for lakes was constructed using Google Earth Engine and MODIS images.
- Classification results for algal blooms were presented based on the time series of algal bloom areas in lakes around the world.
- Spatiotemporal patterns and driving mechanisms were analyzed for algal blooms in lakes globally, which provides decision support for evaluating the water quality and ecological status of lakes.

3.3.1.6 Discussion and Outlook

This case built a global analysis framework for algal blooms in lakes based on MODIS images, presented the spatiotemporal distributions and driving forces of algal blooms in lakes from 2000 to 2020, and provided important scientific data for the assessment of SDG 6.3.2 on the global scale.

This case found that: (1) North America with a developed economy (21 lakes, accounting for 38.8% of the lakes studied in the continent) and Asia with a dense population and rapid economic development (19 lakes, accounting for 33.9% of the lakes studied in the continent) had the largest number of lakes with algal blooms, and it is necessary to reasonably control the discharge of pollutants into lakes, and strengthen the management of the water environment. (2) Lakes in warm temperate and tropical regions with suitable temperature conditions had the highest proportion of algal blooms (59%–66%). (3) Global warming leads

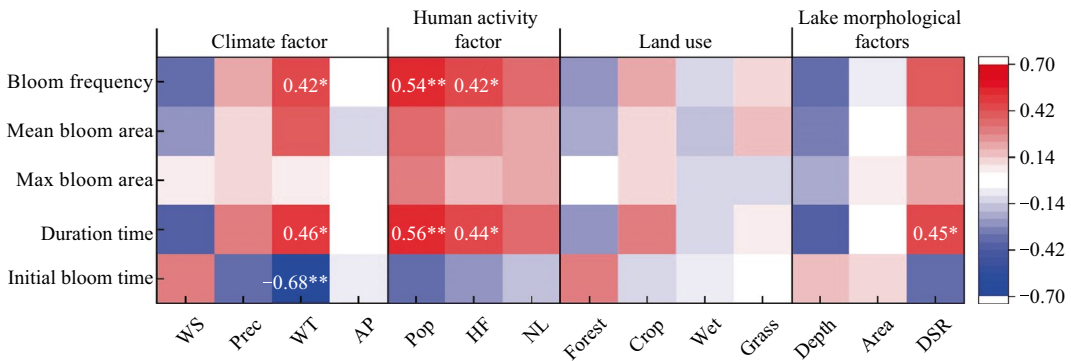


Fig. 3.4 Heat map showing the relationships between algal bloom parameters and driving factors for the lakes with significant algal blooms ($N=22$) worldwide. *Note* The numbers in the boxes are Pearson correlation coefficients. The labels on the x-axis represent specific driving factors, which are WS for wind speed, Prec for

precipitation, WT for winter temperature, AP for air pressure, Pop for population density, HF for human footprint, NL for NTL intensity, Forest for forest coverage, Crop for cropland coverage, Wet for wetland coverage, Grass for grassland coverage, Depth for lake depth, and Area for surface area. * represents $p < 0.05$, ** represents $p < 0.01$

to earlier algal bloom time and increased human activity leads to higher algal bloom frequency and area. (4) This case only analyzed the spatiotemporal distributions and driving forces of lakes at the global scale. Further analysis is needed for specific regions to provide water environment management recommendations for policymakers in regions with special environment and development patterns. The results indicate that the eco-environmental status of lakes worldwide is not optimistic. Global climate change and human social development have already impacted the ecological environment of lakes, posing threats to ecosystems and the sustainable development of human society, and bringing great challenges to the achievement of SDGs. (Modified from Ma et al. 2023).

3.3.2 Global Temporal and Spatial Changes in Water Transparency in Large Lakes

Target: SDG 6.3: By 2030, improve water quality by reducing pollution, eliminating dumping and minimizing release of hazardous chemicals and materials, halving the proportion of untreated wastewater and substantially increasing recycling and safe reuse globally.

Indicator: SDG 6.3.2: Proportion of bodies of water with good ambient water quality time.

3.3.2.1 Background

Water transparency, also known as Secchi disk depth (Z_{SD}), refers to the depth at which light penetrates through the water column, which directly affects the trophic status and primary productivity of the water body, and is an important remote sensing optical index indicating the water turbidity (Lee et al. 2015). The field measurement of water transparency is simple and economical. Generally, the Secchi disk (SD) is gradually sunk into the water on the water surface until it disappears out of the observer's sight, and the vertical distance from the water surface to the submerged SD is called water transparency or Z_{SD} . Water transparency is jointly affected by the three major water color constituents: suspended sediment, phytoplankton pigments, and colored dissolved organic matter. Compared with other optical water quality parameters, water transparency reflects the comprehensive water quality status of the water body to a certain extent. Due to the abovementioned two points, water transparency is listed as one of the most basic water parameters by water environment monitoring and management sectors. There is also a long history and extensive

record of water transparency compared to other parameters in lakes and oceans worldwide.

In situ sampling methods for collecting water quality parameters can no longer meet the needs of the current global dynamic survey of water quality. The water quality data of lakes on a global scale are seriously lacking, and the temporal and spatial changes of water quality in lakes and the assessment and management of sustainable development have always been important issues to be solved (Kavvada et al. 2020; Spyarakos et al. 2020; Tyler et al. 2016). The UN-Water Annual Report 2018 pointed out that for SDG 6, only 52 of the 193 member states in the world have submitted surface water quality monitoring data, and the monitoring data in some of these countries only include a small number of stations (UN-Water 2018). With the development of satellite remote sensing technology and the advancement of water color remote sensing modeling, research on optical remote sensing of inland water bodies has made rapid progress in recent years (Duan et al. 2022; Zhang et al. 2021). Satellite remote sensing data are becoming the most important, low-cost source of surface water quality monitoring data. Its advantages in large-scale, long-term time-series dynamic monitoring provide an effective way to fill data gaps, monitor water quality in lakes, and track the spatial and temporal patterns of water quality in a long-term time series.

This case study relies on Earth observation big data technology, takes water transparency as the indicator of lake water quality, and analyzes the temporal and spatial changes of water transparency in large lakes with surface area larger than 25 km² from 2000 to 2021 based on global satellite remote sensing. It provides a new global remote sensing monitoring dataset of water transparency for the global evaluation of SDG 6.

3.3.2.2 Data

- Satellite Remote Sensing Data: Terra MODIS surface reflectance data with 500 m resolution globally from 2000 to 2021 (MOD09A1).

- In Situ Data: Measured water transparency dataset of surface water bodies in China; measured water transparency dataset from the National Earth System Science Data Center; European Multi Lake Survey (EMLS) shared dataset in Europe; and AquaSat shared dataset in the United States.

3.3.2.3 Methods

This case study used MODIS surface reflectance products as the main data source, and constructed a water transparency estimation model based on the Forel-Ule index (FUI) and hue angle α (Wang et al. 2020). In the model, when the FUI value is small (FUI < 8), the relationship between the hue angle α and water transparency is better; when the FUI value is large (FUI \geq 8), the relationship between the FUI and water transparency is better. Therefore, the water transparency estimation model takes the form of a hybrid model:

$$\text{FUI} < 8 : Z_{\text{SD}} = 3415.63 * \alpha^{-1.49}.$$

$$\text{FUI} \geq 8 : Z_{\text{SD}} = 284.70 * \text{FUI}^{-2.67}$$

In the Z_{SD} estimation model, in order to ensure a smooth transformation of the segmented model, the empirical parameters of the model for FUI < 8 were obtained by fitting the data where $\alpha < 195^\circ$ (that is, FUI < 11). In the model validation, in addition to the model verification based on domestic lake data, the Z_{SD} estimation model was evaluated with the measured dataset of representative surface water bodies around the world.

In the data processing, a simple correction method based on the NIR and SWIR bands was used to correct the potential noise in the MOD09A1 data with band subtraction, and then the surface reflectance was converted to the water-leaving reflectance (Wang et al. 2016). In the automatic extraction of water bodies based on the MOD09A1 data, we used a modified histogram bimodal method to extract large inland water areas (> 25 km²) automatically based on the reflectance of the 1,640 nm band. Then, during the automatic selection of the threshold

value, a buffer zone was created around each connected water area with an area 1.5 times the initial water area. Based upon the expanded area including the initial water area and buffer zone, a histogram of the 1640 nm reflectance was produced for the whole expanded area where water and other land-cover types would be distributed separately in the histogram within the two modes. Finally, the threshold value for this water body area was recognized as the valley value within a specific threshold range in the histogram. Moreover, in order to avoid the land adjacent pixel effect, the water body area was eroded inward by one pixel. In addition, this case study used the Global Lakes and Wetlands Database (GLWD) to calibrate the extracted water bodies to avoid the influence of optically shallow water on the subsequent transparency estimation.

In the statistics of water transparency products, for large lakes with an area $>25 \text{ km}^2$, summer images from June to September were used to calculate the average water transparency in summer for every year, and a summer mean water transparency product was produced for large lakes around the world from 2000 to 2021

with MODIS data. Based on this product, when the pixel count of the summer mean image of the lake was not less than 30% of the pixel count of the standard mask of the specific lake, the summer mean value of the water transparency of this lake would be calculated.

3.3.2.4 Results and Analysis

1. Global Spatial Pattern Analysis of Water Transparency in Large Lakes from 2000 to 2021

The climatological lake transparency map from 2000 to 2021 is shown in Fig. 3.5, and the distribution patterns among continents and different climate zones are shown in Fig. 3.6. It can be seen from Fig. 3.5 that the climatological water transparency distribution of large lakes varied greatly among regions, and the overall distribution was exhibited in a concave profile in the latitudinal direction. That is, the water transparency of lakes in high-latitude areas near the North and South Poles was relatively high, with an average transparency of around 4 m, while the water transparency of lakes in low-latitude

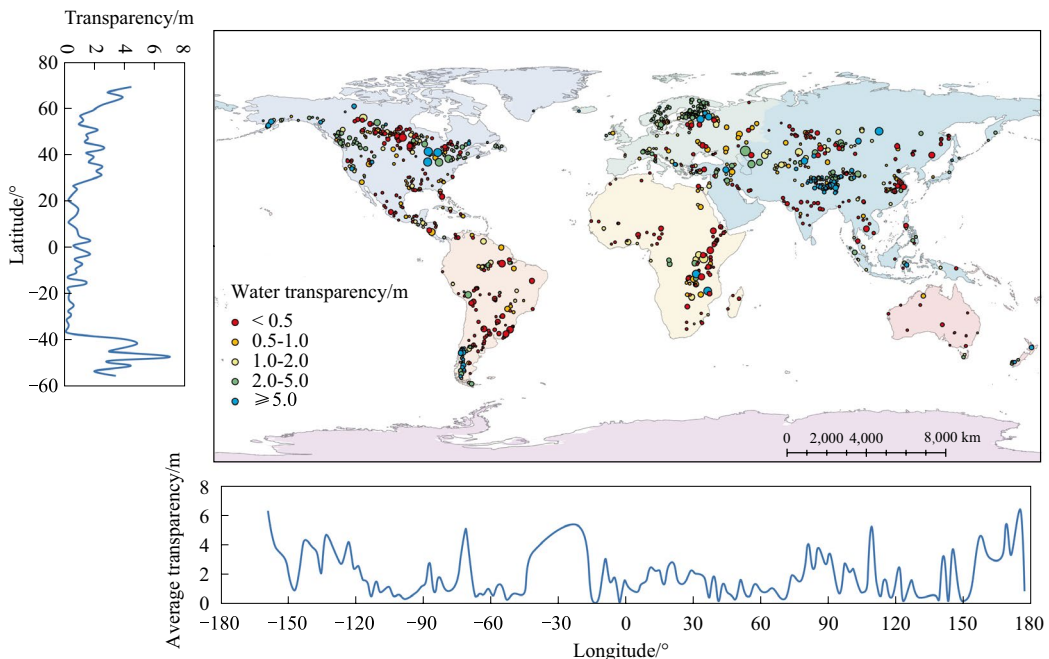


Fig. 3.5 Climatological water transparency map in large lakes around the world from 2000 to 2021

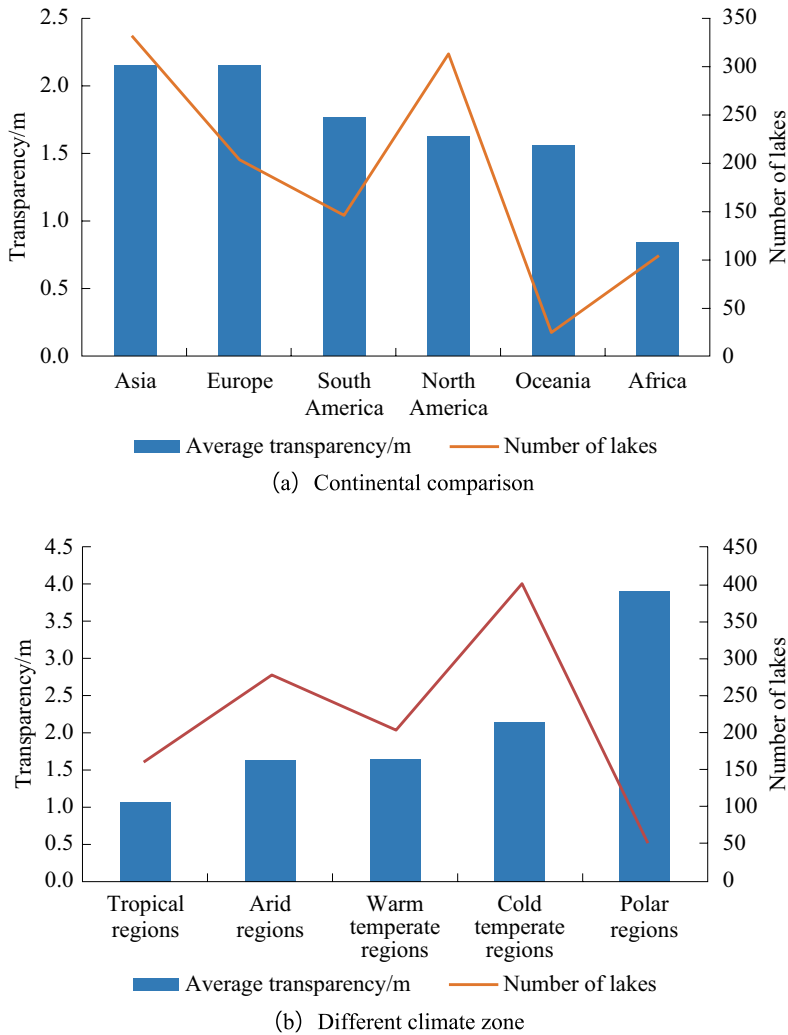


Fig. 3.6 Comparison of the average transparency and number of water bodies of large lakes in different continents and different climate zones from 2000 to 2021

areas within 20° North and South latitudes was relatively low, with an average transparency of less than 1 m. From Fig. 3.6, it can be concluded that in terms of the average water transparency of the continents, the transparency of lakes in Asia and Europe was higher, and the water transparency of lakes in Africa was the lowest. While there were more large lakes in Asia and North America, Oceania had the fewest. In terms of climate zones around the world, the water transparency of lakes in polar and cold temperate regions was higher, and the water transparency of lakes in tropical regions was lower;

while there were more large lakes in the cold temperate and arid regions and fewer large lakes in polar regions.

2. Analysis of the Global Long-Term Time-Series Change in Transparency of Large Lakes from 2000 to 2021

The annual change rate of water transparency in large lakes during 2000–2021 is depicted in Fig. 3.7. The global change rate of water transparency in large lakes showed an obvious regional distribution, with significant differences in regions and climate zones, though overall an

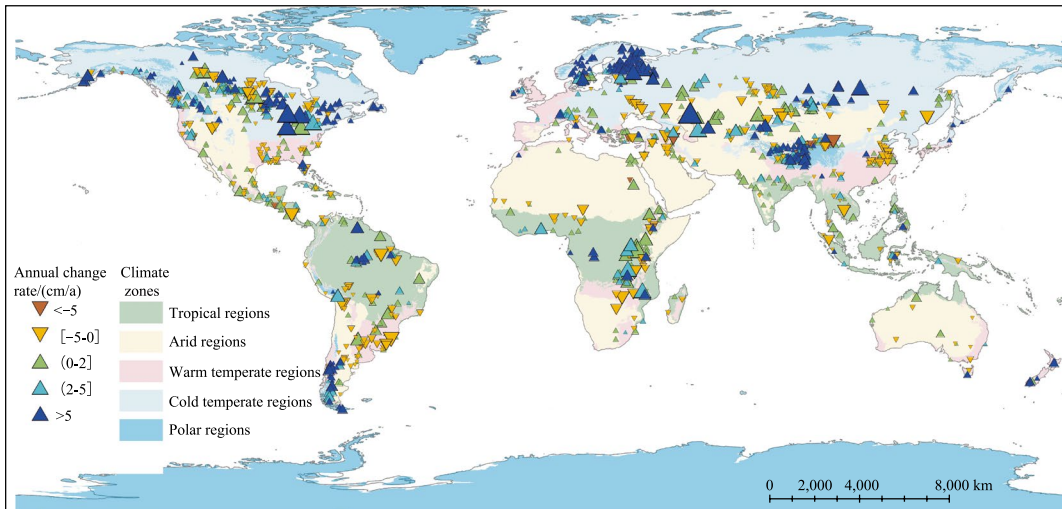


Fig. 3.7 Global annual change rate of water transparency in large lakes during 2000–2021

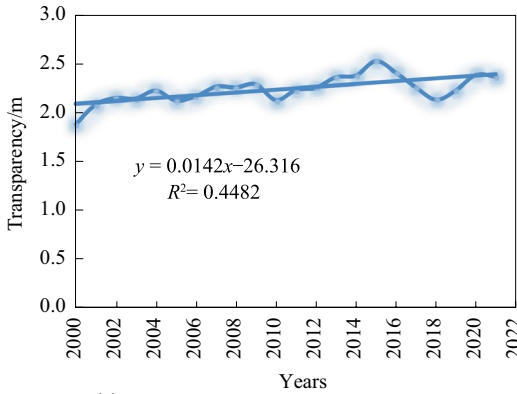
upward trend of water transparency is obvious. The water transparency of 44.2% of large lakes showed a significant upward trend ($p < 0.05$), and only 10.6% of large lakes showed a significant downward trend in water transparency ($p < 0.05$). From the statistics of all continents, the average annual change rates of water transparency in lakes across the six continents were all positive, as shown in Fig. 3.8. Among them, the average water transparency of large lakes in Asia and Africa changed slowly, with average annual change rates of 1.4 cm/a and 1.5 cm/a, respectively. The average water transparency of large lakes in Europe increased significantly, with an average annual change rate of 9.0 cm/a. From the perspective of different climate zones (Figs. 3.9 and 3.10), the water transparency of lakes in the cold temperate region increased most obviously, with an average annual change rate of 6.8 cm/a, and the water transparency of polar lakes increased significantly, with an average annual change rate of 3.5 cm/a. The increase in water transparency in tropical and arid regions was weak, and the water transparency of turbid lakes ($Z_{SD} < 0.5$ m) in the warm temperate region showed a downward trend.

3.3.2.5 Highlights

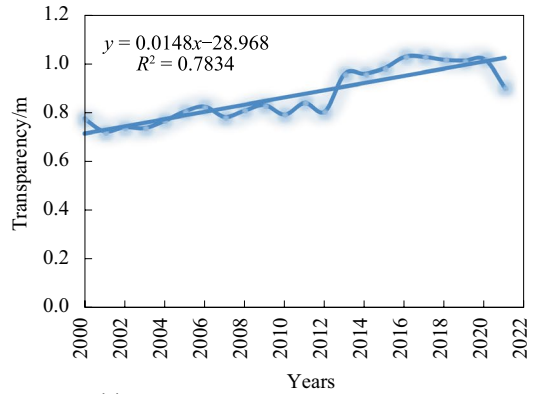
- This case study proposed and validated a water transparency estimation model based on satellite remote sensing data, and produced a global spatial distribution product of water transparency in large lakes from 2000 to 2021.
- Global temporal and spatial change information for water transparency in large lakes were provided to report SDG 6.3.2. It was found that the transparency of water bodies of large lakes around the world showed an overall upward trend from 2000 to 2021. Among them, the water transparency of lakes in cold regions increased significantly, and the water transparency of turbid lakes located in warm temperate regions showed a downward trend.

3.3.2.6 Discussion and Outlook

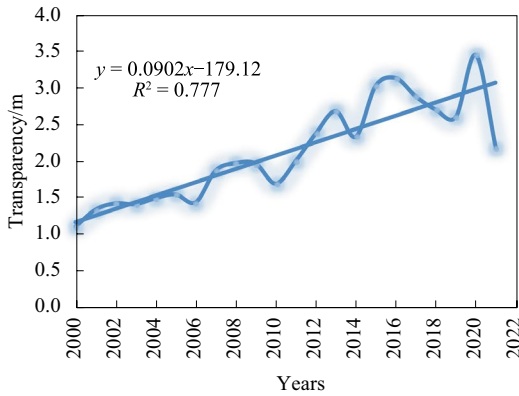
This case study proposed and validated a water transparency estimation model based on satellite remote sensing data, and produced a remote sensing product for water transparency globally for large lakes from 2000 to 2021. Then



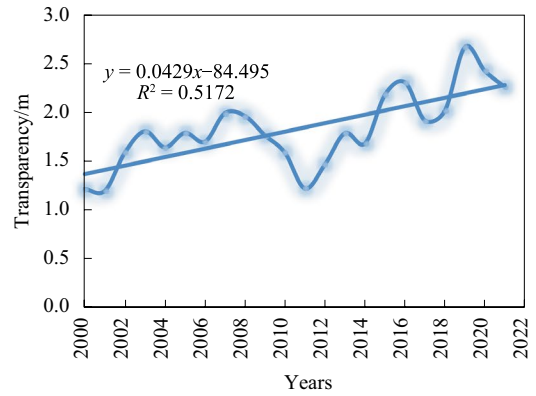
(a) Asian large lakes continental average rate of change 1.4 cm/a



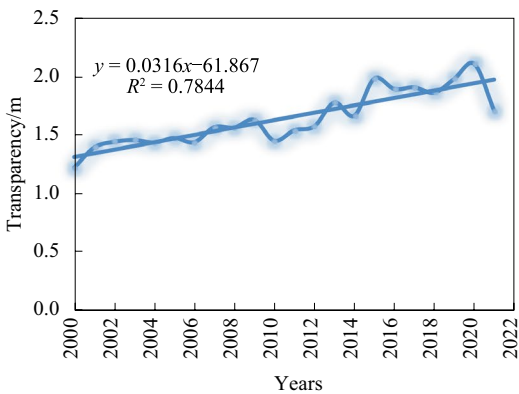
(b) African large lakes continental average rate of change 1.5 cm/a



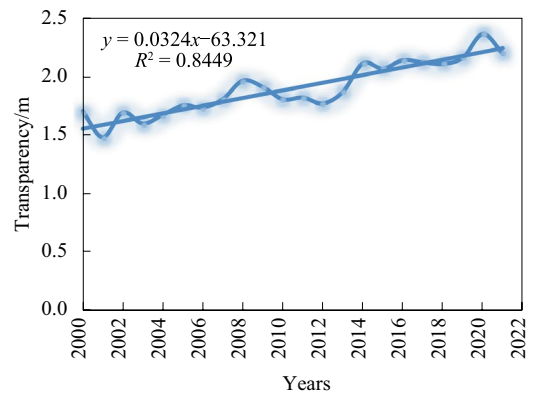
(c) European large lakes continental average rate of change 9.0 cm/a



(d) Oceania large lakes continental average rate of change 4.3 cm/a



(e) North America large lakes continental average rate of change 3.2 cm/a



(f) South America large lakes continental average rate of change 3.2 cm/a

Fig. 3.8 Average water transparency changes of the six continents during 2000–2021

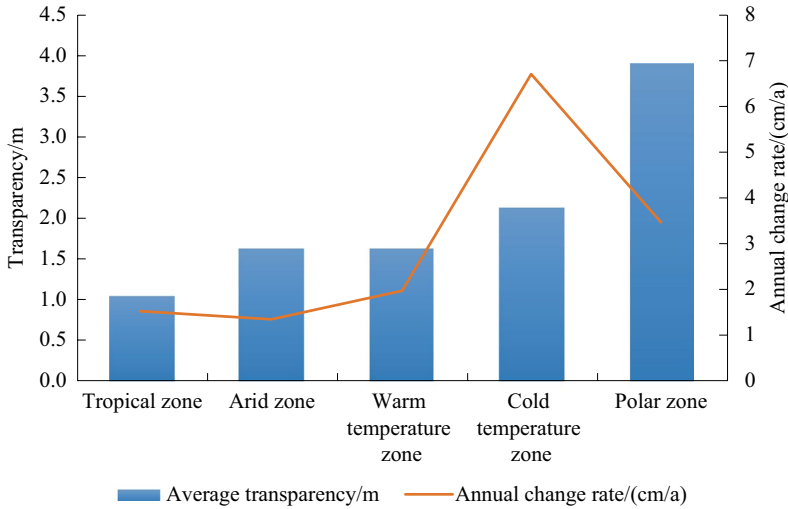


Fig. 3.9 Comparison of average water transparency and the annual change rate of large lakes in climatic zones

water transparency was used to indicate the water quality of surface water bodies for the global evaluation of SDG 6.3.2. The analysis was conducted using continents and global climate zones as geographical units, and pointed out the differences in lake transparency and the changes among continents and climate zones. It was found that the water transparency of large lakes around the world showed an overall upward trend from 2000 to 2021. Among them, the water transparency of lakes in cold regions increased significantly, and the water transparency of turbid lakes located in warm temperate regions showed a downward trend. This case provides important spatial and temporal water quality change data and pattern analysis support to evaluate SDG 6.3.2 and further the achievement of SDG 6.

It should be noted that the surface water quality parameters monitored by remote sensing methods are still mainly optical parameters, such as water transparency monitoring in this case. In future work, first we will further explore the inner relationship between optical water quality parameters, and the “water quality” and “water ecology” in SDG 6 indicators, so that the remote sensing monitoring of lake water quality and SDG 6 indicators can be more closely integrated. Second, multiple remote sensing data

sources will be utilized to improve the reliability of remote sensing monitoring of spatial and temporal changes in water quality, and increase the monitoring of small lakes and rivers to better serve the evaluation of SDG 6.

3.3.3 Dynamic Changes in Water Events in Transboundary Rivers in Central Asia

Target: SDG 6.5: By 2030, implement integrated water resources management at all levels, including through transboundary cooperation as appropriate.

Indicator: SDG 6.5.2: Proportion of transboundary basin area with an operational arrangement for water cooperation.

3.3.3.1 Background

Global climate change has increased the vulnerability and complexity of water resource management. As freshwater becomes increasingly scarce, the issue of water distribution and security in transboundary rivers has become a flashpoint for disputes between different countries and regions. The issue is especially contentious in arid regions where water resources are scarce, and the competitive utilization and fragmented

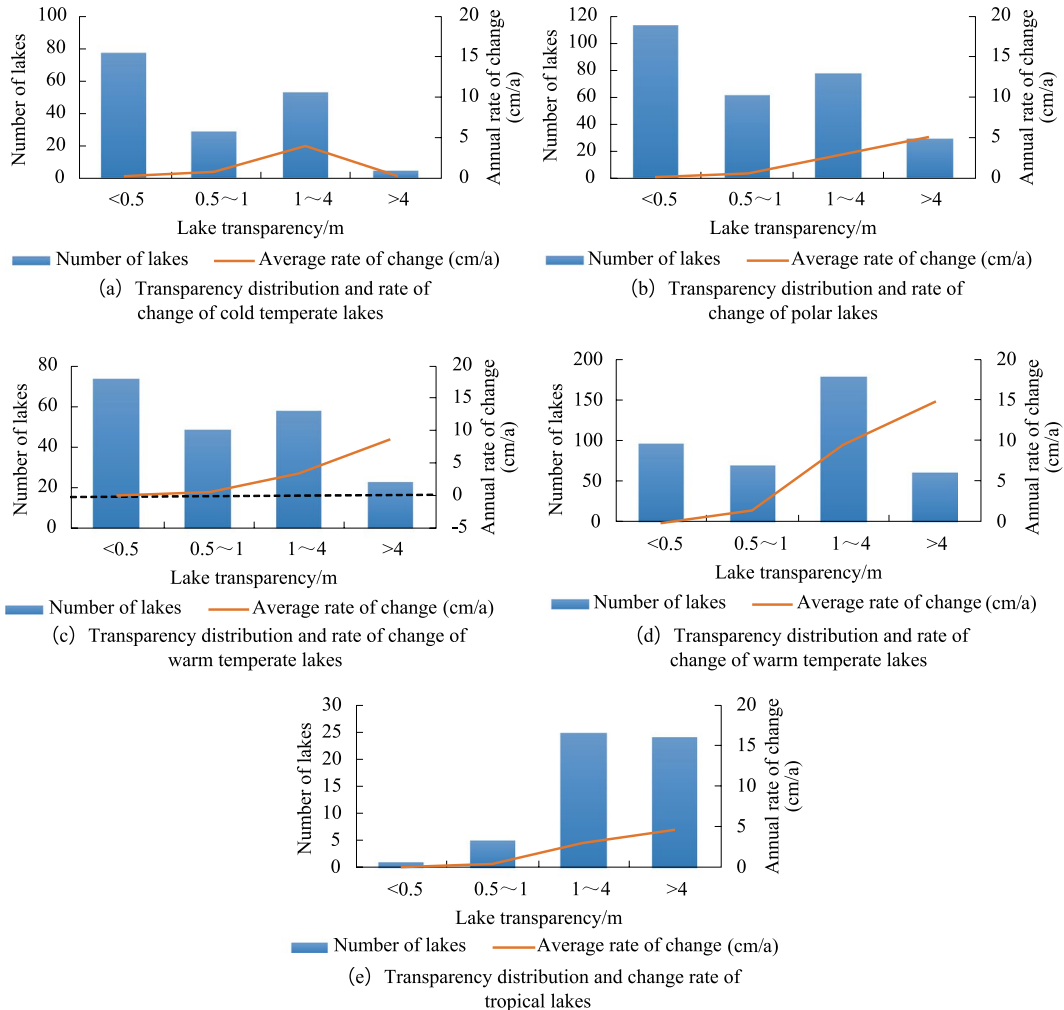


Fig. 3.10 Distribution of water transparency and the annual change rate of large lakes in different climatic zones

management of transboundary water resources have increased the difficulty of managing transboundary water security risks (McCracken and Wolf 2019; Yan et al. 2019; Bernauer and Böhmelt 2020). Central Asia is located in an arid region of Eurasia, with numerous transboundary rivers and an extremely uneven distribution of water resources among countries (Wang et al. 2021). The upstream countries are the main water-producing countries with abundant water resources and scarce land resources. The downstream countries are the main water consumption countries due to abundant land resources and severe water shortage (Nobakht

et al. 2021). There are frequent water disputes and conflicts, making them a key factor affecting the security and stability of the Central Asian region (Chen et al. 2018). Water conflictive and cooperative events are key variables that characterize the regional water security situation (Gleick 2003; Eidem et al. 2012; Madani et al. 2014; Lu et al. 2021). Studying the evolution trend of water conflictive and cooperative events in Central Asia can provide important data support and a theoretical basis for transboundary water cooperation (Gunasekara et al. 2014).

Researchers at Oregon State University established the Transboundary Freshwater Dispute

Database (TFDD) to characterize regional water security. The database records conflictive and cooperative events on water in transboundary rivers around the world, which can effectively reflect the complexity and spatial variability of water-related events and their scales (Schlüeter et al. 2013; Wei et al. 2021). However, the transboundary water events recorded in the database all occurred prior to 2008, and the latest features of water conflictive and cooperative events need to be combined with other supplementary data (Rai et al. 2014). This case study combines the TFDD with the Pacific Institute's Water Conflict Chronology and the Interstate Commission for Water Coordination of Central Asia to coalesce into a new dataset of transboundary river water conflictive and cooperative events in Central Asia from 1951 to 2021. The new dataset includes information on transboundary water events across the five nations on a year-by-year basis and at a basin scale. Further, this case comprehensively analyzes the dynamic changes of water conflictive and cooperative events in the region's transboundary rivers and establishes a water conflict and cooperation network. This case study can provide a scientific reference and technical support for strengthening transboundary water cooperation in Central Asia, and has important theoretical and practical significance for the realization of SDG 6.5 in Central Asia, negotiating water distribution of transboundary rivers, and formulating scientific transboundary river management policies in Central Asian countries.

3.3.3.2 Data

- Self-produced data on water conflictive and cooperative events in transboundary rivers in Central Asia (1951–2021). Time scale of data: year (a total of 71 phases). Spatial scale: basin. Included elements: occurrence time of water events, involved countries, involved basins, intensity levels, types, and detailed description of the events.

3.3.3.3 Methods

Social network analysis (SNA) is an effective method for describing the morphology,

characteristics and structure of a network (Tsekeris and Geroliminis 2013; Yuan et al. 2018). It employs graph theory and algebraic models to express various relational patterns and analyze the impacts of these patterns on the members of a network and the entire network. The SNA method has been widely applied in sociology, geography, information science, and other areas. We use SNA, in combination with the common metrics of network density and degree centrality, to identify the characteristics of water-related conflictive and cooperative networks in Central Asia. The network comprises all the countries involved in water political events in the region's transboundary rivers.

The network density quantifies the degree of connection between each node, with values ranging between 0 and 1. A higher number of contacts indicates a higher network density value. The network density is calculated as follows:

$$D = \frac{\sum_{i=1}^k \sum_{j=1}^k d(n_i, n_j)}{k(k-1)},$$

where D is the network density, k is the number of nodes (here, the number of countries), and $d(n_i, n_j)$ represents the relational quantity between nodes n_i and n_j .

The degree centrality of a node measures how central this node is to the network. The higher the degree centrality of a node, the stronger its direct interconnection with other nodes, and its position within the network will be more significant (central). The degree centrality is calculated as follows:

$$C_D(n_i) = \sum_{j=1}^n X_{ji},$$

where $C_D(n_i)$ denotes the degree centrality of the node n_i , n represents the number of nodes, and X_{ji} represents the connection between the nodes n_i and n_j . If a connection exists between the two nodes, $X_{ji} = 1$; otherwise, $X_{ji} = 0$.

3.3.3.4 Results and Analysis

1. Changing Trends in Water Conflictive and Cooperative events

From 1951 to 2021, 604 transboundary water political events occurred in the transboundary river basins of Central Asia, including 60 conflictive events, 534 cooperative events, and 10 neutral events (Fig. 3.11). The number of cooperative events accounted for 88.41% of all water-related political events, which far exceeded the number of conflictive events, indicating that cooperation occurred more frequently than conflict. The number of water events shows three main stages. From 1951 to 1991 (P1: the Soviet Union), the events decreased slightly, and their fluctuation range was stable. During this period, water resources were uniformly managed and allocated by the Central Government of Moscow, and the principle of division of labor was established to achieve maximum economic output. Then, in the first decade after the collapse of the Soviet Union (P2: 1992–2001), events caused by water politics increased rapidly and then

declined. Specifically, from 1992 to 1997, events increased dramatically, reaching their highest number (77) in 1997. This was mainly because the disintegration of the Soviet Union made most of the rivers in Central Asia become transboundary rivers, and the old water resource allocation system was no longer applicable. Therefore, countries were eager to explore water resource management and allocation policies suitable for the new situation. Because of this exploration, cooperation between the countries was occasionally marred by short-term conflicts (Wang et al. 2021). From 2002 to 2021 (P3), the changes in transboundary water events gradually stabilized, with only five transboundary water events occurring annually.

There were prominent differences in water events across the various transboundary river basins of Central Asia (Fig. 3.12). As a hydro-politically active region, the Aral Sea Basin had the largest number of events (268), accounting for 44.37% of all water-related political events in Central Asia during the 1951–2021 period. The Aral Sea Basin was also the site of the most water conflictive events (25 events).

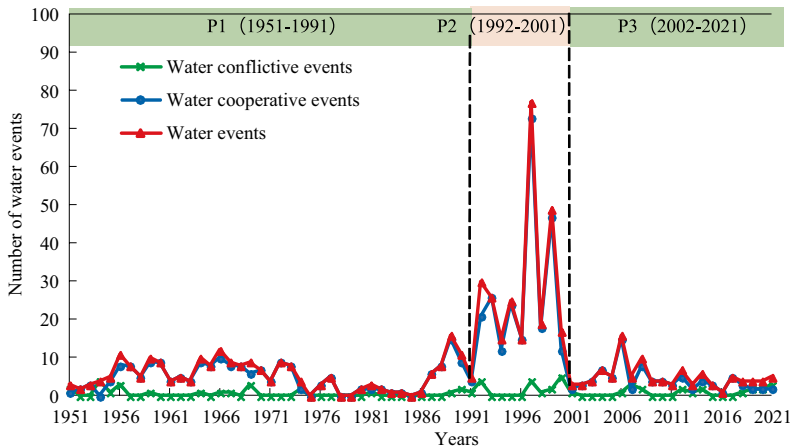


Fig. 3.11 Changing trends in water conflictive events, water cooperative events, and water events in Central Asia from 1951 to 2021. Note P1—stable period; P2—rapid increasing and decreasing period; P3—stable period

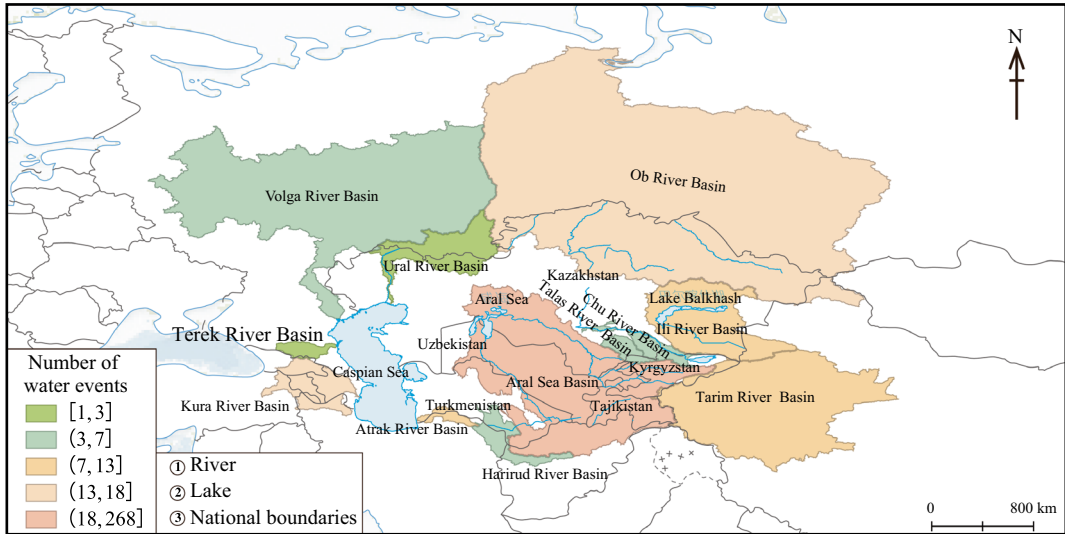


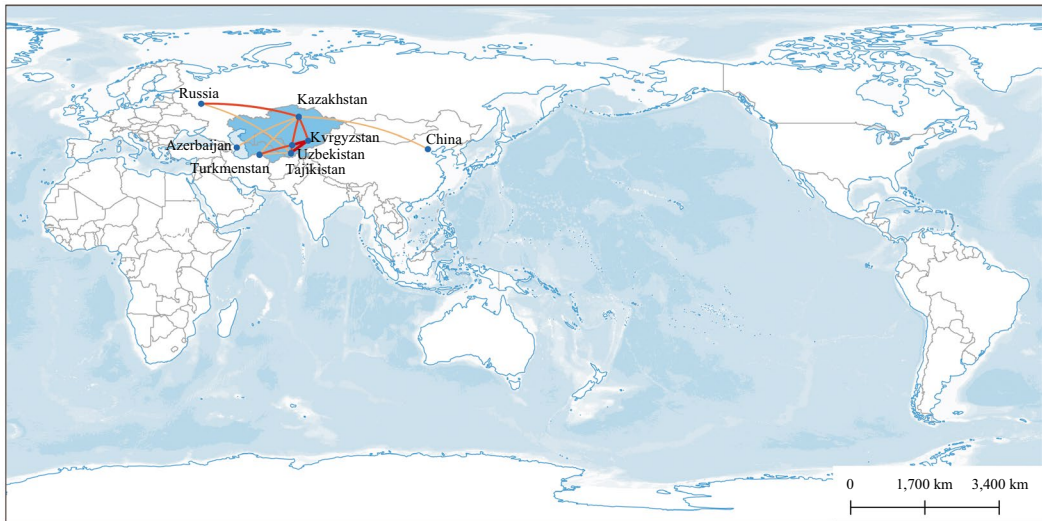
Fig. 3.12 Spatial distribution of water political events in transboundary river basins in and around Central Asia from 1951 to 2021

Water conflictive events in the Aral Sea Basin are mainly due to the allocation and management of water resources in the Amu Darya and Syr Darya rivers by upstream and downstream countries, as well as the complex dams, reservoirs, and irrigation canals (Wang et al. 2021). The upstream countries have great potential for hydropower. In order to ensure the use of electricity in winter, large quantities of water are stored in reservoirs in summer and released downstream in winter. This can lead to insufficient irrigation water downstream to meet the water consumption needs of crops during the growing season (when crops need the most water), resulting in lower crop yields and less arable land, while flooding in winter due to large amounts of upstream water (Han et al. 2022). There were 18 water political events in the Ob River Basin, which is shared by Kazakhstan, Russia, and China. The main themes underlying these events were water quantity and hydropower. In the Ili River Basin, which flows from the Khan Tengri Peak in the Tianshan Mountains through China and Kazakhstan and into Lake Balkhash, 13 water political events occurred, of which 12 were cooperative, mainly focused on water allocation and shipping. In addition, a total of 11 water events occurred in the Atrak

River Basin between southern Turkmenistan and northeastern Iran. A total of seven transboundary water events occurred in the transboundary Harirud River Basin between Afghanistan, Iran and Turkmenistan, and five transboundary water events occurred in the Volga River Basin (Wang et al. 2021). Finally, only three water political events were recorded in the Ural River Basin, which flows through Russia and Kazakhstan to the Caspian Sea.

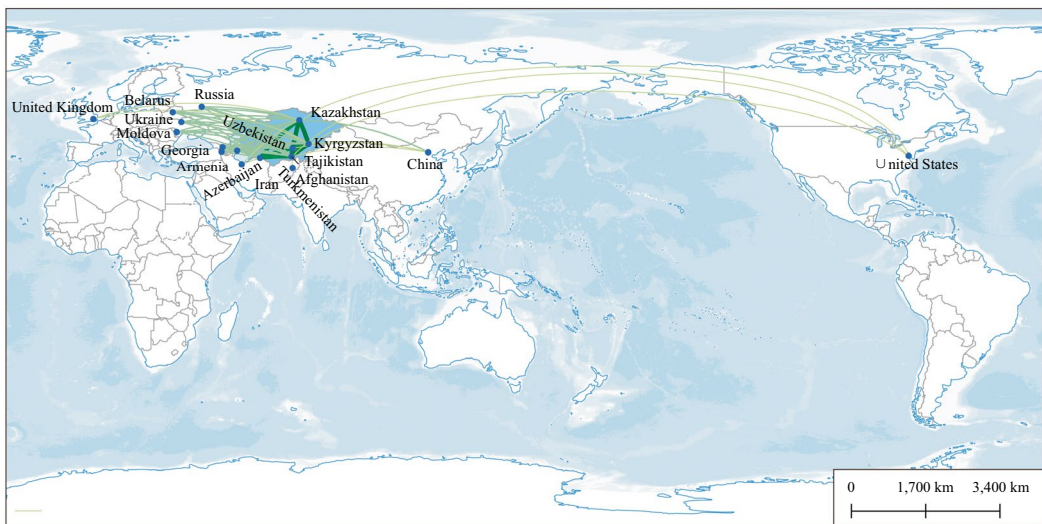
2. Water Conflictive and Cooperative Networks

During the age of the Soviet Union, water conflictive events spilled into neighboring countries, with the Soviet Union at its core, and the network density was 0.20. The disintegration of the Soviet Union had a substantial impact on the hydropolitical structure in Central Asia, where water problems had long been out of control (Wang et al. 2021). From 1992 to 2021, the water conflictive network in Central Asia was mainly distributed in five countries in a crisscross pattern (Fig. 3.13a). From 1992 to 2021, the network density increased to 0.38, indicating an increase in conflict intensity. In terms of degree centrality (Table 3.3), Uzbekistan, with a degree



Water conflictive events — [1, 3] — (3, 6] — (6, 10]

(a) Number of water conflictive events in 1992-2021



Water cooperative events — [1, 10] — (10, 75] — (75, 130] — (130, 187] — (187, 234] — (234, 286]

(b) Number of water cooperative events in 1992-2021

Fig. 3.13 Water conflictive and cooperative networks between Central Asian countries and other countries in the world

centrality of 6, was at the core of the water conflictive network, followed by Kazakhstan and Tajikistan, with a degree centrality of 5 and 4, respectively. The most frequent water conflictive events were between Kyrgyzstan and Uzbekistan (10 conflictive events). These two countries

border each other and share the Syr Darya and Amu Darya Rivers, and their arable land is poorly matched to water resources, thus increasing competition for water resources.

Water cooperative event networks were more complex than water conflictive event networks.

Table 3.3 Degree centrality of water conflictive and cooperative networks for the five Central Asian countries after the disintegration of the Soviet Union (1992–2021)

Water conflictive networks		Water cooperative networks	
Countries	Degree centrality	Countries	Degree centrality
Uzbekistan	6	Kazakhstan	15
Kazakhstan	5	Kyrgyzstan	14
Tajikistan	4	Tajikistan	14
Kyrgyzstan	3	Turkmenistan	12
Turkmenistan	3	Uzbekistan	12

From 1951 to 1991, the scope of water cooperation in Central Asia was extensive, with all networks centered on the Soviet Union and radiating outward, which relates to 12 countries. Of the water cooperative events that occurred, 32 were with Iran, 22 with China, and a few with other countries. From 1992 to 2021, the scope of water cooperation became more concentrated (Fig. 3.13b), while the cooperation intensity greatly increased, and the networks grew denser (up to 0.42). Overall, Kazakhstan showed the highest degree centrality (15), indicating that it played the most prominent role in the cooperation network and had the most frequent water cooperation with other countries. Both Turkmenistan and Uzbekistan cooperated less frequently with other countries (a degree centrality of 12). Cooperation was mainly distributed among the five Central Asian countries, with most of the water cooperative events occurring between Kazakhstan and Kyrgyzstan (286 events).

3. Intensity and Themes of Water Conflictive and Cooperative Events

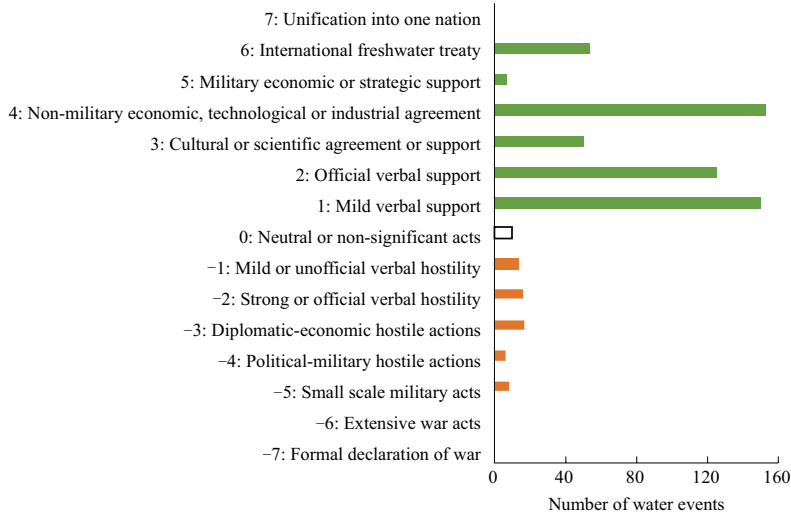
Figure 3.14a depicts the number of water events in Central Asia according to intensity. The green bars indicate cooperative events (graded from level 1 to 7), the orange bars indicate conflictive events (graded from level – 1 to – 7), and the white bar indicates neutral events (level 0). Water cooperative events occurred at all levels except level 7. Most of the water cooperative

events (152 events, accounting for 28.46% of all cooperative events) occurred at level 4 (non-military economic, technological or industrial agreement). Level 5 had the lowest number of events (6 events). In general, a low level of water cooperation was predominant in Central Asia, with less frequent cooperation at higher levels. Water conflictive events occurred at all levels except levels – 7 and – 6. Most conflictive events (17 events) were level – 3 (diplomatic-economic hostile actions).

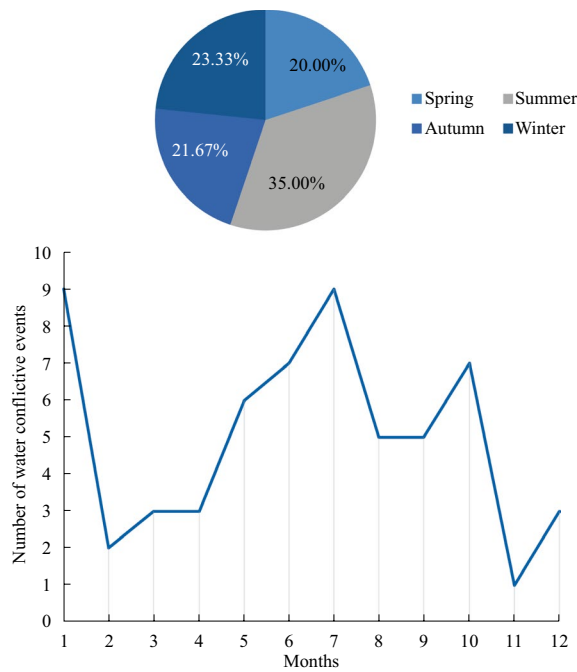
In water conflictive events, water quantity was the most common theme, accounting for 45.61% of all water conflictive events (Fig. 3.15a). The second most dominant theme of water conflictive events was infrastructure/development (24.56% of all water conflictive events), which included infrastructure construction and the development of projects. The water conflictive events also differed according to the time of year, with a clear seasonal distribution pattern emerging (Fig. 3.14b). The frequency of water conflictive events was the highest in January and July (9 cases each month), with the overall event frequency being highest in summer (35.00%) and winter (23.33%). These two seasons have the highest water demand for irrigation and power generation, leaving the upstream and downstream countries more prone to water conflict (Wang et al. 2021). Joint management was the largest theme in water cooperation (Fig. 3.15b), accounting for 30.74% of all cooperative events. This is because Central Asian countries have developed a number of joint transboundary river management measures as an effective means for resolving their water conflictive events.

3.3.3.5 Highlights

- A dataset was produced showing water conflictive and cooperative events in transboundary rivers in Central Asia from 1951 to 2021.
- Overall, 604 water-related political events occurred in Central Asia, including 60 water conflictive events, 534 water cooperative events and 10 neutral events. With the collapse of the Soviet Union, the number of



(a) Intensity of water events in Central Asia



(b) Monthly distribution of water conflictive events in Central Asia

Fig. 3.14 Graph showing the number of water events in Central Asia according to intensity and the monthly distribution of water conflictive events

transboundary water events has increased rapidly since 1991, peaking in 1997 and returning to a relatively stable state between 2002 and 2021.

- In terms of the themes and levels of transboundary water events, joint management was the largest theme in water cooperation, accounting for 30.74% of all

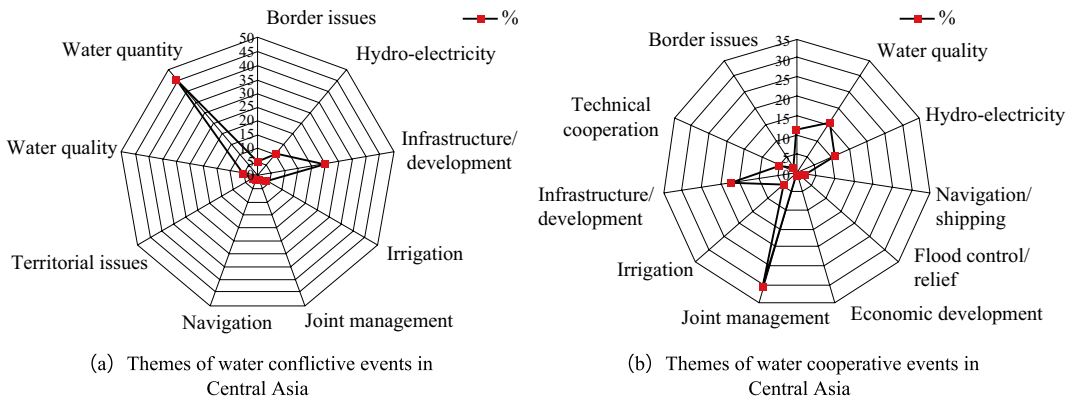


Fig. 3.15 Percentage of water conflictive and cooperative events in Central Asia according to themes

cooperative events. Water conflictive effects mainly occurred in summer and winter, and water quantity was the most important theme, accounting for 45.61% of all water conflict topics. The second was the infrastructure/development.

3.3.3.6 Discussion and Outlook

This case combined the TFDD with the Pacific Institute's Water Conflict Chronology and the Interstate Commission for Water Coordination of Central Asia database to form a new dataset of water conflict/cooperation events in Central Asian transboundary rivers from 1951 to 2021. We analyzed the dynamic changes in transboundary water events in the transboundary rivers of the studied region. This case found that from 1951 to 2021, 604 water-related political events occurred in Central Asia's transboundary river basins, among which water conflictive and cooperative events accounted for 88.41% and 9.93%, respectively. The number of transboundary water events showed three distinct stages, namely, a stable period (1951–1991), a rapidly increasing and decreasing period (1992–2001), and another stable period (2002–2021). Water conflictive events took place mainly in summer and winter, with the Aral Sea Basin experiencing the most water conflictive events (due to the competitive use of water resources from the Syr Darya and Amu Darya rivers), while the Ili River Basin was dominated by cooperation (accounting for 92.00% of transboundary water

events in the Basin). Although water cooperation has an absolute advantage, it is mainly based on low-level cooperation, so the effect of cooperation is not ideal. In addition, affected by climate change, population growth, water and soil resource degradation and other factors, the spatiotemporal matching of water and soil resources in Central Asia is more uneven, which will further intensify water resource competition among Central Asian countries (Li et al. 2020; Wang et al. 2021). Recommendations: (1) countries in Central Asia should focus on the core issues of bilateral or regional water resource management, such as the impacts of climate change on Central Asian rivers, inter-governmental information sharing on water resource management, and how to enhance the effectiveness of regional water resource cooperation platforms; (2) in the growing season of crops, the upstream countries should appropriately increase the water resource allocation for the downstream countries, and the downstream countries provide energy and industrial and agricultural products for the upstream countries, which means the upstream and downstream countries maintain a balance of interests through water and energy trading; (3) countries in Central Asia should build more channels for democratic consultation by the interventional governance of international multilateral development institutions; (4) from the perspective of strategic and institutional building, countries along the basins should effectively cooperate on production capacity, transboundary economy,

water resources, agriculture and poverty reduction, and strike a balance between the transfer of benefits and ecological compensation.

The dataset of the water events in the Transboundary rivers in Central Asia constructed by this case and the research results obtained can provide important data support for reaching SDG 6.5. At the same time, the methods used in this dataset can be extended to other transboundary river basins around the world. In future, the statistical data of Central Asia will be further combined with Big Earth Data, the research scale of water security and water events will be continuously refined, effective countermeasures and suggestions for regional sustainable development will be put forward, and more detailed data support and decision-making support will be provided for water allocation negotiations for transboundary rivers in Central Asia. (Modified from Wang et al. 2021).

3.4 Summary

This chapter indirectly evaluates global changes related to SDG 6.3.2 from 2000 to 2021, based on remote sensing monitoring results of algal blooms in lakes and water transparency in lakes. Furthermore, using transboundary rivers in Central Asia as an example, progress of SDG 6.5.2 in the region was analyzed and studied with the SNA model, based on data on regional water conflictive and cooperative events. The following understanding was formed.

- (1) Based on the algal bloom outbreak area, frequency of lakes, and water transparency data of lakes obtained by satellite remote sensing, it is possible to analyze the water quality changes of lakes in different regions of the world. Compared with an analysis based on site observation data, satellite remote sensing monitoring results are more timely and spatially accurate, making it easier to guide precise policy implementations.
- (2) The results of the case study on dynamic changes in water events in transboundary rivers in Central Asia show that the water

databases collected by different institutions around the world are effective for conducting research on transboundary water cooperation.

References

- Bernaer T, Böhmelt T (2020) International conflict and cooperation over freshwater resources. *Nature Sustain* 3(5):350–356
- Chen YN, Li Z, Fang GH et al (2018) Large hydrological processes changes in the transboundary rivers of central Asia. *J Geophys Res Atmos* 123(10):5059–5069
- Chen Z, Yu B, Yang C et al (2021) An extended time series (2000–2018) of global NPP-VIIRS-like nighttime light data from a cross-sensor calibration. *Earth Syst Sci Data* 13(3):889–906
- Dobson JE, Bright EA, Coleman PR et al (2000) LandScan: a global population database for estimating populations at risk. *Photogramm Eng Remote Sens* 66(7):849–857
- Duan HT, Cao ZG, Shen M et al (2022) Review of lake remote sensing research. *National Remote Sens Bull* 26(1):3–18. <https://doi.org/10.11834/jrs.20221301>. (in Chinese)
- Eidem NT, Fesler KJ, Wolf AT (2012) International cooperation and conflict over freshwater: examples from the western United States. *J Contemp Water Res Educ* 147(1):63–71
- Friedl M, Sulla-Menashe D (2019) MCD12Q1 MODIS/Terra+Aqua land cover type yearly L3 global 500 m SIN grid V006 (Dataset). NASA EOSDIS Land Processes DAAC. <https://doi.org/10.5067/MODIS/MCD12Q1.006>. 30 May 2022
- Gleick PH (2003) Global freshwater resources: Soft-path solutions for the 21st century. *Science* 302(5650):1524–1528
- Gunasekara NK, Kazama S, Yamazaki D et al (2014) Water conflict risk due to water resource availability and unequal distribution. *Water Resour Manage* 28(1):169–184
- Håkanson L, Jansson M (1983) *Principles of Lake Sedimentology*. Springer, Berlin
- Han SM, Xin P, Li HL et al (2022) Evolution of agricultural development and land-water-food nexus in Central Asia. *Agric Water Manag* 273:107874
- Harlin J, Alabaster G, Slaymaker T et al (2021) In need of speed: data can accelerate progress towards water and sanitation for all. <http://sdg.iisd.org/commentary/guest-articles/in-need-of-speed-data-can-accelerate-progress-towards-water-and-sanitation-for-all/>. 09 June 2023
- Hou XJ, Feng L, Dai YH et al (2022) Global mapping reveals increase in lacustrine algal blooms over the past decade. *Nat Geosci* 15(2):130–134

- Hu CM (2009) A novel ocean color index to detect floating algae in the global oceans. *Remote Sens Environ* 113(10):2118–2129
- Hu C, Lee Z, Ma R, Yu K, Li D, Shang S (2010) Moderate resolution imaging spectroradiometer (MODIS) observations of cyanobacteria blooms in Taihu Lake, China. *J Geophys Res Oceans* 115(C4)
- Kavvada A, Metternicht G, Kerblat F et al (2020) Towards delivering on the sustainable development goals using earth observations. *Remote Sens Environ* 247:111930
- Leach TH, Beisner BE, Carey CC et al (2018) Patterns and drivers of deep chlorophyll maxima structure in 100 lakes: the relative importance of light and thermal stratification. *Limnol Oceanogr* 63(2):628–646
- Lee ZP, Shang SL, Hu CM et al (2015) Secchi disk depth: a new theory and mechanistic model for underwater visibility. *Remote Sens Environ* 169:139–149
- Lehner B, Grill G (2014) HydroBASINS: global watershed boundaries and sub-basin delineations derived from HydroSHEDS data at 15 second resolution—technical documentation version 1
- Li Z, Fang G H, Chen Y N et al (2020) Agricultural water demands in Central Asia under 1.5 °C and 2.0 °C global warming. *Agric Water Manage* 231:106020
- Liang QC, Zhang YC, Ma RH et al (2017) A MODIS-based novel method to distinguish surface cyanobacterial scums and aquatic macrophytes in Lake Taihu. *Remote Sensing* 9(2):133
- Lu Y, Tian FQ, Guo LY et al (2021) Socio-hydrologic modeling of the dynamics of cooperation in the transboundary Lancang-Mekong River. *Hydrol Earth Syst Sci* 25(4):1883–1903
- Ma JG, Loiselle S, Cao ZG et al (2023) Unbalanced impacts of nature and nurture factors on the phenology, area and intensity of algal blooms in global large lakes: MODIS observations. *Sci Total Environ* 880:163376
- Ma J, Duan H, He L et al (2020) Spatiotemporal pattern of gypsum blooms in the Salton Sea, California, during 2000–2018. *Int J Appl Earth Obs Geoinf* 89:102090
- Madani K, Zarezadeh M, Morid S (2014) A new framework for resolving conflicts over transboundary rivers using bankruptcy methods. *Hydrol Earth Syst Sci* 18(8):3055–3068
- McCracken M, Wolf AT (2019) Updating the register of international river basins of the world. *Int J Water Resour Dev* 35(5):732–782
- Messenger ML, Lehner B, Grill G et al (2016) Estimating the volume and age of water stored in global lakes using a geo-statistical approach. *Nat Commun* 7:13603
- Mu HW, Li XC, Wen YN et al (2022) A global record of annual terrestrial human footprint dataset from 2000 to 2018. *Scientific Data* 9:176
- Muñoz-Sabater J (2019) ERA5-Land hourly data from 1950 to present. Copernicus Climate Change Service (C3S) Climate Data Store (CDS). <https://doi.org/10.24381/cds.e2161bac>. 30 May 2022
- Nobakht M, Shahgedanova M, White K (2021) New inventory of dust emission sources in Central Asia and Northwestern China derived from MODIS imagery using dust enhancement technique. *J Geophys Res Atmos* 126(4):e2020JD033382
- Paerl HW, Gardner WS, Havens KE et al (2016) Mitigating cyanobacterial harmful algal blooms in aquatic ecosystems impacted by climate change and anthropogenic nutrients. *Harmful Algae* 54:213–222
- Paerl HW, Huisman J (2008) Blooms like it hot. *Science* 320(5872):57–58
- Rai SP, Sharma N, Lohani AK (2014) Risk assessment for Transboundary Rivers using fuzzy synthetic evaluation technique. *J Hydrol* 519:1551–1559
- Rubel F, Kottek M (2010) Observed and projected climate shifts 1901–2100 depicted by world maps of the Köppen-Geiger climate classification. *Meteorol Z* 19(2):135–141
- Schlüter M, Khasankhanova G, Talskikh V et al (2013) Enhancing resilience to water flow uncertainty by integrating environmental flows into water management in the Amudarya River, Central Asia. *Global Planet Change* 110:114–129
- Spyrakos E, Hunter P, Simis S et al (2020) Moving towards global satellite based products for monitoring of inland and coastal waters. Regional examples from Europe and South America. In: 2020 IEEE Latin American GRSS & ISPRS remote sensing conference (LAGIRS). IEEE, pp 363–368
- Tsekeris T, Geroliminis N (2013) City size, network structure and traffic congestion. *J Urban Econ* 76:1–14
- Tyler AN, Hunter PD, Spyrakos E et al (2016) Developments in earth observation for the assessment and monitoring of inland, transitional, coastal and shelf-sea waters. *Sci Total Environ* 572:1307–1321
- UN, UNESCO (2021) Progress on transboundary water cooperation: global status of SDG indicator 6.5.2 and acceleration needs
- UN-Water (2018) Progress on ambient water quality—piloting the monitoring methodology and initial findings for SDG indicator 6.3.2. <https://www.unwater.org/publications/progress-ambient-water-quality-piloting-monitoring-methodology-and-initial-findings>. 18 Nov 2021
- UN-Water (2021) Summary progress update 2021: SDG 6—water and sanitation for all. Version: 1 March 2021. Geneva, Switzerland
- Wang SL, Li JS, Zhang B et al (2016) A simple correction method for the MODIS surface reflectance product over typical inland waters in China. *Int J Remote Sens* 37(24):6076–6096
- Wang SL, Li JS, Zhang B et al (2020) Changes of water clarity in large lakes and reservoirs across China

- observed from long-term MODIS. *Remote Sens Environ* 247:111949
- Wang XX, Chen YN, Li Z et al (2021) Water resources management and dynamic changes in water politics in the transboundary river basins of Central Asia. *Hydrol Earth Syst Sci* 25(6):3281–3299
- Wei J, Wei YP, Tian FQ et al (2021) News media coverage of conflict and cooperation dynamics of water events in the Lancang-Mekong River Basin. *Hydrol Earth Syst Sci* 25(3):1603–1615
- WHO, UN-Habitat (2018) Progress on wastewater treatment: piloting the monitoring methodology and initial findings for SDG indicator 6.3.1. UN-Habitat, Geneva: WHO
- Yan JB, Jia S, Lv A et al (2019) Water resources assessment of China's transboundary river basins using a machine learning approach. *Water Resour Res* 55:632–655
- Yuan JF, Chen KW, Li W et al (2018) Social network analysis for social risks of construction projects in high-density urban areas in China. *J Clean Prod* 198:940–961
- Zhang B, Li J S, Shen Q et al (2021) Recent research progress on long time series and large scale optical remote sensing of inland water. *National Remote Sens Bull* 25(1):37-52. <https://doi.org/10.11834/jrs.20210570>. (in Chinese)

Open Access This chapter is licensed under the terms of the Creative Commons Attribution-NonCommercial-NoDerivatives 4.0 International License (<http://creativecommons.org/licenses/by-nc-nd/4.0/>), which permits any noncommercial use, sharing, distribution and reproduction in any medium or format, as long as you give appropriate credit to the original author(s) and the source, provide a link to the Creative Commons license and indicate if you modified the licensed material. You do not have permission under this license to share adapted material derived from this chapter or parts of it.

The images or other third party material in this chapter are included in the chapter's Creative Commons license, unless indicated otherwise in a credit line to the material. If material is not included in the chapter's Creative Commons license and your intended use is not permitted by statutory regulation or exceeds the permitted use, you will need to obtain permission directly from the copyright holder.



SDG 7, Affordable and Clean Energy

4

4.1 Background

Anthropogenic carbon emissions from the use of fossil fuels are a major cause of global warming. The transformation from fossil fuels to green, low-carbon energy has become a globally shared vision in response to climate change. SDG 7, Affordable and Clean Energy, one of the 17 goals on the 2030 Agenda adopted by the UN, aims to drive global energy transformation. Under it are six targets in four areas—energy access, renewable energy, energy efficiency, and international energy cooperation—to ensure access to affordable, reliable, sustainable, and modern energy for all by 2030.

The Paris Climate Agreement requires countries to update their nationally determined contribution (NDC) emission reduction plans every five years. To date, 58% of the 191 signatories have submitted new NDCs and around two-thirds of the global economy has committed to a net zero emissions target by around mid-century. The European Union, the United States, Canada, Japan, and other countries plan to achieve net zero by 2050.

Renewable energy sources such as solar and wind power, are key to achieving the global energy transition. From 2012 to 2022, solar and wind energy technologies developed rapidly, and

the cost of electricity from solar and wind energy has reached or is close to the cost of coal power, achieving a historic leap forward. In some countries, such as China, solar power has been brought online at parity. However, the world's solar and wind power plants are mainly concentrated in countries and regions such as China, the European Union, and the United States. Developing countries in general, and the BAR countries in particular, are not only facing energy shortages, but also facing technical and financial pressures in the energy transition. Developing countries will present the most difficult challenge to achieving a global energy transition and SDG 7.

This chapter aims to improve the global SDG 7 monitoring and evaluation methodology by using remote sensing, GIS, and other geodata technologies to assess the progress of global SDG 7 indicators. It provides scientific data to support the worldwide achievement of SDG 7 targets, especially in developing BAR countries.

4.2 Main Contributions

This chapter evaluates the progress of SDG 7.1, SDG 7.2, SDG 7.a, and SDG 7.b in China and globally through three case studies. The main contributions are as follows (Table 4.1).

Table 4.1 Cases and their main contributions

Targets	Cases	Contributions
SDG 7.1 By 2030, ensure universal access to affordable, reliable and modern energy services	Global electrification of built-up areas	Data product: global datasets on the state of electrification of built-up areas (BUAs) in 2014 and 2020 Method and model: remote sensing monitoring of electrification of BUAs worldwide Decision support: inform global electrification policies and investment decisions
SDG 7.1 By 2030, ensure universal access to affordable, reliable and modern energy services SDG 7.2 By 2030, increase substantially the share of renewable energy in the global energy mix SDG 7.a By 2030, enhance international cooperation to facilitate access to clean energy research and technology, including renewable energy, energy efficiency and advanced and cleaner fossil-fuel technology, and promote investment in energy infrastructure and clean energy technology SDG 7.b By 2030, expand infrastructure and upgrade technology for supplying modern and sustainable energy services for all in developing countries, in particular least developed countries, small island developing States, and landlocked developing countries, in accordance with their respective programs of support	China's international energy cooperation projects China's international training on solar energy utilization	Data product: dataset on the impacts of China's CIECPs on SDG 7 in developing countries Method and model: methodology for assessing the impacts of China's CIECPs on SDG 7 in developing countries Decision support: inform decisions on China's international energy cooperation Data product: statistical datasets of China's international training on solar energy utilization Decision support: inform policies on China's international training on solar energy utilization

4.3 Case Studies

4.3.1 Global Electrification of Built-Up Areas

Target: SDG 7.1: By 2030, ensure universal access to affordable, reliable, and modern energy services.

4.3.1.1 Background

Electricity shortage is the primary energy challenge faced by developing countries, with about 733 million people worldwide still lacking access to electricity in 2020. Access to electricity is an indicator of SDG 7 reflecting electricity penetration, and timely, accurate data are of practical importance to its universal achievement. At present, global access to electricity data is mainly obtained using statistical surveys, which suffer from untimely data updates, uneven data quality levels, poor data comparability between different countries, uneven quality levels, non-spatialized data, and missing data in some developing countries. In response to these issues, this study developed a 500 m resolution dataset of electrification conditions in BUAs around the world in 2014 and 2020. A new method is proposed for the remote sensing monitoring of electrification in BUAs. The study analyzed the global spatial distribution and change of electrification to address the problems of missing data and untimely updates of existing electrification rates in some countries. The study improves the global monitoring capacity of electrification conditions in BUAs and provides data to inform the formulation of targeted power supply strategies.

4.3.1.2 Data

- European Union Global Human Settlement Layer (GHSL) datasets. <https://ghsl.jrc.ec.europa.eu/download.php?ds=bu>
- NPP-VIIRS night images of the year. https://eogdata.mines.edu/nighttime_light/annual/v20/.
- World Bank data on access to electricity by country. <https://data.worldbank.org/indicator>.

4.3.1.3 Methods

This study presents a new method for remote sensing monitoring of the electrification status of BUAs. The method is based on the significant difference in night light brightness values between electrified and unelectrified BUAs, using European Union global built-up data (Corbane et al. 2018), randomly selecting image elements from non-BUAs as samples from unelectrified areas, and randomly selecting image elements from BUAs as samples from electrified areas from countries with 100% electrification, to construct a sample library, all of which are verified by all samples visually verified by high-resolution remote sensing images. Two-thirds of the samples were randomly selected from the sample pool and classified using the threshold method based on the night light histograms of the samples (Elvidge et al. 2021). The threshold value at which the classification accuracy of the electrified and unelectrified samples was highest was selected as the classification threshold, and the percentage of unelectrified BUAs was calculated for each country worldwide. Finally, the classification results were validated for accuracy using the remaining one-third of the samples in the sample pool (Gao et al. 2022a). More than 10,000 samples were involved in the accuracy validation, and the quality of the product was checked based on the judgment accuracy of the random samples. In this study, the method was used to produce a global dataset of the remote sensing monitoring of electricity access in BUAs for 2014 and 2020.

4.3.1.4 Results and Analysis

Based on global 500 m resolution NTL remote sensing data, a remote sensing monitoring method was proposed (Gao et al. 2022a), by which the electrification of global build-up areas in 2014 and 2020 was monitored. Based on a global test of over 10,000 random sample points, the product has an accuracy of 98.10%. The areas where errors arise are mainly located in rural areas with small floor areas, mainly due to the low resolution of the remote sensing data. Their spatial distribution and temporal variation

patterns were analyzed for the purpose of globally measuring SDG 7.1.1, access to electricity.

The world's unelectrified BUAs were mainly found in Africa and Asia in 2020 (Fig. 4.1), with 76% of the 20 countries having the largest share of unelectrified BUAs located in Sub-Saharan

Africa. Therefore, achieving SDG 7 globally will require additional and greater international support for developing countries.

Global-electrified BUAs increased notably from 2014 to 2020, from 96.95 to 98.68%, by 29,108.62 km² (Fig. 4.2). According to the

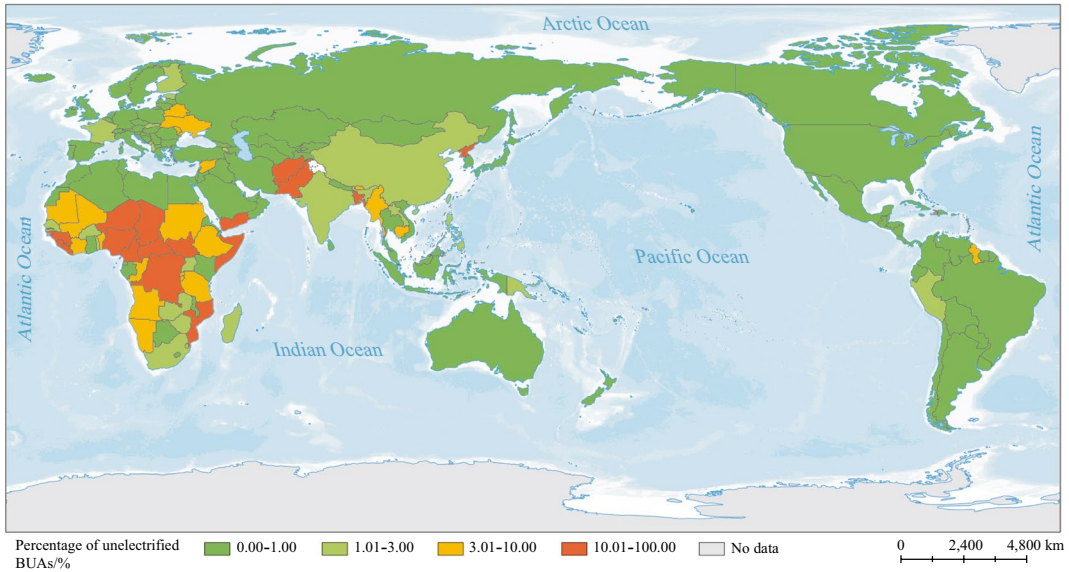


Fig. 4.1 Percentage of global unelectrified BUAs in 2020

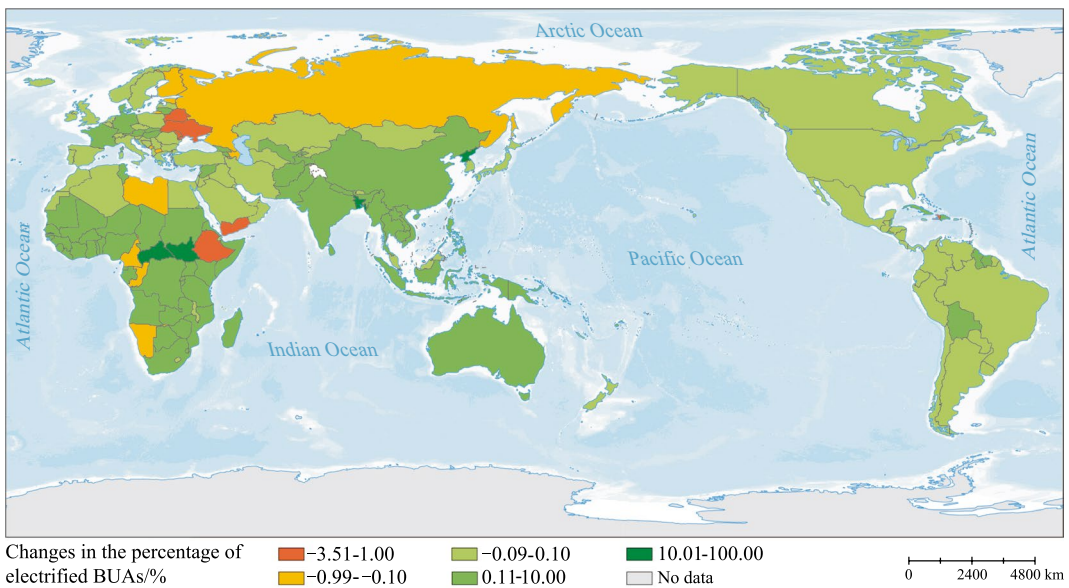


Fig. 4.2 Changes in the percentage of global electrified BUAs in 2020 compared to 2014

Global Power Plant Database of the World Resources Institute, in this period, the share of unelectrified BUAs decreased in 117 countries or regions thanks to the construction of 415 power stations. In contrast, only 17 power stations were constructed in the 18 countries with the largest increase in the share of unelectrified BUAs.

More than half of the countries/regions where unelectrified BUAs increased notably are in fragile and conflictive environments: 32 countries/regions saw their unelectrified BUAs increase—by more than 0.1% in 18 of them. Six of these 18 countries were in medium- to high-intensity conflict (World Bank 2022), one had a fragile social environment, three experienced armed conflicts (riots), and five were in economic recession due to the COVID-19 pandemic. Thus, political unrest, armed conflict, and economic recession are among the main reasons behind the increases in unelectrified BUAs.

4.3.1.5 Highlights

- A global remote sensing monitoring method for buildings and a global remote sensing dataset for 2014 and 2020 were provided to support global electrification policies and investment decisions.
- Electrified BUAs increased significantly around the world, and 29,108.62 km² of such areas were added globally in 2020 compared to 2014, raising their share by 1.73 percentage points, while 117 countries/regions experienced substantial increases in electrified BUAs, and more than half of the countries/regions experiencing decline were in fragile and conflictive environments.

4.3.1.6 Discussion and Outlook

This study focuses on SDG 7.1, energy supply, and proposes a remote sensing monitoring method for the global electrification status of BUAs based on remote sensing data of NTLs, creating a global 500 m resolution remote sensing monitoring dataset of building electrification status for 2014 and 2020, which can quickly and accurately monitor the global electrification

status of BUAs and improve the monitoring capability of the degree of global electrification, and can support policymaking related to electrification.

Developing countries may address their energy shortages by building new power plants, and renewable energy should be the focus of this endeavor. Most of the unelectrified BUAs in the world are found in developing countries, though 117 countries/regions have seen a reduction in unelectrified buildings due to the construction of power plants. Developing countries are suggested to vigorously develop renewable energy, such as solar and wind energy, because those renewable energies are widely available and easy to develop and use.

Further improvement in the capacity of Big Earth Data to support SDG 7 progress is needed, and more big data infrastructure for SDGs should be constructed. Big Earth Data technology has the potential of global application for monitoring SDG 7.1, in support of achieving SDG 7 worldwide. However, due to the limited spatial resolution of satellite remote sensing data, there is still room for improvement in some of the assessment results. In future, a constellation of satellites for sustainable development should be developed to further enhance the supporting capacity of Big Earth Data for SDGs.

4.3.2 China's International Energy Cooperation Projects

Target: SDG 7.1: By 2030, ensure universal access to affordable, reliable and modern energy services.

SDG 7.2: By 2030, increase substantially the share of renewable energy in the global energy mix.

SDG 7.a: By 2030, enhance international cooperation to facilitate access to clean energy research and technology, including renewable energy, energy efficiency and advanced and cleaner fossil-fuel technology, and promote investment in energy infrastructure and clean energy technology.

SDG 7.b: By 2030, expand infrastructure and upgrade technology for supplying modern and sustainable energy services for all in developing countries, in particular least developed countries, small island developing States, and landlocked developing countries, in accordance with their respective programs of support.

4.3.2.1 Background

Developing countries face widespread shortages in energy, finance, and technology on their paths to energy self-sufficiency and transformation. In order to achieve SDG 7, the goal of ensuring universal access to affordable, reliable and modern energy services, the key lies in helping developing countries address energy shortages and energy transformation. To this end, under SDG 7, there are two targets—SDG 7.a and SDG 7.b—to promote developing countries' green and low-carbon energy transformation through international cooperation. China has actively implemented the international cooperation targets under SDG 7 in the 2030 Agenda by helping developing countries develop clean energy and promoting green and low-carbon energy transformation globally under the framework of the Global Development Initiative and South–South Cooperation. Clean energy has always been a focus of China's international cooperation projects. China has provided funding and technologies to energy projects in developing countries through investment, construction, and equipment supply to help them achieve SDG 7.

This study produces a dataset and methodology for measuring the impacts of China's international energy cooperation projects (CIECPs) on SDG 7 in developing countries.

4.3.2.2 Data

- National data on access to electricity, population data, per capita electricity consumption, share of renewable energy generation, and list of fragile and conflict-affected countries. Source: World Bank (<https://data.worldbank.org/cn/indicator>).

- Global Power Plant Database. Source: World Resources Institute (<http://datasets.wri.org/dataset/globalpowerplantdatabase>).
- China Overseas Energy Finance Database. Source: Global Development Policy Center. (<https://www.bu.edu/cgef/#/all/Country>).
- Dataset of CIECPs. Source: Aerospace Information Research Institute, CAS.

4.3.2.3 Methods

China has made significant achievements in the construction of international cooperation projects in clean energy, and has contributed significantly to the achievement of SDG 7 in developing countries, mainly in SDG 7.1, SDG 7.2, SDG 7.a.1, SDG 7.b.1. The CIECPs dataset shows that China has participated in 437 power projects, such as hydro, thermal, wind, photovoltaic, and nuclear power plants, and power transmission and distribution projects. Based on the CIECPs dataset, the main indicators used to describe China's contributions to the construction of international projects in clean energy are the total installed capacity ratio, per capita new electricity consumption, and new power generation/new electricity demand from CIECPs. The total installed capacity ratio is the ratio of the total installed capacity of CIECPs in each country to its total existing installed capacity. Per capita new electricity consumption is the ratio of new electricity generation to population in CIECPs. The new power generation from CIECPs has been estimated (Gao et al. 2022b), and the new electricity demand is the incremental electricity consumption of each country. The impacts of CIECPs on SDG 7.1, energy supply, in 80 countries were evaluated using three parameters, including the ratio of the number of renewable energy plants, the ratio of installed capacity, and the change in the share of electricity generated by renewable energy plants in CIECPs. The impacts of CIECPs on SDG 7.a.1 and SDG 7.b.1 in 80 countries were evaluated by calculating the amount of investment in wind power, photovoltaic, and other renewable energy power plant projects and their share, as well as the installed capacity of per capita renewable

energy power plants. These indicators were calculated for 2015, 2020, and all years of completion of CIECPs to evaluate the impacts of CIECPs on clean energy in each country.

4.3.2.4 Results and Analysis

This study assesses the impacts of CIECPs on the achievement of SDG 7 in developing countries using spatial statistics and analysis of Big Earth Data, including the World Bank's global population and per capita electricity consumption, World Resources Institute's Global Power Plant Database, and an independently developed CIECP dataset. China has been involved in 437 energy projects in 80 countries through investment, construction, or equipment supply (Gao et al. 2022b), making a notable contribution to those countries' implementation of SDG 7 (Fig. 4.3). Specifically, CIECPs have increased the installed capacity ratio and per capita electricity consumption and the ratios of those from renewal sources in the host developing countries. China's investment in renewable energy in developing countries from 2000 to 2020 exceeded USD 100 billion.

Assistance to developing countries in addressing electricity shortages has improved global access to electricity. CIECPs account for more than 50% of the total installed capacity in 13 countries, including Angola and Guinea, and 20–50% in 20 countries, including Myanmar

and Zambia (Fig. 4.4). These projects can meet the demands for additional electricity in 32 countries, including Ethiopia and Pakistan, and help solve their electricity shortage problems. They have increased the per capita electricity consumption in 80 countries, in 10 of which the increase is more than 400 kW·h.

Renewable energy as a share of total electricity increased in 44 host developing countries, promoting a global transformation toward green and low-carbon energy. Over half of the projects were renewable energy power plants (51.26%), with installed capacity making up 41.35% of the total. They have raised the share of renewable energy electricity generation in 44 countries by an average rate of 3.70% and filled the gap of renewable energy power plants in five countries, including Saudi Arabia. In 2020, the installed capacity of CIECPs renewable energy power plants was 1.37 times that of 2015.

Chinese energy funding for developing countries mainly goes into renewable energy to support their development and use of clean energy. According to China's Global Energy Finance Database of the Global Development Policy Center, from 2000 to 2020, the China Development Bank and the Export–Import Bank of China provided USD 234.6 billion in overseas energy investment, of which 42.75% went into renewable energy as direct investment. Power stations received USD 80.3

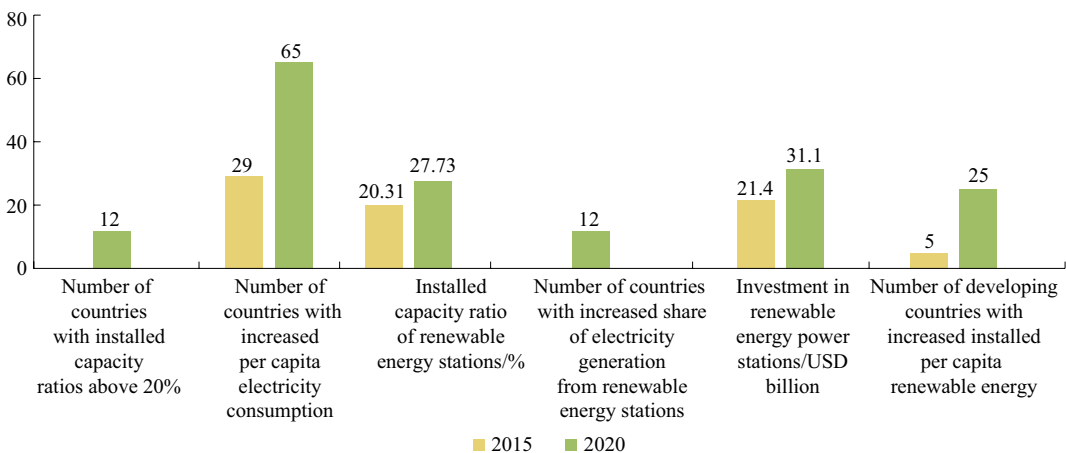


Fig. 4.3 Contribution of CIECPs to the achievement of SDG 7 in 80 countries in 2015 and 2020

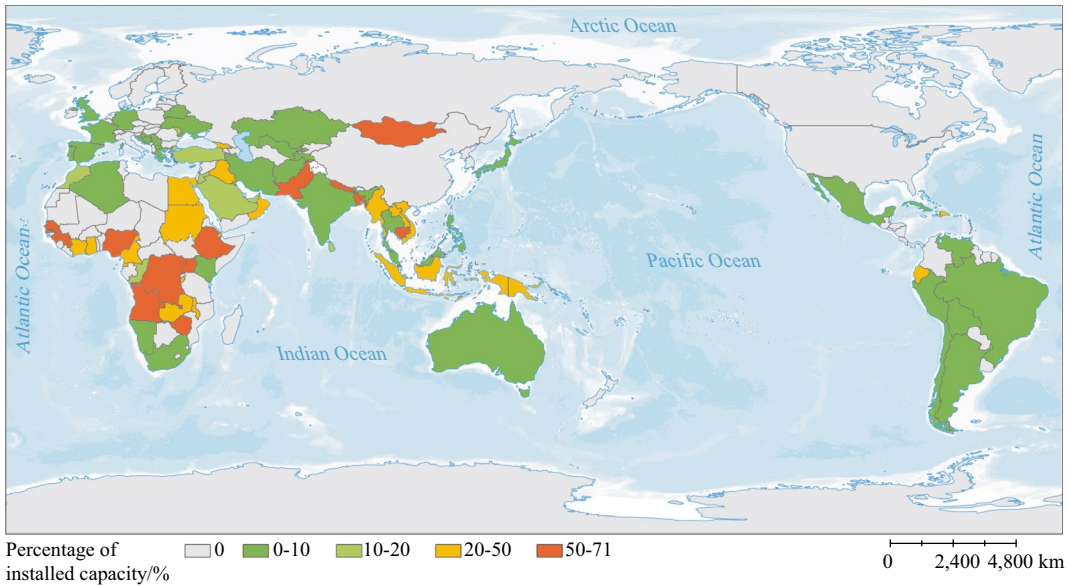


Fig. 4.4 Percentage of the installed capacity of CIECPs to total installed capacity in host developing countries during 2000–2019

billion in direct investment, including 38.73% in renewable energy. In 2021, President Xi Jinping announced that China would no longer build new coal-fired power projects abroad and that renewable energy would become the main destination of Chinese overseas energy investment.

CIECPs have substantially increased per capita renewable energy installed capacity in 49 developing countries, in support of their energy transformation. The total renewable energy installed capacity of CIECPs amounts to 85.42 million kW, or 26.90 W per capita. Renewable CIECPs are located in 55 countries, 49 of which are developing countries. Thanks to them, 12 host developing countries have seen an increase of more than 50 W in their per capita renewable energy installed capacity, with the maximum increase being 189.78 W.

4.3.2.5 Highlights

- China engages in international energy cooperation (2000–2019) to help achieve SDG 7 in developing countries, where China has invested more than USD 100 billion in renewable energy. China's CIECPs have

increased per capita electricity consumption in 80 countries, raising the share of renewable energy power generation in 44 countries and the per capita renewable energy installed capacity in 49 developing countries.

4.3.2.6 Discussion and Outlook

This study produced a methodology and dataset for assessing the impacts of CIECPs on the achievement of SDG 7 targets in developing countries for SDG 7.1, SDG 7.2, SDG 7.a and SDG 7.b. The dataset can be used to support decision-making on the achievement of SDG 7 targets and energy transformation in developing countries, especially international cooperation on clean energy projects.

CIECPs have contributed significantly to the achievement of SDG 7 targets in developing countries, but there is still a long way to go before SDG 7 is achieved globally. A global partnership for development is crucial for developing countries to achieve SDG 7. The international community should give even more support to developing countries, which generally lack the financial resources and technologies to develop renewable energy. Future studies should

assess the impacts of CIECPs on the achievement of SDG 7 targets in developing countries in key regions such as Sub-Saharan Africa and Southeast Asia.

4.3.3 China's International Training on Solar Energy Utilization

Target: SDG 7.2: By 2030, increase substantially the share of renewable energy in the global energy mix.

SDG 7.a: By 2030, enhance international cooperation to facilitate access to clean energy research and technology, including renewable energy, energy efficiency and advanced and cleaner fossil-fuel technology, and promote investment in energy infrastructure and clean energy technology.

4.3.3.1 Background

China has been implementing human resource development and cooperation projects since the early 1950s, and foreign aid human resources training is one of the main patterns, referred to as foreign aid training (An 2013). SDG 7.2 and SDG 7.a set out specific objectives for renewable energy, and solar energy, as a key renewable source, plays a crucial role in energy accessibility and transition for all countries. From 1991 to 2021, China has conducted hundreds of international training courses and seminars on solar energy utilization, sponsored by the Ministry of Foreign Affairs, Ministry of Science and Technology, and Ministry of Commerce of the People's Republic of China, most of which lasted from 15 to 60 days, with the working languages of English, French, Russian, and Arabic. The training programs helped recipient countries cultivate their own managers and technicians in the areas of planning, policy formulation, project implementation, skill improvement, and international cooperation (The Administrative Center for China's Agenda 21 2020). The case study, in terms of characteristics of China's foreign aid training, analyzed the role of international training programs in enhancing the

participants' abilities, boosting the development of the solar industry, and strengthening bilateral and multilateral cooperation and exchange, so as to provide decision support for the development of foreign aid training on solar energy utilization, thus continuously improving the training program and promoting international cooperation for the realization of the 2030 Agenda.

4.3.3.2 Data

- Statistical data on recipient countries and participants under China's foreign aid training programs on solar energy utilization from 1991 to 2021.
- Statistical data from the International Energy Agency (IEA), International Renewable Energy Agency (IRENA), and General Administration of Customs of the People's Republic of China from 2012 to 2020.

4.3.3.3 Methods

- (1) Perform statistical analysis on the number of countries and trainees under China's foreign aid training programs on solar energy utilization from 1991 to 2021 to find the spatial and temporal distribution and then analyze the characteristics of the program.
- (2) Analyze the impacts of foreign aid training, through illustrative examples, on international exchange, cooperation, and technology promotion and transfer.

4.3.3.4 Results and Analysis

- (1) China has been adhering to the framework of South–South Cooperation on foreign aid training, reflecting the cooperative development relationship of mutual support and assistance between China and other developing countries.

As shown in Fig. 4.5, the countries and regions benefiting from China's foreign aid training programs on solar energy utilization spread across five continents, involving 133 countries, of which 124 are developing countries, accounting

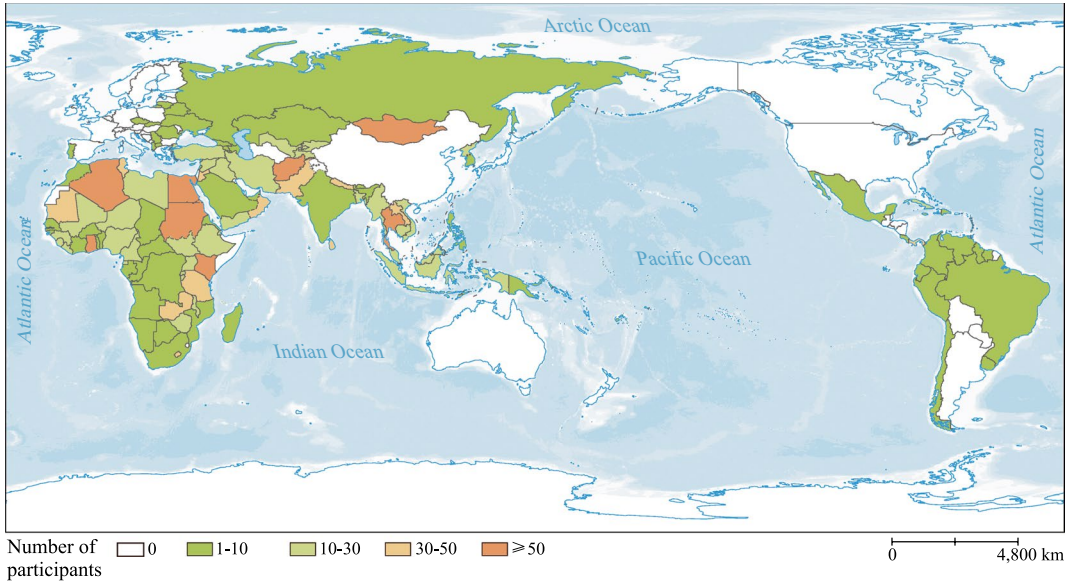


Fig. 4.5 Distribution of participants under China’s foreign aid training programs on solar energy utilization (1991–2021)

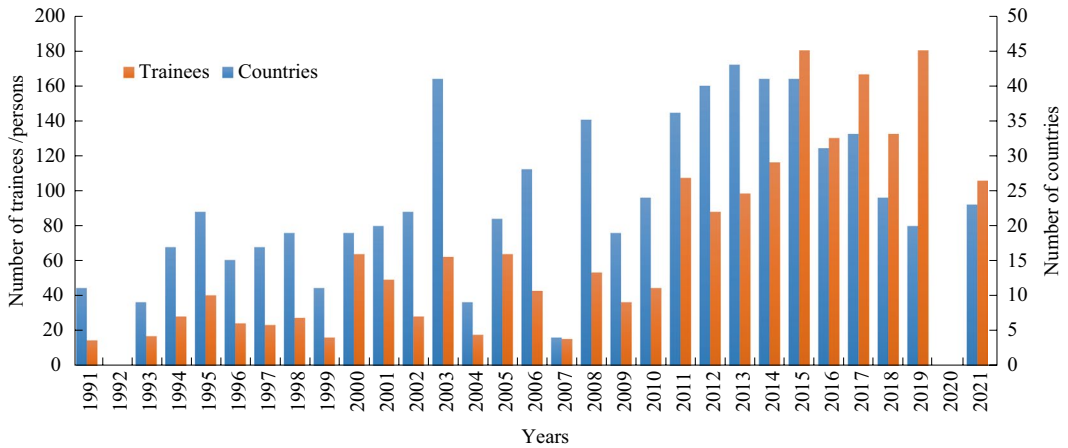


Fig. 4.6 Number of trainees and countries under China’s foreign aid training programs on solar energy utilization (1991–2021). *Note* No data available for 1992 and 2020

for 93.23%. Through foreign aid training, China has effectively implemented global development cooperation and jointly promoted the implementation of the SDGs.

Figure 4.6 shows the data of trainees and countries under China’s foreign aid training programs from 1991 to 2021. By the end of 2021, about 2,000 participants had been trained, with

a maximum of 180 trainees in 2015 and 2019. The number of trainees and countries has been increasing year on year, and the scale has been expanding, especially after 2013 when the average annual growth rate of participants climbed to 12.93%. This indicates that since China proposed the BAR initiative in 2013, it has increased its training efforts in BAR countries.

Figure 4.7 demonstrates that 95.07% of participants under China’s foreign aid training are from the Asian, African, and American regions, with Africa accounting for 49.70% of the total. This reflects that China’s assistance to developing countries is mainly based on the framework of South–South Cooperation.

- (2) In line with the concept of “teaching people how to fish”, under the foreign aid training programs, China has provided human resource support in enhancing the capacity of developing countries to develop on their own.

With the increased use of solar energy throughout the world, more people are needed in this field. Figure 4.8 reflects the number of employed people in the global solar industry from 2012 to 2020, with the population increasing from 2.25 million to 4.8 million, reaching an average annual growth rate of 9.93%. Since 2012,

the number of trainees under the programs has increased rapidly, by an average of 10.76% annually. The growing number of employed people in the solar industry has led to a greater demand for professional training in this area. China, as the largest country in solar energy utilization, has strengthened cooperation with developing countries and shared its experience to enhance the capability of those employed people in recipient countries. For example, Mr. Koblan Aluko Narcisse from the Ministry of Mines, Petroleum and Energy of Côte d’Ivoire, became a project manager promoting solar products after attending the training course back in his home country; Mr. Mukesh from the Alternative Energy Promotion Centre in Nepal and Mr. Komal from the Nepal Electricity Authority were both promoted and appointed to key positions shortly after their training in China.

- (3) Adhering to the principle of “mutual benefit”, under foreign aid training programs, China has promoted economic and trade cooperation and facilitated the development of solar energy utilization in developing countries.

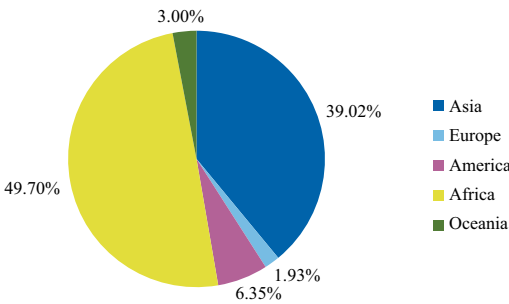


Fig. 4.7 Continental share under China’s foreign aid training programs on solar energy utilization (1991–2021)

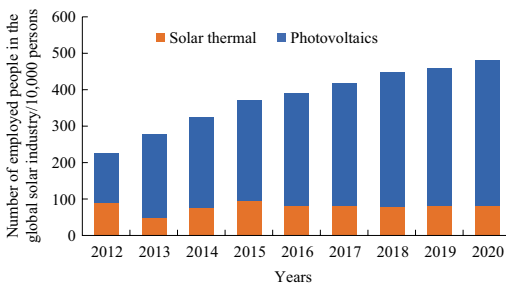


Fig. 4.8 Number of employed people in the global solar industry (2012–2020)

The foreign aid training programs help to bridge the information gap between China’s solar enterprises and various countries, facilitating better international business for Chinese enterprises and enabling more technologies and products to reach the international market. Figure 4.9 shows that from 2014 to 2020, China’s solar cell exports grew from 691 million to 2,722 million, with the export value increasing from CNY 75.757 billion to CNY 137.005 billion. In the face of declining prices, both China’s export volume and export value of solar cells grew by an average of 31.55% and 12.58% annually. China is the world’s largest producer of solar products. During the training course, participants were arranged to visit Chinese companies for on-site teaching, while with the help of such platforms, companies also made efforts to showcase their advantages. By visiting enterprises, participants were able to directly learn about technology and product information from China, plan cooperation, and actively promote the implementation of cooperation projects after

returning to their homeland, thereby increasing the export volume of Chinese solar products.

- (4) China has been adhering to the principle of openness on foreign aid training, strengthening cooperation with international organizations, and facilitating technology promotion and transfer for the realization of the SDGs.

By the end of 2021, China has enhanced multi-lateral cooperation with more than 10 international organizations and institutions, including the United Nations Development Programme (UNDP) and the United Nations Industrial Development Organization (UNIDO). So far, the training programs have supported more than 240 officials and experts from international agencies to come to China to give lectures or conduct technical exchanges. More than 3200 foreign leaders, envoys, and experts from 120 countries visited the training institutions in China, and cooperation agreements between China and more than 50 of those countries have been reached. Under the training programs, international organizations have strengthened exchange and propelled the transfer of advanced and applicable solar technologies worldwide to developing countries. The “International Solar Energy Center for Technology Promotion and Transfer” project, carried out by the Chinese government and UNIDO, was rated as one of the six major

achievements of UNIDO at its 50th anniversary (UNIDO 2016). Professor Johannes A. van Ginkel, former Under-Secretary-General of the UN, delivered a special report on “Prospects for sustainable energy development in low-lying countries”, introducing to the participants the current status and future of solar energy utilization in developed countries, which can be a good reference for developing countries.

4.3.3.5 Highlights

- From 1991 to 2021, developing countries accounted for 93.23% of trainees receiving foreign training on solar energy utilization in China, while countries in Asia, Africa, and America accounted for 95.07% of the total number of trainees. Among them, African trainees accounted for 49.70% of the total, indicating that China’s foreign training on solar energy utilization in developing countries is mainly based on the framework of South–South Cooperation. Since 2013, the number of training countries and trainees has increased rapidly, with an average annual growth of 12.93%, which indicates that China has continuously increased its cooperation with countries under the BAR Agreement and deepened South–South Cooperation.
- From 2012 to 2020, the average annual growth rate of global solar energy utilization

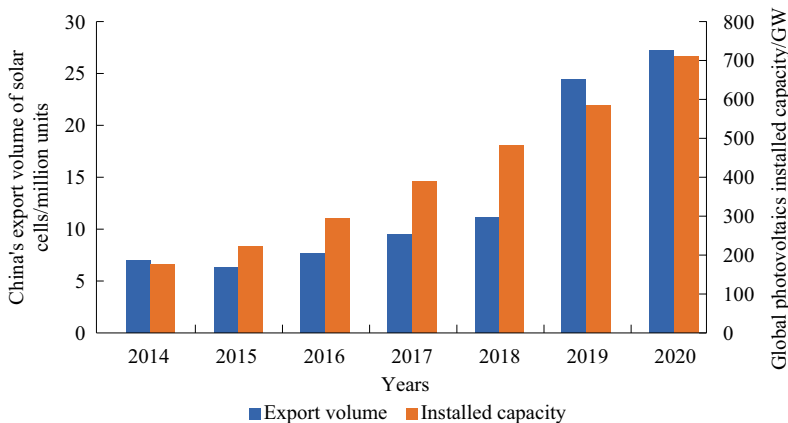


Fig. 4.9 Global installed capacity of photovoltaics and China’s export volume of solar cells (2014–2020)

practitioners was 9.93%, increasing the demand for technical training and exchange. China's training not only enhances trainees' personal abilities and shares China's development experience, but also brings together multiple international institutions, strengthens multilateral cooperation, and promotes global solar energy technology transfer. From 2014 to 2020, the average annual growth rate of China's export volume and export value of solar cells was 31.55% and 12.58%, respectively. Chinese enterprises established communication and information bridges through foreign aid training, expanded international business, and increased export volume.

4.3.3.6 Discussion and Outlook

- (1) About 733 million people around the world still lack access to electricity, and hence it is urgent to accelerate energy accessibility. Foreign aid training programs are a less expensive and more effective way to realize their energy goals. In particular, the training programs for the least developed countries can improve the policy and skill level of employed people in the solar industry, further promote the use of solar energy, and ultimately improve energy utilization in recipient countries.
- (2) Solar energy plays a vital role in achieving the goal of significantly increasing the proportion of renewable energy in the global energy mix. Foreign aid training programs enable developing countries to learn from China's experience in solar energy utilization and provide them with assistance in policy formulation, energy transition, and planning to increase the share of renewable energy.
- (3) Through foreign aid training, China will further expand international cooperation, jointly carry out international scientific and technological cooperation projects with developing countries, and provide them with technical advice and

demonstrations, product applications, and services, so as to promote the transfer of more solar technologies and products to developing countries.

- (4) Foreign aid training is an important part of international cooperation. Under the Global Development Initiative, more efforts should be made to continuously strengthen foreign aid training programs on solar energy utilization, make the programs more targeted and effective, and help recipient countries enhance their capacity for independent development and jointly implement the SDGs.

4.4 Summary

This chapter examines methodologies for monitoring and analyzing progress in SDG 7 based on Big Earth Data, centering on two themes under SDG 7: access to electricity and international energy cooperation. The results show that notable progress on SDG 7 has been made globally and in China in recent years. To facilitate the global realization of SDG 7, we offer the following recommendations.

- (1) Further improvement in the capacity of Big Earth Data to support SDG 7 is needed and more big data infrastructure for SDGs should be constructed. Big Earth Data technology has the potential for global monitoring of SDG 7.1. Due to the limited spatial resolution of satellite remote sensing data, however, there is still room for improvement in some of the assessment results. In future, a constellation of satellites for sustainable development should be developed to further enhance the supporting capacity of Big Earth Data for the SDGs.
- (2) Developing countries may address their energy shortages by building new power plants, and renewable energy should be the focus of this endeavor. Most of the unelectrified BUAs in the world are found

in developing countries, but 117 countries have seen a reduction in unelectrified buildings due to the construction of power plants. Developing countries are suggested to vigorously develop renewable energy, such as wind and solar, because these renewable energy sources are widely available and easy to develop and use.

- (3) A global partnership for development is crucial for developing countries to achieve SDG 7. The international community should give even more support to developing countries, which generally lack the financial resources and technologies to develop renewable energy. CIECPs play an important role in helping developing countries achieve the targets of SDG 7 globally, which requires greater attention and support from the international community to developing countries.

The costs of new energy sources, such as wind power and photovoltaic power generation, are already comparable to those of traditional fossil energy sources. In future, new energy sources will gradually become the mainstay of the energy systems of countries around the world, significantly reducing the carbon emissions of the global energy system and enhancing the energy autonomy of countries.

References

- An Y (2013) Analysis on the history and problems of China's foreign aid training. Beijing, Master's Thesis of China Foreign Affairs University (in Chinese)
- Corbane C, Florczyk A, Pesaresi M, et al. (2018) GHS built-up grid, derived from Landsat, multitemporal (1975–1990–2000–2014), R2018A. <https://doi.org/10.2905/jrc-ghsl-10007>
- Elvidge C, Zhizhin M, Ghosh T et al (2021) Annual time series of global VIIRS nighttime lights derived from monthly averages: 2012 to 2019. *Remote Sens* 13:922
- Gao XM, Wu MQ, Li C et al (2022a) Influence of China's overseas power stations on the electricity status of their host countries. *Int J Digital Earth* 15(1):416–436
- Gao XM, Wu MQ, Niu Z et al (2022b) Global identification of unelectrified built-up areas by remote sensing. *Remote Sensing* 14(8):1941
- The Administrative Center for China's Agenda 21, Ministry of Science and Technology of the People's Republic of China & Center for South-South Cooperation in Technology Transfer (2020) Exploration of renewable energy technology transfer model in South-South cooperation. Beijing, Science Press (in Chinese)
- The United Nations Industrial Development Organization, The Ministry of Commerce, China (2016) Marking the 50th Anniversary of UNIDO UNIDO-China Cooperation
- World Bank (2022) FY22 List of fragile and conflict-affected situations. The World Bank Group. <https://thedocs.worldbank.org/en/doc/bb52765f38156924d682486726f422d4-0090082021/original/FCSList-FY22.pdf>

Open Access This chapter is licensed under the terms of the Creative Commons Attribution-NonCommercial-NoDerivatives 4.0 International License (<http://creativecommons.org/licenses/by-nc-nd/4.0/>), which permits any noncommercial use, sharing, distribution and reproduction in any medium or format, as long as you give appropriate credit to the original author(s) and the source, provide a link to the Creative Commons license and indicate if you modified the licensed material. You do not have permission under this license to share adapted material derived from this chapter or parts of it.

The images or other third party material in this chapter are included in the chapter's Creative Commons license, unless indicated otherwise in a credit line to the material. If material is not included in the chapter's Creative Commons license and your intended use is not permitted by statutory regulation or exceeds the permitted use, you will need to obtain permission directly from the copyright holder.





SDG 11, Sustainable Cities and Communities

5

5.1 Background

Cities are the engine of economic growth, contributing about 60% of the global gross domestic product (GDP). At the same time, they are the main battleground in our fight against climate change. Cities generate about 70% of the global carbon emissions and use more than 60% of all resources. SDG 11 aims to make cities and human settlements “inclusive, safe, resilient, and sustainable,” which means, among other problems, overcoming the challenges of congestion, lack of funds, and infrastructure damage in ways that allow them to continue to thrive and grow, improve resource use, and reduce pollution and poverty. However, the average worldwide urban solid waste collection rate was 82% by 2022, and the rate under management in controlled urban facilities was 55%. Only 3% of the 6475 cities in 117 countries and regions around the world do not exceed the threshold of air quality guidelines of the World Health Organization (WHO).

With the development and progress of Earth observation and big data technology, Big Earth Data methods that pull together remote sensing,

statistics, and geographic information play an important role in the monitoring and evaluation of SDG 11 indicators and are becoming widely used in evaluating sustainability, such as the evaluation of the urban atmospheric environment, sustainable land use, and social and economic development. In the process of advancing the SDGs, the focus of research has been shifting from the construction of SDG indicator systems to the monitoring and evaluation of SDG progress.

Centering on three themes—monitoring and evaluating the urbanization process, World Heritage protection, and urban green space for SDG 11 at a community scale—this chapter draws on the research from the previous three editions of the report and uses Big Earth Data to monitor and evaluate individual and multiple SDG 11 targets at the global scale.

5.2 Main Contributions

This chapter evaluates the progress of SDG 11.3, SDG 11.4, and SDG 11.7 through six case studies at the global scale. The main contributions are as follows: (Table 5.1).

Table 5.1 Cases and their main contributions

Targets	Cases	Contributions
SDG 11.3 By 2030, enhance inclusive and sustainable urbanization and capacity for participatory, integrated, and sustainable human settlement planning and management in all countries	Comprehensive assessment of global urban land use efficiency, 2000–2020	Data product: a dataset of 1,702 UBAs (population > 300,000) from 2000 to 2020 Decision support: inform policies and offer recommendations on the sustainable development of cities globally
	Changes in global nighttime light intensity	Data product: 2000–2021 global “NPP-VIIRS-like” NTL annual composited dataset Method and model: cross-sensor calibrated Defense Meteorological Satellite Program-Operational Linescan System (DMSP-OLS) and national polar-orbiting partnership-visible infrared imaging radiometer suite (NPP-VIIRS) NTL data Decision support: basic NTL remote sensing data for monitoring the efficiency of urban land use (SDG 11.3.1)
SDG 11.4 Strengthen efforts to protect and safeguard the world’s cultural and natural heritage	Ratio of global land consumption and population growth under future scenarios	Data product: global Urban Land Use Extents under various SSPs from 2020 to 2100 Method and model: per capita urban area dynamics using the sigmoid model under diverse socioeconomic pathways in different regions, and spatially explicit future urban extent dynamics using the urban cellular automaton model Decision support: varying growth rates of population and urban extent
	Land cover change monitoring of global World Cultural Heritage sites	Data product: the world’s first dataset of land cover change for World Cultural Heritage sites Method and model: a technical solution to semi-automatic change detection using high spatial resolution remote sensing Decision support: scientific guidelines for the sustainable protection of cultural heritage
	Multiscale monitoring and evaluation of global natural and mixed World Heritage site boundary areas	Data product: land cover change dataset of global natural heritage sites boundary areas (2 km inside and outside the boundary) from 2010 to 2020 Method and model: Land use change rate of heritage site boundary areas and boundary areas-human intervention degree (BA-HID) model of heritage sites Decision support: sustainable protection and global governance of World Natural and Mixed Heritage site boundary areas

(continued)

Table 5.1 (continued)

Targets	Cases	Contributions
SDG 11.7 By 2030, provide universal access to safe, inclusive and accessible, green and public spaces, in particular for women and children, older persons and persons with disabilities	Global change in urban greenness and beneficiary population in large cities	Data product: dataset on the global trends of greenness with 250 m spatial resolution from 2001 to 2021 Method and model: nonparametric Mann–Kendall test to calculate the trend and significance level of each urban pixel and calculate the ratio of BUA pixels with a significant greening trend to the total BUAs for each city Decision support: low-cost solution for urban sustainability monitoring in developing countries

5.3 Case Studies

5.3.1 Comprehensive Assessment of Global Urban Land Use Efficiency, 2000–2020

Target: SDG 11.3: By 2030, enhance inclusive and sustainable urbanization and capacity for participatory, integrated, and sustainable human settlement planning and management in all countries.

5.3.1.1 Background

Since the beginning of the twenty-first century, cities have increasingly become the center of the global discussion on sustainable development, and urbanization has become a key agenda in international development policies. SDG 11.3.1 is the ratio of land consumption rate to population growth rate (LCRPGR). The LCRPGR indicator aims to determine urban land use efficiency, providing an important tool for monitoring and evaluating the sustainable development of cities. However, SDG 11.3.1 is a Tier II indicator, meaning it must urgently address the issue of missing data. Therefore, this case discusses the monitoring and assessment of urban land use efficiency at a global scale, the results of which can inform decisions on the sustainable development of cities around the world.

5.3.1.2 Data

- A dataset of 1702 urban built-up areas (population > 300,000) from 2000 to 2020 according to the database released by the UN World Urbanization Prospects 2018 (<https://population.un.org/wup/>).
- This case study independently generated data products for a global 30 m urban impervious surface in five periods from 2000 to 2020.

5.3.1.3 Methods

According to the National Geomatics Center of China’s minimum urban land mapping unit standard, an 8 × 8-pixel window was considered

the optimal scale for remote sensing images with a spatial resolution of 30 m. Therefore, the area of the smallest plot was 57,600 m² in the main urban area, connecting the gaps within the primary urban area, each with an area of 57,600 m², to create continuous zones. Meanwhile, all the patches with a distance of less than 200 m were aggregated into one intact zone. The densely populated peripheral urban area was also regarded as an urban built-up area (UBA). In addition, public spaces were considered parts of UBA, such as man-made parks and green patches. After the spatial transformation of UBA, we performed an artificial check and calibration of the initial UBA products with the help of high-resolution Google Earth imagery. Finally, we obtained quality-controlled UBA products for 1702 cities. The details of the method are shown in Fig. 5.1.

In addition, this case used layer stacking techniques for data post-processing to ensure that urban land identified as UBAs in earlier years remained unchanged, while non-urban land was

excluded from UBAs in earlier years. Our independently generated global standardized UBA dataset not only includes the precise boundaries of impervious surfaces in cities, but also retains the continuous distribution pattern of UBAs, consistent with visual interpretation results based on high-resolution Google Earth imagery.

According to our independently generated data products and the population data released by the UN World Urbanization Prospects in 2018, we used SDG 11.3.1 to calculate land use efficiency for cities with a population above 300,000 around the world. The LCRPGR calculating procedures were written as the following equation:

$$\text{LCRPGR} = \frac{\text{LCR}}{\text{PGR}} = \frac{\ln(\text{Urb}_{t+n}/\text{Urb}_t)}{\ln(\text{Pop}_{t+n}/\text{Pop}_t)},$$

where Urb_t represents the total area of the city's UBA in the year t , Urb_{t+n} represents the total UBA of the city in the year $t+n$, n represents the year between the two periods, Pop_t is the total population in the year t , and Pop_{t+n} is the total

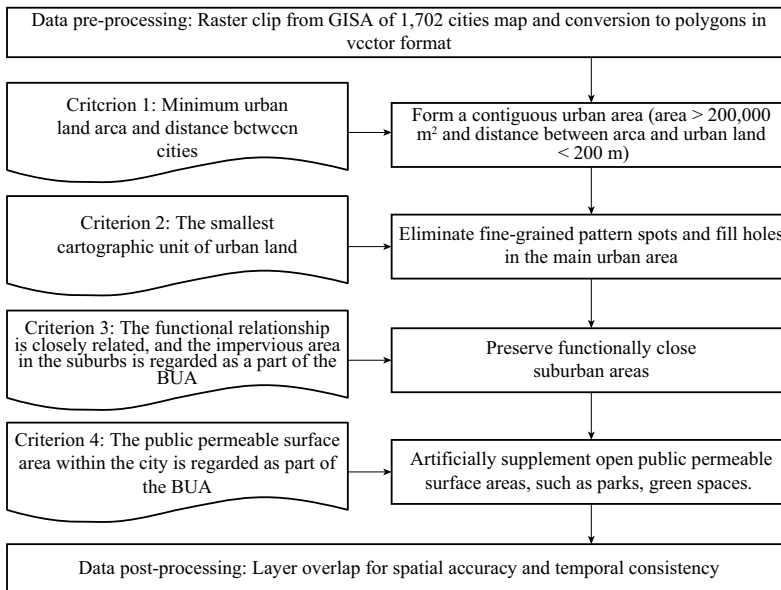


Fig. 5.1 Flowchart showing the process of converting the impervious surface area map to the UBA product

population in the year $t+n$. LCR and PGR represent the land consumption rate and population growth rate, respectively.

5.3.1.4 Results and Analysis

1. Map of the global urban built-up area dataset (GUBAD)

The UN Human Settlements Programme (Atlas of Urban Expansion) (<http://www.atlasofurbanexpansion.org/>) and the World Bank (<https://www.worldbank.org/en/home>) also produced their own UBA datasets. The UN-Habitat dataset provided UBA data only for 220 cities in 2000 and 2015 (Angel et al. 2016), and the World Bank provided UBA data for about 1000 Asian cities in 2000 and 2010. Our global urban built-up area dataset (GUBAD) products have more extensive coverage than other datasets. We chose 76 matching pairs of corresponding cities from GUBAD and the UN-Habitat dataset. The results show that GUBAD has higher correlations with the UN-Habitat dataset ($R^2=0.70$ in 2000 and $R^2=0.83$ in 2015) than the World Bank dataset ($R^2=0.60$ in 2000 and $R^2=0.68$ in 2010), as shown in Fig. 5.2c and d. In total, our dataset has broader coverage and higher accuracy, and therefore, it has more potential for urban analysis.

This case study independently generated data products for a global 30 m urban impervious surface in five periods from 2000 to 2020. Using the definition of a UBA recommended by the UN-Habitat, we converted impervious surfaces into standardized UBA products (Jiang et al. 2021, 2022). Combining them with the population data of 1702 cities with a population above 300,000 provided by the 2018 Revision of World Urbanization Prospects, we calculated SDG 11.3.1 to comprehensively compare, analyze, and evaluate global urban land use efficiency (Fig. 5.3).

While global urbanization has developed in a more balanced way, land urbanization still outpaces population urbanization. The proportions of cities in different LCRPGR categories among

typical cities worldwide from 2000 to 2020 reveal that the LCR was still faster than PGR between 2015 and 2020, but compared with the period between 2000 and 2005, the global urban land expansion and population growth were moving in a more balanced way. The proportion of cities with LCRPGR larger than 1.0 decreased from 65.10 to 63.57%; those with LCRPGR between 0.0 and 1.0 increased from 28.91 to 30.91%; those with negative population growth (with LCRPGR below 0) fell from 6.00% to 5.52% (Fig. 5.4a). The change in LCRPGR in globally representative cities from 2000 to 2020 showed a drop from 1.65 in the 2000–2005 period to 1.31 in the 2015–2020 period in the indicator of global urban land use efficiency, demonstrating a positive trend of balanced development of global urbanization, but the speed of land urbanization still exceeded that of population urbanization (Fig. 5.4b).

Global urbanization shows significant regional differences, with land urbanization in Europe occurring faster than population urbanization. The change in the LCRPGR indicator of typical cities across major continents from 2000 to 2020 (as shown in Fig. 5.5) indicates that, at different times, except for Asia, the LCRPGR indicator has exhibited a decreasing trend on all continents. Taking the period from 2015 to 2020 as an example, the results are ranked in the following order: Europe (2.76)>Asia (1.59)>North America (1.41)>Africa (1.13), South America (1.13),>Oceania (1.01), indicating that the LCR in Europe is significantly higher than the PGR, mainly due to Europe's slow or negative population growth.

5.3.1.5 Highlights

- Independent production of a dataset of 1702 UBAs (population>300,000) from 2000 to 2020.
- Global urbanization is generally developing in a more balanced way. The indicator of global land use efficiency decreased from 1.65 in 2000–2005 to 1.31 in 2015–2020, but

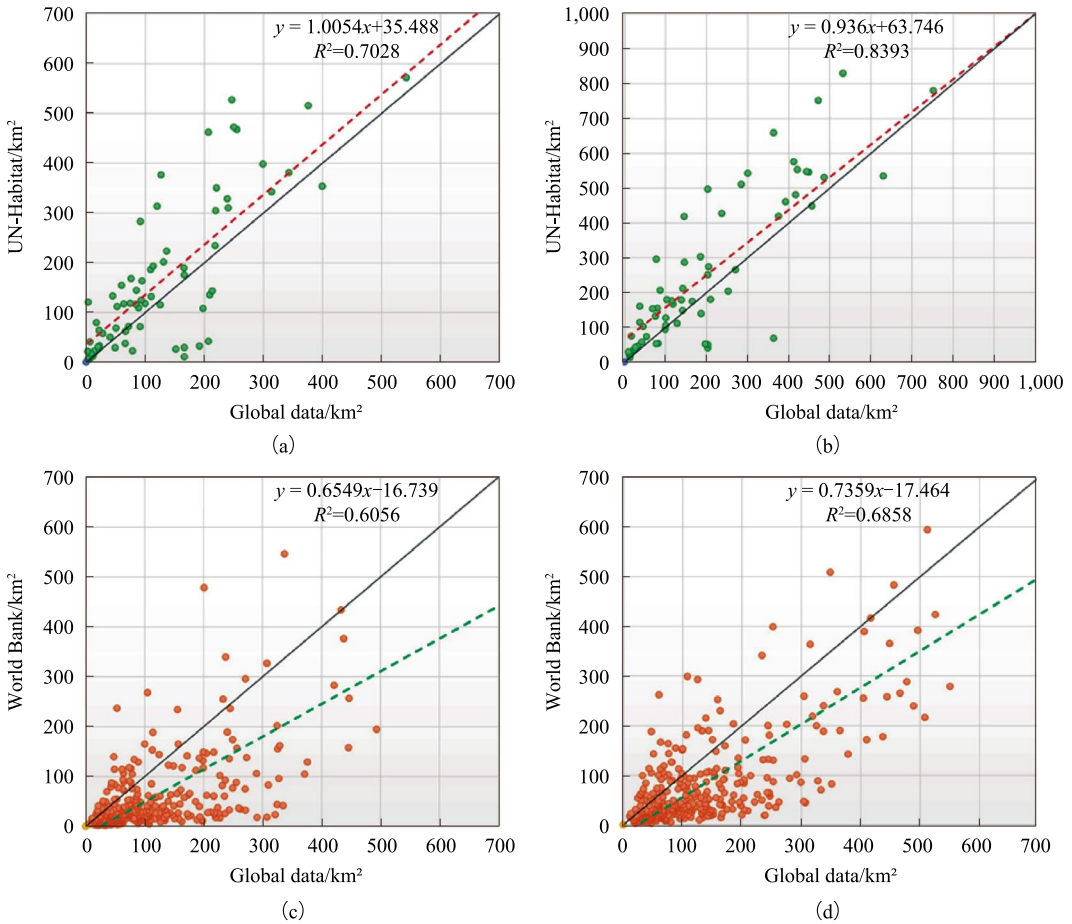


Fig. 5.2 Corresponding to the scatter plot of matching cities, each point represents a value of the UBA of the city. The plots show comparisons of: **a** UN-Habitat data with

the global data in 2000, **b** UN-Habitat data with the global data in 2015, **c** World Bank data with the global data in 2010, and **d** World Bank data with the global data in 2010

the speed of land urbanization still exceeds that of population urbanization.

- There are obvious regional differences in global urbanization. In Europe, the speed of land urbanization is much faster than that of population urbanization.

5.3.1.6 Discussion and Outlook

This case study independently generated a product of 1702 UBA (population > 300,000) for a global 30 m urban impervious surface from 2000 to 2020, and impervious surfaces were

converted into standardized UBA products. The ratio of LCRPGR was used to analyze the spatiotemporal differentiation patterns of global urbanization from the perspectives of land and population and evaluate the global urbanization process. In the future, the plan is to achieve spatial coupling between population and economic data within UBA, and improve the quantitative methods for coordinating the relationship between land, population, and economic urbanization, in order to monitor and evaluate the urbanization process at a global scale.

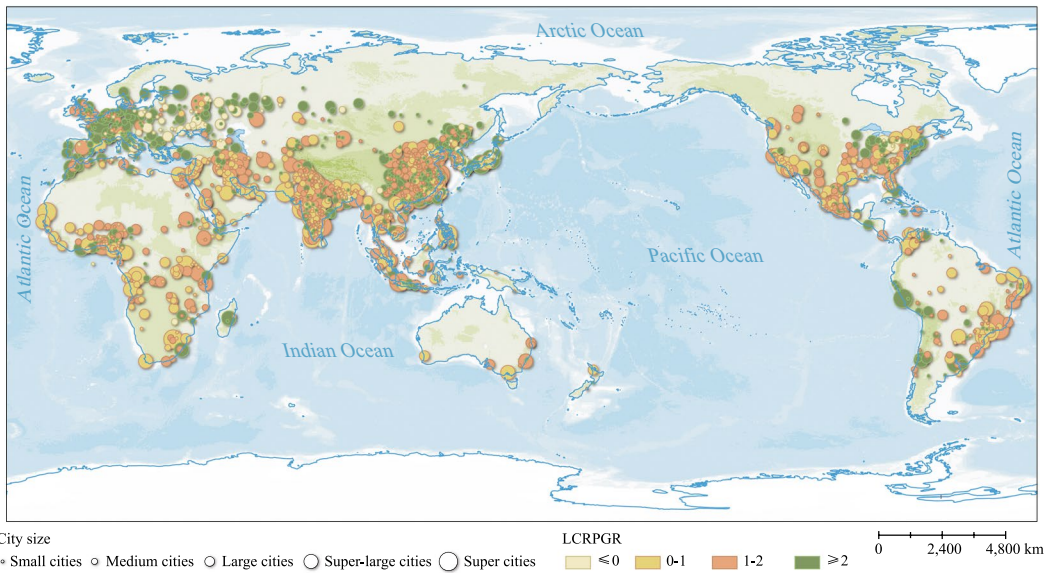


Fig. 5.3 Change in the LCRPGR indicator of global cities from 2000 to 2020

5.3.2 Changes in Global Nighttime Light Intensity

Target: SDG 11.3: By 2030, enhance inclusive and sustainable urbanization and capacity for participatory, integrated, and sustainable human settlement planning and management in all countries.

5.3.2.1 Background

Reasonable utilization of urban land resources supports the Urban Sustainable Development Goals (Wu et al. 2011) and affects biodiversity and ecosystem services (Estoque and Murayama 2016; McDonald et al. 2020). The pre-conditions of assessing land use efficiency are to measure the urbanization rate and quantify urban land use. Traditionally, most of the indicators used to measure the urbanization rate are derived from statistical data, which always have a fixed spatiotemporal scale and low update frequency. The DMSP-OLS and NPP-VIIRS NTL data have been an alternative proxy, but they are incomparable since their sensor designation and data quality are different. Consequently, they cannot be directly adopted to assess long-term land use efficiency. Moreover, diverse urban

functions usually require various spatial combinations of land cover. Thus, the spatial combination of land cover should be taken into account when assessing land use efficiency aside from the traditional indicators of land cover (e.g., patch count and area).

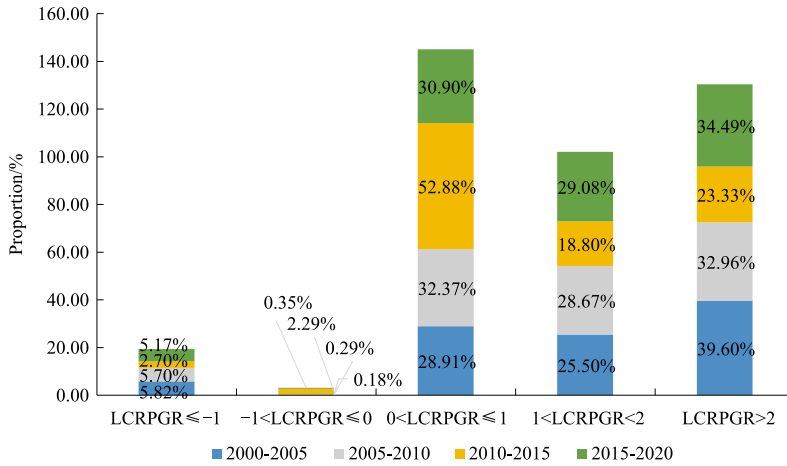
5.3.2.2 Data

- DMSP-OLS NTL annual composited data (2000–2013).
- NPP-VIIRS NTL monthly composited data (January 2012–December 2021).
- GlobeLand30 land cover dataset (2010 and 2020).

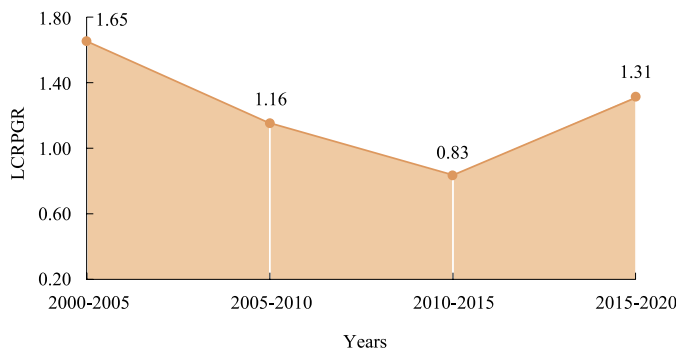
5.3.2.3 Methods

1. **Construction of an extended time series (2000–2021) of global “NPP-VIIRS-like” NTL data**

The median value of NPP-VIIRS NTL monthly composited data from 2012 to 2021 was calculated year by year to composite the NPP-VIIRS annual data. Based on DMSP-OLS NTL data and NPP-VIIRS NTL data from 2012 and 2013, the relationship between the two datasets was



(a) The proportion of cities with different levels of LCRPGR from 2000 to 2020



(b) The change in LCRPGR in the world's typical cities in 5 periods from 2000 to 2020

Fig. 5.4 LCRPGR in the world from 2000 to 2020

simulated based on an improved auto-encoder model, and then the DMSP-OLS NTL data from 2000 to 2012 were corrected into “NPP-VIIRS-like” NTL data based on the simulated relationship. Because 2000–2012 “NPP-VIIRS-like” NTL data have the same quality as 2013–2021 NPP-VIIRS NTL data, these two datasets can be directly combined into an extended time-series (2000–2021) NTL dataset (Chen et al. 2021).

2. Extraction of Land Cover Characteristic Information

Two types of land cover characteristic information were set up in this case study, including (1) the traditional indicators of land cover, mainly

including the area and number of land cover patches; and (2) the spatial combinations of land cover based on the adjacent times between any two land covers (Barnsley and Barr 1996).

3. Evaluation of Land Use Efficiency Considering the Combined Spatial Characteristics of Land Cover

Parcels in Fuzhou, China, were taken as research units. The total intensity of night light was counted parcel by parcel as an indicator reflecting the urbanization level, that is, the dependent variable. The area and number of land cover patches, as well as the spatial combination of land cover extracted parcel by parcel, were used

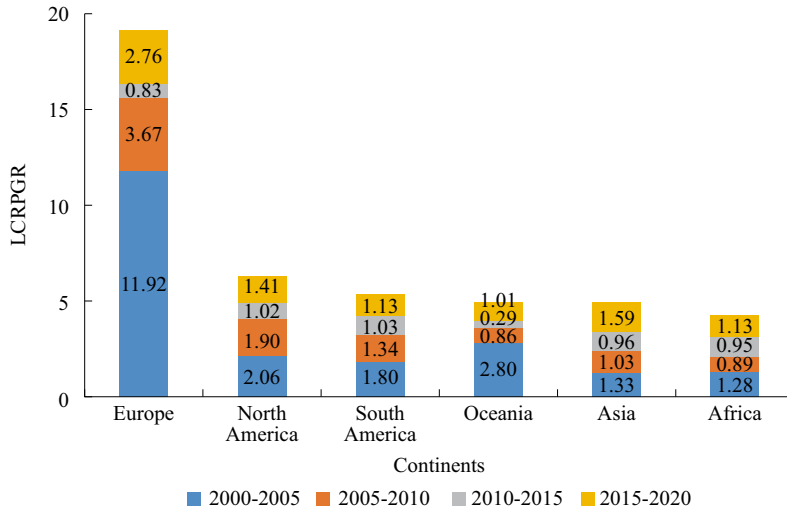


Fig. 5.5 Change in the LCRPGR indicator on each continent around the world from 2000 to 2020

as independent variables. The eXtreme Gradient Boosting (XGBoost) model was adopted to evaluate whether the spatial combination of land cover can better explain the urbanization level.

5.3.2.4 Results and Analysis

The high NTL intensities were clustered in the region from 20°N to 45°N, while those with lower values were located in the Southern Hemisphere (Fig. 5.6). The region from 30°N to 45°N had no significant change in the NTL intensity during the 2000–2010 period, but saw a great enhancement after 2010. For the region from 15°N to 30°N, the NTL intensity increased from 2000 to 2015, which was mostly caused by China’s development. In the longitudinal direction, one of the NTL intensity peaks within the Western Hemisphere was mostly located in the United States (from 70°W to 100°W). In the Eastern Hemisphere, there were three significant peaks in Europe, the Middle East, and China (from west to east). In addition, on the urban scale, the extended time-series NTL dataset in this case can provide more detailed information for the assessment of urbanization, including the identification of road networks and urban spatial structures.

The global economy showed an orderly growth amid a volatile trend during 2000–2021 (Fig. 5.7). In the periods 2009–2011 and 2020–2021, the global economy experienced temporary downturns due to the global Great Recession and the COVID-19 pandemic. At the national scale, China was affected by the global Great Recession but with low impacts, and is still in the stage of robust development; the United States, Italy, Australia, and other countries were greatly affected, and the NTL intensity decreased significantly; Brazil, South Africa, and other countries were slightly affected by the crisis and entered a stage of rapid development afterward.

To quantify whether the spatial combination of land cover will affect land use efficiency, the above explanatory variables were combined into six variable sets in this case study, as shown in Table 5.2. The results show that the XGBoost model has the highest R^2 in both 2010 and 2020, when the spatial combination of land cover was added, which proves that the spatial combination of land cover is an important factor for the evaluation of land use efficiency.

Based on the SHapley Additive exPlanations (SHAP) values in Fig. 5.8, we found that the

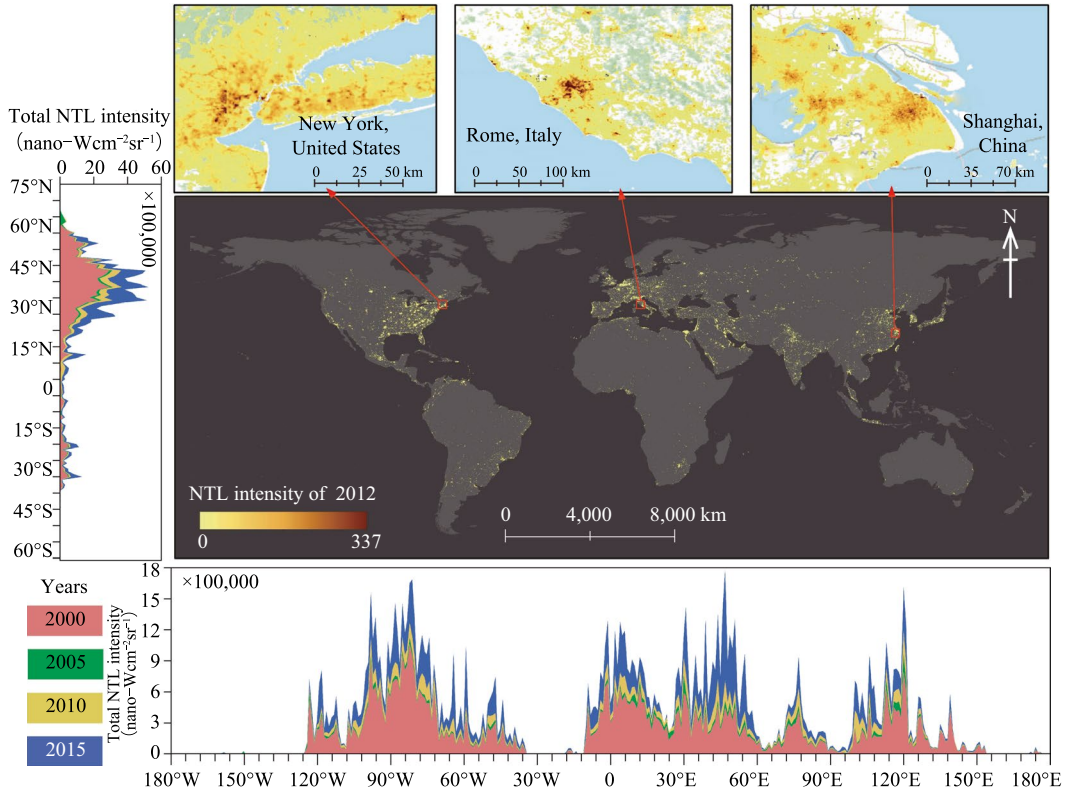


Fig. 5.6 Distribution of the intensity of “NPP-VIIRS-like” NTL data

spatial combination of land cover had significant effects on NTL intensity, as well as the traditional indicators of land cover. In 2010, the area of artificial surface (AS-a), the area of cultivated land (CL-a), the spatial combination between artificial surface and bare land (AS-B), the area of forest (F-a), the area of bare land (B-a), the spatial combination between water body and artificial surface (WB-AS), the patch count of cultivated land (CL-c), the spatial combination between cultivated land and forest (CL-F), and the patch count of ice (I-c) had the highest impacts on NTL intensity, while AS-a, CL-a, the area of water body (WB-a), the patch count of artificial surface (AS-c), F-a, WB-AS, the spatial combination between forest and bare land (F-B), the spatial combination between cultivated land and bare land (CL-AS), and the spatial combination between cultivated land and grassland

(CL-G) had the highest impacts on NTL intensity in 2020. Generally, the spatial combination of land cover associated with artificial surfaces and non-artificial surfaces can differently affect the NTL intensity.

The spatial combination of land cover associated with an artificial surface is the largest contributor to NTL intensity. For example, in 2020, the spatial combination between water bodies and artificial surfaces (WB-AS) had an increasing contribution (Fig. 5.9). The Min River and Wulong River are the two most important water bodies in Fuzhou, with many settlements and commercial activities concentrated near the two rivers. Meanwhile, the contribution of the spatial combination between grassland and artificial surfaces (G-AS) in residential and industrial areas is positive, while in the mountainous and hilly areas, the contribution changes to negative (Fig. 5.9).

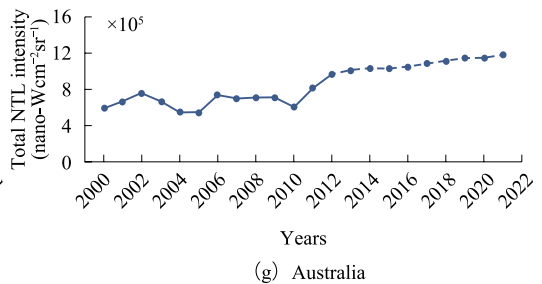
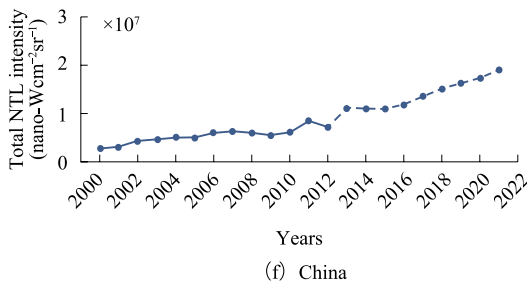
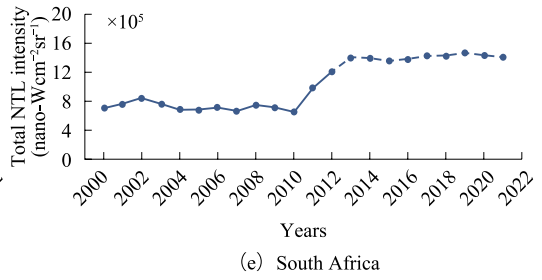
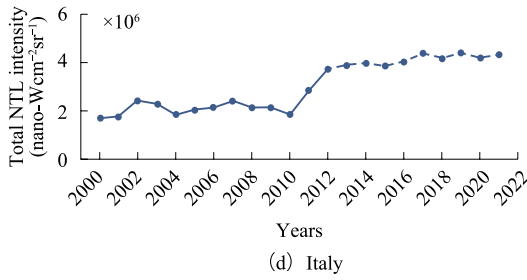
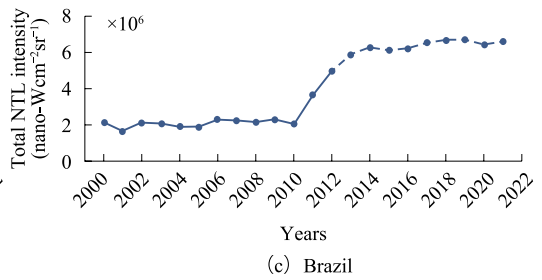
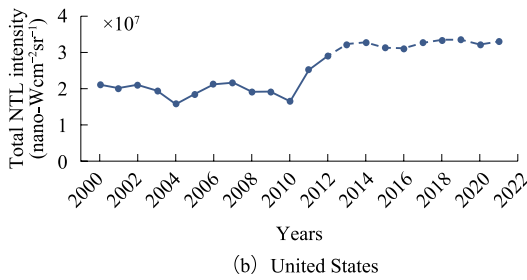
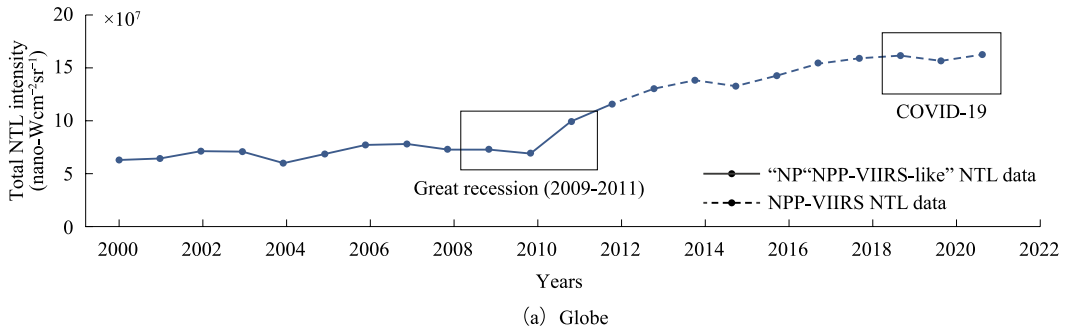


Fig. 5.7 Variation of the total NTL intensity globally and in six representative countries during 2000–2021

The spatial combination between forests and artificial surfaces (F-AS) has a “U-shape” contribution to NTL intensity (Fig. 5.10). The low contributions were concentrated in rural areas, while the high contributions were mostly located in urban areas. These results imply that since urban

greening can improve air quality and living conditions, more human activity will be attracted.

The spatial combination of land cover associated with non-artificial surfaces has negative effects on the NTL intensity. For example, the spatial combination between cropland and

Table 5.2 Evaluation accuracy of land use efficiency

Indicators	Model 1	Model 2	Model 3	Model 4	Model 5	Model 6
Land cover	C	A	SC	C+SC	A+SC	C+A+SC
R^2 (2010) (%)	63.4	69.1	67.0	74.9	77.5	82.4
R^2 (2020) (%)	71.8	83.9	79.6	85.1	91.0	98.1

Note C represents the number of land cover patches in each parcel, A represents the area of land cover in each parcel, and SC represents the spatial combination of land cover in each parcel

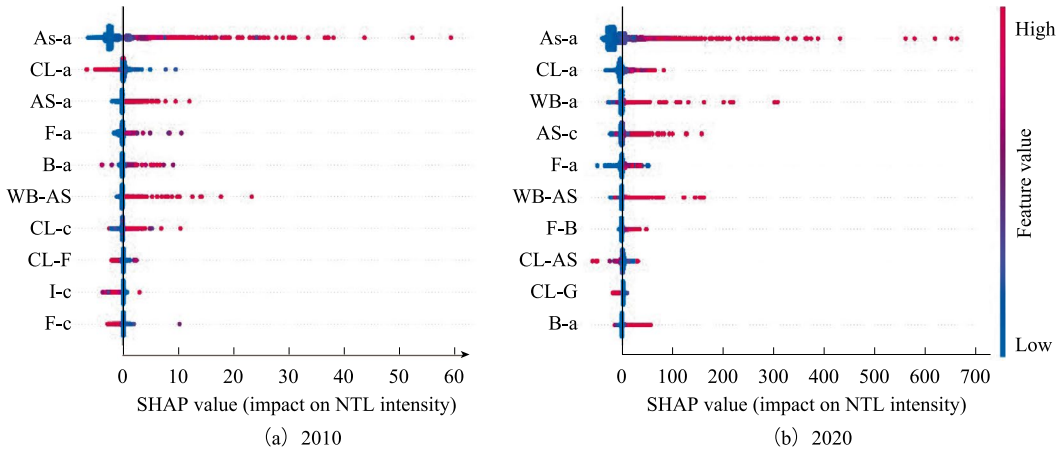


Fig. 5.8 SHAP value of Model 6 in 2010 and 2020

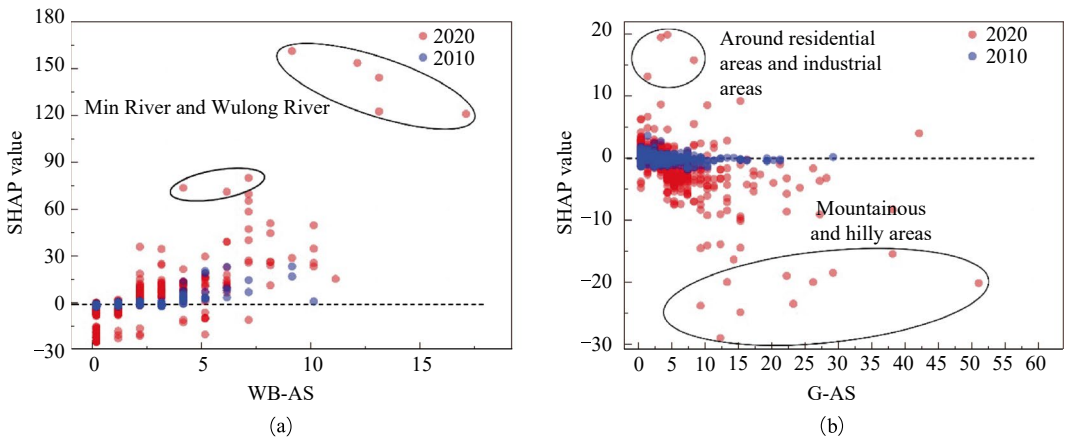


Fig. 5.9 SHAP value of WB-AS and G-AS in 2010 and 2020

grassland (CL-G) had low contributions to NTL intensity since its SHAP value was equal to 0 in 2010. But in 2020, the SHAP value had a sharp decrease to a negative value (Fig. 5.11). During

the ten years, the population and urbanization rates in Fuzhou were increasing, as well as the interactions within Fuzhou City. Sequentially, the non-artificial surfaces became sensitive to

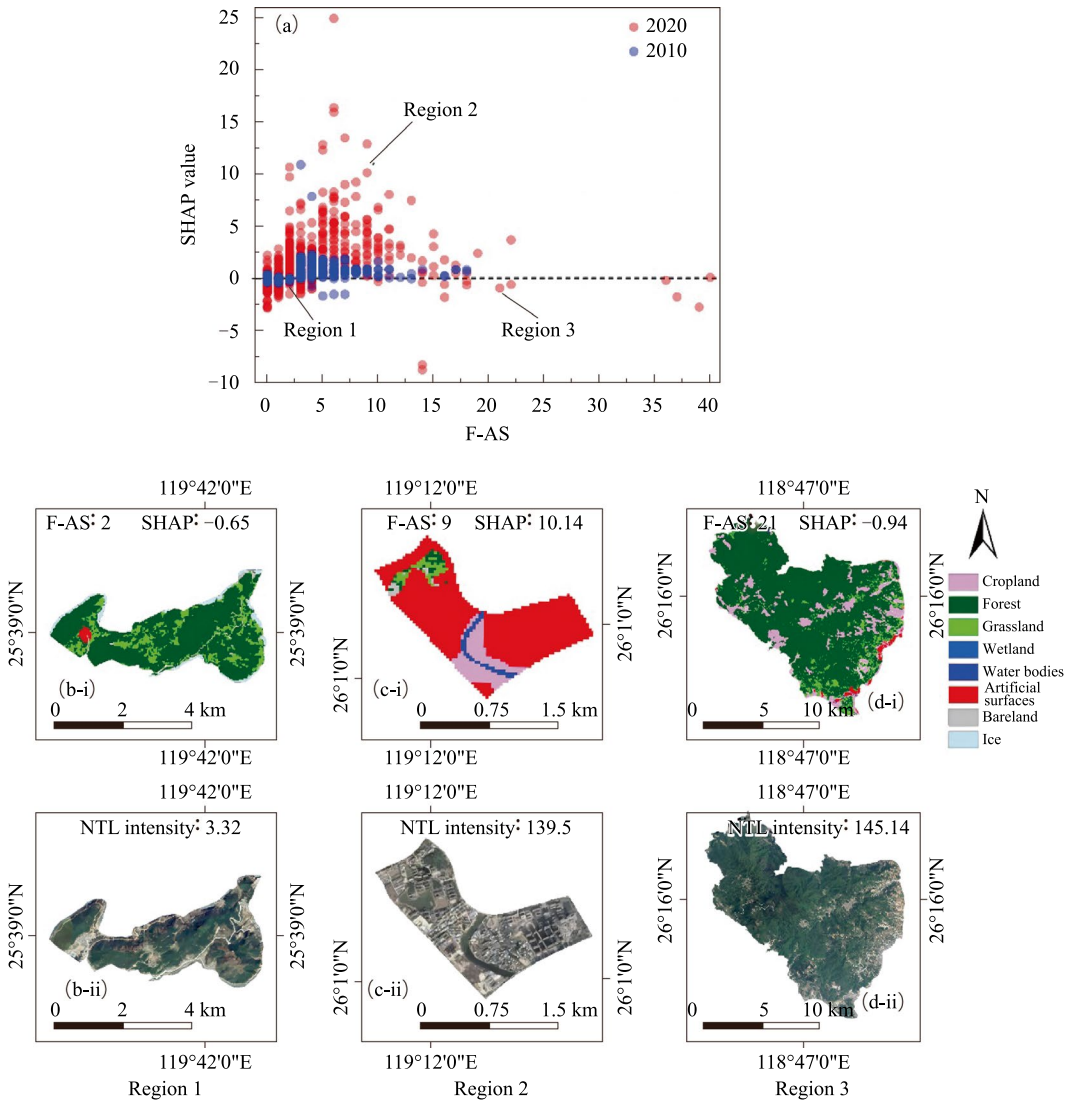


Fig. 5.10 SHAP value of F-AS in 2010 and 2020

NTL. In addition, a region with high CL-G means that there is dense vegetation, which means it is difficult to concentrate a human population in the region.

5.3.2.5 Highlights

- A global “NPP-VIIRS-like” NTL annual composited dataset was produced.
- Expanding the perspective of SDG 11.3.1, the spatial combinations of land cover indeed

have an effect on the urbanization process and must be taken into account when measuring land use efficiency.

5.3.2.6 Discussion and Outlook

The global “NPP-VIIRS-like” NTL remote sensing datasets from 2000 to 2021 were generated based on the widely used DMSP-OLS and NPP-VIIRS NTL data. The new NTL dataset has a strong capacity to reveal economic change at different spatial scales. We proved that the

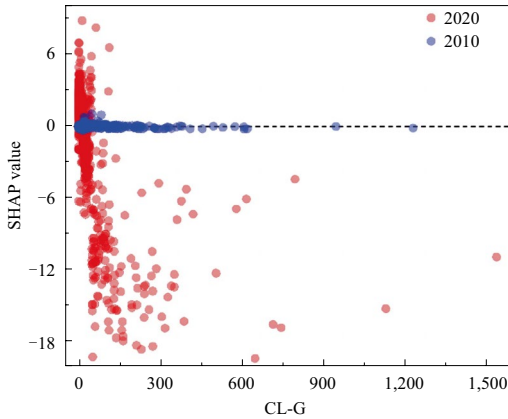


Fig. 5.11 SHAP value of CL-G in 2010 and 2020

spatial combination of land cover can effectively improve the accuracy of evaluation in land use efficiency. In the future, to further support sustainable urban development, we will explore and discuss the degree of contribution that different spatial combinations of land cover make to NTL intensity, so as to quantify land use efficiency.

5.3.3 Ratio of Global Land Consumption and Population Growth Under Future Scenarios

Target: SDG 11.3: By 2030, enhance inclusive and sustainable urbanization and capacity for participatory, integrated, and sustainable human settlement planning and management in all countries.

5.3.3.1 Background

According to the 2018 Revision of World Urbanization Prospects, the global urban population has increased rapidly from 750 million in 1950 to 4.46 billion in 2021 (Lu et al. 2015; Sanchez Rodriguez et al. 2018). The world's urban population is anticipated to reach approximately 7 billion by the mid-twenty-first century (2050), with developing countries in Africa and Southeast Asia as the main engines for future population growth (Burke et al. 2021). The swift increase in the urban population has resulted in

the rapid expansion of global urban areas, leading to various ecological and environmental challenges for urban infrastructure, ecological environments, and energy and emissions. Hence, comprehending the regional discrepancies in urban land and population growth in the future holds great practical significance in evaluating potential risks faced by urbanization in different countries and regions and achieving sustainable urban development.

Predicting future urban land dynamics is predominantly implemented using the cellular automata (CA) models. However, existing studies have limitations in the temporal context of urban evolution, and the spatial resolution of global studies is relatively coarse. Consequently, significant uncertainties exist in future urban land projections concerning development trends and spatial details (Li and Gong 2016). Advancements in remote sensing technology enable the acquisition of long-term urban evolution information through Earth observation data, providing continuous observations for modeling future urban evolution, which is essential for accurately identifying hotspots in rapidly developing urban areas. This study aims to use global urban extent dynamics obtained from long-term remote sensing data to quantitatively assess the internal linkage between urban area expansion and socioeconomic development, to model the global urban land use dynamics under five future SSPs, and further to support the analysis of changes in the growth rates of global urban land area and population.

5.3.3.2 Data

- Global annual urban extent time-series data derived from NTL (1992–2013).
- Historical and future socioeconomic (i.e., population and GDP) time-series data derived from the World Bank Databases (<http://data-bank.worldbank.org/>) and the International Institute for Applied Systems Analysis (IIASA) (<https://tntcat.iiasa.ac.at/SspDb/>), respectively.
- Global spatial proxies, including road networks, terrain, and land cover.

5.3.3.3 Methods

In our study, we employed the sigmoid model to characterize the distinct spatial differences in per capita urban areas among various countries or regions driven by varying levels of socioeconomic development. We projected future urban areas and analyzed spatial evolution in different countries and regions by combining population growth and GDP development projections (Li et al. 2019; Li et al. 2020). Population distribution data across different administrative units were obtained, and we calculated the global population growth rates for different SSPs at 1 km resolution between 2020 and 2100. We modeled the global urban land use maps for different SSPs using the following equations. Next, we analyzed the rate difference between population growth and urbanization, using quantitative land use efficiency in different regions under different scenarios. Thus, sensitive regions with allometric growth rates were identified in our study:

$$PG_n = \frac{P_{2100} - P_{2020}}{P_{2020}}$$

$$UG_n = \frac{U_{2100} - U_{2020}}{U_{2020}},$$

where PG_n represents the population growth rate of the n -th country or region from 2020 to 2100; UG_n represents the urban land growth rate of the n -th country or region from 2020 to 2100; P_{2020} represents the population of the country or region in 2020; P_{2100} represents the population of the country or region in 2100; U_{2020} represents the urban area of the country or region in 2020; and U_{2100} represents the urban area of the country or region in 2100.

5.3.3.4 Results and Analysis

1. Global urban growth patterns under various future SSPs

From a global perspective, the differences in global urban areas under various scenarios before 2050 are insignificant. However, the differences in global urban areas from 2050 to 2100 under different scenarios gradually become

more significant. They can be characterized by three primary trends: rapid urban area growth under the fossil-fueled development (SSP5) scenario, moderate urban area growth under the sustainability (SSP1) and the middle of the road (SSP2) scenarios, and slow urban area growth under the regional rivalry (SSP3) and the inequality (SSP4) scenarios (as illustrated in Fig. 5.12). Overall, the trends in our results are generally consistent with other relevant studies (Gao and O'Neill 2020; Chen et al. 2020). However, there are still some deviations in specific scenarios and regions. For instance, the study by Gao et al. (2020) did not consider the heterogeneous characteristics of urban growth rates at different stages due to the lack of long-term temporal data on urban extent obtained from remote sensing data. Consequently, their results show relatively large urban growth increments that differ from observations obtained from satellite observations in some regions (such as the United States) under multiple SSPs. With the benefit of remotely derived long-term urban land use data, the differences and changes in urban sprawl rates at different stages in our results are more consistent with the historical temporal changes.

In this case, further comparative analysis focuses on SSP4, SSP2, and SSP5 scenarios. In the SSP4 scenario, the urban areas expand significantly in regions such as India and Africa. In the SSP2 scenario, the trend of urban expansion in 2100 generally aligns with historical extrapolation, with conventional urban increments in China, the United States, Europe, and Africa. Population and GDP will increase significantly in the rapidly developing SSP5 scenario, leading to much higher urban increments in developed countries by 2100. Additionally, regions with significant population growth, such as Nigeria, are characterized by significant urban expansion. The spatial evolution of urban areas at a resolution of 0.5° in China shows that due to China's population peak in 2030, the spatial distribution differences in urban areas in 2100 are not very pronounced. The future scenario development in these typical regions is consistent with the UN World Urbanization Prospects

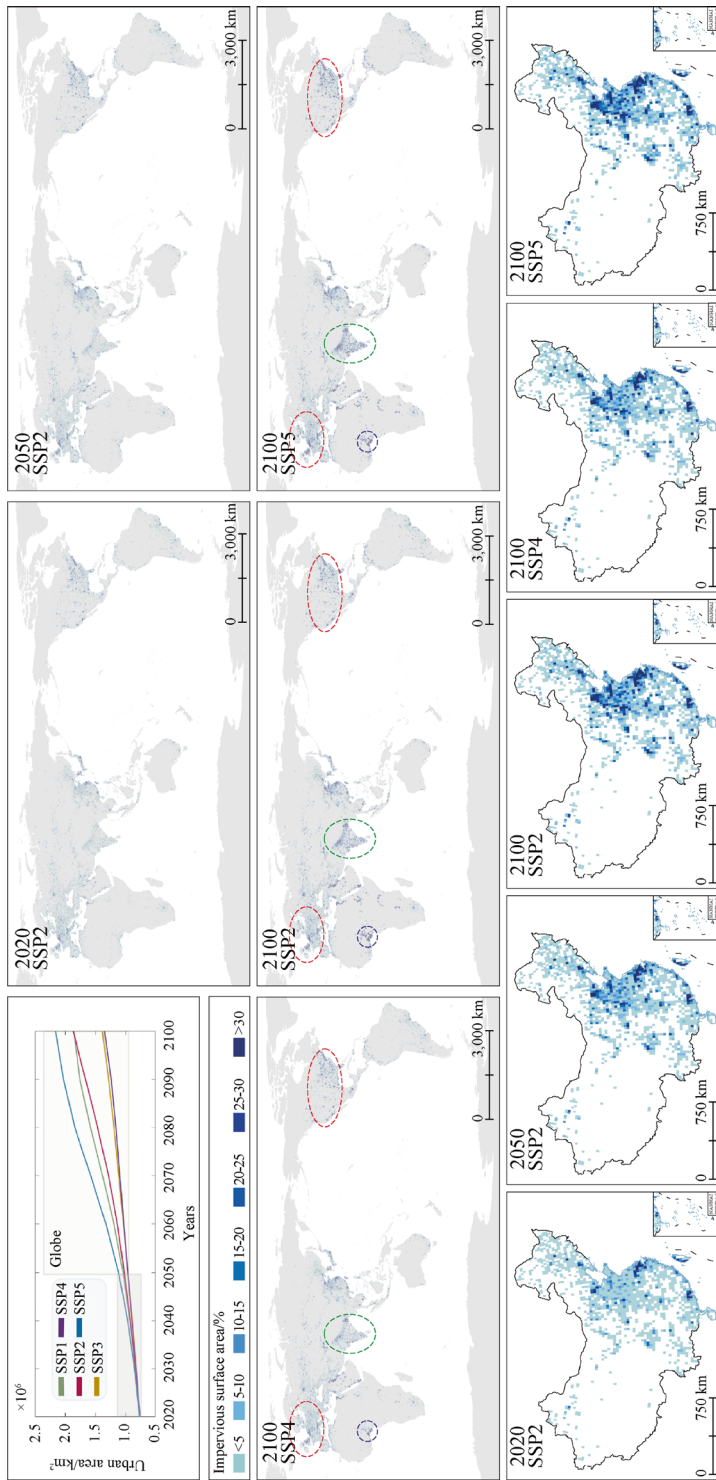


Fig. 5.12 Spatial distribution of urban land in different countries and regions under different future SSPs

(UN 2019b). In other words, the primary engines of future urbanization are mainly concentrated in developing countries/regions in Asia, Africa, and South America.

2. Global land consumption and population growth rates in different regions under different SSPs

In 2100, global urban growth and population growth under different SSP scenarios exhibit significant spatial heterogeneity (Fig. 5.13). Considering that urban land is generally difficult to transform into non-urban land due to population or GDP decline, the global urban growth rate is generally non-negative. However, due to negative population growth expected in some regions in the future, global population growth shows pronounced regional disparities. Taking Europe and Africa as examples, urban and population growth vary significantly under different scenarios. In South-South countries, mainly India and those in Africa, urban land growth is significantly higher than population growth. Overall, at the global scale, the urbanization of land is much greater than population urbanization. This trend is also relatively consistent with high-resolution global urban dynamic data obtained from remote sensing (Liu et al. 2020), indicating the need for a more sustainable approach to global urban expansion.

3. Differences in global land consumption and population growth in different regions under different SSPs

Overall, in 2100, urban growth rates under different SSP scenarios were higher than population growth rates, with many countries experiencing negative population growth (Fig. 5.14). In the SSP4 scenario, urban land changes relatively little with changes in population and GDP, resulting in smaller differences between urban and population growth rates than in other scenarios. Typical developing countries like China and India exhibit different trends

in urban area and population growth: China is expected to peak in 2030 and gradually decline, while urban areas show some increase due to an increase in per capita urban land with urban development. India's population is expected to continue rising into the mid-twenty-first century, with a relatively pronounced increase in the urban land increment (Fig. 5.14). Compared to population changes, estimates of urban land increment, which incorporate urban growth time-series data, to some extent consider the stage characteristics of per capita urban land with socioeconomic development (Li et al. 2019).

5.3.3.5 Highlights

- We comprehensively explored the temporal contexts of long-term and annual urban extent dynamics, based on which the urban area growth model was developed, and the urban sprawl model was adopted. We also provided spatially explicit maps for global urban extent from 2020 to 2100 at 1 km resolution, freely available for download.
- We analyzed the difference between the urbanization rate and population growth. Thus, sensitive areas with accelerated growth can be identified, which helps support future sustainable development and decision-making.

5.3.3.6 Discussion and Outlook

This study highlights the importance of using remote sensing data to better understand urbanization patterns and trends and the need for more accurate and reliable data to inform urban planning and policymaking. This study also emphasizes the importance of considering different scenarios and their potential impacts on urban growth, population growth, and land consumption to better prepare for future challenges and opportunities. By incorporating a range of socioeconomic factors and spatially explicit data, this study provides valuable insights into the complex dynamics of urbanization and its impacts on society, economy, and environment.

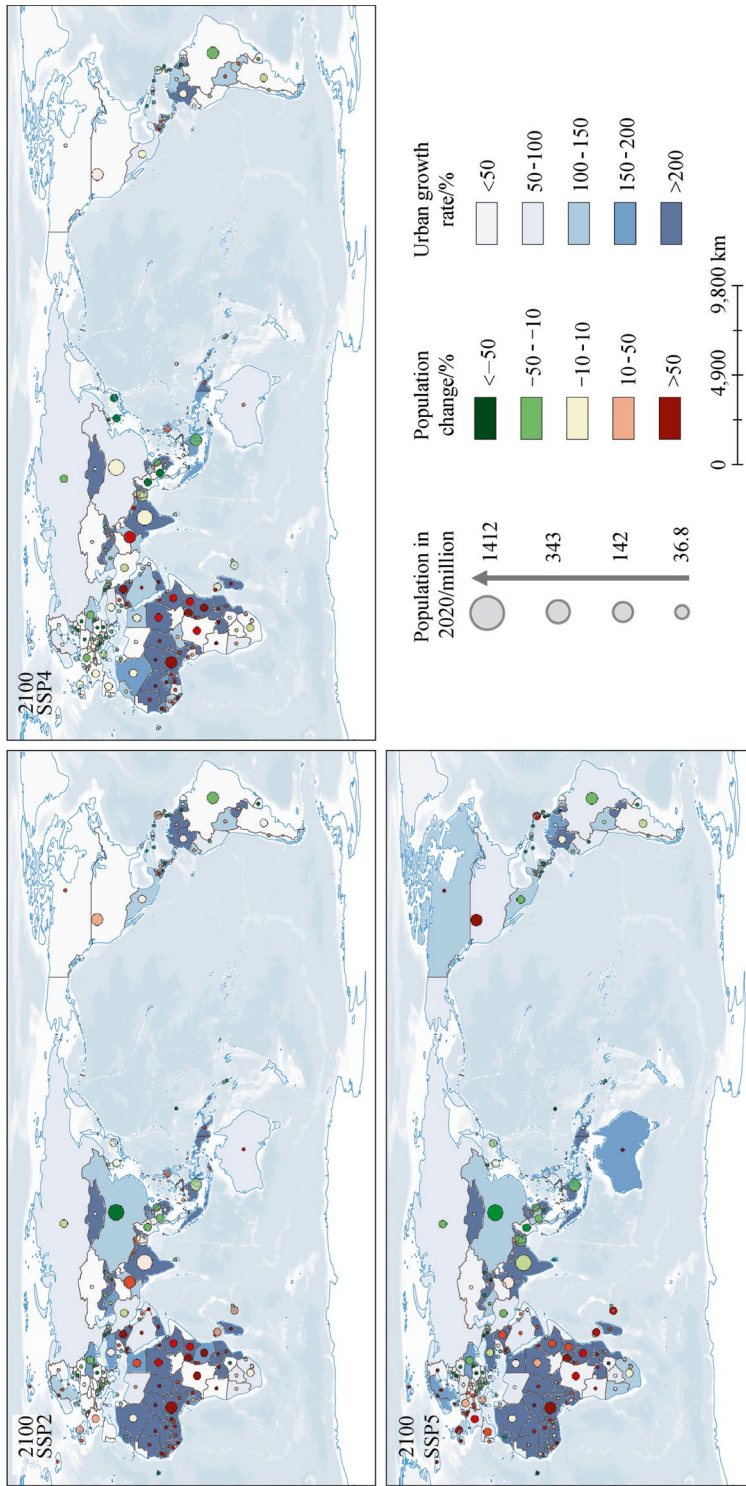


Fig. 5.13 Spatial patterns and distributions of global urban expansion and population growth in different regions under different SSPs

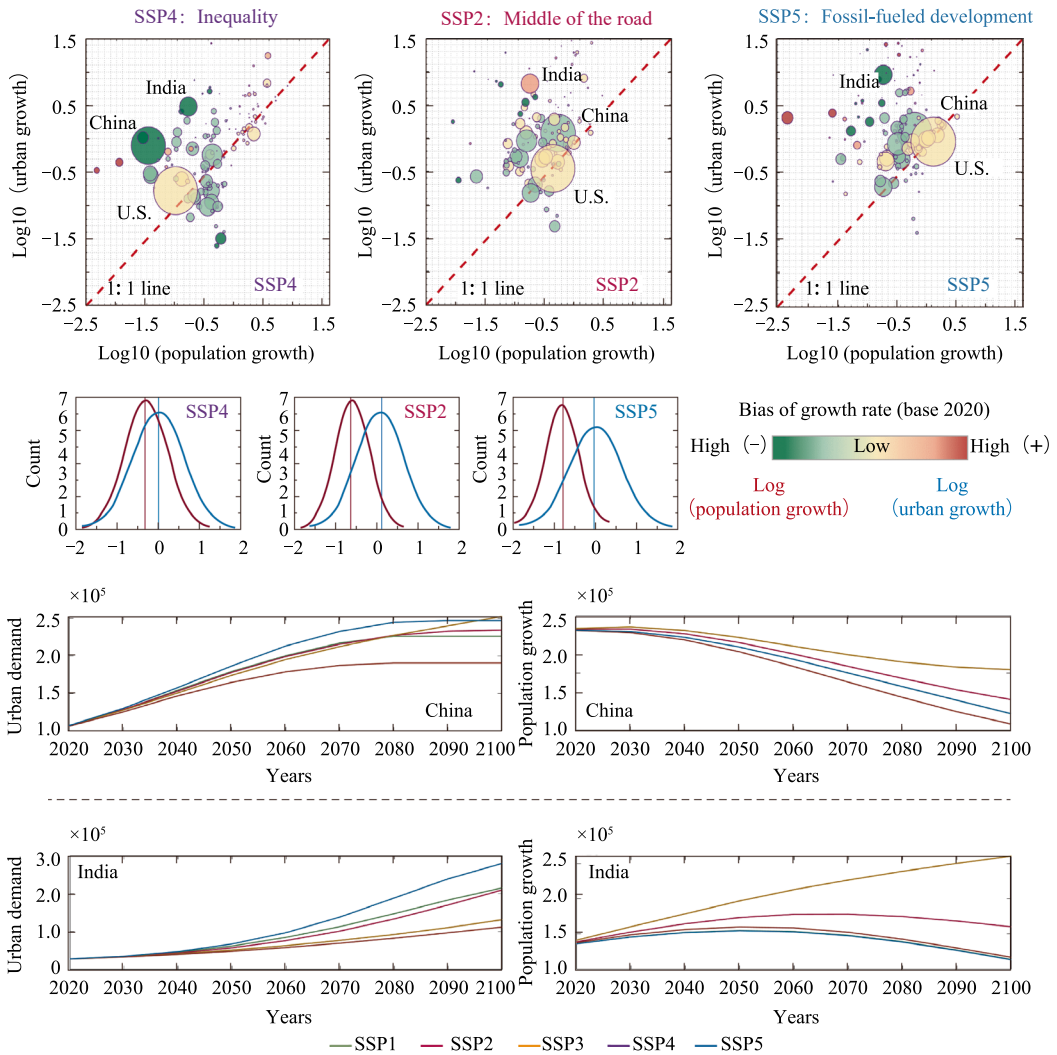


Fig. 5.14 Deviation of global land consumption and population growth under different SSPs

5.3.4 Land Cover Change Monitoring of Global World Cultural Heritage Sites

Target: SDG 11.4: Strengthen efforts to protect and safeguard the world’s cultural and natural heritage.

5.3.4.1 Background

World Cultural Heritage is commonly acknowledged to be of great significance and outstanding universal value, and therefore effective risk

management and assessment are extremely important. SDG 11.4 belonged to Tier III when initially proposed, which means it had no supporting indicators and corresponding evaluation methods. It now belongs to Tier II (i.e., insufficient data and imperfect methods) after re-evaluation in 2019 (UN 2019a). From the survey data in 2020, less than 60% of all countries worldwide were able to acquire relevant statistical indicators (UN Statistics Division 2021). Only one indicator, 11.4.1, is related to SDG 11.4, which is over-simplified and not effective in achieving

the protection and evaluation of cultural heritage (Nocca 2017). Other quantitative indicators are urgently required to quantify the preservation status of heritage sites (Tang et al. 2022).

In recent years, the fast development of cities, the rapid growth of population, and great changes in climate and environment have interfered with cultural heritage sites (Ashrafi et al. 2021). According to the principles of authenticity and integrity for World Heritage protection, the impacts caused by both natural and anthropogenic factors need to be quantitatively evaluated for the timely discovery of potential threats to the sites. This case study proposed a method to monitor land cover change and an indicator to measure SDGs in the protected areas of cultural heritage sites. A dataset of heritage boundary and land cover change for global World Cultural Heritage from 2015 to 2020 was produced in this case study to provide first-hand scientific data for achieving SDG 11.4. The relationship between the SDG indicators related to land cover change and the per capita GDP of host countries was further studied to reveal the importance of capital investment reflected by social development to the sustainable development of cultural heritage.

5.3.4.2 Data

- The heritage boundary data of the global World Cultural Heritage sites at heritage areas and buffer zones.
- High-resolution Google Earth images with a sub-meter spatial resolution in 2015 and 2020.
- Population and GDP data provided by Population Dynamics, Department of Economic and Social Affairs of the UN in 2015 and 2020, which can be acquired from <https://data.un.org/en/index.html>.

5.3.4.3 Methods

First, according to the map of the United Nations Educational, Scientific and Cultural Organization (UNESCO) World Heritage Centre, the heritage areas and buffer zones of

heritage sites were manually drawn to produce the vector boundary data of World Cultural Heritage, with an overall error of less than 15%. Based on high-resolution Google Earth images in 2015 and 2020, object-based analysis and the ResNet-50 deep learning method (He et al. 2016) were used to extract the land cover change within the protected areas. The extraction results were checked and corrected in high-resolution images to ensure that the accuracy of the extracted changes was higher than 90%. The percentages of changed area in the heritage areas and buffer zones were calculated separately and defined as the land cover change ratio. The causes and trends of land cover change at each heritage site were analyzed, with a positive or negative evaluation value assigned. Positive changes represent the changes that are conducive to the development of heritage sites, such as the construction of heritage parks and museums, whereas negative changes represent changes that are unfavorable to the development of heritage sites, such as vegetation degradation, expansion of cultivated land, and urban development. The land cover change combined with the positive/negative evaluation was standardized to obtain an SDG indicator to measure the sustainable development of heritage sites. The per capita GDP values of countries and regions containing heritage sites were analyzed to reveal the impacts of the level social development on the sustainable development of cultural heritage sites, so as to provide first-hand scientific data and technical support for the protection of cultural heritage.

5.3.4.4 Results and Analysis

According to UNESCO and the World Heritage Centre (World Heritage Centre 2009), heritage areas have a strict protection status, where human intervention must be kept to a minimum. A buffer zone may set limits to protect heritage, but may also positively encourage the development of surrounding resources that would be beneficial to the site (UNESCO 2005). Therefore, the heritage area should include no change, and a low land cover change ratio

indicates good protection. The changes in the buffer zone should not be too much, and a high land cover change ratio means the site needs to be monitored and assessed in the long term.

Figure 5.15 shows the land cover change ratios in the heritage areas and buffer zones of the World Cultural Heritage sites for different countries, where the ratio is significantly higher in the buffer zone than that in the heritage area. The results are as follows. (1) In general, the land cover change in European countries was at very low (< 0.10%) and low levels (0.10%-0.50%) in the heritage areas, with some occasional uneven distribution. The land cover change in the buffer zones was generally below the intermediary level (0.50–1.00%), but a few countries showed a very high value (> 2.00%). Lithuania, for example, was affected by newly increased construction and the land cover change ratio in both heritage areas and buffer zones was at a very high level. (2) Most of the land cover changes in the heritage areas in Asian countries fell into very low to intermediary

levels, in which China was at the intermediary level, and the Philippines showed a very high value due to the construction of buildings and roads. The changes in the buffer zones were significantly different. Due to the dual influence of natural disasters and human activity, the land cover changes in some countries (e.g., Nepal) were at a very high level. As for China, the land cover change in the buffer zones was at a high level (1.00–2.00%) due to environmental management. (3) The land cover changes of heritage areas in most American countries were mostly from very low to intermediary levels, whereas the United States showed high changes (1.00–2.00%) due to the construction of museums. The changes in the buffer zones in North America were at a low level, and a few high values existed in Central and South America. For example, due to newly built roads, the changes in Panama were very high for both heritage areas and buffer zones. (4) The land cover changes in African countries were generally low in the heritage areas, with a few high

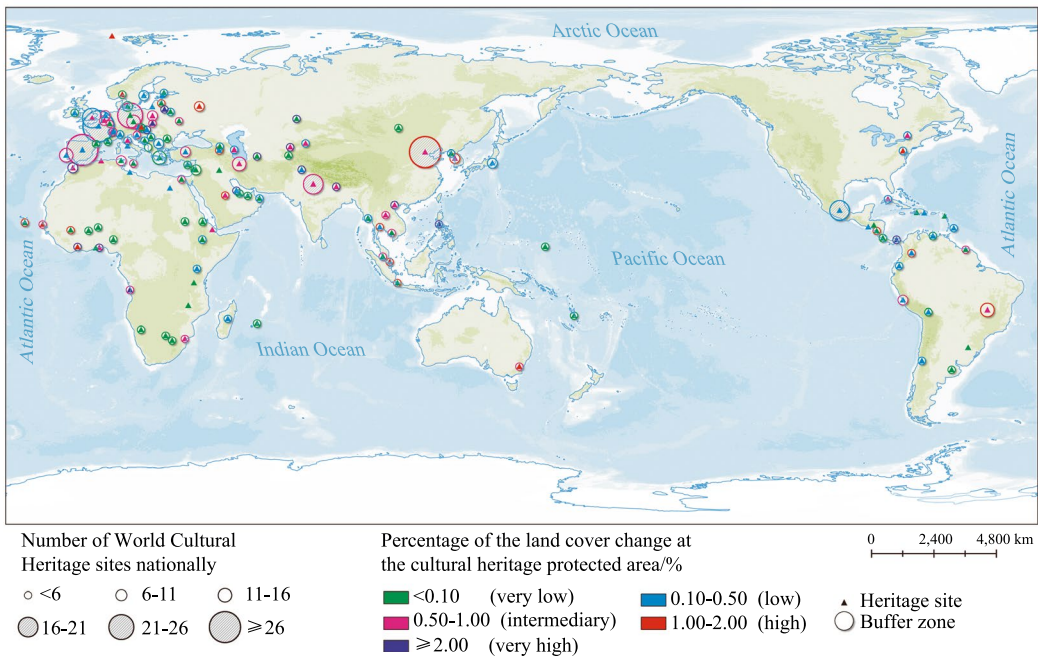


Fig. 5.15 Distribution of the land cover change ratios from 2015 to 2020 in the heritage areas and buffer zones of World Cultural Heritage sites

values, while Angola showed a very high value due to increased developed land. The land cover changes in the buffer zones were generally lower than the intermediary level, while a few high and very high levels are shown in West African countries.

Figures 5.16 and 5.17 show the relationship between SDG indicator measurement of

World Cultural Heritage sites and per capita GDP growth in each country and region of the world, respectively, from 2015 to 2020. SDG indicator values close to 1 indicate that the land cover change is suitable for the protection of heritage sites, while those close to -1 indicate otherwise. The results show that the SDG indicator measurements of most heritage

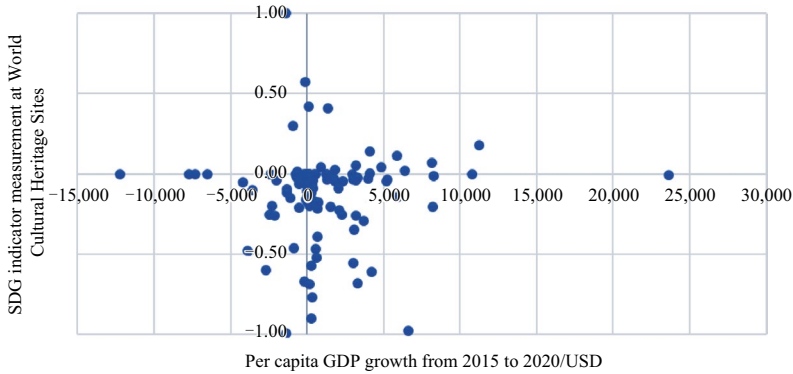


Fig. 5.16 Relationship between the SDG indicator measurement of World cultural heritage sites in each country and per capita GDP growth from 2015 to 2020

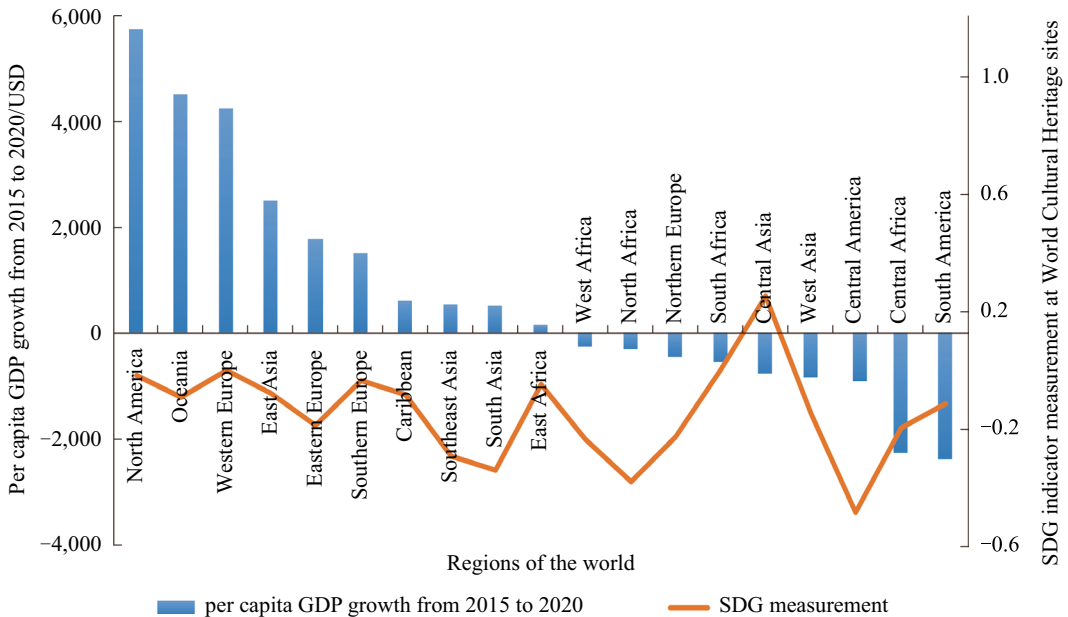


Fig. 5.17 Relationship between the SDG indicator measurement of World cultural heritage sites in each region of the world and per capita GDP growth from 2015 to 2020

sites were near zero, indicating that most countries maintained the principle of keeping human intervention to a minimum. In all these changes, the negative changes are more than the positive changes, indicating that conflict existed between the demands of construction and heritage protection. Countries with a negative SDG indicator measurement, most of which had slow or negative GDP growth, revealed the driving role of capital investment on the sustainable utilization of heritage. According to the SDG indicator measurement at the regional scale, Central Asia was the only region showing a positive value. In developing countries represented by China, the changes in heritage sites were mainly positive such as vacating residential areas, as well as constructing service facilities and museums. Developed countries, such as those in North America, Europe, and Oceania, did not have many changes. Only Southeast Asia resulted in a large negative value. In less developed countries with slow economic development, such as Central America and North Africa, the changes were mainly caused by newly built roads and buildings. These activities gave priority to local economic development, which had a negative effect on the protection of cultural heritage.

5.3.4.5 Highlights

- A new indicator was proposed to measure the sustainable development of cultural heritage. A dataset of heritage boundary and land cover change for global World Cultural Heritage from 2015 to 2020 was produced to solve the problems of insufficient data and imperfect indicators for SDG 11.4.
- The relationship between the land cover change of the World Cultural Heritage sites in each country and per capita GDP reveals that a correlation exists between the cultural heritage protection level and the social economic development level, and capital investment in the sites has promoted their sustainable utilization.

5.3.4.6 Discussion and Outlook

The proposed land cover change extraction method based on high-resolution remote sensing realized the elaborate monitoring of global World Cultural Heritage sites. SDG indicator measurement for cultural heritage can directly reflect the changes and trends of surface elements, thus providing data support from a single heritage site to the national level for achieving SDG 11.4. The efficient acquisition of Big Earth Data based on cloud platforms and intelligent deep learning technology provides feasible technical solutions to regularly monitor and quantitatively evaluate global cultural heritage.

Benefits from the development of Earth observation technology for high spatiotemporal remote sensing, annual monitoring, and SDG indicator assessment are suggested to update the land cover change of World Cultural Heritage sites, according to the specific requirements of cultural heritage authorities. The proposed method has provided the potential for timely control of the situation and future development trends for cultural heritage protection using spatial technology.

5.3.5 Multiscale Monitoring and Evaluation of Global Natural and Mixed World Heritage Site Boundary Areas

Target: SDG 11.4: strengthen efforts to protect and safeguard the world's cultural and natural heritage.

5.3.5.1 Background

SDG 11.4 includes one indicator, SDG 11.4.1, "total per capita expenditure on the preservation, protection and conservation of all cultural and natural heritage, by source of funding (public, private), type of heritage (cultural, natural) and level of government (national, regional, and local/municipal)." Prior to 2020, domestic and foreign research based on this indicator mostly remained at the theoretical stage and proposed various improvement methods. In the

SDG reports from 2020 (CBAS 2020) and 2021 (CBAS 2021), our research team proposed the human intervention degree (HID) index based on land cover data and its measurement method, and conducted a global measurement of Natural World Heritage sites to test the global applicability of the index, achieving global comparability of measurement results. Based on the continuous accumulation and verification of research results in recent years, the internal state of natural and mixed World Heritage site core areas was generally stable, while human intervention factors were mainly concentrated in the boundary areas. Therefore, in this case, we focused on the boundary areas within and outside the core areas of natural and mixed World Heritage sites, which are 2 km wide (a circular area with a width of 4 km), for multiscale and fine monitoring and evaluation.

5.3.5.2 Data

- The 2021 version of the global natural and mixed World Heritage site boundary vector and attribute data was produced based on the World Database on Protected Areas (WDPA) dataset and the official website of UNESCO World Heritage Centre (<http://whc.unesco.org/>) in the Big Earth Data Science Project.
- The GlobeLand30 dataset for global land cover in 2010 and 2020 was created and released by the Ministry of Natural Resources of the People's Republic of China (<http://www.globallandcover.com/>).
- The land cover datasets for land cover classification in 2017 and 2021 from ESA were produced by Esri using a deep learning model and 10 m Sentinel-2 images.
- High-resolution historical image data was obtained from Google Earth.

5.3.5.3 Methods

The monitoring, analysis, and evaluation of global natural and mixed World Heritage site boundary areas were conducted at three resolutions: 30, 10 and 2m. The 30 m monitoring utilized the GlobeLand30 land cover data, which

covers 173 natural and mixed World Heritage sites worldwide, with a coverage rate of 71.8%.

First, the ratio of land cover change (LC) of the natural and mixed World Heritage site boundary areas was calculated, which can be expressed as:

$$LC = \left(\frac{\sum_{i=1}^n \Delta LU_{i-j}}{2 \sum_{i=1}^n LU_i} \right) \times 100\%,$$

where LU_i is the area of land use type i at the beginning of the monitoring period and ΔLU_{i-j} is the absolute value of the area where land use type i was converted to a non- i land use type during the monitoring period.

Second, based on the monitoring results of the natural and mixed World Heritage site land cover elements, the HID (Wang et al. 2022) and BA-HID of the natural and mixed World Heritage sites were calculated. The model for BA-HID can be expressed as:

$$BA - HID = \frac{a_1 x_1 + a_2 x_2 + \dots + a_i x_i}{x} \times 100\%,$$

where x is the sum of the boundary area of the core areas of the natural and mixed World Heritage site; x_i is the area of the type i intervention element within the boundary area; a_i represents the weight of intervention elements such as cultivated land or artificial facilities on the degree of intervention in the natural and mixed World Heritage site (referred to as type weight), with the determined type weights for cultivated land and artificial facilities being 0.4 and 0.6, respectively, in this case.

Finally, based mainly on the LC in the boundary area, the results of HID in the natural and mixed World Heritage site and the boundary area (BA-HID) were comprehensively ranked, determining the natural and mixed World Heritage sites with significant changes in land cover in the boundary area for fine monitoring at scales of 10 and 2m.

For 10 m monitoring, Esri's Land Cover datasets were utilized to calculate the ratio of land cover change of a certain type (LC_i) in the boundary area of the natural and mixed World Heritage sites:

$$LC_x = \frac{\Delta LU_x}{LU} \times 100\%,$$

where LU represents the total area of the natural and mixed World Heritage sites; and ΔLU_x is the difference in area of a particular land use type between the end and beginning of the monitoring period. Based on the calculation results and high-resolution image data, natural and mixed World Heritage sites with relatively significant land cover changes were selected for fine characterization at a resolution of 2 m.

For 2 m monitoring, high-resolution historical image data from Google Earth was utilized, and the object-based image analysis (OBIA) method (Tang et al. 2022) was employed. First, an unsupervised image segmentation method was used to extract potential change objects, and then a supervised machine learning method was used to refine the classification of the segmentation results among several models (random forest, decision tree, nearest neighbors, SVM classifier, XGBoost), choosing the most effective one to obtain information about land cover changes.

5.3.5.4 Results and Analysis

The natural and mixed World Heritage sites were numbered according to the comprehensive ranking results of LC in the boundary areas, HID, and the BA-HID in the dynamic change map from 2010 to 2020 (Fig. 5.18). The results show that the changes in the BA-HID values of natural and mixed World Heritage sites globally remained relatively stable from 2010 to 2020 (maintained within $\pm 4\%$), and the trend of the three indicators remained consistent. However, BA-HID was generally higher than that of the overall natural and mixed World Heritage sites, indicating the need for targeted monitoring of the boundary area.

The BA-HID values of natural and mixed World Heritage sites were generally within 1%, and the LC values were generally within 10%, indicating an overall good condition. However, a small number of natural and mixed World Heritage sites were strongly affected by human intervention, and their land cover changes were also substantial. These natural and mixed World

Heritage sites should be given extra attention in the future.

The top 20 natural and mixed World Heritage sites with the largest changes in their boundary areas were selected for land cover monitoring at 10m, and a land cover type change map from 2017 to 2021 was produced (Fig. 5.19). The results show that the majority of artificial facility areas in the 20 natural and mixed World Heritage sites increased, and some natural and mixed World Heritage sites saw a significant increase in cropland area, while the corresponding reduction in forest and grassland areas reflects the conflicts and pressures between heritage conservation and local community development.

Further fine monitoring at 2m was carried out on the boundary areas of the natural and mixed World Heritage sites with significant changes, and multiscale monitoring results were obtained (Fig. 5.20). The results show that the LC value in the boundary area of Mount Taishan in China is about 8%, and the BA-HID value is about 1.9%; the LC value in Turkey's Göreme National Park is about 5%, and the BA-HID value is about 1.4%. The artificial facility areas in both places continued to expand during 2010–2020, indicating some impacts of human activity on the natural and mixed World Heritage sites. Previous studies have also shown that Mount Taishan, adjacent to urban areas, has always been one of the World Heritage sites under the greatest human pressure (Allan et al. 2017). With the development of the socio-economy, the artificial facility areas gradually replaced other land use types including cropland, resulting in significant impacts on the boundary areas of natural and mixed World Heritage sites. The main land use type in the boundary area of Turkey's Göreme National Park is cropland, combined with multiple small towns. The ecological environment is relatively fragile and easily disturbed. In recent years, due to increasing human intervention, the land cover of the park has changed to a certain extent. This also serves as a warning for more natural and mixed World Heritage sites facing similar situations, emphasizing the need to balance urban and agricultural development with heritage conservation.

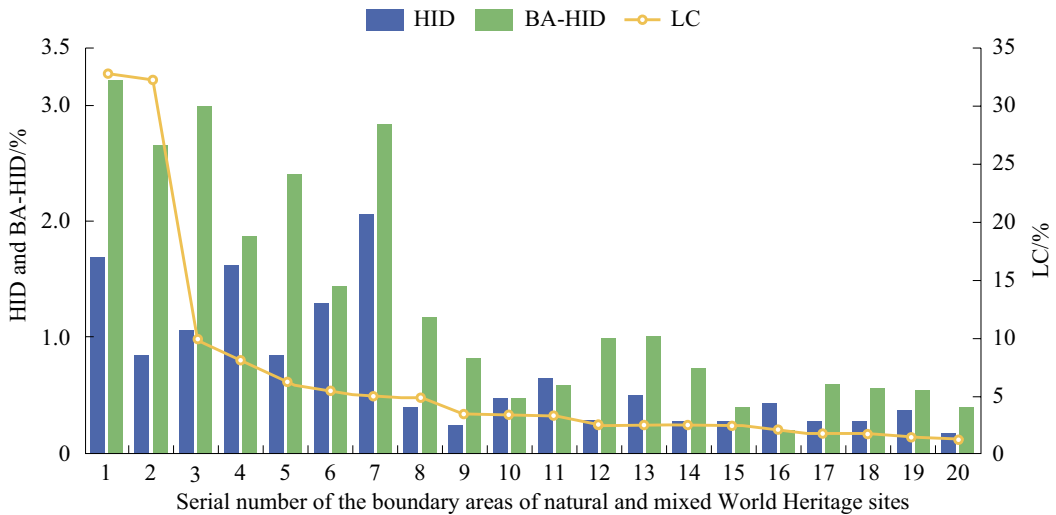
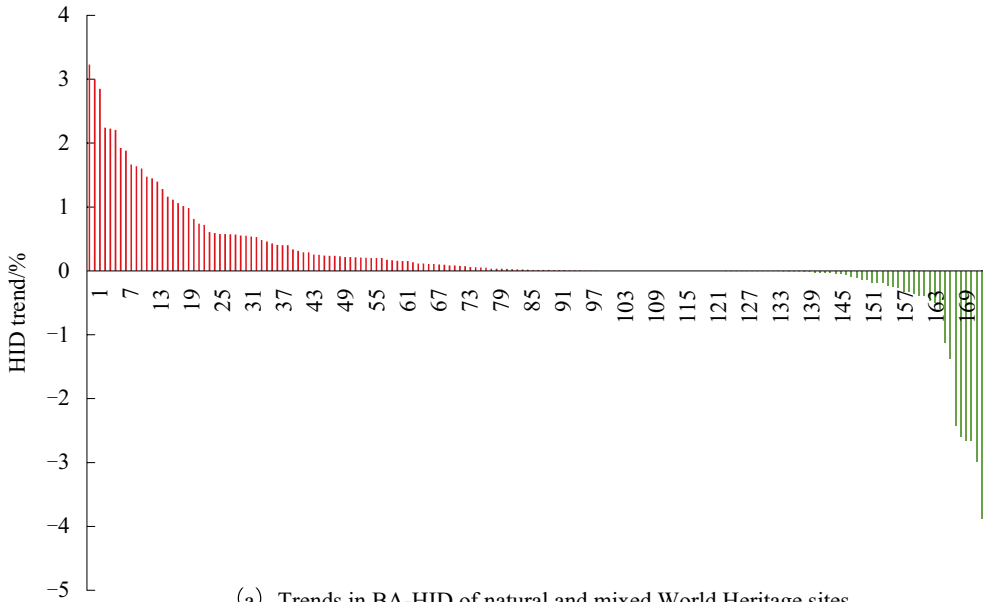


Fig. 5.18 Monitoring results of the boundary areas of natural and mixed World heritage sites from 2010 to 2020

5.3.5.5 Highlights

- Based on Big Earth Data, a multiscale monitoring and evaluation method for natural and mixed World Heritage site boundary areas

has been proposed. The monitoring results demonstrate that this method can reflect the protection levels of natural and mixed World Heritage site boundary areas and can better evaluate the sustainable development

Kinabalu Park		- 0.07	0.03			0.04			
Mount Taishan	- 0.03	- 0.04	- 0.22		0.11	0.17	0.01		
Mosi-oa-Tunya / Victoria Falls	- 0.05	- 0.13	- 0.62		- 0.03	0.66	- 0.03	0.2	
Mount Wuyi	0.03	0.06	0.21		- 0.92	0.63			
Ichkeul National Park	- 0.01	0.87	- 1.22		0.04	0.32			
Meteora		0.57	- 0.07		- 1.17	0.63	0.04	- 0.01	
Phong Nha-Ke Bang National Park	- 0.02	- 1.39	1.24		0.13	0.05			
Vredefort Dome		- 0.98	0.44		- 0.52	1.19	- 0.14		
Tikal National Park	1.07	- 0.1	0.78	0.01	0.26	- 0.44	- 1.6		
Trang An Landscape Complex	- 0.05	- 2.41	2		- 0.14	0.61			
Mount Sanjingshan National Park	0.65	1.21	- 2.65	0.15	- 0.46	1.09			
Mount Emei Scenic Area	0.27	1.55	- 3.46	0.84	- 0.05	0.88	- 0.04		
Keoladeo National Park			- 0.11		- 0.83	3.84	- 1.91		
Hierapolis-Pamukkale	0.01	3.47	- 5.83	- 0.11	2.36	0.1			
Goreme National Park and the		- 2.19	5.23		- 5.98	2.96	- 0.02		
Rock Sites of Cappadocia	- 3.31	- 1.47	5.8	- 3.59	0.5	0.29	1.78		
Mount Taishan	- 0.08	- 6.47	- 1.97	- 0.01	7.06	1.36	0.17	- 0.06	
Chengjiang Fossil Site	0.01	- 6.77	- 3.19		7.09	0.77	2.09		
Kaziranga National Park	3.29	2.61	- 0.38	0.05	- 10.62	5.11	- 0.03	- 0.01	
Djoudj National Bird Sanctuary	- 0.15	0.87	- 10.82	1.1	12.86		- 3.86		
		Water body	Forest	Grassland	Wetland	Cropland	Artificial facilities	Bare land	Ice/Snow/ (%) Cloud

Fig. 5.19 Land cover type changes in the top 20 natural and mixed World Heritage sites from 2017 to 2021. *Note* Yellow represents a decrease in the area of the type, darker red represents a greater increase in the area of the type, gray represents no change in the area. Values are the rate of change (%)

capacity and status of natural and mixed World Heritage sites by focusing on the key elements of the boundary areas.

- From 2010 to 2020, the rate of land cover change in natural and mixed World Heritage site boundary areas was generally within 10%, and HID was generally within 1%, indicating an overall good condition. However, there are still natural and mixed World Heritage sites where the areas of artificial facilities and cultivated land have increased, reflecting conflicts and pressures between heritage conservation and local community development.

5.3.5.6 Discussion and Outlook

By using multi-source data of global land cover and satellite imagery, this case presents a multiscale monitoring and evaluation method for natural and mixed World Heritage site boundary areas, achieving effective monitoring results in boundary areas of some natural and mixed World Heritage sites worldwide. This provides

an important reference for the overall protection and sustainable development issues faced by natural and mixed World Heritage sites globally.

The high-resolution data used in this case study mainly targeted the boundary areas of natural and mixed World Heritage sites with significant land use changes. In the future, the monitoring scope can be further expanded to meet the requirements of fine boundary monitoring and reasonable boundary evaluation. The method used in this case is an operable method that is applicable to a global scale and conforms to the SDG indicator system. The results are globally consistent and comparable. However, due to the differences between land cover data of different resolutions, the calculated results cannot fully represent the accurate numbers of specific indicators for each natural and mixed World Heritage site. Nevertheless, the results of this case study provide an important reference for understanding the implementation process of SDG 11.4 at the national and regional scales.

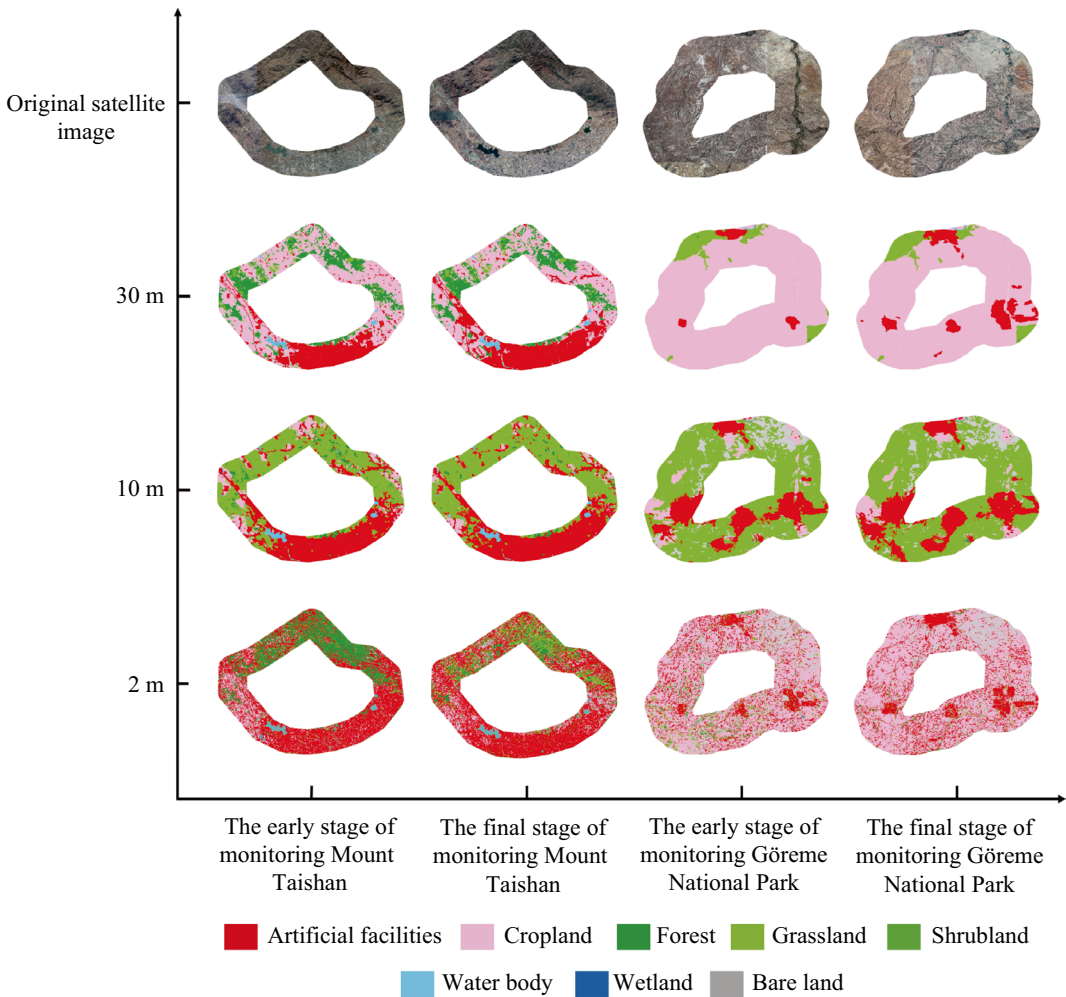


Fig. 5.20 Multiscale surface coverage monitoring results of typical heritage site boundary areas

5.3.6 Global Change in Urban Greenness and Beneficiary Population in Large Cities

Target: SDG 11.7: By 2030, provide universal access to safe, inclusive and accessible, green and public spaces, in particular for women and children, older persons and persons with disabilities.

5.3.6.1 Background

The UN reported that the total global population is expected to reach 8.5 billion by 2030, of which 64% (5.4 billion) will live in cities (UN

2019b). The sustainable development of cities is directly related to the future of humankind, but differences in socioeconomic development levels have led to an extremely uneven global urbanization process (Sun et al. 2020). In developed countries, municipal green infrastructure is relatively complete, and urban residents can enjoy good green space as public services. Relatively speaking, in many developing countries and underdeveloped countries, cities not only lack basic infrastructure (such as sanitary drinking water, reliable energy supply, health and education resources) but also lack public green space. On a global scale, the continuous dynamic

monitoring of urban green spaces in time and space is critical to the achievement of SDG 11.

Since 2004, the National Afforestation Committee and the National Forestry and Grassland Administration have launched the “National Forest City” evaluation process. As of November 2022, China’s national forest cities had increased to 219, advancing the country’s goal of establishing an “ecological civilization” in urban areas. However, quantitative comparative research has been insufficient for identifying the most important aspects urban greenness in the construction of an urban ecological civilization.

5.3.6.2 Data

- 2020 MODIS land cover type data [MCD12Q1, International Geosphere-Biosphere Programme (IGBP) classification] at a spatial resolution of 500 m.
- EVI data from the MODIS dataset (MOD13Q1) from 2001 to 2021, at a spatial resolution of 250 m and a temporal resolution of 16 days.
- Global gridded population data in 2020 from WorldPop, LandScan, Gridded Population of the World, v.4 (GPWv4) at a spatial resolution of 1000 m.
- Classification of country income levels (published by the World Bank, 2020–2021).

5.3.6.3 Methods

This study used the 2020 land cover type data (IGBP classification) in the MCD12Q1 dataset to screen urban patches with a contiguous urban built-up area (UBA) larger than 50 km² (large cities, hereafter). There are 1783 such cities worldwide. Further, using EVI data with 250 m spatial resolution as a greenness indicator, we applied the Mann–Kendall method to evaluate the trend of the annual maximum EVI (V_{\max}) for each urban pixel of the 1,783 large cities from 2001 to 2021.

Then, we calculated the ratio (R_g) of the area of the pixels with a significantly increasing V_{\max} trend ($P < 0.05$) to the UBA in 2020 of the

corresponding city. Using this method, we evaluated urban greening change from 2001 to 2021.

Urban greening is an important part of the urban ecosystem. It not only has many benefits such as regulating rainwater, reducing air pollution, and reducing the urban heat island effect, but also reduces violent crimes and has a positive effect on the physical and mental health of urban residents (Giles-Corti et al. 2016). Therefore, this study regards the residents living in the UBA pixels with significant greening trends as the direct beneficiary population. Through the spatial overlay analysis of significant urban greening in UBAs and three sets of global gridded population data (WorldPop, LandScan, GPWv4), an average value can be estimated in each city for the population directly benefiting from urban greening.

5.3.6.4 Results and Analysis

1. China has the largest urban area of significant greening in the world

Figure 5.21 shows the spatial distribution of R_g and the beneficiary population in 1783 cities around the world from 2001 to 2021. Globally, the cities with large values of R_g (indicated by blue and green points on the map) are located mainly in East Asia, Europe, and the Eastern United States in North America, and sparsely in Africa, Oceania, and South America. The 316 selected Chinese cities accounted for only 19% of the global UBAs, but contributed 28% of significantly greening UBAs among the 1,783 cities in the world compared in this study.

2. Nearly half of the world’s population benefiting from significant urban greening are in China

Globally, about 310 million urban dwellers live in significant greening UBAs. The proportions of the beneficiary population by continent are as follows: Asia (70.6%), Europe (11.9%), North America (7.6%), South America (5.9%), Africa (3.4%), and Oceania (0.4%) (Fig. 5.22a). Approximately 147 million of them, or 47% of the global beneficiary

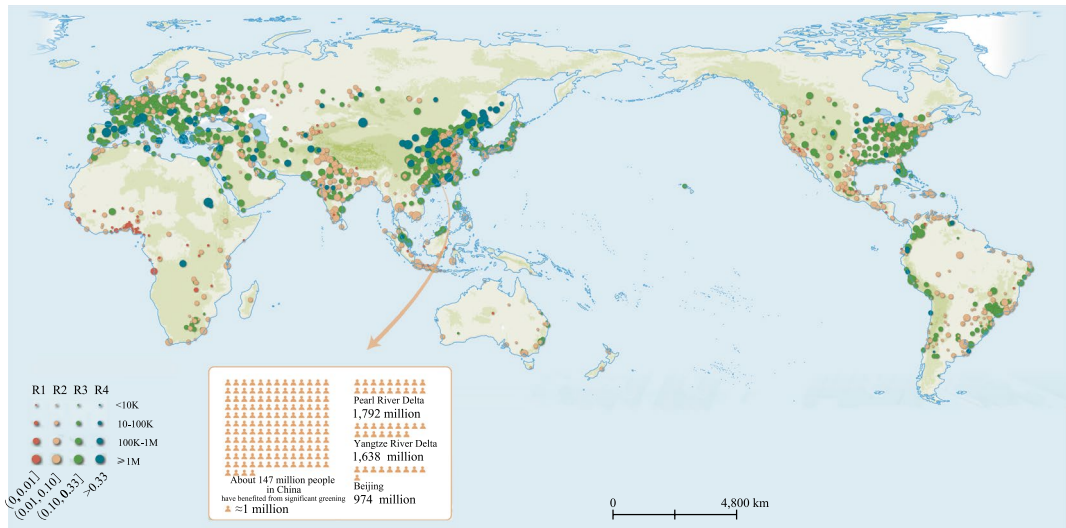


Fig. 5.21 Distribution of R_g and the beneficiary population in 1783 cities

population, are in China. The top three cities with the largest beneficiary population in the world are the Pearl River Delta (17.92 million), the Yangtze River Delta (16.38 million), and Beijing (9.74 million).

3. The improvement in urban ecosystems is closely related to income level, with the most notable improvement seen in upper-middle-income countries

The average values of R_g ranging from high to low for the income groups defined by the World Bank are 15.45% for upper-middle-income countries (UM), 14.00% for high-income countries (H), 11.78% for low-income countries (L), and 9.79% for lower-middle-income countries (LM) (Fig. 5.22b, bar graph). Using the average value of annual maximum greenness from 2019 to 2021 to represent the current environmental status of cities (EVI_{city}) (Fig. 5.22b, broken line graph), it was found that the EVI_{city} is the highest (0.40) in high-income countries, while it is 0.353, 0.35, and 0.30 in upper-middle-income, lower-middle-income, and low-income countries respectively, suggesting the need for a major improvement in their urban environments.

5.3.6.5 Highlights

- Based on global vegetation index data, land cover type data from MODIS satellite, and gridded population data, we screened 1,783 cities or urban agglomerations around the world with a UBA of more than 50 km². Then we evaluated the changes in greenness of UBAs and the direct beneficiary population in these cities from 2001 to 2021.
- With only 19% of the world's total UBAs, China accounted for 28% of the significant greening UBAs. Globally, 310 million people directly benefit from such UBAs, and about 47% of them live in China.
- The Pearl River Delta, the Yangtze River Delta, and Beijing have the largest populations in the world benefiting from the significant greening of cities.

5.3.6.6 Discussion and Outlook

This study used the EVI of MOD13Q1 data, land cover change data, gridded population data, and national income level data to calculate the trends of annual maximum EVI and significance levels of UBAs in 1,783 cities around the world

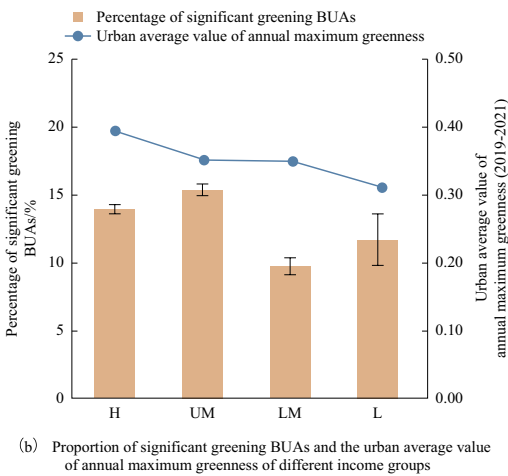
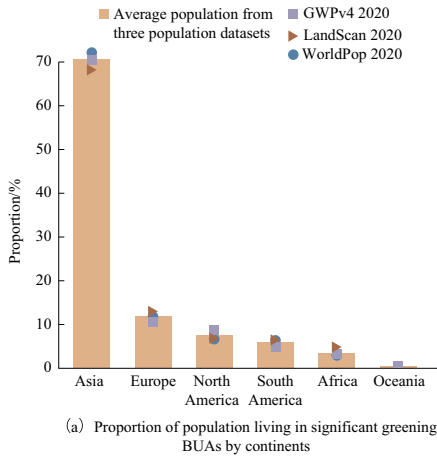


Fig. 5.22 Distribution of the population living in greening UBAs

from 2001 to 2021. This study further analyzed the different ratios of greening UBAs of cities at different income levels and then evaluated the distribution of the direct beneficiary population in 2020.

Compared with the traditional scheme of calculating the changes of urban green space areas, the method used in this study does not rely on high-resolution data, but also monitors the overall greenness change of urban pixels at mesoscale resolution. The method detects changes in the greenness of urban pixels caused by newly added parks and green spaces on UBA pixels and even detects changes in greenness caused by the natural growth of trees on streets.

In the context of global climate change, as a major contributor to urban carbon sinks, the significant increase in urban greening in cities will help China achieve high-quality development. At the same time, for most developing countries, the results of this study can provide data support, improve urban governance for these countries, and provide low-cost solutions for urban sustainable development monitoring in developing countries.

5.4 Summary

This chapter discusses progress in three themes: monitoring and evaluating the urbanization process, World Heritage protection, and urban green space.

Based on the studies, we offer the following recommendations.

- (1) In terms of future research directions, further exploration and evaluation of the impacts of urbanization on the environment and ecology, such as air pollution and carbon emissions, will be valuable. Additionally, it is crucial to consider the impacts of climate change on urbanization patterns and to develop strategies for adapting to these changes. Future research directions include exploring the potential of smart urban development and the application of new technologies, such as artificial intelligence, in order to optimize the location of urban land use and enhance urban sustainability. Furthermore, integrating social and economic factors into urban modeling could provide a more comprehensive understanding of the interactions between urbanization and sustainable development.
- (2) According to World Heritage protection evaluated using SDG 11.4.1, the study found that the positive/negative effects of land cover change on cultural heritage protection are highly correlated with per capita GDP. It is suggested to strengthen the monitoring and evaluation of the World Heritage SDG indicators in accordance with

the Convention Concerning the Protection of the World Cultural and Natural Heritage and the Operational Guidelines for the Implementation of the World Heritage Convention, increase investment in heritage protection, and focus on properly resolving the conflicts between World Heritage protection and community development in the middle-income countries and regions of the world.

- (3) Regarding SDG 11.7.1, urban open space, the study found that while China's total BUAs are only 19% of the world's total, China accounted for 28% of significant greening BUAs and 47% of the global population benefitting from such BUAs. Countries, especially developing ones, are advised to strengthen urban planning and invest more in green infrastructure amid rapid urbanization.

Future studies should help understand the transformation toward sustainable urbanization and continue to explore the capacity of digital technology, represented by Big Earth Data, in monitoring and evaluating sustainable cities and communities, so as to provide scientific solutions for the realization of SDG 11 by filling data gaps, expanding the indicator system, and informing government decision-making.

References

- Allan JR, Venter O, Maxwell S et al (2017) Recent increases in human pressure and forest loss threaten many natural World heritage sites. *Biol Cons* 206:47–55. <https://doi.org/10.1016/j.biocon.2016.12.011>
- Angel S, Blei A M, Parent J, et al. (2016) Atlas of urban expansion—2016 Edition, Volume 1, Areas and densities. Cambridge, Lincoln Institute of Land Policy
- Ashrafi B, Kloos M, Neugebauer C (2021) Heritage impact assessment, beyond an assessment tool: a comparative analysis of urban development impact on visual integrity in four UNESCO World Heritage properties. *J Cult Herit* 47:199–207
- Barnsley M, Barr S (1996) Inferring urban land use from satellite sensor images using kernel-based spatial reclassification. *Photogramm Eng Remote Sens* 62:949–958
- Burke M, Driscoll A, Lobell D B, et al. (2021) Using satellite imagery to understand and promote sustainable development. *Science* 371(6535):eabe8628
- CBAS (2020) Big Earth Data in Support of the Sustainable Development Goals 2020. Beijing, CBAS. <http://www.cbas.ac.cn/en/publications/reports/202108/P020220402433225206982.pdf>
- CBAS (2021) Big earth data in support of the sustainable development goals 2021. Beijing, CBAS. <http://www.cbas.ac.cn/en/publications/reports/202109/U020220401630362820943.pdf>
- Chen GZ, Li X, Liu XP et al (2020) Global projections of future urban land expansion under shared socioeconomic pathways. *Nat Commun* 11:537
- Chen Z, Yu B, Yang C et al (2021) An extended time series (2000–2018) of global NPP-VIIRS-like nighttime light data from a cross-sensor calibration. *Earth Syst Sci Data* 13(3):889–906
- Estoque RC, Murayama Y (2016) Quantifying landscape pattern and ecosystem service value changes in four rapidly urbanizing hill stations of Southeast Asia. *Landscape Ecol* 31(7):1481–1507
- Gao J, O'Neill BC (2020) Mapping global urban land for the 21st century with data-driven simulations and shared socioeconomic pathways. *Nat Commun* 11:2302
- Giles-Corti B, Vernez-Moudon A, Reis R et al (2016) City planning and population health: a global challenge. *The Lancet* 388(10062):2912–2924
- He KM, Zhang XY, Ren SQ, et al. (2016) Deep residual learning for image recognition. In: Proceedings of the IEEE conference on computer vision and pattern recognition. pp 770–778
- Jiang HP, Sun ZC, Guo HD et al (2021) An assessment of urbanization sustainability in China between 1990 and 2015 using land use efficiency indicators. *NPJ Urban Sustain* 1:34
- Jiang HP, Sun ZC, Guo HD et al (2022) A standardized dataset of built-up areas of China's cities with populations over 300,000 for the period 1990–2015. *Big Earth Data* 6(1):103–126
- Li XC, Gong P (2016) Urban growth models: progress and perspective. *Science Bulletin* 61(21):1637–1650
- Li XC, Zhou YY, Eom J et al (2019) Projecting global urban area growth through 2100 based on historical time series data and future shared socioeconomic pathways. *Earth's Future* 7(4):351–362
- Li XC, Zhou YY, Chen W (2020) An improved urban cellular automata model by using the trend-adjusted neighborhood. *Ecol Process* 9:1–13
- Liu XP, Huang YH, Xu XC et al (2020) High-spatiotemporal-resolution mapping of global urban change from 1985 to 2015. *Nature Sustain* 3(7):564–570
- Lu Y, Nakicenovic N, Visbeck M et al (2015) Policy: five priorities for the UN sustainable development goals. *Nature* 520(7548):432–433

- McDonald RI, Mansur AV, Ascensão F et al (2020) Research gaps in knowledge of the impact of urban growth on biodiversity. *Nature Sustain* 3(1):16–24
- Nocca F (2017) The role of cultural heritage in sustainable development: multidimensional indicators as decision-making tool. *Sustainability* 9:1882
- Sanchez Rodriguez R, Ürge-Vorsatz D, Barau AS (2018) Sustainable development goals and climate change adaptation in cities. *Nat Clim Chang* 8(3):181–183
- Sun LQ, Chen J, Li QL et al (2020) Dramatic uneven urbanization of large cities throughout the world in recent decades. *Nat Commun* 11:5366
- Tang YW, Chen FL, Yang W et al (2022) Elaborate monitoring of land-cover changes in cultural landscapes at heritage sites using very high-resolution remote-sensing images. *Sustainability* 14(3):1319
- UN Statistics Division (2021) SDG indicator metadata. <https://unstats.un.org/sdgs/metadata/files/Metadata-11-04-01.pdf>
- UN (2019b) World urbanization prospects: the 2018 revision. New York, UN
- UN (2019a) Tier classification for global SDG indicators. https://unstats.un.org/sdgs/files/Tier%20Classification%20of%20SDG%20Indicators_28%20Dec%202020_web.pdf
- UNESCO (2005) Operational guidelines for the implementation of the World heritage convention. UNESCO World Heritage Centre, Paris
- Wang P, Yang RX, Liang YQ et al (2022) Research on sustainable development goals of UNESCO designated sites in China based on multi-source data. *J Univer Chinese Acad Sci* 39(6):754–763. [https://doi.org/10.7523/j.ucas.2021.0021.\(inChinese\)](https://doi.org/10.7523/j.ucas.2021.0021.(inChinese))
- World Heritage Centre (2009) World Heritage and buffer zones. In: Martin O, Piatti G (eds) Proceedings of the international expert meeting on world heritage and buffer zones, Davos, Switzerland. Paris, UNESCO-World Heritage Centre, pp 25
- Wu DW, Mao HY, Zhang XL et al (2011) Assessment of urban land use efficiency in China. *Acta Geogr Sin* 66(8):1111–1121 (in Chinese)

Open Access This chapter is licensed under the terms of the Creative Commons Attribution-NonCommercial-NoDerivatives 4.0 International License (<http://creativecommons.org/licenses/by-nc-nd/4.0/>), which permits any noncommercial use, sharing, distribution and reproduction in any medium or format, as long as you give appropriate credit to the original author(s) and the source, provide a link to the Creative Commons license and indicate if you modified the licensed material. You do not have permission under this license to share adapted material derived from this chapter or parts of it.

The images or other third party material in this chapter are included in the chapter's Creative Commons license, unless indicated otherwise in a credit line to the material. If material is not included in the chapter's Creative Commons license and your intended use is not permitted by statutory regulation or exceeds the permitted use, you will need to obtain permission directly from the copyright holder.





6.1 Background

Climate change is triggering unpredictable responses from the land, ocean, and atmosphere, with lasting, far-reaching impacts on sustainable development and the ecological environment (World Meteorological Organization 2022). According to data released by the EM-DAT International Disaster Database, disasters and economic losses caused by extreme weather events across the world increased significantly from 2000 to 2022. The mitigation of climate change requires all countries to take the most urgent actions to reduce greenhouse gas emissions and increase carbon sinks through forest protection, soil management, and carbon capture (IPCC 2022).

In order to cope with the threats of climate change to the sustainable development of humankind, SDG 13 was established to “take urgent action to combat climate change and its impacts” (hereinafter referred to as “Climate Action”). Targets under this goal include, among others, strengthening resilience to natural disasters, reducing greenhouse gas emissions, and improving education and early warning. China has actively responded to the call for Climate

Action by setting its carbon peaking and neutrality targets and implementing disaster prevention and reduction strategies. Furthermore, in 2022, the Chinese government released the National Climate Change Adaptation Strategy 2035, which proposes to build a climate-resilient society by 2035 by improving climate change monitoring, early warning, and response capabilities.

Currently, among all 17 SDGs, Climate Action suffers the most severe shortage of data (UN 2021). Therefore, this chapter focuses on the three themes of disaster monitoring and reduction, climate change early warning, and global land/marine carbon sink estimation and describes the use of Big Earth Data methods to generate data products to monitor Climate Action progress and conduct spatiotemporal analysis to support decision-making.

Compared with the reports of the previous three years, the big data in this report is of broader scope and spatial scale and with greater relevance to SDG indicators. The worldwide progress on measuring two indicators of SDG 13 was assessed, and global-scale disaster and carbon sink data products were generated to make a greater contribution to climate change response and adaptation.

6.2 Main Contributions

This chapter evaluates the global progress of two targets, SDG13.1 and SDG13.2, through four cases. The main contributions are as follows (Table 6.1).

6.3 Case Studies

6.3.1 Global Heat Wave Disaster Changes and Their Impacts

Target: SDG 13.1: Strengthen resilience and adaptive capacity to climate-related hazards and natural disasters in all countries.

6.3.1.1 Background

Heat waves are prolonged periods of abnormally high temperatures that can cause harm to humans, animals, and plants due to their inability to adjust to these extreme conditions (Qin 2015). They have already become an important meteorological disaster for humans under global warming with an increase in the frequency, intensity, and duration of heat waves, and about 30% of the global population is suffering from the impacts of more deadly 20-day duration heat waves per year (Mora et al. 2017). Currently, there are limitations to the quantification of heat wave occurrences on a large scale, especially how to provide consistent heat wave identification under different temperature tolerances of local dwellers and ecosystems across climate zones. Therefore, threshold methods based on thermal infrared (TIR) remote-sensing datasets are proposed to derive relatively consistent heat wave distribution and analyze their spatial pattern differences. Satellite-based datasets have advantages in analyzing land surface processes on a large scale due to their global coverage for surface parameters, and the multi-platform combination of LST datasets will break the limitation of single point observation of stations for deeply understanding spatial distribution, evolution, and impacts of heat waves.

This study analyzed global heat wave changes and identified their impacts from 2011 to 2020 using Big Earth Data from satellite detection and station observation and further assessed the impacts of heat waves on the global population using SDG indicators to serve disaster monitoring or mitigation actions for global heat waves.

6.3.1.2 Data

- Global station observation datasets from 1979 to 2020 were collected from the Global Historical Climatology Network (GHCN).
- Global fusion data of LST from 1979 to 2009 were collected from Princeton University (Coccia et al. 2015).
- Global daily LST data from 2003 to 2020 were collected from the Terra/Aqua Project Team.
- Global population data from 2010, 2015 and 2020 were collected from the GPWv4.

6.3.1.3 Methods

A heat wave event is quantified by consecutive days hotter than normal in a collective period according to the relative threshold method (Perkins 2015). Each heat wave event has at least three consecutive days above the 90th percentile for maximum surface temperature. We conducted an empirical cumulative distribution function (CDF) for each pixel of surface temperature sequences using a 15-day window. Then, the value of the 90th percentile from the CDF of each pixel was derived as the threshold for detecting hot days at the global scale. Each heat wave event was identified by more than three consecutive hot days, and the statistical information of all heat wave events was aggregated to calculate heat wave indices.

Here, the frequency and duration of heat waves were used to analyze global heat wave changes from 2011 to 2020 and further identify hotspots of global heat wave occurrences. The extent of heat wave hazards that happened in a region was quantified according to the annual statistical results of the frequency of heat waves,

Table 6.1 Cases and their main contributions

Targets	Cases	Contributions
SDG 13.1 Strengthen resilience and adaptive capacity to climate-related hazards and natural disasters in all countries	<p>Global heat wave disaster changes and their impacts</p> <p>Ocean physical environment changes under global warming</p>	<p>Method and model: identification of the intensity and frequency of heat waves and the size of the affected population on a global scale by combining the relative and absolute thresholds</p> <p>Data product: gridded datasets of global OHC, salinity, and stratification for the past 60 years</p> <p>Decision support: Changes in the marine physical environment caused by global warming seriously threaten marine ecosystems and their sustainable development</p>
SDG 13.2 Integrate climate change measures into national policies, strategies and planning	<p>Analysis of temporal and spatial changes in net ecosystem productivity of global terrestrial ecosystems, 2000–2020</p> <p>Variability of global ocean carbon sink, 1992–2020</p>	<p>Data product: global terrestrial NEP products from 2000 to 2020</p> <p>Data product: partial pressure of CO₂ in the global ocean surface from 1992 to 2020</p> <p>Method and model: estimation of CO₂ flux absorbed by global oceans from the atmosphere</p>

such as general, strong, and severe heat waves with an annual frequency greater than 10, 15, and 20, respectively. Then, we classified annual heat waves in different regions and further examined how many people were influenced by different heat wave events using the indicator of SDG 13.1.1 (“number of deaths, missing persons and directly affected persons attributed to disasters per 100,000 population”).

6.3.1.4 Results and Analysis

1. Spatial Distribution of Global Heat Waves

Probability statistics of heat waves from 2011 to 2020 found that 85% of the global land area was affected by extreme heat events in one-tenth of the days of the year, while 28% of the global land area was affected by heat waves in one-fourth of the days of the year (Fig. 6.1). There are similarities and annual changes in the spatial distribution of global heat waves, mainly occurring in the mid-to-low latitudes around the 30° N and 30° S latitudes, such as southwestern North America, Southern Europe, North Africa, Southwest Asia, and Oceania, where the largest annual

occurrence of heat waves can reach 35. It was also found that there were obvious inter-annual changes in heat wave occurrences and their distribution in Southeast Asia and Northern Europe.

2. Trends and Hotspots of Global Heat Waves from 2011 to 2020

About 55% of the global land area experienced an increase in heat wave frequency from 2011 to 2020, with significant spatial variations (Fig. 6.2). Australia was most heavily influenced by heat waves from 2011 to 2020, with the regional average heat wave frequency increasing from 5 to 11. South Africa and Namibia also significantly experienced heat wave impacts, with their regional average heat wave frequencies increased by 50%. In East Asia, East China and the Russian Far East also experienced a rapid increase in heat wave occurrences, while more heat waves could be detected in the central and southern parts of Europe. It is worth noting that more extreme heat events (the most heat waves) appeared in Eurasia and northern North America near the Arctic in 2019. Extremely high

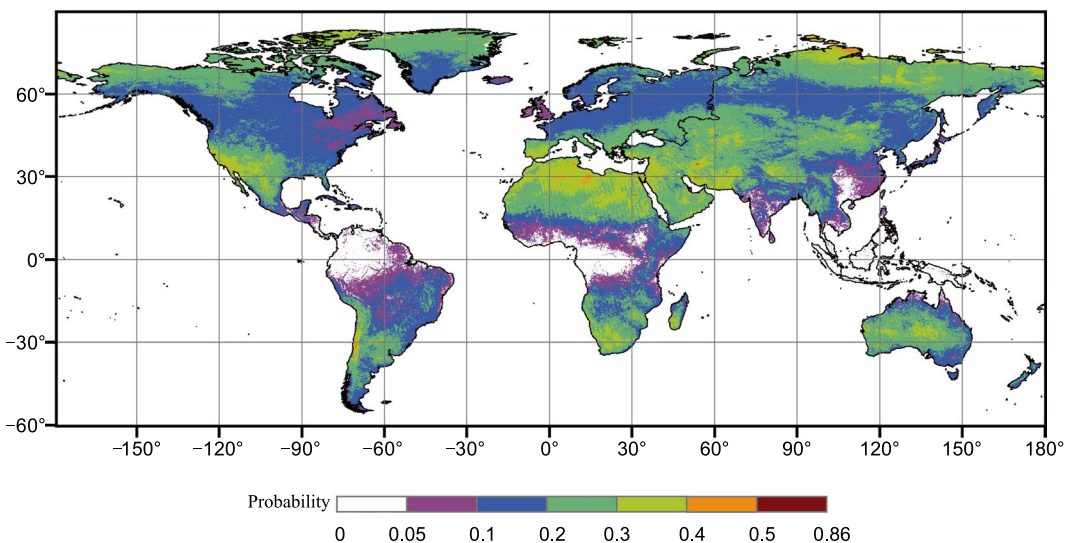


Fig. 6.1 Annual averaged probability of global heat wave occurrence from 2011 to 2020

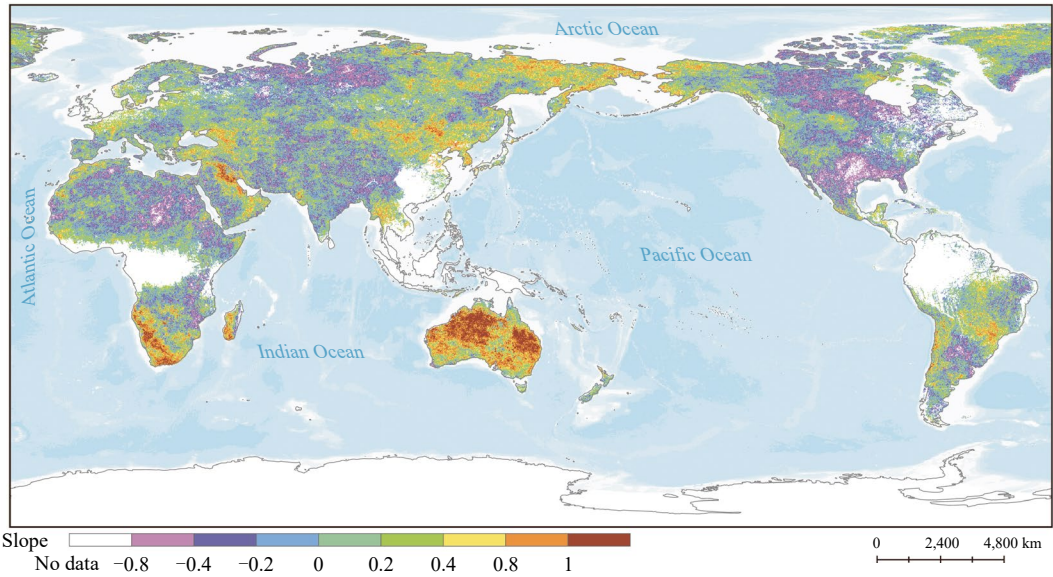


Fig. 6.2 Trend of global heat wave frequency from 2011 to 2020

temperatures have caused damage to the natural environment and economic development, especially in developing countries.

3. People Influenced by Heat Waves at a Global Scale

Approximately 480 million people worldwide are influenced by more than 10 heat waves every year, while 87.47 million and 1.67 million people are affected by 15 or 20 heat waves, respectively. According to the assessment framework of SDG 13.1.1, the severity of heat wave impacts can be quantified as the global population directly exposed to heat wave disasters during 2011–2020. Approximately 6300 people per 100,000 people suffered from heat waves at a general hazard level, while 1200 people per 100,000 people were directly affected by heat waves at a strong level.

6.3.1.5 Highlights

- Big Earth Data and threshold methods were used to estimate the spatial distribution of regions affected by global heat waves,

with approximately 85% of the land area being impacted by heat waves for more than 36 days during 2011–2020.

- According to the assessment framework of SDG 13.1.1, about 6300 people per 100,000 were affected by moderate-intensity heat waves each year, while around 1200 people per 100,000 were impacted by severe-intensity heat waves annually over the course of the decade-long investigation.

6.3.1.6 Discussion and Outlook

In order to provide a comprehensive evaluation for SDG 13.1.1, this study analyzed the impacts and changes of global heat waves from 2011 to 2020 and qualitatively assessed the impacts of heat wave hazards on the global population. The produced datasets can provide early warning or disaster mitigation actions for dealing with heat wave disasters. Generally, global heat wave events increased from 2011 to 2020. Meanwhile, the intensity and expansion of their impacts increased, leading to many challenges for human health and environmental protection. The record-breaking heat events probably indicate the potential shifts of global climate change, which need to be further explored in

future studies. With the accumulation of satellite data, accurate calibration technology, and data fusion, more consistent spatial datasets will be produced to contribute to the achievement of the 2030 Agenda.

6.3.2 Physical Environment Changes in Oceans Under Global Warming

Target: SDG 13.1: Strengthen resilience and adaptive capacity to climate-related hazards and natural disasters in all countries.

6.3.2.1 Background

Oceans cover 71% of Earth's surface and are a key component of the climate system and a key location of biodiversity. Under global climate change, the ocean environment has also changed pervasively, leading to more climate disasters that threaten human beings, ocean ecosystems, and the achievement of the SDGs.

The increased concentration of greenhouse gases in the atmosphere from human activity traps heat within the climate system and increases ocean heat content (OHC). Over 90% of Earth's energy imbalance in the climate system is stored in the ocean; thus, OHC is a central indicator of climate change. As OHC is less impacted by internal climate variability [e.g., El Niño and Southern Oscillation (ENSO)], it is a particularly robust metric of global climate change.

Salinity is another key physical property of seawater, and together with temperature, it determines the water density, which is a vital driver of ocean circulation. The changes in ocean salinity reflect the global exchange of surface freshwater. Evaporation refers to the transfer of freshwater from a water body to the atmosphere, leaving behind liquid water that is higher in salinity. Precipitation injects freshwater into saline water, resulting in freshening. The salinity anomalies associated with surface freshwater exchange are then dispersed in the ocean through ocean circulation and mixing. Consequently, salinity changes integrate

effects over broad areas and indicate water cycle change and variability. The change of the water cycle leads to a pattern of change where “the fresh get fresher and the salty get saltier” in much of the ocean, which indicates a “dry get drier and wet get wetter” paradigm, which describes the amplification of the water cycle driven by global warming.

Temperature and salinity changes alter the ocean density and lead to changes in vertical stratification. Seawater generally forms stratified layers with lighter waters near the surface and denser waters at greater depth, i.e., warmer waters are atop colder ones. This stable configuration, named stratification, acts as a barrier to water mixing that impacts the efficiency of the vertical exchange of heat, carbon, oxygen, and other constituents. Therefore, stratification is a central element of the climate system, and understanding its change with global warming has great scientific, societal, and ecological consequences.

OHC, salinity, and stratification are important as metrics for quantifying climate change, as well as through the influence of the ocean on weather, society, and SDGs (Abraham et al. 2022). Ocean warming strengthens the tropical cycles, causes more extremes, and raises the global sea level, causing more risks to the low-lying and coastal regions (e.g., saltwater intrusion and land erosion). Ocean temperature and stratification increase, reduce the efficiency of ocean carbon uptake, leave more CO₂ in the air, and exacerbate global warming. Moreover, stronger ocean vertical stratification prohibits the vertical exchange of oxygen, leading to ocean deoxygenation and threatening ocean life.

6.3.2.2 Data

- Global ocean temperature, salinity, stratification observational gridded dataset [Institute of Atmospheric Physics (IAP), CAS], 1955–2021, with 1° × 1° horizontal resolution, monthly temporal resolution, and 0–2000 m coverage.
- In situ profile dataset from the World Ocean Database (WOD) from the National Centers

for Environmental Information (NCEI) at the National Oceanic and Atmospheric Administration (NOAA), 1955–2021.

- Global ocean temperature dataset from deep ocean remote sensing (DORS), 1993–2020 (<https://doi.org/10.57760/sciencedb.01918>).
- Multi-source satellite observation data: sea surface height, sea surface temperature, and sea surface wind, with $1^\circ \times 1^\circ$ spatial resolution, monthly temporal resolution, 1993–2020.
- Array for Real-time Geostrophic Oceanography (Argo) gridded product includes in situ temperature and salinity observation with global upper 2000 m coverage, spatial resolution of $1^\circ \times 1^\circ$, and monthly temporal resolution, 2005–2021.

6.3.2.3 Methods

This study applied data quality control, bias correction, and mapping techniques to the ocean in situ temperature and salinity observations to reconstruct global $1^\circ \times 1^\circ$ horizontal resolution gridded temperature and salinity products (Cheng et al. 2022). OHC, salinity-contrast index, and stratification changes were then calculated based on the derived gridded datasets. The data quality control (QC) system developed by CAS IAP and the CAS Institute of Oceanology was applied to remove erroneous measurements, which includes 13 modules (Tan et al. 2023). Expendable bathythermograph (XBT) biases have been corrected for CAS IAP by Cheng et al. (2014), and mechanical bathythermographs (MBT) biases have been corrected by Gouretski et al. (2022). After data QC and bias correction, a mapping technique was applied for spatial interpolation. The mapping is an ensemble optimal interpolation approach with a dynamical ensemble (Cheng and Zhu 2016) and can unbiasedly reconstruct the temporospatial variability of ocean changes. The “no data, no signal” biases have been reduced with this mapping and account for the anisotropic feature of the ocean variability.

Moreover, the DORS techniques were developed for detecting the ocean’s interior information based on remote-sensing big data and artificial intelligence. A new long-term and

multi-level global ocean subsurface temperature remote-sensing dataset (DORS) was reconstructed using the convolutional neural network long short-term memory (CNN-LSTM), which combined satellite remote-sensing observations (sea surface height, sea surface temperature, and sea surface wind) and Argo float observations (Su et al. 2021, 2022). The advantage of the DORS dataset is that it improves the estimation accuracy of the 3D ocean thermal structure from remote-sensing observations, fills the gaps of float observation during the pre-Argo period, extends the length of the time-sequential float observation, and finally provides a new perspective and dataset for monitoring and analyzing the ocean thermal environment change based on satellite remote sensing.

Here, we combined the self-developed ocean data products (IAP and DORS) to analyze the impacts of climate change on the ocean’s physical environment.

6.3.2.4 Results and Analysis

Figure 6.3a shows the changes of the global upper 2000 m OHC from 1955 to 2021, when the global upper 2000 m OHC experienced an unabated increase, with a linear rate of $5.7 \times 10^{22} \text{ J}/10\text{a}$ (Fig. 6.3a). The warming rate has increased since the 1990s. From 1991 to 2021, the upper 2000 m ocean warming rate was $9.5 \times 10^{22} \text{ J}/10\text{a}$, four times the rate of 1955–1990. When considered on an annual basis, 2021 was the hottest year ever recorded in the world’s oceans. Its OHC exceeded that of 2020 by $1.4 \times 10^{22} \text{ J}$ and exceeded that of the 1981–2010 baseline by $23.5 \times 10^{22} \text{ J}$. Collectively, 2012–2021 were the hottest ten years in history. Five basins (the North Pacific, Atlantic, Mediterranean Sea, Indian Ocean, and Southern Ocean) recorded their highest OHC since the 1950s. Ocean warming has consequences for humans and ecosystems. It raises the global sea level, reduces the efficiency of ocean carbon uptake, increases the frequency/intensity of marine heat waves, strengthens tropical cycles, and causes more extreme rainfall.

The existing salinity pattern has been amplified, showing “the fresh get fresher and the

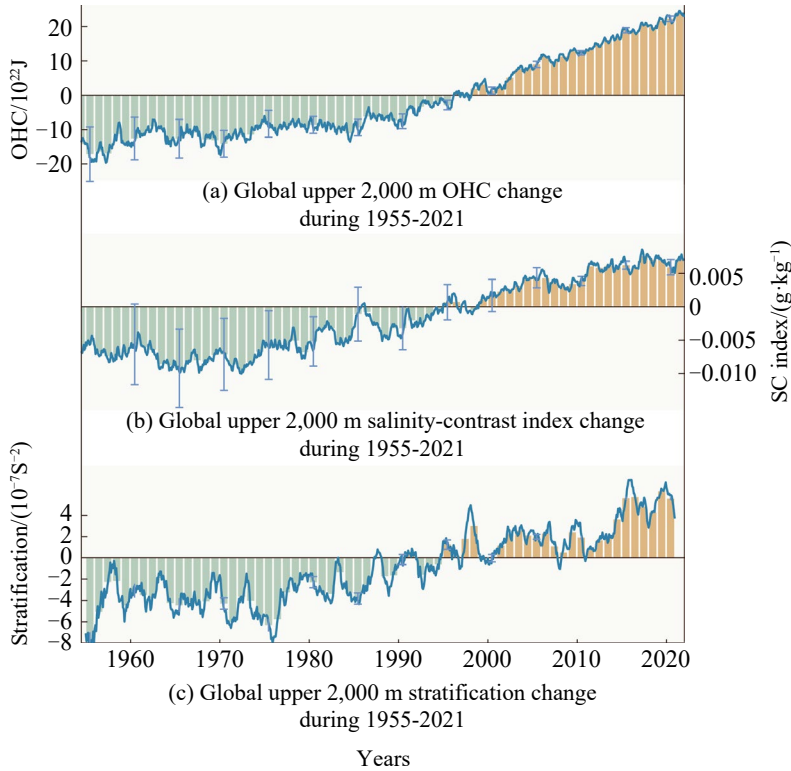


Fig. 6.3 Changes in the physical environment of the ocean

salty get saltier” in much of the ocean. In order to quantify this pattern of change, the salinity contrast (SC) index was used, which is defined as the difference between the salinity averaged over high-salinity and low-salinity regions (Fig. 6.3b). For the 1955–2021 period, the global upper 2000 m SC index increased by 1.6% (Cheng et al. 2020). In 2021, the SC index reached the second highest level since 1955. The data show that most of the Pacific and East Indian Oceans, which are already relatively fresh climatologically, are currently undergoing freshening, while relatively saline areas such as the mid-latitude Atlantic Ocean are becoming more saline. The salinity change is attributed to the global water cycle intensification, which has already been amplified by 2%–4%/°C since 1960. Because the water-related extremes, including droughts, tropical cyclones, storms, ENSO, and snow, are all associated with the

water cycle, its changes have severe social and economic implications.

Within 1960–2021, global upper 2,000 m stratification increased by 5.3% (Fig. 6.3c), approximately 1% per decade. An even stronger ocean stratification increase, 5%–18%, has been observed for the upper 150 m. In the middle and high latitudes, significant increases in ocean stratification appear within 1,500–2,000 m, implying an impact on deep ocean stability by climate change. The increase in vertical stratification is mainly caused by stronger upper ocean warming than the deep ocean, but the contributions of salinity changes are also crucial locally (Li et al. 2020). For example, the salinity change in the western tropical Pacific Ocean contributes to >50% of the stratification increase; in the polar regions, the sea ice decline and ice sheet mass loss dominate the ocean stratification change.

Furthermore, we adopted the DORS dataset to quantitatively analyze the spatial variation trend and vertical evolution characteristics of the global ocean subsurface temperature upper 2,000 m from 1993 to 2020. The results indicated that all ocean basins dramatically warmed under global warming from 1993 to 2020, and the global ocean warming had a certain degree of spatial heterogeneity (Fig. 6.4). The ocean warming signal exhibits a distinctive vertical evolution characteristic from the upper layer to the subsurface and deeper layers, indicating that more and more heat is sequestered and stored by the subsurface and deeper ocean (SDO), and the SDO is playing an increasingly important role in regulating the energy balance of Earth's climate system (Fig. 6.5). Overall, the new DORS dataset revealed that the ocean warming from 1993 to 2020 was worldwide and systematic. The global ocean is experiencing unprecedented warming during recent global climate change. The warming signal in the SDO is enhancing, and more and more heat is absorbed and stored in the SDO.

6.3.2.5 Highlights

- Based on the IAP global ocean-gridded observational dataset combined with the remote-sensing reconstruction dataset (DORS), the ocean changes under global warming have been assessed, including global upper 2,000 m temperature, salinity, and stratification in recent decades.
- From 1955 to 2021, the upper 2000 m of the global ocean has gotten warmer, and the warming has been accelerating. Ocean warming has consequences for human beings and ecosystems. It raises the global sea level, reduces the efficiency of ocean carbon uptake, increases the frequency/intensity of marine heat waves, strengthens tropical cycles, and causes more extreme rainfall.
- From 1955 to 2021, the existing salinity pattern has been amplified by 1.6%, with a “fresh get fresher and the salty get saltier” pattern in much of the ocean, indicating the “dry get drier and wet get wetter” paradigm of the amplification of the water cycle. This

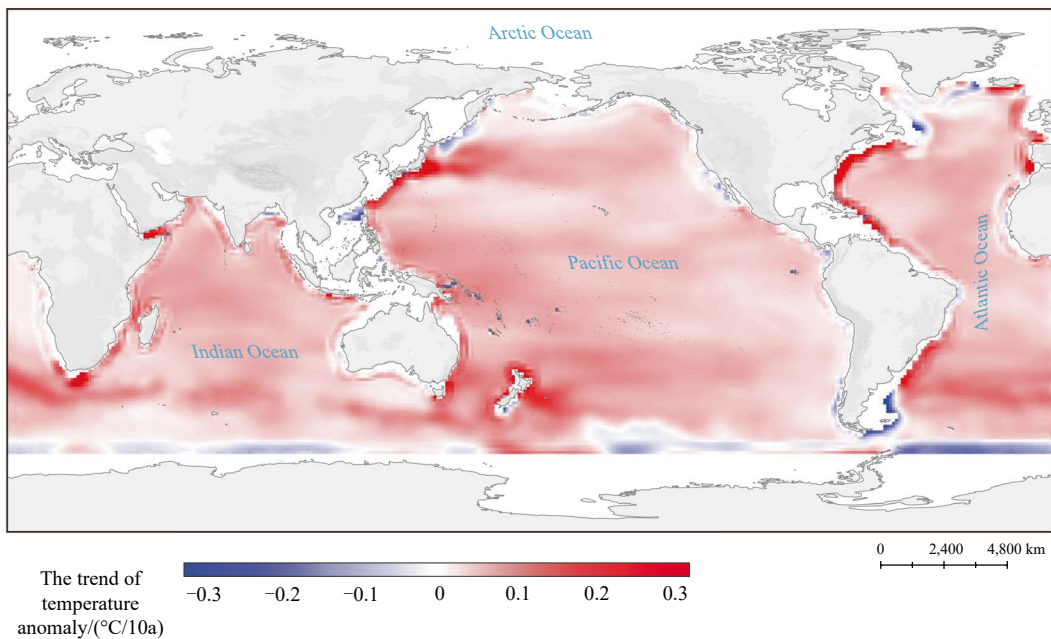


Fig. 6.4 Trend of temperature anomaly in the global upper 2000 m ocean from 1993 to 2020 (baseline: 1993–2012)

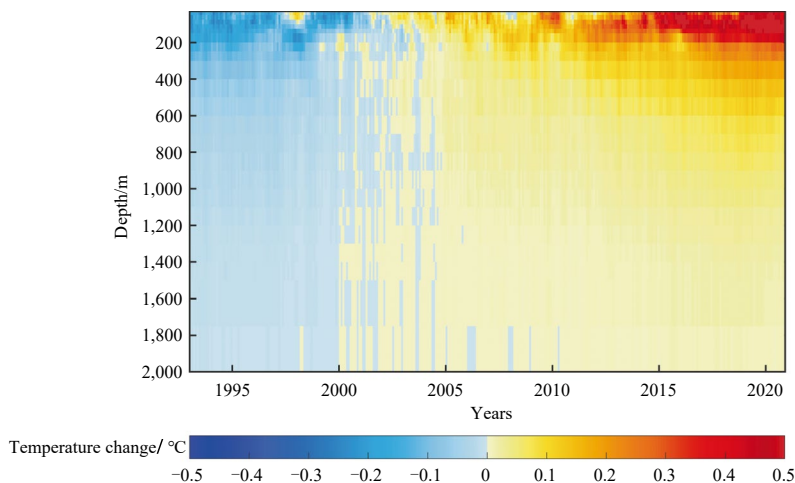


Fig. 6.5 Long-term change in the global ocean temperature vertical profile from 1993 to 2020 (baseline: 1993–2012)

implies the intensification of water-associated extremes.

- Since 1960, global upper 2000 m stratification has increased by 5.3%, reducing the efficiency of the vertical exchanges of heat, carbon, dissolved oxygen, and other constituents, increasing the surface warming level by reducing the ocean carbon uptake.

6.3.2.6 Discussion and Outlook

This study used the IAP global ocean-gridded observational dataset in combination with DORS remote-sensing reconstruction data products to assess the global changes of the key ocean physical parameters, including temperature, salinity, and stratification, which supports the achievement of SDG 13.1 and SDG 13.3. We want to stress that because of the slow response of the ocean to greenhouse gas emissions, emerging changes such as ocean warming and stratification changes caused by past carbon emissions will be committed for hundreds of years. Thus, ocean-related Climate Actions are critical in achieving SDGs and combating climate change (Abraham et al. 2022). To this end, ocean environment changes should be integrated into climate risk assessments, and attention should be paid to the impacts of ocean warming and sea level rise on ecological challenges.

This study focused on the upper 2000 m ocean because the Argo network, the key component of the global ocean observing system, mainly covers the upper 2000 m. Below 2000 m, the data are sparse and insufficient to observe deep ocean changes, requiring further study. The data distributions are still sparse in the coastal regions, polar regions, Indonesian Through Flow, and major inner seas. More observations are needed in these regions to reduce the uncertainty in climate monitoring. Furthermore, based on the perspective of satellite remote-sensing big data and artificial intelligence, the DORS retrieval and reconstruction technology can also provide important remote-sensing observation data support for the study of changes in the 3D physical environment of the global ocean, thus serving climate change action and the SDGs.

6.3.3 Analysis of Temporal and Spatial Changes in Net Ecosystem Productivity of Global Terrestrial Ecosystems, 2000–2020

Target: SDG 13.2: Integrate climate change measures into national policies, strategies, and planning.

6.3.3.1 Background

Terrestrial ecosystems play an important role in the global carbon cycle (Friedlingstein et al. 2020). The net ecosystem production (NEP) of terrestrial ecosystems is the difference between the carbon fixed by ecosystem photosynthesis and the carbon lost by ecosystem respiration. It also represents the net carbon accumulation rate of the ecosystem (Woodwell et al. 1978). As an important index of the carbon balance of terrestrial ecosystems, NEP is important for understanding the impacts of global climate change and achieving regional or global sustainable development. The accurate estimation of NEP is crucial for the scientific assessment of the carbon sequestration capacity of terrestrial ecosystems and better formulation of climate change responses (Eshel et al. 2019; Jung et al. 2020). However, since NEP is a smaller difference between two larger carbon fluxes (i.e., gross primary productivity of vegetation and ecosystem respiration), its estimation is subject to significant uncertainty.

In this study, based on the net ecosystem exchange (NEE) of CO₂ between terrestrial ecosystems and the atmosphere (NEP = -NEE) observed by the global flux network and data on environmental factors affecting the spatial and temporal variation of NEP, a random forest model driven mainly by multi-source remote-sensing data was constructed to estimate the global terrestrial NEP from 2000 to 2020. Through the quantitative analysis of the spatial and temporal changes of global terrestrial NEP and its response to climate and land cover factors in the last 20 years, we can comprehensively understand the spatial and temporal patterns of global terrestrial ecosystem carbon sinks and their response to global climate change.

6.3.3.2 Data

- Global FLUXNET2015 Dataset (<https://fluxnet.org/data/fluxnet2015-dataset/>).
- Terrestrial products of MODIS from 2000 to 2020 (https://lpdaac.usgs.gov/product_search/),

including surface temperature at 1 km spatial resolution and LAI, evapotranspiration, surface reflectance, and land cover products at 500 m spatial resolution. Temporal resolution is monthly for all data products except land cover products, which are annual.

- Global climate zoning and ecological zoning datasets.
- Air temperature and precipitation data from the 2000–2020 ERA5-Land reanalysis climate dataset, Palmer drought severity index (PDSI) from the CRU climate dataset.

6.3.3.3 Methods

In this study, the global terrestrial NEP was estimated using a spatial big data-driven random forest model. There were three main processes. (1) The NEE (NEE = -NEP) observations at 212 global flux sites were combined with data on environmental factors affecting the spatial and temporal variation of NEP. For this, we used a random forest model for the estimation of monthly NEE at the global flux site scale (Huang et al. 2021). (2) Using the random forest model constructed at the flux site scale combined with the spatially gridded prediction variables, we estimated the monthly NEE at the global scale from 2000 to 2020 and used its negative number to obtain the global terrestrial monthly NEP products from 2000 to 2020 (with a spatial resolution of 1 km). (3) We accumulated the monthly NEP products over years to obtain the global terrestrial annual NEP products and analyzed the spatial and temporal variations and driving mechanisms of global terrestrial NEP from 2000 to 2020. In addition, we combined the Theil–Sen median trend analysis and Mann–Kendall trend test to estimate the temporal change trends of NEP at global and regional scales. A partial correlation analysis method was used to analyze the response of NEP to climate factors (air temperature, precipitation, and PDSI) and land cover factors (tree cover, short vegetation cover, and bare ground cover) at global and regional scales.

6.3.3.4 Results and Analysis

1. Spatial Distribution Pattern of Global Terrestrial NEP

There are significant differences in the spatial distribution pattern of the global terrestrial annual mean NEP from 2000 to 2020 (Fig. 6.6). Among them, the tropical NEP is the largest, accounting for 69.9% of the global total NEP, followed by temperate (20.6%), cold (7.8%), and polar (1.4%) zones, and the smallest is the arid zone (0.3%). Specifically, the high value areas of NEP are located in tropical, subtropical, and cold-temperate forests, and the low value areas are widely distributed in arid and semi-arid regions, including the mid-western USA, Kazakhstan, northern Mongolia, and Australia.

2. Temporal Change Trends in Global Terrestrial NEP

From 2000 to 2020, the total global terrestrial NEP showed a significant increasing trend (0.05 Pg C/a, $p < 0.05$). The tropical

NEP showed a significantly increasing trend (0.016 Pg C/a, $p < 0.05$), followed by the arid (0.015 Pg C/a, $p < 0.05$), cold (0.014 Pg C/a, $p < 0.05$), and temperate zones (0.013 Pg C/a, $p < 0.05$). The polar NEP showed a non-significant decreasing trend (Fig. 6.7a). From 2000 to 2020, the increasing area of global terrestrial NEP was larger than the decreasing area. The significantly increasing area accounted for 22% of the total area, and the significantly decreasing area only accounted for 10%. The area percentage of different NEP change trends in all climate zones showed a similar pattern to the global scale, except for the polar zone (Fig. 6.7b). At the spatial scale, the increase in NEP was concentrated in the global forest ecoregions, including tropical moist forest, tropical dry forest, tropical mountain system, subtropical humid forest, subtropical dry forest, temperate continental forest, temperate montane, and boreal coniferous forest, while the decrease was concentrated in the tropical rainforest, boreal mountain system, boreal tundra woodland, and polar ecoregions (Fig. 6.7c).

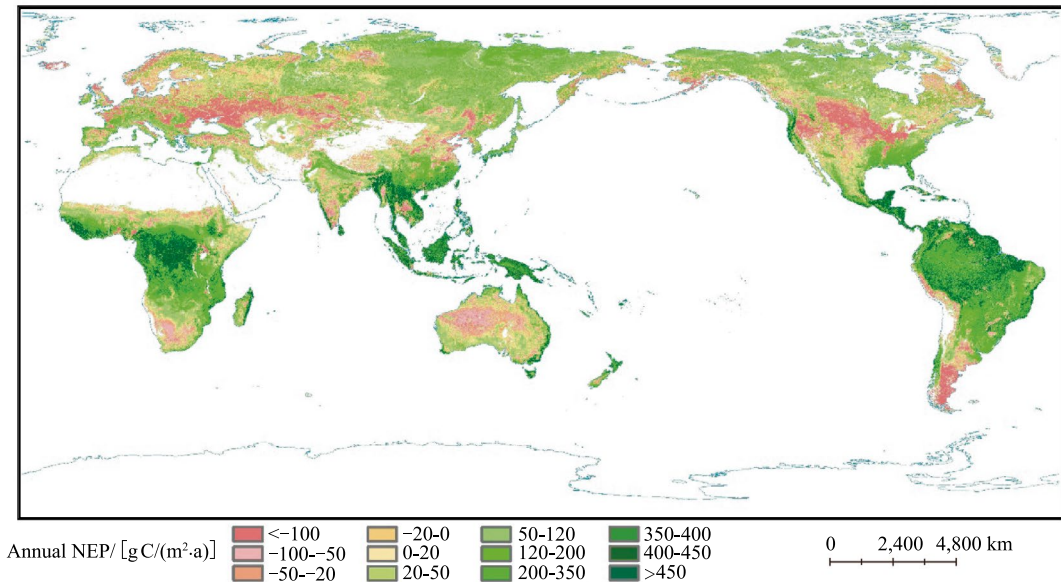


Fig. 6.6 Spatial distribution pattern of the global terrestrial annual mean NEP from 2000 to 2020 (1 km × 1 km)

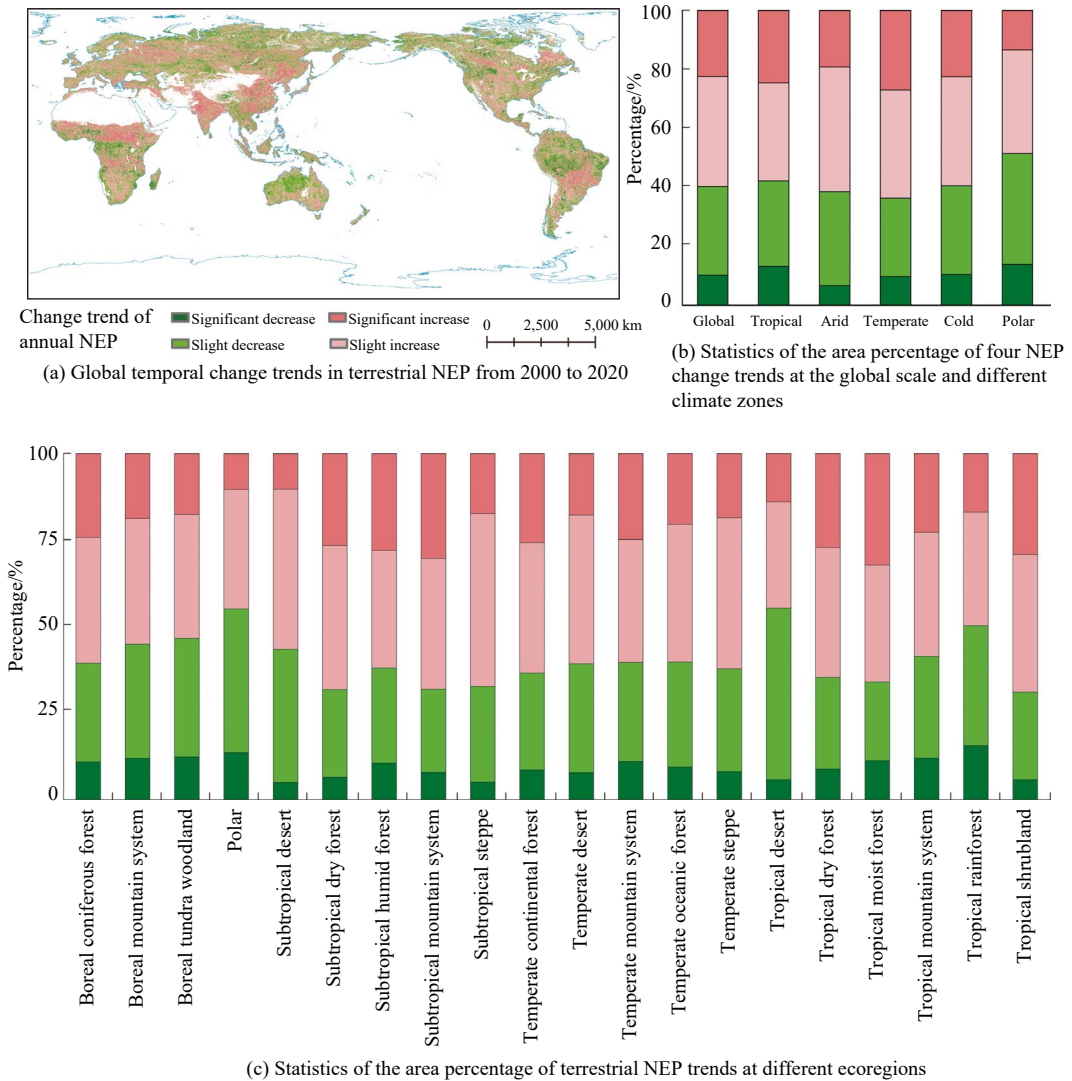


Fig. 6.7 Statistics of global temporal change trends in terrestrial NEP from 2000 to 2020

3. Analysis of the Driving Factors of Spatial and Temporal Changes in Global Terrestrial NEP

At the global scale, NEP showed a significant correlation with air temperature and forest cover (Fig. 6.8), indicating that the increase in global terrestrial NEP from 2000 to 2020 was mainly due to the increase in global air temperature and forest cover. At the regional scale, the correlation between NEP and the driving factors showed significant spatial

heterogeneity (Fig. 6.8). The comparative analysis of the partial correlation coefficients revealed that the changes in NEP in tropical and arid zones were more influenced by climate factors. However, the polar zone was more influenced by land cover factors, and the temperate zone was influenced by both climate and land cover factors.

The correlation between NEP and climate factors (air temperature, precipitation, and PDSI) is significantly stronger than that between

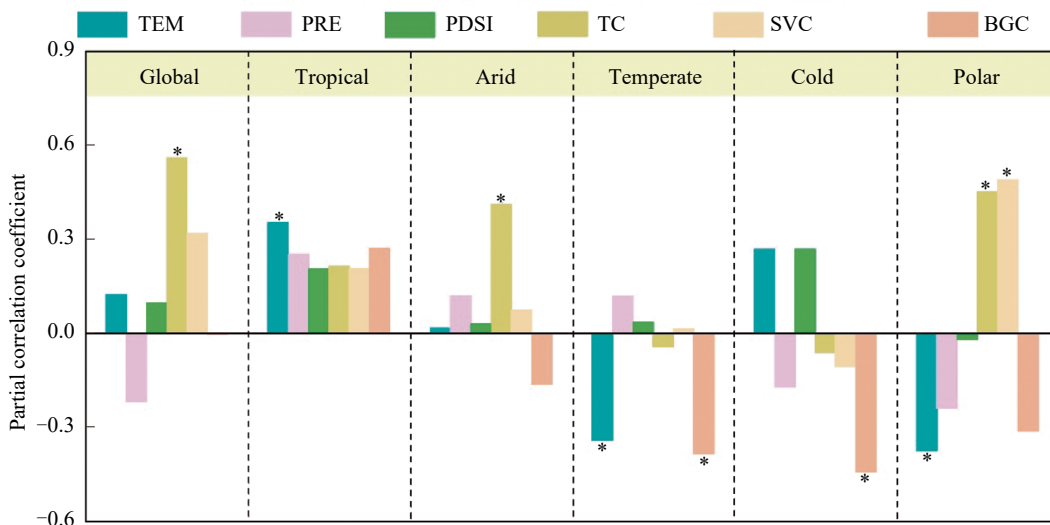


Fig. 6.8 Partial correlation coefficients between terrestrial NEP and climate and land cover factors at the global scale and different climate zones. *Note* for this and subsequent figures: Climate factors include air temperature (TEM),

precipitation (PRE), and PDSI. Land cover factors include tree cover (TC), short vegetation cover (SVC), and bare ground cover (BGC). * indicates that the partial correlations between the two factors are significant at a $p < 0.05$

NEP and land cover factors (tree cover, short vegetation cover, and bare ground cover) in ecologically fragile regions, such as global desert regions, temperate grassland regions, and mountainous regions in the north and tropics, where vegetation growth is more restricted by hydrothermal conditions (Fig. 6.9). This indicates that the changes in NEP in these ecoregions from 2000 to 2020 were mainly influenced by climate change, while the changes in NEP in other ecoregions were influenced by both climate and land cover factors.

6.3.3.5 Highlights

- From 2000 to 2020, the global terrestrial NEP was mainly distributed in the tropic (69.9% of the total global NEP), followed by the temperate (20.6%), cold (7.8%), and polar (1.4%) zones, and the smallest was the arid zone (0.3%).
- From 2000 to 2020, the total NEP of global terrestrial ecosystems showed a significant increasing trend, and the increase in temperature and forest cover was the main reasons for the increase in global terrestrial NEP.

6.3.3.6 Discussion and Outlook

Based on Earth observation big data technology, this study uses a data-driven approach to estimate global terrestrial NEP from 2000 to 2020 and analyzes its spatial and temporal changes and responses to climate and land cover factors. This study provides important data support for SDG 13.2 monitoring of global terrestrial carbon sources and sinks. It was found that the global terrestrial NEP showed a significant increasing trend from 2000 to 2020, and the increasing temperature and forest cover were the main factors for the increase in global terrestrial NEP. Our study is generally consistent with the results of previous studies on enhanced global terrestrial carbon sinks. In this study, observed data at global flux sites were used to construct a data-driven model. Since flux sites are usually set up in areas that do not contain the effects of disturbance factors, such as logging and fire, the global terrestrial NEP estimated by upward extrapolation of flux site data may be overestimated and will lead to uncertainties in the analysis of spatial and temporal changes in NEP.

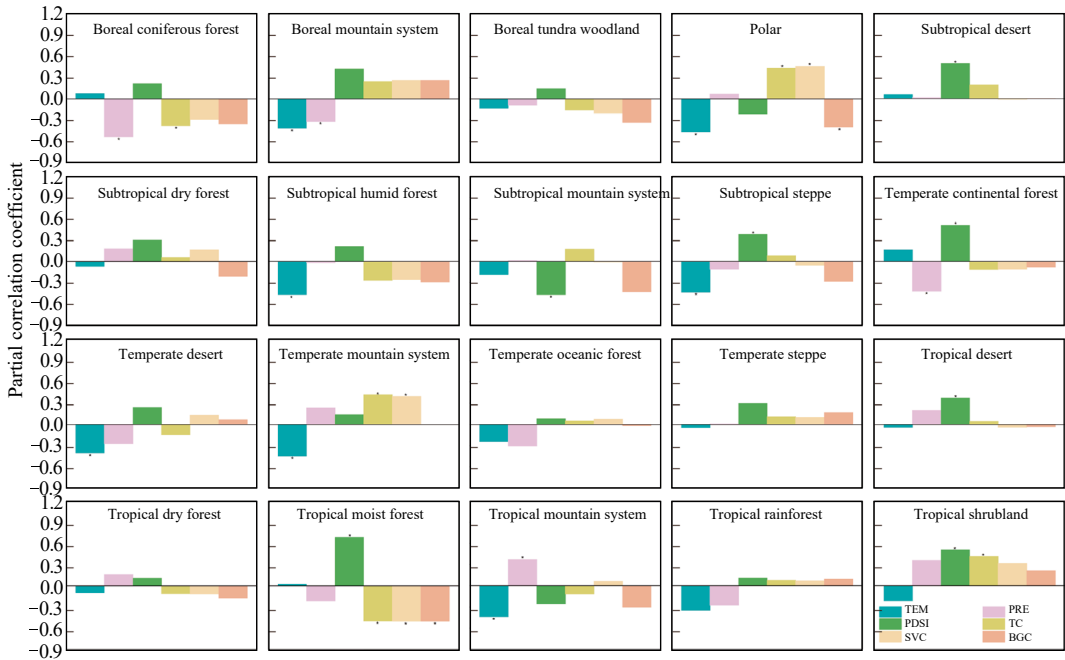


Fig. 6.9 Partial correlations between terrestrial NEP and climate and land cover factors for different global ecoregions

The spatial and temporal changes of global terrestrial NEP can be influenced by various factors. In this study, only climate and land cover factors were analyzed, and factors such as atmospheric CO_2 concentration and nitrogen deposition were not considered. Moreover, except for large-scale hydrothermal conditions and vegetation types, the influences of land use and land management on global terrestrial NEP are important in many human-intensive regions. Therefore, the influences of anthropogenic factors need to be considered when using global terrestrial NEP data to assess sustainable development processes.

6.3.4 Variability of Global Ocean Carbon Sink, 1992–2020

Target: SDG 13.2: Integrate climate change measures into national policies, strategies, and planning.

6.3.4.1 Background

Since the industrial revolution, increasing CO_2 emitted into the atmosphere by human activity has driven a rapid increase in atmospheric CO_2 concentration, from preindustrial levels of 280 ppm to the current levels of approximately 420 ppm (<https://gml.noaa.gov/ccgg/trends>). As a result, a series of environmental issues, such as global warming, have arisen. The CO_2 emitted into the atmosphere has three destinations: a portion remains in the atmosphere, contributing to the continuous rise of atmospheric CO_2 concentration; a portion is absorbed by terrestrial ecosystems, leading to a considerable increase in total global terrestrial NEP; and the remaining portion with a significant amount of CO_2 is taken up by the ocean. The ability of the global ocean to absorb CO_2 is typically measured by the sea-air CO_2 flux across the interface. When the sea-air CO_2 flux is negative, the ocean absorbs atmospheric CO_2 and is considered a carbon sink. Conversely, when the sea-air CO_2

flux is positive, the ocean releases CO₂ into the atmosphere and is considered a carbon source. The ocean is acknowledged as one of Earth's two primary carbon sinks, but there is considerable uncertainty in estimating the global air-sea CO₂ flux. The limited and unevenly distributed measurement of surface ocean partial pressure of CO₂ (*p*CO₂) is a crucial parameter for flux calculation. Various artificial neural network methods have been applied to fit the relationship between *p*CO₂ and other environmental factors for constructing global ocean-gridded *p*CO₂ products. However, the resulting carbon budget has exhibited significant differences, with differences reaching as high as 0.6 PgC/a in specific years. Such uncertainty has far-reaching impacts on the scientific understanding and accurate assessment of the global ocean carbon budget, further affecting climate change mitigation strategies. Therefore, it is imperative to improve the construction method of gridded *p*CO₂ products, reduce the uncertainty of CO₂ flux estimation, and further clarify the evolution of global ocean CO₂ uptakes. To this end, we designed a stepwise feedforward neural network (Stepwise FFNN) algorithm, constructed a global surface ocean-gridded *p*CO₂ product from 1992 to 2020, and conducted research on the trends in global ocean carbon sink intensity in 2022.

6.3.4.2 Data

- Global surface ocean *p*CO₂ data during 1992–2020 from the 1° Stepwise FFNN algorithm product (Zhong et al. 2022).
- Dry air mixing ratio of atmospheric CO₂ (*x*CO₂) data during 1992–2020 from the 1° NOAA Greenhouse Gas Marine Boundary Layer Reference product.
- Surface ocean temperature and salinity data during 1992–2020 from the 1° Estimating the Circulation and Climate of the Ocean (ECCO2) cube92 product.
- Sea ice coverage data during 1992–2020 from the 1° ERA5 product.
- Wind speed data during 1992–2020 from the 1° High-resolution Cross-Calibrated Multi-Platform product.

6.3.4.3 Methods

The estimation of global sea-air CO₂ flux includes two main steps. First, the Stepwise FFNN algorithm was formulated to construct the global surface ocean *p*CO₂ data. Specifically, the global ocean was divided into specific regions using the self-organizing map (SOM). Subsequently, in each region, optimal *p*CO₂ predictors minimizing the data construction error were selected by implementing the Stepwise FFNN algorithm from various environmental parameters, including temperature, salinity, dissolved oxygen, nitrate, phosphate, silicate, longitude, latitude, time series, year, month, mixed layer depth, sea surface height, the vertical velocity of ocean current, sea level pressure, atmospheric pressure, dry air mixing ratio of atmospheric CO₂ (*x*CO₂), El Niño index, bathymetry, wind speed, and chlorophyll concentration. Using the selected *p*CO₂ predictors and the forward feedback neural network with refined neuron sizes, gridded surface ocean *p*CO₂ data were constructed step by step in each SOM-divided region.

Second, the global sea-air CO₂ flux across the interface was estimated. The monthly CO₂ flux in each 1° grid was estimated using the formula:

$$F = k \cdot a \cdot (pCO_{2w} - pCO_{2atm}),$$

where *p*CO_{2w} represents the surface ocean *p*CO₂, the atmospheric *p*CO₂ (*p*CO_{2atm}) is obtained from the *x*CO₂ product, the gas transfer velocity (*k*) is computed through wind speed, and the solubility of CO₂ in seawater (*a*) is determined based on the temperature and salinity. Subsequently, the total annual CO₂ flux for each region was determined by integrating the products of monthly sea-air CO₂ flux and surface ocean areas in all 1° grids. Based on this analysis, the variability of ocean carbon sink was evaluated on both global and regional scales, and the primary factors responsible for the change in the carbon sink intensity were explored during the past three decades.

6.3.4.4 Results and Analysis

As suggested by the inter-annual variability of surface ocean *p*CO₂ from 1992 to 2020 (Fig. 6.10), global surface ocean *p*CO₂ increased

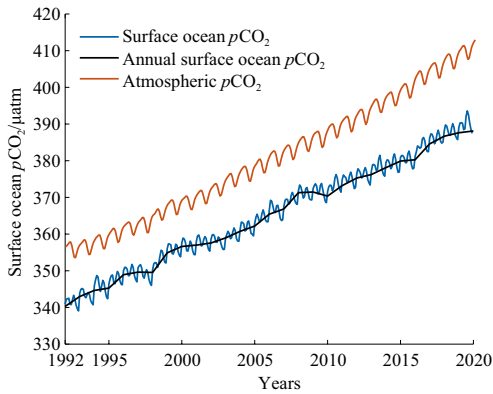
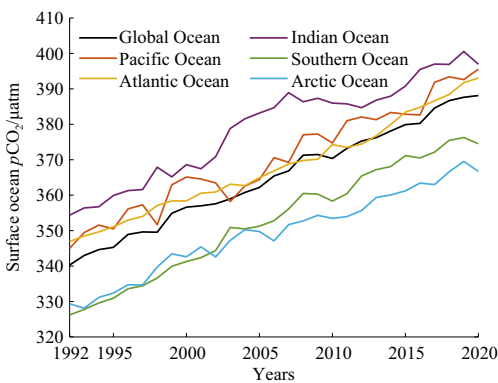
(a) Global average surface ocean $p\text{CO}_2$ in the past three decades(b) Regional average surface ocean $p\text{CO}_2$ in the past three decades

Fig. 6.10 Variability of **a** global and **b** regional average surface ocean $p\text{CO}_2$ in the past three decades

as the atmospheric CO_2 rose, but in an asynchronous manner. The decadal average growth rate of the atmospheric $p\text{CO}_2$ was $1.6 \mu\text{atm/a}$ from 1992 to 1999, $1.9 \mu\text{atm/a}$ from 2000 to 2009, and $2.4 \mu\text{atm/a}$ from 2010 to 2020, while the average growth rate of the surface ocean $p\text{CO}_2$ was $1.91 \mu\text{atm/a}$, $1.77 \mu\text{atm/a}$, and $2.08 \mu\text{atm/a}$ in the recent three decades, respectively. Since 2000, the atmospheric $p\text{CO}_2$ has increased more slowly than the surface ocean, leading to an increasing sea-air $p\text{CO}_2$ difference across the interface. The surface ocean $p\text{CO}_2$ and its growth rate varied significantly in different regions. On the basin scale, the average surface ocean $p\text{CO}_2$ was the highest in the Indian Ocean and the lowest in the Arctic Ocean, while the average growth rate was the highest in the Southern Ocean ($1.87 \mu\text{atm/a}$) and the lowest in the Arctic Ocean ($1.39 \mu\text{atm/a}$). These

differences caused the different carbon sink capacities across the oceans.

The annual average global ocean carbon sink intensity from 1992 to 2020 was estimated to be 1.61 PgC/a , with the majority taking place in the temperate oceans and the subpolar North Atlantic Ocean, while the equatorial Pacific was the leading carbon source (Fig. 6.11). In addition, carbon sources appeared in the subpolar North Pacific, Northwest Indian Ocean, equatorial Atlantic, and the Southern Ocean south of 50°S , contributing to the significant regional difference in global sea-air CO_2 flux.

The variability of global sea-air CO_2 flux during 1992–2020 can be divided into four periods based on the trend (Fig. 6.12): weakening during 1992–2001 from -1.77 PgC/a to -1.19 PgC/a ; rapid strengthening during 2002–2003 until -1.59 PgC/a ; another weakening during 2004–2008 until 1.24 PgC/a ; and continuous strengthening since 2008, reaching 2.22 PgC/a until 2020. During the recent strengthening period from 2008 to 2020, the global ocean carbon sink increased by 0.98 PgC/a , with an average strengthening trend of 0.08 PgC/a . On the regional scale, the variability of sea-air CO_2 flux was mainly in the Pacific Ocean, followed by the Southern Ocean. The variability of the Pacific carbon sink was almost synchronous with the global ocean carbon sink. They were the results of El Niño and La Niña events on the equatorial Pacific carbon source. The enhanced upwelling in the eastern equatorial Pacific Ocean transported more deep waters with a high concentration of dissolved inorganic carbon (DIC) to the surface, leading to the enhancement of the carbon source there and the corresponding weakening of the global ocean carbon sink. The equatorial Pacific carbon source significantly weakened during the 1997–1998 and 2015–2016 El Niño events and strengthened at the end of El Niño events and the beginning of La Niña events. Although tropical areas in other basins were also carbon sources, the influences of El Niño and La Niña events were insignificant. The fluctuating equatorial Pacific carbon source drives the short-term variability of global ocean carbon sink.

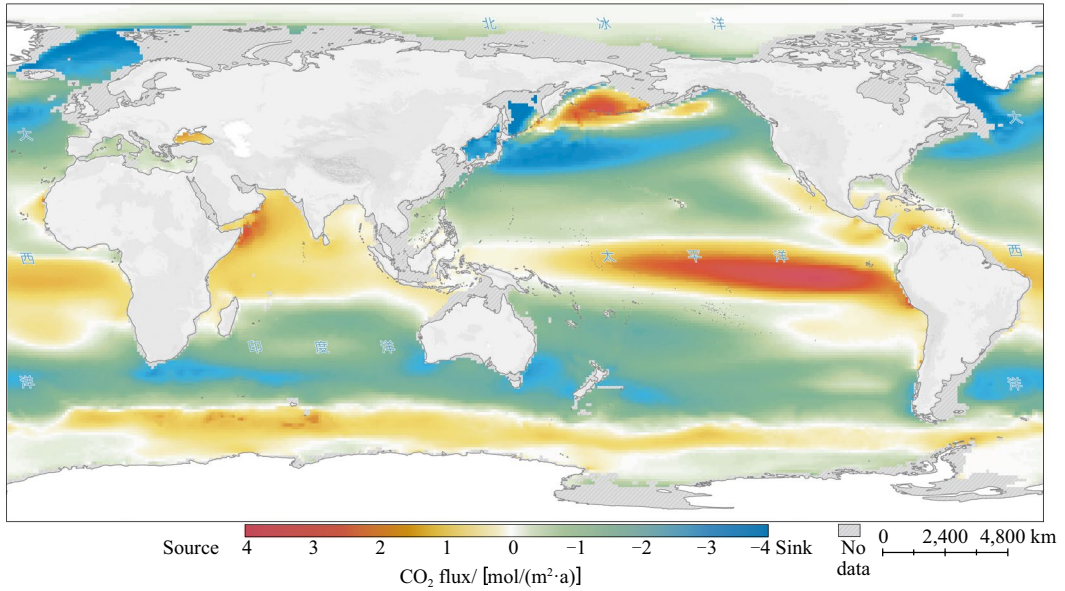


Fig. 6.11 Spatial distribution of average global sea-air CO₂ flux during 1992–2020

Since 2008, the continuously strengthening carbon sinks in the Indian Ocean, Atlantic Ocean, and Southern Ocean have driven the expanded ocean carbon sink, substantially slowing the rise of atmospheric CO₂.

6.3.4.5 Highlights

- Based on the Stepwise FFNN algorithm, optimal $p\text{CO}_2$ predictors were selected in different global ocean regions, reducing the construction error of gridded data and the uncertainty in global ocean carbon sink estimation.
- The global ocean is generally a strong sink of atmospheric CO₂, and since 2008, it has strengthened continuously, but with major fluctuations due to El Niño and La Niña events during 1992–2020.

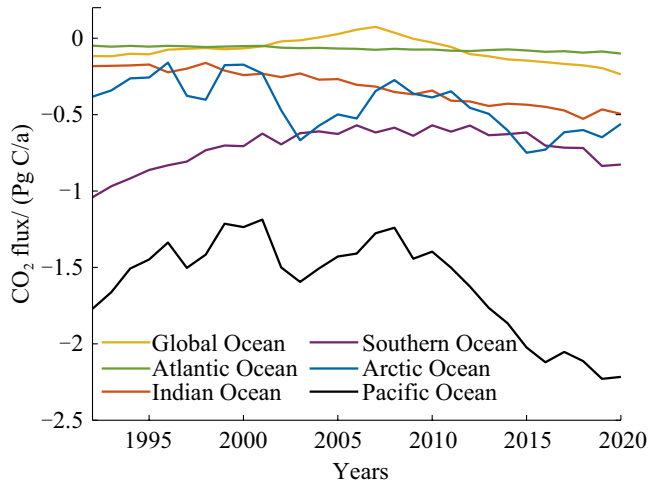
6.3.4.6 Discussion and Outlook

In this case study, the monthly global $1^\circ \times 1^\circ$ gridded $p\text{CO}_2$ data were constructed using the Stepwise FFNN algorithm, based on which the global sea-air CO₂ flux and its variability during 1992–2020 were estimated, providing

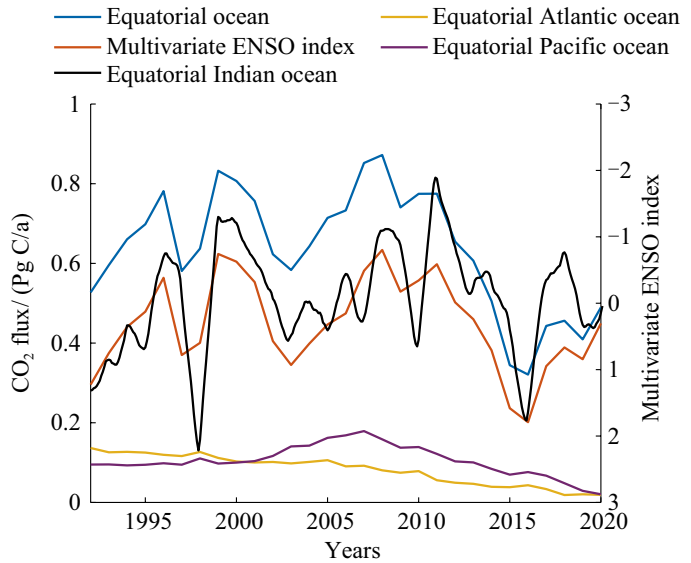
substantial data support for the monitoring of CO₂ in SDG 13.2.

The global ocean is overall a strong carbon sink for atmospheric CO₂. Since 2008, the global ocean carbon sink has continuously strengthened, with significant short-term fluctuations over the period 1992–2020. In addition to the atmospheric CO₂ concentration, natural factors such as wind speed, temperature, phytoplankton, and upwelling affect the intensity of ocean carbon sinks. Any behavior or phenomenon that can cause changes in these factors may also affect the intensity of ocean carbon sinks, such as global warming, El Niño and La Niña events, and the reduction of anthropogenic carbon emissions. Theoretically, as long as atmospheric CO₂ concentrations continue to increase, the intensity of ocean carbon sinks will also increase. However, under the scenario of increasing terrestrial carbon sinks and potential future reductions in CO₂ emissions, the increasing rate in the atmospheric CO₂ concentration and the subsequent rise in ocean carbon sink intensity will be slower. Whether the global ocean will continue to absorb CO₂ emitted by human activity in the future is crucial

Fig. 6.12 Variability of **a** the global sea-air CO₂ flux and **b** equatorial carbon sources



(a) Variability of global and regional sea-air CO₂ flux



(b) Comparison between equatorial sea-air CO₂ flux and multivariate ENSO index

for formulating global climate change counter-measures. Future research on ocean carbon sinks should concentrate on monitoring the time when the rate of atmospheric CO₂ increase begins to decelerate, as well as the response of ocean carbon sinks, both globally and regionally.

6.4 Summary

This chapter focuses on three specific goals of SDG 13, Climate Action: disaster monitoring and reduction, climate change early warning, and global land/marine carbon sink estimation.

Big Earth Data was used to successfully measure and monitor two indicators of SDG 13 (SDG 13.1.1, losses from disasters, and SDG 13.2.2, greenhouse gas emissions). We have also developed global climate change and carbon balance data products to provide decision-making support for Climate Action.

Based on the research in this chapter, we note the following:

- (1) Regarding SDG 13.1.1, research has shown an increase in the frequency and intensity of global heat waves and ocean warming, and therefore, it is still necessary to improve disaster resistance, increase technological means, and enhance our ability to withstand more extreme disasters.
- (2) As global warming, forest coverage, and atmospheric CO₂ concentrations increase, the carbon sequestration capacity of the global land and oceans is also increasing. These changes reflect both the necessity of continuing to implement afforestation policies, and the risk that the increase in marine carbon sink may lead to ocean acidification. In the future, we need to pay attention to the systematic problems of changes in terrestrial and marine ecosystems.

Big Earth Data has shown significant advantages in monitoring the indicators of progress toward SDG 13. In the future, it is necessary to explore the monitoring of natural disasters and greenhouse gas emissions.

References

- Abraham J, Cheng LJ, Mann ME et al (2022) The ocean response to climate change guides both adaptation and mitigation efforts. *Atmos Oceanic Sci Lett* 15(4):100221
- Cheng LJ, Abraham J, Trenberth KE et al (2022) Another record: ocean warming continues through 2021 despite La Niña conditions. *Adv Atmos Sci* 39(3):373–385
- Cheng LJ, Trenberth KE, Gruber N et al (2020) Improved estimates of changes in upper ocean salinity and the hydrological cycle. *J Clim* 33(23):10357–10381
- Cheng L, Zhu J, Cowley R et al (2014) Time, probe type, and temperature variable bias corrections to historical expendable bathythermograph observations. *J Atmos Oceanic Tech* 31:1793–1825
- Cheng L, Zhu J (2016) Benefits of CMIP5 multimodel ensemble in reconstructing historical ocean subsurface temperature variations. *J Clim* 29:5393–5416
- Coccia G, Siemann AL, Pan M et al (2015) Creating consistent datasets by combining remotely-sensed data and land surface model estimates through Bayesian uncertainty post-processing: the case of land surface temperature from HIRS. *Remote Sens Environ* 170:290–305
- Eshel G, Dayalu A, Wofsy SC et al (2019) Listening to the forest: an artificial neural network-based model of carbon uptake at Harvard forest. *J Geophys Res Biogeosci* 124(3):461–478
- Friedlingstein P, O’Sullivan M, Jones MW et al (2020) Global carbon budget 2020. *Earth Syst Sci Data* 12:3269–3340
- Gouretski V, Cheng L, Boyer T (2022) On the consistency of the bottle and CTD profile data. *J Atmos Oceanic Tech* 39:1869–1887. <https://doi.org/10.1175/JTECH-D-22-0004.1>
- Huang N, Wang L, Zhang YL et al (2021) Estimating the net ecosystem exchange at global FLUXNET sites using a random forest model. *IEEE J Sel Top Appl Earth Observations Remote Sens* 14:9826–9836
- IPCC (2022) Climate change 2022: mitigation of climate change. In: Working group III contribution to the sixth assessment report of the intergovernmental panel on climate change. IPCC working group 1992. The IPCC supplementary report. Cambridge University Press
- Jung M, Schwalm C, Migliavacca M et al (2020) Scaling carbon fluxes from eddy covariance sites to globe: Synthesis and evaluation of the FLUXCOM approach. *Biogeosciences* 17(5):1343–1365
- Li GC, Cheng LJ, Zhu J et al (2020) Increasing ocean stratification over the past half-century. *Nat Clim Chang* 10(12):1116–1123
- Mora C, Dousset B, Caldwell I et al (2017) Global risk of deadly heat. *Nat Clim Chang* 7:501–506
- Perkins SE (2015) A review on the scientific understanding of heatwaves—their measurement, driving mechanisms, and changes at the global scale. *Atmos Res* 164–165:242–267
- Qin DH (2015) China National Assessment Report on risk management and adaptation of climate extremes and disasters (refined edition). Science Press, Beijing (in Chinese)
- Su HA, Jiang JW, Wang A et al (2022) Subsurface temperature reconstruction for the global ocean from 1993 to 2020 using satellite observations and deep learning. *Remote Sensing* 14(13):3198
- Su H, Zhang TY, Lin MJ et al (2021) Predicting subsurface thermohaline structure from remote sensing data based on long short-term memory neural networks. *Remote Sens Environ* 260:112465

- Tan ZL, Cheng V, Gouretski B et al (2023) A new automatic quality control system for ocean profile observations and impact on ocean warming estimate. *Deep Sea Res Part I* 194:103961. <https://doi.org/10.1016/j.dsr.2022.103961>
- UN (2021) The sustainable development goals report 2021. UN, New York
- Woodwell GM, Whittaker RH, Reiners WA et al (1978) The biota and the world carbon budget: the terrestrial biomass appears to be a net source of carbon dioxide for the atmosphere. *Science* 199(4325):141–146
- World Meteorological Organization (2022) State of the global climate 2021. <https://library.wmo.int/records/item/56300-state-of-the-global-climate-2021>
- Zhong GR, Li XG, Song JM et al (2022) Reconstruction of global surface ocean pCO₂ using region-specific predictors based on a stepwise FFNN regression algorithm. *Biogeosciences* 19(3):845–859

Open Access This chapter is licensed under the terms of the Creative Commons Attribution-NonCommercial-NoDerivatives 4.0 International License (<http://creativecommons.org/licenses/by-nc-nd/4.0/>), which permits any noncommercial use, sharing, distribution and reproduction in any medium or format, as long as you give appropriate credit to the original author(s) and the source, provide a link to the Creative Commons license and indicate if you modified the licensed material. You do not have permission under this license to share adapted material derived from this chapter or parts of it.

The images or other third party material in this chapter are included in the chapter's Creative Commons license, unless indicated otherwise in a credit line to the material. If material is not included in the chapter's Creative Commons license and your intended use is not permitted by statutory regulation or exceeds the permitted use, you will need to obtain permission directly from the copyright holder.





7.1 Background

Covering 71% of Earth's surface, oceans are the largest ecosystem on Earth and home to more than 80% of the world's life. SDG 14, as part of the 2030 Agenda and its 17 transformative goals, emphasizes the need to conserve and sustainably use sea and marine resources. Globally, however, the implementation of most of the SDG 14 targets has been unsatisfactory. The UN's Second World Ocean Assessment released in April 2021 reported that many pressures from human activity have continued to degrade the oceans since 2015, including important habitats such as mangroves and coral reefs (UN 2021). In July 2022, the UN Ocean Conference adopted the Lisbon Declaration, calling for increased science and innovation-based action to address current ocean emergencies.

Derived mainly from large-scale marine scientific experimental devices with spatial properties, detection equipment, remote sensors, socioeconomic observations, and computer simulation processes, Big Earth Data has become the "new key" to our understanding of the oceans and the "new engine" of knowledge

discovery. In recent years, Chinese research institutions, universities, and government departments have made great efforts to explore Big Earth Data and its related technologies and methods to serve the implementation of SDG 14 and have accumulated rich practical experience in the production of datasets and the construction of evaluation models. In this chapter, we focus on the two themes of reducing marine pollution and protecting marine ecosystems, focusing on the research results in the distribution of harmful red tide organisms, the monitoring of coral reef bleaching and the thermal environment, and the analysis of marine phytoplankton particle size structure, in order to better promote the realization of SDG 14.

7.2 Main Contributions

The three case studies in this chapter demonstrate the monitoring and evaluation of SDG 14.1 and SDG 14.2 in China and its surrounding areas. The main contributions are as follows (Table 7.1).

Table 7.1 Cases and their main contributions

Targets	Tiers	Cases	Contributions
SDG 14.1 By 2025, prevent and significantly reduce marine pollution of all kinds, in particular from land-based activities, including marine debris and nutrient pollution	Tier II	Spatial distribution characteristics of harmful algal bloom species in the South China Sea and surrounding waters	<p>Data product: spatial distribution dataset of harmful algal bloom species in the South China Sea and the surrounding waters</p> <p>Method and model: Canonical correspondence analysis (CCA) was used to study the relationship between the relative abundance of important harmful algal bloom species and environmental factors</p>
SDG 14.2 By 2020, sustainably manage and protect marine and coastal ecosystems to avoid significant adverse impacts, including by strengthening their resilience, and take action for their restoration in order to achieve healthy and productive oceans	Tier II	Monitoring and early warning of coral reef bleaching and the thermal environment in China-ASEAN seas	<p>Data product: ASEAN sea coral reef bleaching and thermal environment monitoring and early warning dataset</p> <p>Method and model: a computational model for the thermal environment of coral reef bleaching</p> <p>Decision support: support for government agencies in environmental assessment, protection, and policy formulation of coral reefs</p>
		Dynamic changes in phytoplankton size class in the North Indian Ocean	<p>Data product: dataset on the distribution of phytoplankton size class in the NIDO</p> <p>Method and model: regionally adjusted three-component inversion model of phytoplankton for the NIDO</p> <p>Decision support: scientific support on the formation of surface algal blooms and the management of ecological impacts of tropical cyclones in the NIDO</p>

7.3 Case Studies

7.3.1 Spatial Distribution Characteristics of Harmful Algal Blooms Species in the South China Sea and Surrounding Waters

Target: SDG 14.1: By 2025, prevent and significantly reduce marine pollution of all kinds, in particular from land-based activities, including marine debris and nutrient pollution.

7.3.1.1 Background

According to the statistics of the Intergovernmental Oceanographic Commission (IOC) of UNESCO, there are more than 200 marine harmful algal bloom (HAB) species, of which dinoflagellates account for more than 70%. Several diatoms (e.g., *Pseudo-nitzschia pungens*), raphidophyte (e.g., *Chattonella marina*), and haptophyte (e.g., *Phaeocystis globosa*) species also form HABs (Lundholm et al. 2022).

HABs devastate the marine environment, human health, and social economy. Some species are able to produce hemolytic toxins, which will directly lead to the mortality of other marine organisms, especially cultured fish and shellfish. Other species produce toxins that will be further accumulated and transformed after feeding by fish or shellfish and endanger human health and even cause death through the food chain. According to the symptoms of poisoning due to human consumption of contaminated fish or shellfish, the toxins can be divided into paralytic shellfish poison (PSP), diarrhetic shellfish poison (DSP), neurotoxic shellfish poison (NSP), amnesic shellfish poison (ASP), and ciguatera fish poisoning (CFP).

According to a report issued by the FAO, the South China Sea is one of the most important mariculture areas in the world. China accounts for 57% of the world's fish production. Grouper and other important economic fish are mainly cultivated in Hainan and Guangdong, and China ranks among the top ten countries in terms of shellfish production in the world (FAO 2020).

Southeast Asian countries had witnessed 333 HABs by December 2019, and most food poisoning was caused by PSP-producing species (Hallegraeff 2021). *Gymnodinium catenatum*, *Alexandrium tamiyavanichi*, and *Pyrodinium bahamense* are the dominant PSP-producing species in the South China Sea. The first two species are widely distributed in the South China Sea, while the latter is only found in the Philippines and Indonesia (Yñiguez et al. 2021; Gu et al. 2022). In addition, *Alexandrium fragae*, which was reported to produce PSP recently, was also detected in the Gulf of Thailand (Fu et al. 2021), but it is unclear whether it exists in the other parts of the South China Sea as well. Although few other poisons, such as DSP, have been reported in Southeast Asian countries, species producing such toxins also occur in this area. In the context of global change, HABs may increase in frequency and scale in the South China Sea, posing a serious threat to sustainable marine development.

Ichthyotoxic species including *Chattonella marina*, *Karlodinium australe*, and *Margalefidinium polykrikoides*, frequently broke out in the South China Sea and caused losses to marine aquaculture recently (Yñiguez et al. 2021). For example, *Karlodinium australe* blooms in Johor Strait caused the mortality of hundreds of tons of fish in 2014 (Lim et al. 2014).

The main goal of SDG 14.1 is to prevent and significantly reduce various types of marine pollution, especially nutrient pollution from land-based sources. Excessive nutrient emissions can induce changes in the community structure of phytoplankton, especially leading to the dominance of HAB species. Many HAB species are usually difficult to preserve, and their morphological characteristics are subtle, so it is important to rely on molecular characteristics for identification. Compared with the traditional morphological observation method, the metabarcoding method based on high-throughput sequencing technology can accurately and comprehensively reveal the diversity of HAB species in water samples. On the basis of an earlier investigation in the Gulf of Thailand (Fu et al.

2021), this case expanded the research scope to other sea areas in the South China Sea, and the sampling was carried out nearly synchronously to fully understand the geographical distribution characteristics of HAB species in this region.

7.3.1.2 Data

Supported by the China-ASEAN Maritime Cooperation Fund, Asia Regional Cooperation Special Fund, and the National Natural Science Foundation of China, the Third Institute of Oceanography of the Ministry of Natural Resources carried out surveys independently and with partners of ASEAN countries. A total of 130 stations were sampled in the Pearl River Estuary, East of Hainan Island, Beibu Gulf (Weizhou Island), Gulf of Thailand (Sichang Island), Malay Peninsula, Semerak, Johor Strait, Malacca Strait, and Lombok Island from August to November 2019 (Fig. 7.1). The HAB species data are originated from the high-throughput sequencing results of these samples. The environmental data were collected from the field surveys, and the inorganic nitrogen and inorganic phosphate data of some stations were obtained through satellite remote sensing inversion (<http://marine.copernicus.eu/services-portfolio/access-to-products>). Data format includes species name, abundance, station, longitude and latitude, inorganic nitrogen, inorganic phosphorus, silicate, temperature, salinity, and dissolved oxygen.

7.3.1.3 Methods

A YSI multi-parameter water quality instrument was used to measure temperature, salinity, dissolved oxygen, chlorophyll *a* (Chl*a*), and other environmental factors in situ. Nitrate, phosphate, and silicate were determined by the nutrient automatic analyzer. One-liter surface water samples were collected and filtered on a polycarbonate membrane with 0.22 μm pore diameter and stored at $-20\text{ }^{\circ}\text{C}$. The environmental deoxyribonucleic acid (DNA) was extracted and amplified with the primer targeting the internal transcribed spacer region (ITS1). The amplicons were sequenced using a HiSeq 2500 platform

(Illumina) based on a paired-end strategy ($2 \times 250\text{ bp}$). The reads obtained from HiSeq sequencing were analyzed using USEARCH v11.0.667 and VSEARCH v2.14.2. Reads were clustered to a zero-radius operational taxonomic unit (ZOTU) according to 97% similarity and the most abundant read was selected as the representative read for each ZOTU. Finally, ZOTU annotation was conducted on the representative read of each ZOTU against the in-house curated ITS database, with the similarity at a cutoff level of 99%. CCA was used to investigate the relationship between the relative abundance of dominant HABs species and environmental factors.

7.3.1.4 Results and Analysis

1. Dinoflagellate Community Composition

In all, 416 ZOTUs were obtained by clustering based on the high-throughput sequencing results targeting ITS1. Among them, 84 species were annotated with 26 HAB species, including six PSP-producing, five DSP-producing, and six ichthyotoxin species. This method can effectively obtain background data on HABs in the sea areas, thus strengthening the ability to resist HAB disasters and promoting sustainable management and protection of the marine and coastal ecosystems.

The similarity analysis results of dinoflagellate community composition showed that the differences within a sea area were smaller than those between areas, except for the large differences between the Semerak (located in a nearshore lagoon) of the Malay Peninsula and its surrounding waters. Therefore, Semerak is listed separately, and the study area is divided into nine sea areas (Fig. 7.1).

The community composition of HAB species in the three areas of Malaysia (Semerak, Malay Peninsula, and Malacca Strait) was similar, and *Alexandrium pseudogonyaulax* and *Karlodinium australe* were the dominant species. In addition, there were abundant *Dinophysis tripos* in the Malacca Strait. *Alexandrium pseudogonyaulax*, *Karlodinium austral*, and *Karenia papilionacea* were abundant in Sichang Island,

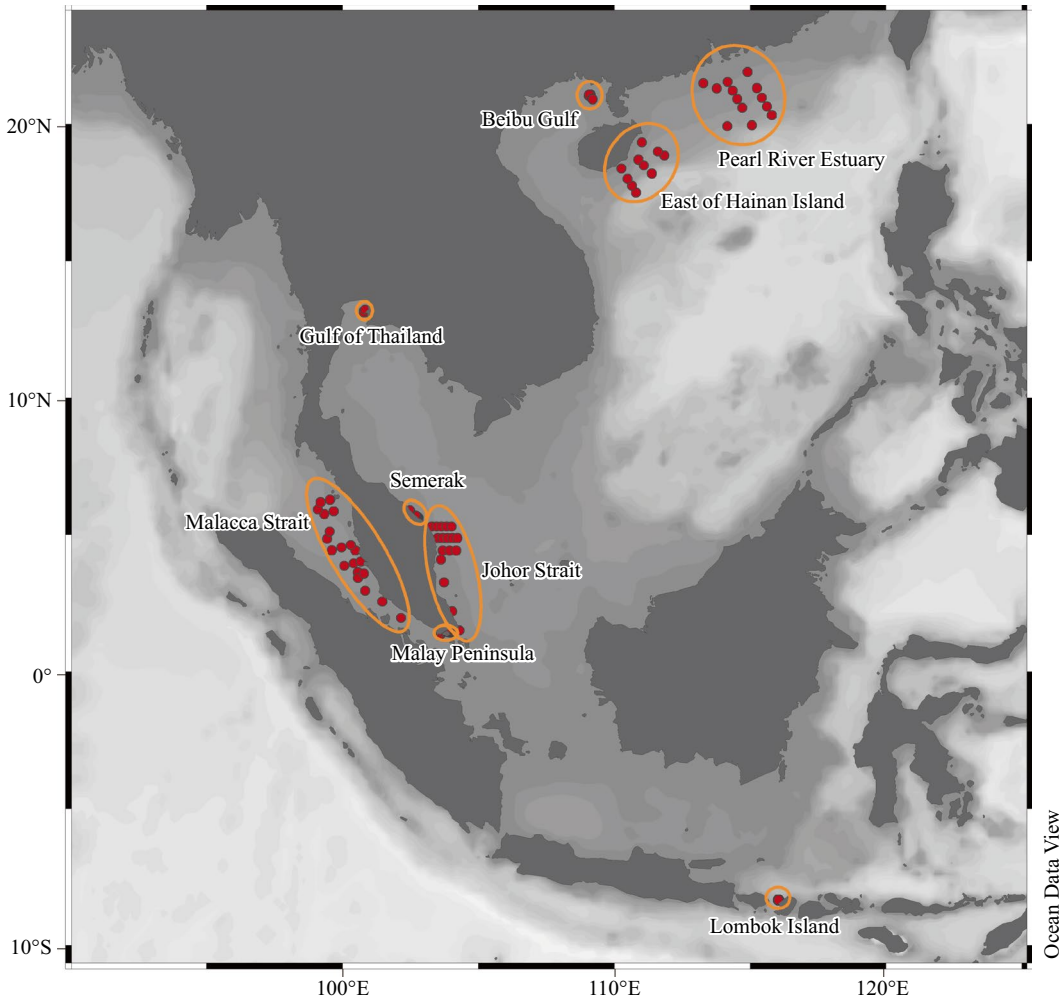


Fig. 7.1 Sampling stations and sea area division

Gulf of Thailand. The dominant species in the Johor Strait were *Prorocentrum steidingerae* and *Dinophysis caudata*. *Prorocentrum steidingerae* was also detected in the Pearl River Estuary, and additional *Azadinium spinosum* ribotype A and *Prorocentrum obtusidens* were also detected in the Pearl River Estuary and the East of Hainan Island. A large number of *Alexandrium pseudogonyaulax* and *Ostreopsis ovata* were found in Weizhou Island in the Beibu Gulf. There were abundant *Prorocentrum obtusidens* and *Alexandrium pseudogonyaulax* in Lombok Island, Indonesia (Fig. 7.2).

2. Distribution Characteristics of HAB Species

A total of six PSP-producing species have been found, among which *Alexandrium fraga* was distributed in the East of Hainan Island and Malacca Strait. *Alexandrium minutum* ribotype C was distributed in Semerak and Weizhou Island in the Beibu Gulf, and *Alexandrium ostenfeldii* was distributed in the Pearl River Estuary, Sichang Island in the Gulf of Thailand, Malacca Strait, Malay Peninsula, and Lombok Island. *Alexandrium*

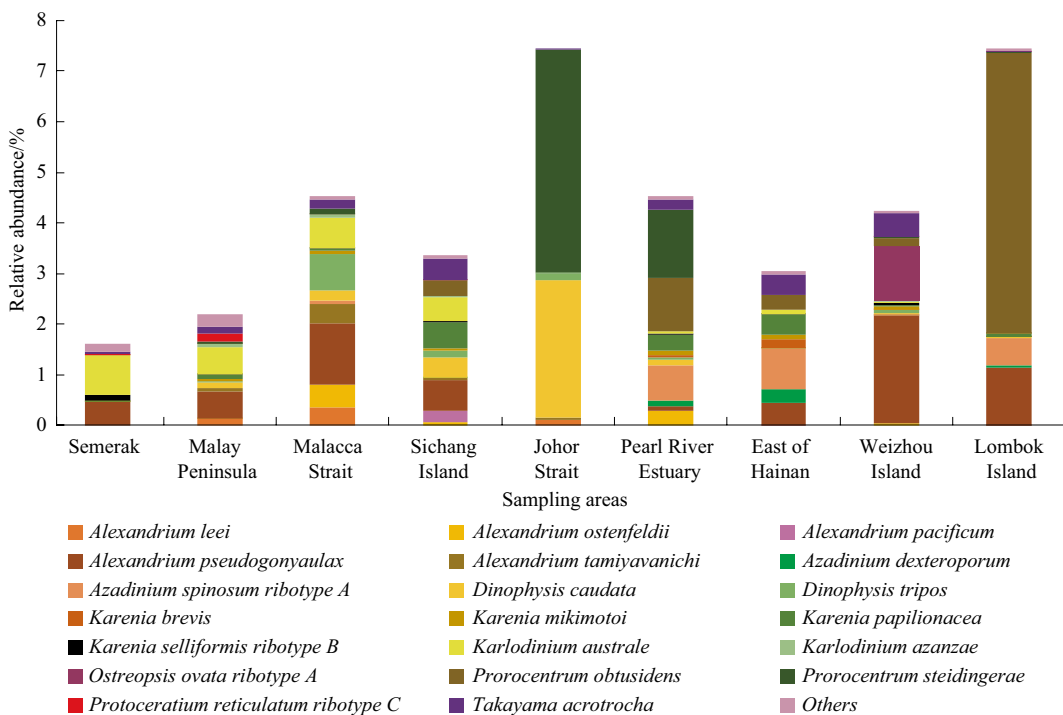


Fig. 7.2 Relative abundance of the main HAB species in nine sea areas

pacificum was distributed in the East of Hainan Island, Sichang Island in the Gulf of Thailand, and Lombok Island. *Alexandrium tamiyavanichi* was distributed in the Malay Peninsula, Johor Strait, Malacca Strait, and Sichang Island in the Gulf of Thailand. *Centrodinium punctatum* only appeared in the Pearl River Estuary (Fig. 7.3a).

Five DSP-producing species have been found. Among them, *Dinophysis caudata* and *Dinophysis tripos* were widely distributed in the South China Sea, but *Dinophysis sacculus* appeared in the Pearl River Estuary only. *Prorocentrum lima* was detected in Lombok Island, but *Prorocentrum steidingerae* was distributed in the Pearl River Estuary, Weizhou Island in the Beibu Gulf, Malay Peninsula, Johor Strait, Malacca Strait, and Lombok Island (Fig. 7.3b).

Six ichthyotoxin species were recorded. Among them, *Karenia brevis* was distributed in the Pearl River Estuary, East of Hainan Island, Weizhou Island in the Beibu Gulf, and Lombok Island, and *Karenia mikimotoi*,

Karenia selliformis, and *Karenia australe* were distributed in all areas except the Johor Strait. *Karlodinium digitatum* appeared in all areas except the Johor Strait and Semerak, and *Margalefidinium fulvescens* appeared in the Pearl River Estuary, East of Hainan Island, Malay Peninsula, and Lombok Island (Fig. 7.3c).

3. Relationship Between the Abundance of HAB Species and Environment

The CCA analysis showed that the two axes explained 16.03% ($P=0.007$) of the relationship between environmental factors and the relative abundance of the main HAB species, respectively (Fig. 7.4). The relative abundance of *Dinophysis caudata* was positively related to the concentration of phosphate and Chla, but it was negatively related to salinity and dissolved oxygen. The distribution of *Dinophysis caudata* was widespread, but the relative abundance was the highest in the Johor Strait, which may

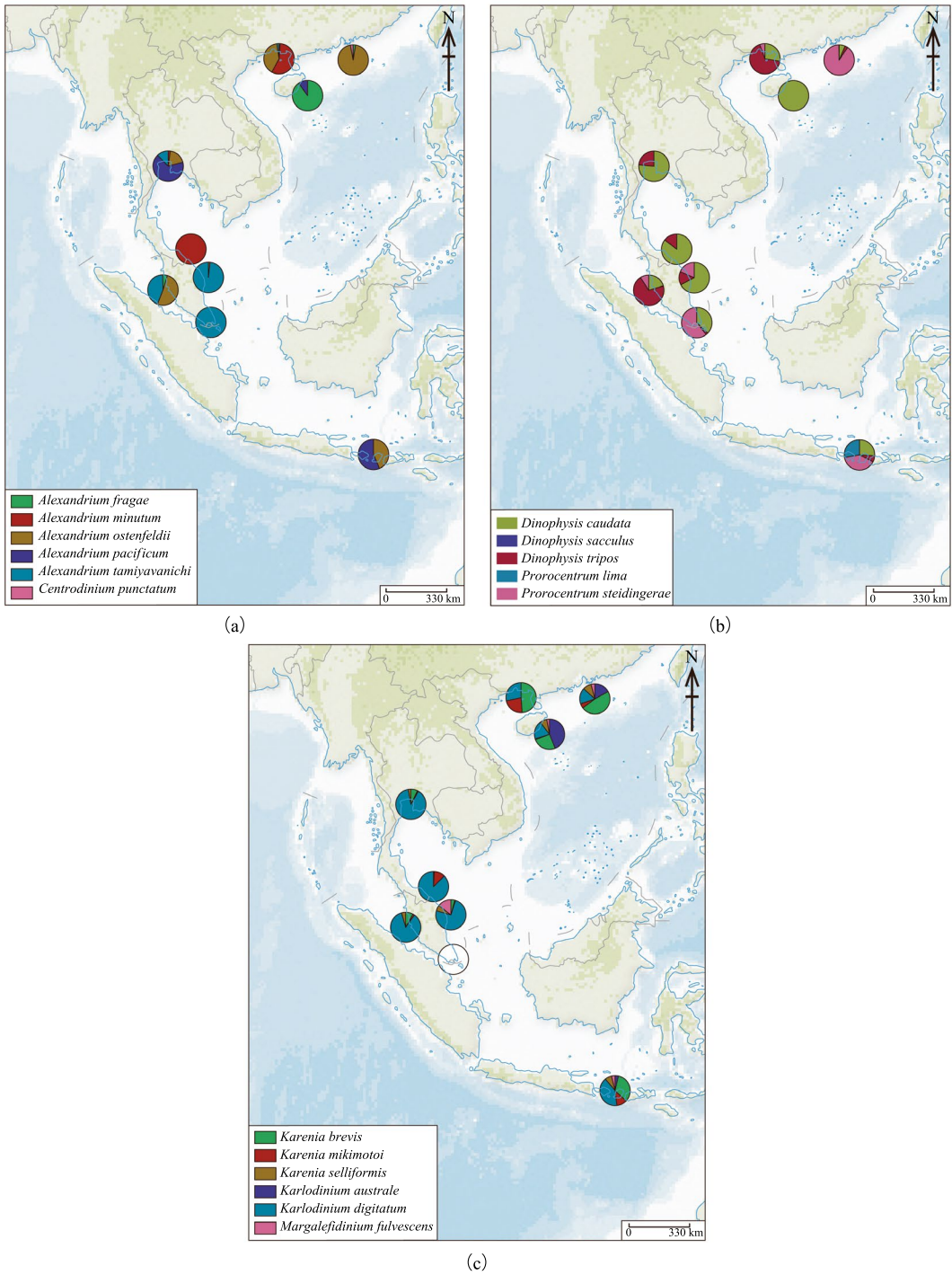


Fig. 7.3 Distribution of HAB species producing PSP (a), DSP (b), and ichthyotoxin (c)

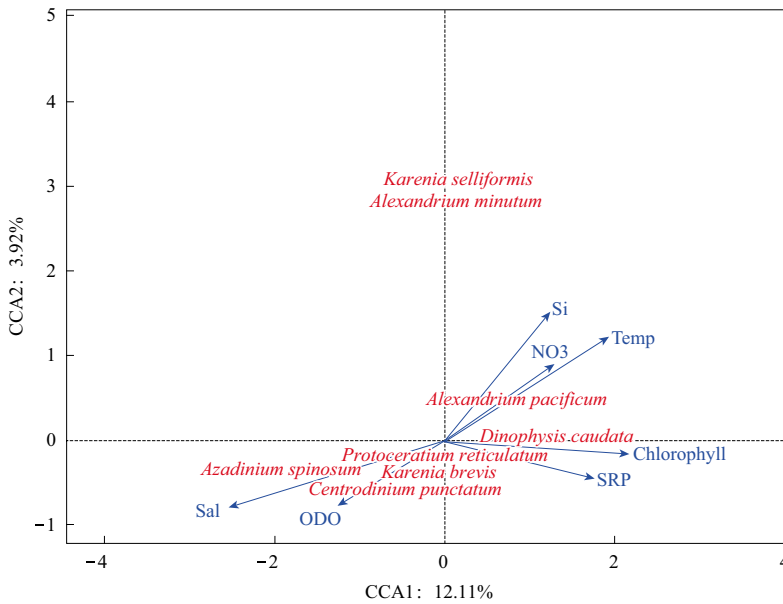


Fig. 7.4 CCA of environmental factors and relative abundance of the main HAB species

be related to the eutrophication and hypoxia caused by the river input in the Johor Strait. The relative abundances of *Centrodinium punctatum*, *Karenia brevis*, and *Azadinium spinosum* were positively related to salinity and dissolved oxygen, but they were negatively related to silicate, temperature, and nitrate, indicating that these groups prefer high-salinity, low-temperature, and oligotrophic environments. They mainly inhabit the outer sea of the Pearl River Estuary and East of Hainan Island, where salinity and dissolved oxygen are high and water quality is relatively good. The relative abundances of *Karenia selliformis* and *Alexandrium minutum* ribotype C were positively related to silicate, temperature, and nitrate, but they were negatively related to salinity and dissolved oxygen. These groups are mainly distributed in the eutrophic, hypoxic, and brackish coastal Semerak lagoon.

7.3.1.5 Highlights

- Harmful algal bloom species were investigated in nine areas of the South China Sea and its surrounding waters using the

metabarcoding method based on high-throughput sequencing technology for the first time.

- The distribution of harmful algal bloom species is controlled by the local marine environment in the South China Sea and its surrounding waters.
- Seventeen harmful algal bloom species that produce PSP, DSP, and ichthyotoxins were found.
- New methods for monitoring harmful algal bloom species contribute to strengthening disaster resistance and achieving SDGs.

7.3.1.6 Discussion and Outlook

Compared with the traditional research on HAB species by morphological observation, the metabarcoding method based on high-throughput sequencing technology has been applied widely, as it can accurately and comprehensively reveal the diversity of HAB species in water samples. Based on our initial attempt in the Gulf of Thailand (Fu et al. 2021), this case expands the study area to the South China Sea. Unlike the three areas in Malaysia where the composition of HAB species is similar, other areas show obvious regional characteristics that are related

to local environmental factors. For example, Semerak and the Johor Strait both show a trend of eutrophication, but their structures are completely different. Semerak mainly has a high concentration of nitrate, while the Johor Strait has a relatively high concentration of nitrate and phosphate. The dominant HAB species in these two areas are also different. The environmental factors collected in this case have a low degree of explanation for the relative abundance of species, indicating that the process driving the relative abundance of species is complex and may be more affected by other environmental factors such as tidal currents.

Seventeen species producing PSP, DSP, and ichthyotoxins were found, some of which had never been reported before. For example, *Alexandria minutum* ribotype C was found for the first time in the Semerak of Malaysia and Weizhou Island in the Beibu Gulf, presenting a new toxic ribotype found only in the East China Sea. In addition to the other two ribotypes found in the South China Sea (Liu et al. 2022), our results show that there are at least three ribotypes of *Alexandria minutum* in this area. The occurrence of both toxic and non-toxic ribotypes adds difficulties to monitoring and highlights the necessity to develop rapid detection methods based on specific molecular markers. *Centrodinium punctatum* was only found in the waters of Mexico, the Republic of Korea and France before and strains from the East China Sea were able to produce PSP (Shin et al. 2020). This is the first record in the South China Sea. *Karenia brevis* often forms large-scale blooms in the Gulf of Mexico in the USA, leading to the mortality of thousands of tons of fish and marine animals, which is also the first recording in the South China Sea.

This case is based on the results of a single survey in various sea areas of the South China Sea. In order to fully reveal the diversity of HAB species, more intensive surveys in the South China Sea are needed in the future. The metabarcoding method based on high-throughput sequencing technology has revealed many newly recorded HAB species in the South China Sea, but they need to be verified by the

traditional morphological observation method. In addition, the metabarcoding method based on high-throughput sequencing technology can only quantify the relative abundance of HAB species. In order to accurately quantify the abundance of HAB species, other molecular methods, such as quantitative PCR, are needed as beneficial supplements. The metabarcoding method based on high-throughput sequencing technology is helpful to strengthen the ability to mitigate HABs disasters, which can be spread to more sea areas and countries in the future. This case also provides methodological support for evaluating SDG 14.1 in preventing and significantly reducing nutrient pollution from land-based sources.

7.3.2 Monitoring and Early Warning of Coral Reef Bleaching and the Thermal Environment in China-ASEAN Seas

Target: SDG 14.2: By 2020, sustainably manage and protect marine and coastal ecosystems to avoid significant adverse impacts, including by strengthening their resilience, and take action for their restoration in order to achieve healthy and productive oceans.

7.3.2.1 Background

The coral reef ecosystem is one of the most important marine ecosystems in the world, supporting hundreds of thousands of marine species and providing food and income for hundreds of millions of people (Burke et al. 2011). However, in the context of global warming and ocean acidification, extreme high-temperature events in the ocean have become more frequent and intense, resulting in the gradual intensification of coral reef bleaching in the ocean. The process of coral reef bleaching is mainly due to the breakdown of the symbiotic relationship between the coral host and its endophytic algae, resulting in the process of bleaching itself. Coral bleaching is mainly due to the increase in sea temperature, which is also related to the influences caused by frequent human activity.

The bleached coral will die quickly if it is left unprotected and managed. The problem of coral bleaching in the China-ASEAN seas is becoming increasingly serious, especially in April and May every year, when the hot weather makes the surface temperature of seawater reach above 30°C, and the seawater is maintained at a high temperature for a long time, which endangers the growth of coral. Under normal conditions, coral can recover about 3%–5% per year, but the recovery rate of coral in tourist areas and bleaching areas is only 1%. The bleaching of coral reefs will lead to the serious degradation of coral reef ecosystems, endangering the balance of marine ecosystems (Hughes et al. 2018; Skirving et al. 2019), and also lead to a sharp decline in biodiversity in coral reef areas, seriously affecting fishery production and taking away a valuable biological gene pool, and at the same time aggravating the erosion of coastal waves. With the improvement of satellite remote sensing and monitoring means (Hedley et al. 2016; Haya and Fujii 2017), large-scale coral reef growth monitoring has become possible, and combined with environmental monitoring data on coral bleaching, it is possible to study the overall status of coral reef bleaching and predict the future survival of coral reefs. Ocean temperature is the most critical environmental factor affecting the growth of coral reefs. Studies have found that the abnormal increase in ocean temperature is the main cause of large-scale coral reef bleaching. After the accurate measurement of dead large coral reefs, it has been found historically that the year of coral reef death corresponds to the high-temperature year.

Based on the above requirements, this case study examines the coral reef bleaching environment in the South China Sea and its adjacent sea area of common concern to China and ASEAN. Through the analysis of the sea surface temperature data monitored by satellite remote sensing and the FIO-COM model reanalysis of ocean temperature data, a cognition of the coral reef bleaching environment in the studied waters was formed. In addition, a dataset of environmental parameters was generated for coral reef bleaching in the study area from 2016 to 2021, and

finally, dataset analysis results were obtained for the environmental conditions of coral reef bleaching. This case will explore the construction of a real-time system for monitoring and early warning of coral reef bleaching and provide scientific and technological support for coral reef protection and restoration.

7.3.2.2 Data

Ocean temperature data in the climatic state are the benchmark for calculating the environmental parameters of coral reef bleaching. In this case, the World Ocean Atlas (WOA) generated by the National Oceanographic Data Center (NODC) under NOAA was used, and satellite remote sensing sea surface temperature data were introduced. Remote sensing data are a data product (optimum interpolation sea surface temperature, OISST) provided by the National Climate Data Center, NOAA, which is a fusion of advanced very high-resolution radiometer (AVHRR) and advanced microwave scanning radiometer (AMSR) observations, and the optimal interpolation method was used to obtain the daily average sea surface temperature (SST) dataset with a resolution of $1/4^\circ \times 1/4^\circ$ (Reynolds et al. 2007).

The Global Coral Bleaching Database (GCBD) was used, which comes from seven main sources, including 34,846 coral bleaching observations from 14,405 sites in 93 countries, with a time span of 40 years from 1980 to 2020. At the same time, the database also has other data parameters related to coral reef bleaching, namely: whether there is coral reef bleaching, the threshold of coral reef bleaching in a certain area, distance from land, average turbidity of the marine environment, and sea surface temperature at the time of the observation. The data website is <https://www.ncei.noaa.gov/access/metadata/landing-page/bin/iso?id=gov.noaa.nodc:0228498>.

The numerical prediction results of the global ocean wave-tide-circulation coupled model developed by the First Institute of Oceanography, Ministry of Natural Resources, were introduced to calculate the thermal environment of coral reef bleaching. This global high-resolution marine environment prediction

system consists of several modules: the FIO-COM numerical model, ensemble adjustment Kalman filter assimilation module, control scheduling module, operational observation database, numerical model database, and data post-processing module. Figure 7.5 shows the framework of the forecast system.

The global ocean wave-tide-circulation coupled forecast system (OFS) with 0.1° resolution generates high-resolution global ocean forecast products. The required atmospheric driving field data come from the Global Forecast System (GFS) of NCEP, and the initial field comes from the assimilation module. The system starts to report at 12:00 (Universal Time) every day, and the forecast time is 120 h. The forecast variables include seawater temperature, salinity, horizontal velocity, sea surface height, sea ice density, and sea ice thickness, with a horizontal resolution of 0.1. Three-dimensional variables were vertically divided into 54 layers. The minimum layer thickness of the surface layer was 2 m, and the time resolution of the forecast product was 3 h. In this case, the data products generated by the system operation from 2016 to 2021 were mainly used to carry out research on the thermal

environment of coral reef bleaching, and a real-time early warning system was developed for the study area based on the forecast data.

7.3.2.3 Methods

Based on the various data collected, the calculation of the coral reef bleaching thermal environment mainly includes two parameters: coral bleaching HotSpot and the high-temperature accumulation value experienced by the coral reef area over a period of time, which is called coral bleaching degree heating weeks (DHW).

1. Coral Bleaching HotSpot

Corals are prone to bleaching when the sea temperature exceeds that typically experienced during the hottest months. This indicator highlights the period when the local SST is higher than the monthly average SST of the highest climate. The HotSpot value was only positive, because only a temperature higher than the maximum would bring pressure to coral reef bleaching, and the HotSpot of 1.0°C was taken as the thermal stress threshold leading to coral bleaching.

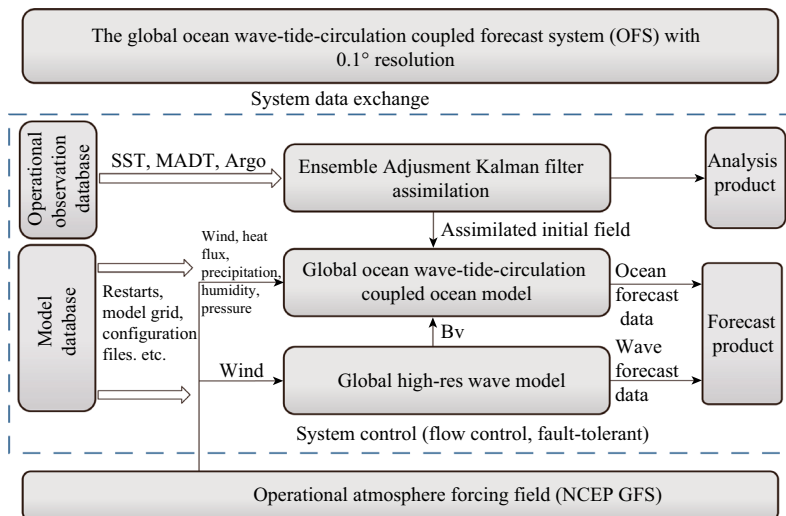


Fig. 7.5 Framework of the global ocean wave-tide-circulation coupled forecast system (OFS) with 0.1° resolution

2. DHW

Coral bleaching is a stress response caused by a prolonged increase in sea temperature, so satellite data and forecast data were used to determine the cumulative value of high-temperature anomalies experienced by coral reef areas over 12 weeks.

$DHW = A \times \text{sum of HotSpots in the previous 12 weeks.}$

$A = 1/7$ (for calculating a HotSpot every day).

$A = 1/2$ (for two HotSpots per week).

3. Classification of Early Warning Levels

According to whitening level requirements and users' actual demand for data warning, the bleaching thermal stress was classified according to Table 7.2, and the specific threshold was set for visual display on the webpage display side of the visualization system.

7.3.2.4 Results and Analysis

This case study mainly focuses on the South China Sea and its adjacent sea area (90° E–130° E, 20° S–25° N), which is the core area of coral reefs in the world and the sea area with the most abundant coral reef environments. The historical observation data showed that the coral reef bleaching situation in this area is very serious (Sully et al. 2019; van Woesik and Kratochwill 2022). Figure 7.6 shows the map of coral reef bleaching status in the study area

according to the measured data. The data come from open data online including a coral bleaching dataset integrated with various global field observations, literature reports, field pictures, and satellite images. From the historical observation data, it can be seen that the coral reef bleaching status in this sea area is relatively serious, especially in the main tourist areas of ASEAN countries (Thailand, Malaysia, Cambodia, etc.), and a large part of the coral bleaching rate even exceeds 50%. Therefore, it is urgent to carry out research on the coral reef bleaching environment in this sea area and take relevant actions for coral reef protection and restoration according to the research records.

1. Historical Dataset of the Coral Reef Bleaching Environment in the China-ASEAN Seas

This case study forms a complete set of historical datasets on the coral reef bleaching environment in the study area from 2016 to 2021 to better understand the phenomenon. We can see from the average coral reef heat from 2016 to 2021 that the coral reef bleaching pressure in this sea area is greater in spring and summer, and the relative pressure is smaller in autumn and winter in the Northern Hemisphere. Moreover, during the study period, the bleaching pressure faced by coral reefs in this sea area showed a significant inter-annual change. In 2016, 2017, and 2021, the bleaching pressure faced by coral reefs was greater, but in 2018–2020, the bleaching pressure faced by coral reefs was relatively light. This is closely related to the inter-annual variation of the marine environment. The research shows that the occurrence of coral reef bleaching events is closely related to the extreme rise in ocean temperature (Sully et al. 2019). From the study period given by the dataset, extreme high-temperature events in the sea area have become frequent, which brings great pressure to the bleaching of marine coral reefs in the region. The continuous study of global warming has shown that the extreme rise of sea surface

Table 7.2 Bleaching grading standard

Bleaching grades	Grading standards
No bleaching pressure	$\text{HotSpot} \leq 0$
Needs attention	$0 < \text{HotSpot} < 1$
Bleaching early warning	$1 \leq \text{HotSpot}$ and $0 < \text{DHW} < 4$
Bleaching early warning Level 1	$1 \leq \text{HotSpot}$ and $4 \leq \text{DHW} < 8$
Bleaching early warning Level 2	$1 \leq \text{HotSpot}$ and $8 \leq \text{DHW}$

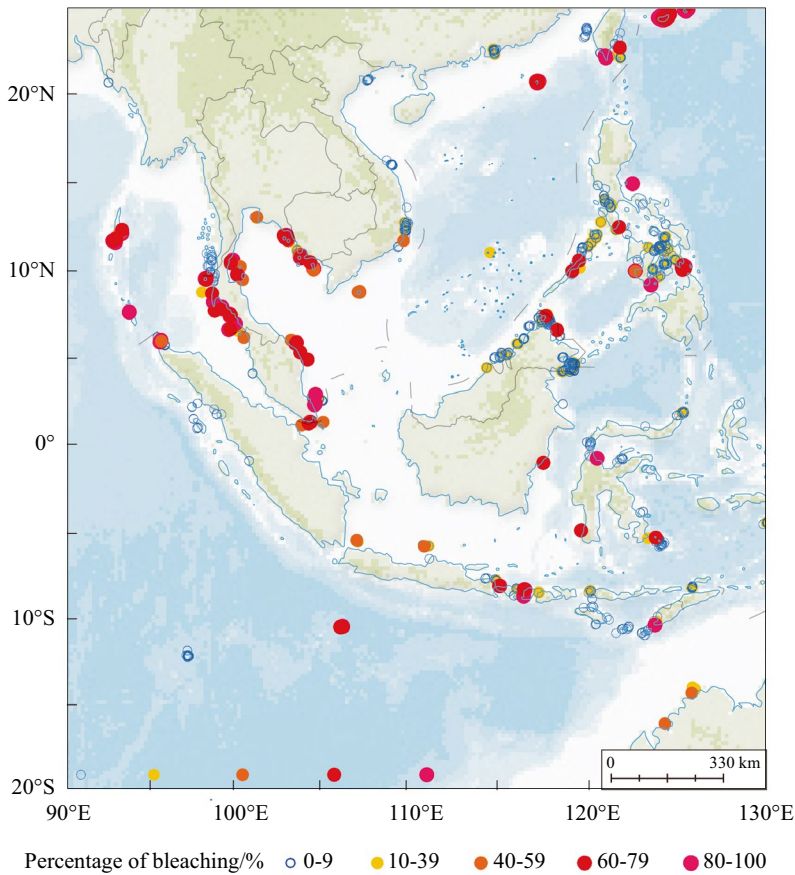


Fig. 7.6 Observed coral bleaching status in the study area. *Note* The value is the percentage of bleaching

temperature will occur more frequently, which indicates that coral reef bleaching events will occur far into the future (Fig. 7.7).

2. Real-Time Early Warning System of the Thermal Environment of Coral Reef Bleaching in the China-ASEAN Seas

A real-time early warning system was established for the thermal environment of coral reef bleaching in the South China Sea and its adjacent sea area using the above-mentioned calculation methods based on the real-time acquisition of sea surface temperature (OISST) monitored by satellite and the global

system for marine environment numerical forecasting (<http://144.123.38.62:2021/#/>). The system can directly serve China and ASEAN countries (also known as the China-ASEAN marine coral reef bleaching early warning system) and realize real-time assessment and forecasting of coral reef bleaching in the China-ASEAN seas (Figs. 7.8 and 7.9). It provides a scientific basis for China and ASEAN countries to understand the bleaching environment faced by coral reefs in the region and provides strong scientific and technological support for assessment, protection, and restoration policies based on the system sub-regions.

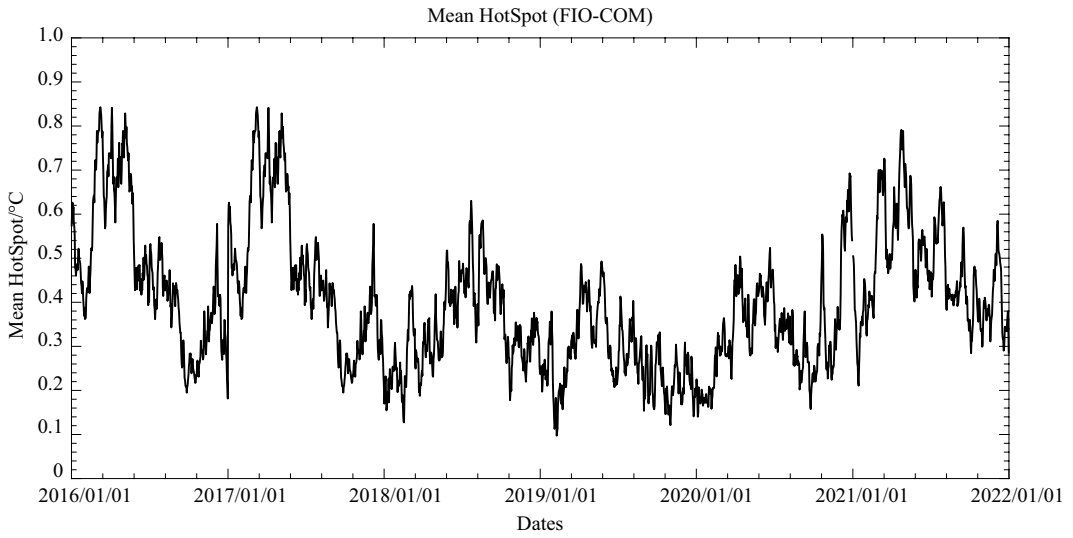


Fig. 7.7 Average HotSpot in the China-ASEAN seas (90° E–130° E, 20° S–25° N)

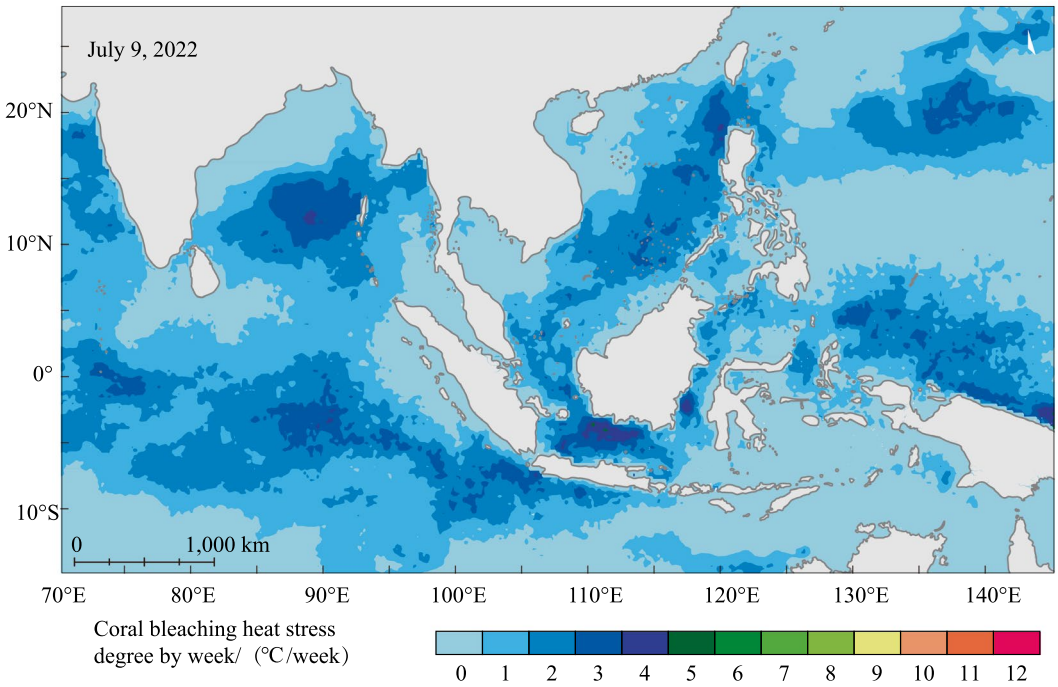


Fig. 7.8 China-ASEAN marine coral reef bleaching early warning system (DHW)

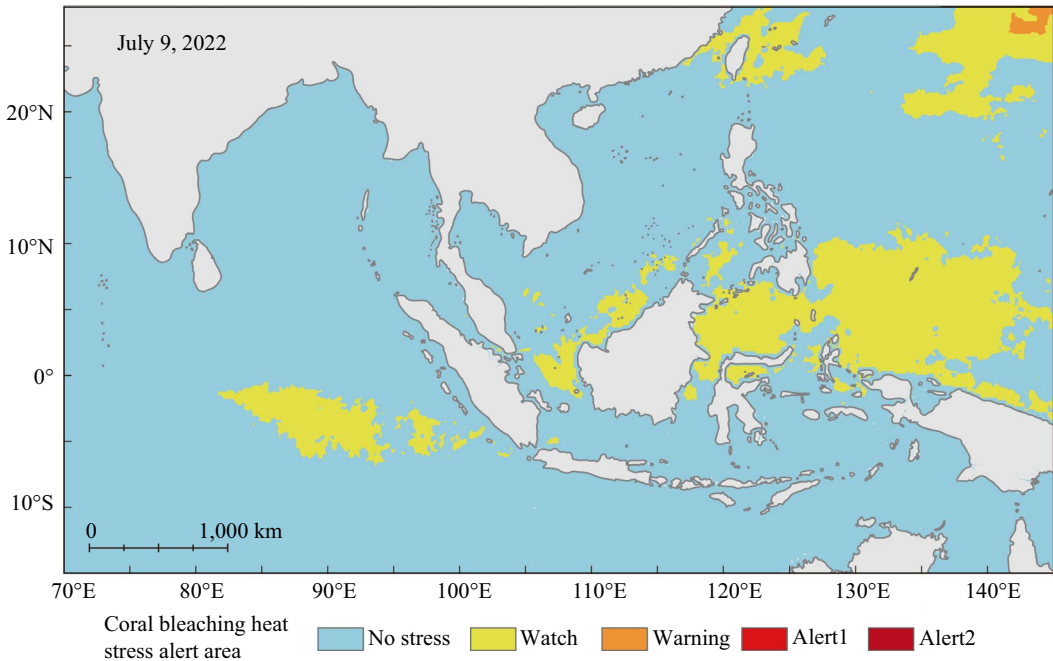


Fig. 7.9 China-ASEAN marine coral reef bleaching early warning system (bleaching environment classification)

7.3.2.5 Highlights

- Based on satellite observation data and a high-resolution marine reanalysis dataset, a dataset was generated for the coral reef bleaching environment in the South China Sea and its adjacent sea area during 2016–2021, allowing a comprehensive evaluation of the status of the coral reef environment.
- Using satellite observation data and high-resolution numerical forecast data, we established a real-time early warning system for the coral reef bleaching environment in the South China Sea and its adjacent sea area, for the first time, to directly serve the China-ASEAN seas and provide the possibility for a real-time grasp of the coral reef bleaching environment in the region.

7.3.2.6 Discussion and Outlook

In this case, an internationally shared dataset was made by using the internationally common coral reef bleaching environment calculation scheme, which meets the requirements of SDG

14.2 for analyzing and evaluating the carrying status and health level of offshore environments and ecosystems. The dataset was then analyzed to evaluate the coral reef bleaching status in the South China Sea and its adjacent sea area from 2016 to 2021. With the support of this case study, a real-time coral reef bleaching early warning system has been formed. It has a real-time display of the regional coral reef environment, which provides a scientific basis for China and ASEAN countries to understand the bleaching and provides strong scientific and technological support for evaluation, protection, and restoration policies.

In the future, it is planned to use more abundant international public data and unique reanalysis datasets, reuse the assessment and forecast scheme of this case study, carry out the production and analysis of global coral reef bleaching environment data, expand the access of real-time online coral reef on-site observation and monitoring equipment, and develop a more comprehensive and real-time online early warning system for global coral reef bleaching.

7.3.3 Dynamic Changes in Phytoplankton Size Class in the North Indian Ocean

Target: SDG 14.2: By 2020, sustainably manage and protect marine and coastal ecosystems to avoid significant adverse impacts, including by strengthening their resilience, and take action for their restoration in order to achieve healthy and productive oceans.

7.3.3.1 Background

There is a strong correlation between phytoplankton size class (PSC) and its function type, which is an important characterization of the composition of phytoplankton communities. PSC largely determines the intensity of carbon fixation and output in the ocean and therefore plays a key role in the global carbon cycle (Alvain et al. 2008; Brewin et al. 2012). Phytoplankton is divided into three components according to their sizes: pico-phytoplankton (C_p) ([0.2, 2) μm), nano-phytoplankton (C_n) ([2–20) μm), and micro-phytoplankton (C_m) ([20–200) μm) (Sieburth et al. 1978). With the development of optical instruments and the launch of remote sensing satellites, new technologies and many bio-optical models for the long-term and large-scale monitoring of PSC have been released. Among all bio-optical models, the three-component model of phytoplankton proposed by Brewin et al. (2012) is the most commonly used one as it only requires Chla concentration as an input parameter, and it is simple and efficient.

Covering the Arabian Sea and the Bay of Bengal, the North Indian Ocean (NIDO) is a key sea area of the BAR. There are many countries along this route, most of which are developing countries, and research on its marine ecological environment is relatively slow. The NIDO is frequently affected by tropical cyclones (TC, about 10 per year) and dust storms (especially in the northwestern Arabian Sea). Dynamic monitoring of the impacts of these disasters on the ecological environment of the NIDO is a key step for countries along the BAR to sustainably manage and protect marine and coastal ecosystems.

Studies have been carried out on the temporal and spatial distribution of total phytoplankton biomass in the NIDO (Chen et al. 2013; do Rosário Gomes et al. 2016), the impacts of tropical cyclones on total phytoplankton biomass (Vidya et al. 2017), and the impacts of dust storms on total phytoplankton biomass. However, due to the lack of data in the global pigment dataset in the Bay of Bengal, the applicability of the three-component model in the NIDO still needs to be further verified (Brewin et al. 2012, 2014), making the large spatiotemporal distribution of PSC and the impacts of meteorological disasters (tropical cyclones and dust storms) on the temporal and spatial variation of PSC still unclear in the NIDO. Therefore, the understanding of the dynamic changes of PSC in the NIDO is still in the Tier II category (that is, indicators with clear methods but lack of relevant data). From the perspective of scientific and technological innovation promoting the SDGs, the research on the dynamic distribution of PSC and its impacts on meteorological disasters has scientific implications for understanding the formation mechanism of algal blooms and the impacts of meteorological disasters on the marine ecological environment in the NIDO. It is in line with the goals of SDG 14.2 to strengthen disaster resilience and improve sustainable ocean management and ecosystem protection and is of great significance to achieve the SDGs related to the ocean.

7.3.3.2 Data

- L3 level Chla concentration data and photosynthetically active radiation (PAR) data fused by MODIS Aqua and Terra from 2003 to 2022, with a temporal resolution of 1 day and spatial resolution of 4 km.
- Fluorescence of Chla data in the NIDO from 2003 to 2022, obtained from the International Argo Program.
- Chla concentration from two cruise data in June 2017 and June 2019.
- Reanalysis data of dust concentration and dust movement from Modern-Era Retrospective analysis for Research and

Applications from NASA (MERRA) in 2003–2022, with a temporal resolution of monthly and spatial resolution of $0.625^\circ \times 0.5^\circ$.

- The center position and maximum sustained wind speed data of tropical cyclones every 6 h from 2003 to 2022 are free to download from NCEI.

7.3.3.3 Methods

1. Inversion Model of PSC and Its Calibration

The total Chla is the sum of the corresponding Chla for C_p , C_n , and C_m (Brewin et al. 2012, 2014):

$$\text{Chla} = C_p + C_n + C_m,$$

where C_p , C_n , and C_m indicate the Chla for pico-phytoplankton, nano-phytoplankton, and micro-phytoplankton, respectively, and $C_{p,n}$ indicates the sum of Chla for pico- and nano-phytoplankton. $C_{p,n}$ and C_p can be calculated as follows (Brewin et al. 2012, 2014):

$$C_{p,n} = C_{p,n}^m \left[1 - \exp \left(-\frac{D_{p,n}}{C_{p,n}^m} \text{Chla} \right) \right],$$

$$C_p = C_p^m \left[1 - \exp \left(-\frac{D_p}{C_p^m} \text{Chla} \right) \right],$$

where $C_{p,n}^m$ is the asymptotic maximum of $C_{p,n}$; C_p^m is the asymptotic maximum of C_p ; $D_{p,n}$ and D_p are the initial slope of $C_{p,n}$ and C_p , respectively; C_n (Chla for nano-phytoplankton) is the difference of $C_{p,n}$ and C_p ; and C_m is the difference between Chla and $C_{p,n}$.

The fraction of PSC can be calculated as follows:

$$F_p = \frac{C_p}{\text{Chla}},$$

$$F_n = \frac{C_n}{\text{Chla}},$$

$$F_m = \frac{C_m}{\text{Chla}},$$

where F_p , F_n , and F_m indicate the fraction of C_p , C_n , and C_m to the total Chla of phytoplankton, respectively.

2. Coordinate System of the Tropical Cyclone Center

With the central point of each tropical cyclone as the coordinate origin, the Cartesian coordinate system of each grid point was converted into polar coordinates, and all grid points within a radius of 2° were displayed. The advancing direction of the tropical cyclone at each central point was then unified to the north. Finally, the new polar coordinate values were converted back to the Cartesian coordinate system.

3. Pixel-By-Pixel Time-Series Correlation Analysis

By resampling the daily average data of each element to the spatial resolution of the daily averaged PSC, the correlation analysis between each element and the PSC was carried out pixel by pixel, and the correlation coefficient R was obtained. Finally, the spatial distribution results of the temporal correlation between each element with PSC were drawn.

7.3.3.4 Results and Analysis

Figure 7.10 shows the variations of the daily averaged climatology distribution of PSC caused by tropical cyclones in the NIDO during 2003–2022 in the coordinate system of the tropical cyclone center. Before tropical cyclones arrived, phytoplankton biomass in the Arabian Sea was higher than that in the Bay of Bengal. Meanwhile, the pico-phytoplankton dominated the Bay of Bengal, while the nano-phytoplankton contributed more than pico-phytoplankton and dominated the Arabian Sea. During the first 1–2 weeks after the arrival of tropical cyclones, the biomass of pico-, nano-, and micro-phytoplankton all increased with larger dominated size of phytoplankton, and regional variations were as follows: PSC changed

from nano-phytoplankton-dominated into micro-phytoplankton-dominated in the Arabian Sea, while PSC changed from pico-phytoplankton-dominated into nano-phytoplankton-dominated in the Bay of Bengal. In the third week after the arrival of tropical cyclones, the biomass of all PSC was decreasing to the original magnitude before the arrival of tropical cyclones. In a word, tropical cyclones can induce an increase in the contribution of larger PSC, including fraction of micro-phytoplankton in the Arabian Sea, and fraction of nano-phytoplankton in the Bay of Bengal.

The invitation of dust storms can transport nutrients from the atmosphere to the ocean through the deposition of dust and reduce the PAR on the ocean surface (Sarangi et al. 2013). Figure 7.11a shows the spatial variations of regional climatology distribution of the concentrations and movements of dust in the NIDO during 2003–2022.

The dust storms mainly affected the northwest of the Arabian Sea in the NIDO, and the movement of dust was from the northwest to the southeast. This suggests that the dust mostly came from land deserts in the Middle East. Figure 7.11b–d show the spatial correlation between monthly PSC and ocean-surface dust concentrations in the NIDO during 2003–2022. Figure 7.11e–g shows the spatial correlation between monthly PSC and ocean-surface PAR in the NIDO during 2003–2022. The Northwestern Arabian Sea was significantly affected by the dust storms, where the pico-phytoplankton was in a high degree of light saturation (Fig. 7.11e), and there was no relationship between the biomass of pico-phytoplankton and dust concentrations [R : -0.3 to 0.3] (Fig. 7.11b). This suggests that the influences of atmospheric nutrient deposition and PAR reduction due to dust storms on the biomass of pico-phytoplankton were weak. Besides this, the nano-phytoplankton was in a low degree of light saturation (Fig. 7.11f), but most areas showed positive relationships between the biomass of nano-phytoplankton and dust concentrations. This suggests that the growth of nano-phytoplankton was regulated by both atmospheric nutrient

deposition and PAR reduction due to strong dust storms. In addition, the micro-phytoplankton was not in a state of light saturation (Fig. 7.11g), and the biomass of micro-phytoplankton was positively correlated with dust concentrations in the whole Northwestern Arabian Sea, implying that the influences of dust storm-induced atmospheric nutrient deposition on the increment in the micro-phytoplankton were stronger than the influences of dust storm-induced PAR reduction on the decrease in the micro-phytoplankton. Therefore, in the NIDO, the dust storms affected the increment of micro-phytoplankton due to the atmospheric nutrient deposition and affected the growth of nano-phytoplankton under the united control of atmospheric nutrient deposition and PAR reduction. In short, the influences of dust storms in the NIDO on the biomass of micro- and nano-phytoplankton were stronger than those of pico-phytoplankton.

7.3.3.5 Highlights

- The three-component model of PSC was adjusted regionally in the NIDO and applied to MODIS satellite remote sensing chlorophyll products, providing method support for the dynamic monitoring of PSC on the surface of the NIDO, serving SDG 14.2.
- One to two weeks after the passage of tropical cyclones, the dominant size of phytoplankton in the Arabian Sea will change from nano-size to micro-size, while that in the Bay of Bengal will change from pico-size to nano-size. This will provide scientific support for understanding the formation of sea surface algal blooms and the governance of the ecological impacts of tropical cyclones in the NIDO.
- The impacts of dust storms on the NIDO are mainly concentrated in the northwestern part of the Arabian Sea. The variation in larger-sized phytoplankton is mainly controlled by the dust deposition, while the growth of smaller-sized phytoplankton is mainly affected by the deposition and light-blocked effect of dust. These results are helpful in

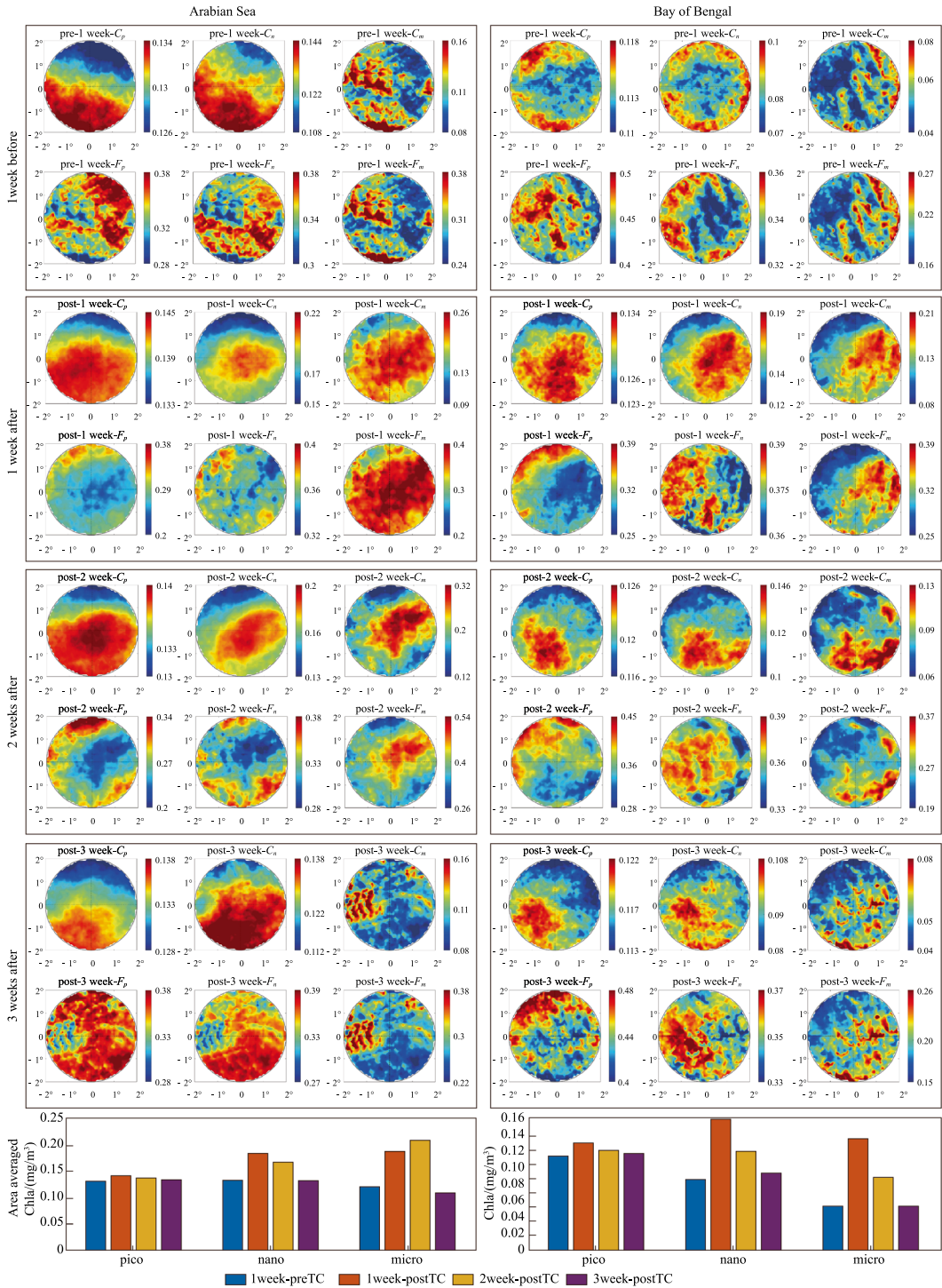


Fig. 7.10 Variations in daily averaged climatology distribution of PSC caused by TC in the NIDO during 2003–2022 in the coordinate system of the tropical cyclone center

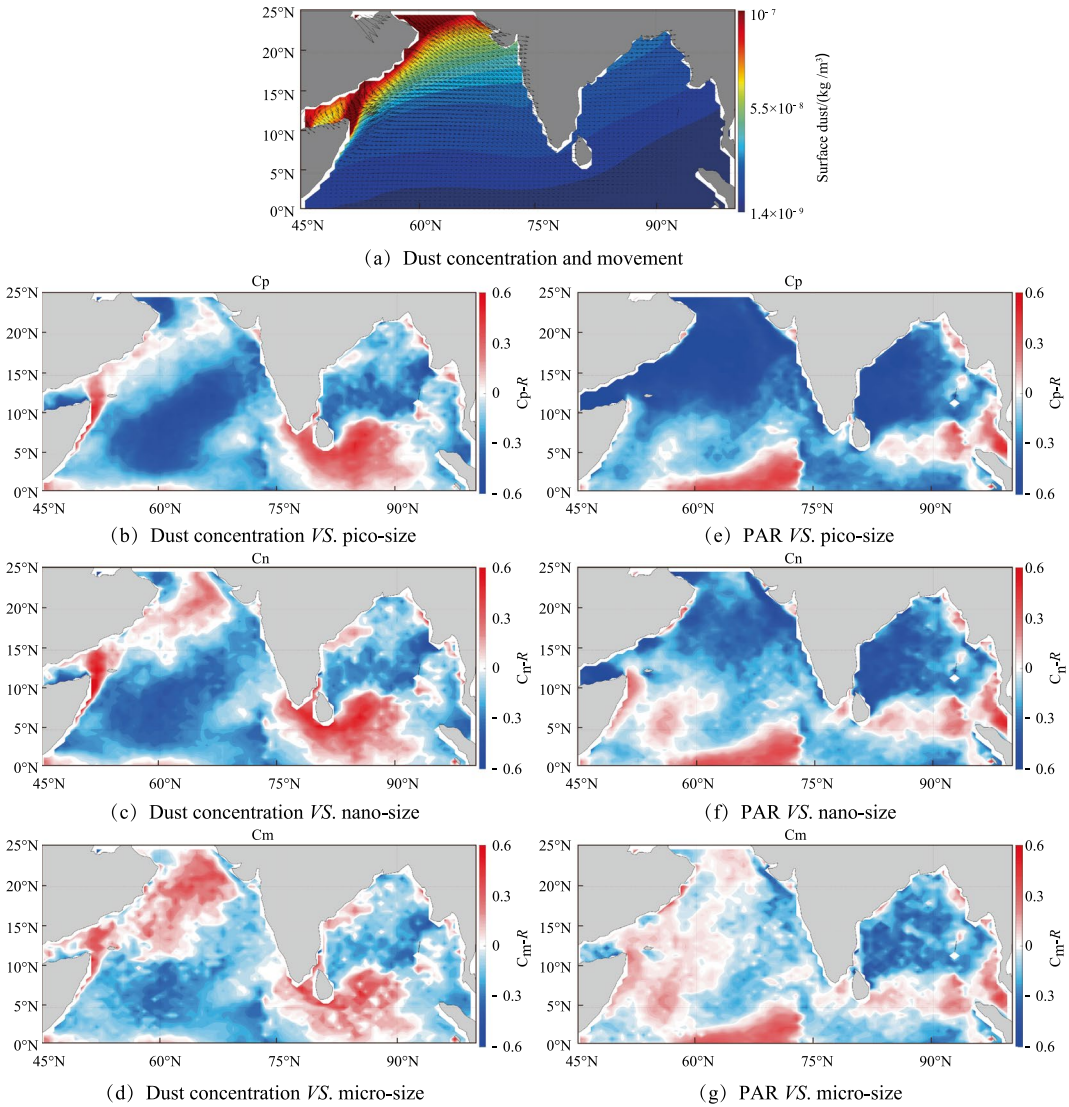


Fig. 7.11 Spatial variations in climatology distribution of dust concentration in the NIDO during 2003–2022, and the spatial correlation between monthly PSC with dust concentration and PAR, respectively

providing scientific support for the ecological management of offshore dust storms in countries along the NIDO.

7.3.3.6 Discussion and Outlook

In this case study, the three-component model for PSC estimations was reparametrized in the NIDO, based on the satellite remote sensing dataset of 2003–2022, the Biogeochemical-Argo (BGC-Argo) dataset and the MERRA dust reanalysis dataset, as well as the field dataset of

the cruise in 2017 and 2019. Then, the characteristics of the climatology of the surface distribution of PSC in the NIDO were studied, the tropical cyclone-induced variation of surface PSC in the NIDO was analyzed, and the influences of dust storms on the variation of PSC in the NIDO were also discussed. Results show that in the NIDO: (1) tropical cyclones can modified the surface Arabian Sea from nano-phytoplankton-dominated to micro-phytoplankton-dominated and modified the surface Bay of

Bengal from pico-phytoplankton-dominated to nano-phytoplankton-dominated; (2) the increment of micro-phytoplankton was affected by dust storm-induced atmospheric nutrient deposition, and the growth of nano-phytoplankton was affected by both of dust storm-induced atmospheric nutrient deposition and PAR reduction. The methods in this case can provide important technical support for the monitoring and prevention of phytoplankton blooms, as well as the sustainable development of fisheries. Furthermore, this case can also provide a decision-making basis and scientific services to strengthen the resistance capabilities of meteorological disasters and enhance the sustainable management and protection capabilities of the marine and coastal ecosystems in the countries along the BAR. Moreover, this case also provides important information support for ocean sustainable development and construction along the Maritime Silk Road that meets SDG 14.2.

A combination of the physical and biological processes to further analyze the mechanism of variation of PSC induced by meteorological disasters is an effective way for ecological impact assessment, the prevention and control of meteorological disasters, the prevention and control of phytoplankton blooms, and oceanic carbon sink, along the BAR. In the future, more ecological parameters and physical parameters can be included to develop more accurate PSC models and more comprehensive ecological impact assessment systems for meteorological disasters and can combine artificial intelligence to further realize the goal of big data mining and analysis on the dynamic monitoring of PSC and ecological impact assessment of meteorological disasters. Faced with international needs, this research can provide more comprehensive support for SDG 14.2, strengthen disaster resistance for the China Association of Marine Affairs (CAMA), GEO, and other institutions, improve the ability of sustainable management and protection of marine and coastal ecosystems, and maintain data support and decision-making services for marine health.

7.4 Summary

The Chinese government has always attached great importance to and supported the UN agenda for sustainable marine development and has actively carried out international cooperation on scientific marine research and scientific surveys of the continental shelf. In addition, China and its neighboring countries have actively implemented the maritime SDGs through various multilateral mechanisms, including taking an active part in the actions under the Asia-Pacific regional Sustainable Development Framework within the UN system, and strengthening cooperation with East and Southeast Asian countries in relevant sub-regional cooperation mechanisms to narrow the regional development gap. In addition, by promoting South-South Cooperation, North-South Cooperation, and tripartite cooperation, we have strengthened synergy with the 2030 Agenda and made much positive progress in marine ecological protection and other fields. Worldwide, however, the crisis of marine ecosystem degradation is not abating, but is at risk of worsening. The case studies in this chapter carried out research on the progress of the protection and sustainable utilization of oceans and marine resources in representative areas around the globe to promote sustainable development; generated datasets on the spatial distribution of HAB species in the South China Sea and its surrounding sea area; produced monitoring and early warning datasets for the thermal environment of coral reef bleaching in the China-ASEAN seas; and created spatial datasets of PSC in the NIDO. In addition, the chapter presents a model for the relationship between the relative abundance of HAB species and environmental factors, a calculation model for the thermal environment of coral reef bleaching, and analysis of the influence of tropical cyclones and dust storms on the grain size structure of phytoplankton in the NIDO. The chapter is a beneficial exploration of the use of Big Earth Data technology to support the realization of SDG 14.

In the future, we will continue to improve the sharing and application capacity of Big Earth Data in the field of marine sustainable development, promote the timely sharing and dissemination of data and knowledge by building data-sharing platforms, online computing platforms, and data service platforms, enhance the development of the blue economy and the innovation level of marine science and technology, and actively participate in the “United Nations Decade of Ocean Science for Sustainable Development (2021–2030)”, contributing to the understanding and protection of the ocean.

References

- Alvain S, Moulin C, Dandonneau Y et al (2008) Seasonal distribution and succession of dominant phytoplankton groups in the global ocean: as satellite view. *Global Biogeochem Cycles* 22:GB3001
- Brewin RJW, Hirata T, Hardman-Mountford NJ et al (2012) The influence of the Indian Ocean Dipole on interannual variations in phytoplankton size structure as revealed by earth observation. *Deep Sea Res Part II* 77–80:117–127
- Brewin RJW, Sathyendranath S, Tilstone G et al (2014) A multicomponent model of phytoplankton size structure. *J Geophys Res Oceans* 119(6):3478–3496
- Burke L, Reyter K, Spalding M et al (2011) *Reefs at Risk Revisited*. World Resources Institute, The Nature Conservancy, WorldFish Center, International Coral Reef Action Network, UNEP World Conservation Monitoring Centre and Global Coral Reef Monitoring Network, Washington
- Chen XY, Pan DL, Bai Y et al (2013) Episodic phytoplankton bloom events in the Bay of Bengal triggered by multiple forcings. *Deep Sea Res Part I* 73:17–30
- do Rosário Gomes H, deRada S, Goes JI et al (2016) Examining features of enhanced phytoplankton biomass in the Bay of Bengal using a coupled physical-biological model. *J Geophys Res Oceans* 121(7):5112–5133
- FAO (2020) The state of world fisheries and aquaculture 2020. <https://www.fao.org/state-of-fisheries-aquaculture/2020/en/>
- Fu ZX, Piumsomboon A, Punnarak P et al (2021) Diversity and distribution of harmful microalgae in the Gulf of Thailand assessed by DNA metabarcoding. *Harmful Algae* 106:102063
- Gu HF, Wu YR, Lü SH et al (2022) Emerging harmful algal bloom species over the last four decades in China. *Harmful Algae* 111:102059
- Hallegraeff GM (2021) Global HAB status report. a scientific summary for policy makers. In: Hallegraeff GM, Enevoldsen H, Zingone A (eds) UNESCO, Paris. (IOC Information Document, 1399.)
- Haya LOMY, Fujii M (2017) Mapping the change of coral reefs using remote sensing and in situ measurements: a case study in Pangkajene and Kepulauan Regency, Spermonde Archipelago Indonesia. *J Oceanogr* 73(5):623–645
- Hedley J, Roelfsema C, Chollett I et al (2016) Remote sensing of coral reefs for monitoring and management: a review. *Remote Sensing* 8(2):118
- Hughes TP, Anderson KD, Connolly SR et al (2018) Spatial and temporal patterns of mass bleaching of corals in the Anthropocene. *Science* 359(6371):80–83
- Lim HC, Leaw CP, Tan TH et al (2014) A bloom of *Karlodinium australe* (Gymnodiniales, Dinophyceae) associated with mass mortality of cage-cultured fishes in West Johor Strait, Malaysia. *Harmful Algae* 40:51–62
- Liu ML, Krock B, Yu RC et al (2022) Co-occurrence of *Alexandrium minutum* (Dinophyceae) ribotypes from the Chinese and Malaysian coastal waters and their toxin production. *Harmful Algae* 115:102238
- Lundholm N, Churro C, Fraga S et al (2022) IOC-UNESCO taxonomic reference list of harmful microalgae. <https://www.marinespecies.org/hab>. 09 May 2022
- Reynolds JF, Smith DMS, Lambin EF et al (2007) Global desertification: building a science for dryland development. *Science* 316(5826):847–851
- Sarangi RK (2013) Spatiotemporal variability of MODIS-Aqua-derived aerosol and its impact on surface chlorophyll-a in the Indian coastal and offshore waters. *J Appl Remote Sens* 7(1):073501
- Shin HH, Li Z, Réveillon D et al (2020) *Centrodinium punctatum* (Dinophyceae) produces significant levels of saxitoxin and related analogs. *Harmful Algae* 100:101923
- Sieburth JM, Smetacek V, Lenz J (1978) Pelagic ecosystem structure: Heterotrophic compartments of the plankton and their relationship to plankton size fractions. *Limnol Oceanogr* 23(6):1256–1263
- Skirving WJ, Heron SF, Marsh BL et al (2019) The relentless march of mass coral bleaching: a global perspective of changing heat stress. *Coral Reefs* 38(4):547–557
- Sully S, Burkepile DE, Donovan MK et al (2019) A global analysis of coral bleaching over the past two decades. *Nat Commun* 10:1264
- UN (2021) The second world ocean assessment (WOA II). UN, New York. <https://www.un.org/regularprocess/woa2>
- van Woesik R, Kratochwill C (2022) A global coral-bleaching database, 1980–2020. *Sci Data* 9:20
- Vidya PJ, Das S, Mani MR (2017) Contrasting Chl-a responses to the tropical cyclones Thane and Phailin in the Bay of Bengal. *J Mar Syst* 165:103–114
- Yñiguez AT, Lim PT, Leaw CP et al (2021) Over 30 years of HABs in the Philippines and Malaysia: what have we learned? *Harmful Algae* 102:101776

Open Access This chapter is licensed under the terms of the Creative Commons Attribution-NonCommercial-NoDerivatives 4.0 International License (<http://creativecommons.org/licenses/by-nc-nd/4.0/>), which permits any noncommercial use, sharing, distribution and reproduction in any medium or format, as long as you give appropriate credit to the original author(s) and the source, provide a link to the Creative Commons license and indicate if you modified the licensed material. You do not have permission under this license to share adapted material derived from this chapter or parts of it.

The images or other third party material in this chapter are included in the chapter's Creative Commons license, unless indicated otherwise in a credit line to the material. If material is not included in the chapter's Creative Commons license and your intended use is not permitted by statutory regulation or exceeds the permitted use, you will need to obtain permission directly from the copyright holder.





8.1 Background

SDG 15 focuses on sustainably managing forests, combating desertification, halting and reversing land degradation, and halting biodiversity loss. Eight years after the adoption of the UN 2030 Agenda, we are still facing a critical situation, as the global forest area (SDG 15.1.1) continues to steadily decline (FAO 2020), and approximately 75% of the world's land is still degrading (SDG 15.3.1) (IPBES 2019). The proportion of globally important protected biodiversity sites has increased (SDG 15.1.2, SDG 15.4.1), but the Red List Index (SDG 15.5.1) continues to decline (UNEP 2021), and at the current rate, SDG 15 will be difficult to achieve by 2030 (UN 2019).

Assessing progress toward SDG 15 is key to identifying gaps and effective interventions. With improved data availability and technical methodologies, eight of the fourteen indicators covered by SDG 15 are in Tier I (with methods and data). However, the methods for obtaining these indicators are mainly based on statistical instruments, which lack scalability (global–regional–national–local), and many countries with limited data availability are unable to provide data on a regular basis. Therefore, it is necessary to further develop multiscale and spatialized research on

key technologies for monitoring the status and progress of SDG 15 indicators using cutting-edge technologies, such as Earth observation, artificial intelligence, and public science, to contribute from the perspectives of data, methods, tools, and decision-making recommendations, and thus provide scientific and technological support for the realization of SDG 15.

This chapter will focus on three directions: forest protection and restoration, land degradation and restoration, and biodiversity conservation. It focuses on specific objectives such as sustainable management of all types of forests (SDG 15.2), land degradation neutrality (SDG 15.3), and habitat protection of endangered species (SDG 15.5). The goal is to dynamically monitor and evaluate the sustainable development process of terrestrial organisms through Big Earth Data technology in the entire area or typical areas of the BAR and provide scientific and technological support for the monitoring and evaluation of SDG 15 indicators.

8.2 Main Contributions

To address the data gaps in the assessment of terrestrial biodiversity SDG progress, we produced forest cover data products, and

distribution data products, land degradation data products for five Central Asian countries, and spatial distribution products of suitable habitats for wild camels in China and Mongolia for current and future scenarios (2050 and 2070), which can provide important support for the assessment of terrestrial biodiversity SDGs at regional and global scales (Table 8.1).

8.3 Case Studies

8.3.1 Interannual Changes in Global Tree Cover

Target: SDG 15.2: By 2020, promote the implementation of sustainable management of all types of forests, halt deforestation, restore degraded forests, and substantially increase afforestation and reforestation globally.

8.3.1.1 Background

Forests are one of the most important carbon sinks in terrestrial ecosystems and play a key role in preventing soil erosion, mitigating climate change, and sustaining biodiversity. The status of forest cover and its dynamics are significant indicators to evaluate SDG 15.2, sustainable management of all types of forests. Reliable long-term forest cover maps can help to assess the impacts of forest change on carbon and water cycles and ecosystem functions and provide data support for forest management.

Dynamic monitoring of forest cover can be achieved through satellite remote sensing technology. Categorical forest/non-forest datasets or land cover datasets provide the spatial extent of forest land, which can depict the land cover type alternation between forest and non-forest. However, the categorical data cannot capture the variations of density within forests. Fractional tree cover data present the proportion of areas covered by tree crowns to the total area in pixels, which can improve the characterization of forest density and change. Several global fractional tree cover datasets have been made available. However, several disadvantages were reported for the existing datasets, such as

interannual instability, discontinuous spatial distribution, and notable uncertainty in sparse forests (Hanan et al. 2014; Brandt et al. 2016; Yang and Crews 2019), which makes it hard to obtain a reliable change trend of forest cover (Masiliūnas et al. 2021).

We generated a new global fractional tree cover product, GLOBMAP Fractional Tree Cover, from the MODIS land surface reflectance data. The fractional tree cover estimation was improved by extracting several phenological metrics with high separability for trees and near-global sample training data. The interannual stability and spatial continuity were improved. This study assessed the interannual changes of tree cover around the world and in representative regions using the GLOBMAP Fractional Tree Cover dataset. This study can support SDG 15.2 to monitor forest ecosystems and promote the implementation of the sustainable management of forests.

8.3.1.2 Data

The GLOBMAP Fractional Tree Cover dataset provides global annual fractional tree cover maps from 2000 to 2020 at the spatial resolution of 250 m. The data were generated from MODIS land surface reflectance products MOD09Q1 and MOD09A1. Nine phenological metrics with high separability and global applicability were extracted as input features based on the distinctive shape of seasonal greenness curves between trees and herbaceous vegetation. Then, approximately 1.01 million training sample points were generated by aggregating the global forest maps of GlobeLand30 and PALSAR Forest/Non-Forest (FNF). A feedforward neural network was trained and used to generate global fractional tree cover data. Compared with 1140 reference sample points interpreted from very high-resolution imagery from Google Earth, the coefficient of determination (R^2), RMSE, and mean absolute error (MAE) reached 0.93, 11.78%, and 7.39%, respectively. Compared with the existing tree cover percentage products such as MODIS Vegetation Continuous Fields, the interannual stability, spatial continuity, and dense forest performance were improved, which

Table 8.1 Cases and their main contributions

Indicators/targets	Cases	Contributions
<p>SDG 15.2 By 2020, promote the implementation of sustainable management of all types of forests, halt deforestation, restore degraded forests, and substantially increase afforestation and reforestation globally</p>	<p>Interannual changes in global tree cover</p>	<p>Data product: global fractional tree cover maps (GLOBAL Fractional Tree Cover) during 2000–2020 with high interannual stability and spatial continuity Decision support: identifying the hotspots of global forest change, which helps sustainable forest management</p>
<p>SDG 15.3 By 2030, combat desertification, restore degraded land and soil, including land affected by desertification, drought and floods, and strive to achieve a land degradation-neutral world</p>	<p>Dynamic monitoring of global sand dunes/lands</p>	<p>Data product: Global 30 m sand dune/land datasets for 2000, 2010, and 2020</p>
	<p>Land degradation neutrality process and its attribution in five Central Asian countries</p>	<p>Method and model: establishing new indicators of optimal land degradation index (OLDI) in arid zones, which can provide new data to support the evaluation of SDG 15.3.1 in arid zones Decision support: identifying the main areas of anthropogenic land degradation in Central Asia, which can provide a decision reference for governments to implement the recovery plan of zero-growth land degradation initiatives</p>
<p>SDG 15.5 Take urgent and significant action to reduce the degradation of natural habitats, halt the loss of biodiversity, and by 2020, protect and prevent the extinction of threatened species</p>	<p>Assessment of the impacts of climate change and human activity on wild camels and their habitats</p>	<p>Data product: spatial distribution of suitable wild camel habitats in 2050 and 2070 under current and future climate change conditions Decision support: under future climate change conditions, the area of suitable habitat for wild camels will gradually decrease in 2050 and 2070, and the survival of wild camels will face serious challenges</p>

enables our dataset to be used to estimate gradual forest changes.

8.3.1.3 Methods

The interannual changes in tree cover were evaluated worldwide and in typical regions based on the GLOBMAP Fractional Tree Cover dataset. The forest dynamics were evaluated using the linear trend of tree cover based on the least squares principle at the pixel scale. The *t*-test method was used to determine the significance of the linear trend, with $p < 0.05$ as the significant trend. Referencing the forest definition by the FAO, we defined the lands with a fractional tree cover of less than 10% for more than ten years as non-forest and masked in the following assessment. The forest area was calculated by multiplying the fractional tree cover with the area of a pixel. Then, the total forest area in typical regions was estimated as the sum of the areas for all forest pixels.

According to the distribution patterns of climate zones and forest regions, nine typical regions from tropical, temperate, and northern high-latitude areas were selected to evaluate the interannual dynamics in tree cover. Tropical typical regions include the Amazon (10°S–10°N, 78°W–48°W), the Congo Basin (3.5°S–4.5°N, 10°E–30°E), the Sahel region (12°N–22°N, 18°W–43°E), and Southeast Asia (10°S–28.5°N, 92°E–140°E). Temperate typical regions include North American temperate forests (32°N–45°N, 128°W–64.5°W) and East Asia temperate forests (23.5°N–54°N, 73°E–150°E). The northern high-latitude areas are primarily covered by boreal forests, with typical regions including North America (45°N–72°N, 169°W–52°W), Europe (53°N–71°N, 0°E–74°E), and Russia (50°N–82°N, 82°E–179°E).

8.3.1.4 Results and Analysis

The spatial distribution of global fractional tree cover in 2020 and the change trend from 2000 to 2020 are shown in Fig. 8.1. Up to 2020, the total global forest area was 38.56×10^8 hm², accounting for approximately 25.88% of the total land area. Forests are primarily distributed in the tropical rainforest regions of the equator, the

temperate forests of Eurasia and North America, and the northern high-latitude forest regions of the Northern Hemisphere. More forests are covered in the Northern Hemisphere than those in the Southern Hemisphere. The tropical rainforests and the southern part of the boreal forests show the highest tree cover, reaching over 90%. The tree cover in the forest area exhibits a pattern of latitude change. For example, the tree cover in the African forests decreases from the equator to the north and the south and that in the boreal forests decreases with the increasing of latitude.

The global forest area increased at a rate of 24,108,100 hm²/a (Fig. 8.2a), with the total area increasing by 6.73×10^9 hm². A rapid increase rate was found from 2008 to 2015, and the rate gradually stabilized from 2015 to 2020. Regional discrepancies were observed in the changes of fractional tree cover, showing significant gains in China, the northern parts of the boreal forests and the savannah areas of Africa, with the change trends of fractional tree cover mostly exceeding 2%/a, while losses in fractional tree cover were found in rainforests of South America, Africa, and Southeast Asia, and the southern parts of the boreal forests.

The dynamics of forest areas in nine typical regions from the tropical, temperate, and northern high-latitude areas showed different change patterns during the period 2000–2020 (Fig. 8.2b–d). Forest changes in tropical regions were complex. The forest area fluctuated in the Amazon forests, with the fractional tree cover decreasing significantly for some regions, which may be related to forest fires, burning cultivation, and logging. The forest area in the Congo Basin showed a decreasing trend followed by an increasing trend. The woody plant area in the Sahel region of Africa also fluctuated obviously, which was probably related to the significant impacts of precipitation on local vegetation growth. The total forest area (including trees and shrubs) exhibited a weak increasing trend, suggesting the expansion of woody vegetation in the Sahel region. Although the forest area of Southeast Asian tropical rainforests showed an upward trend over the study period, deforestation could be observed in several parts of the

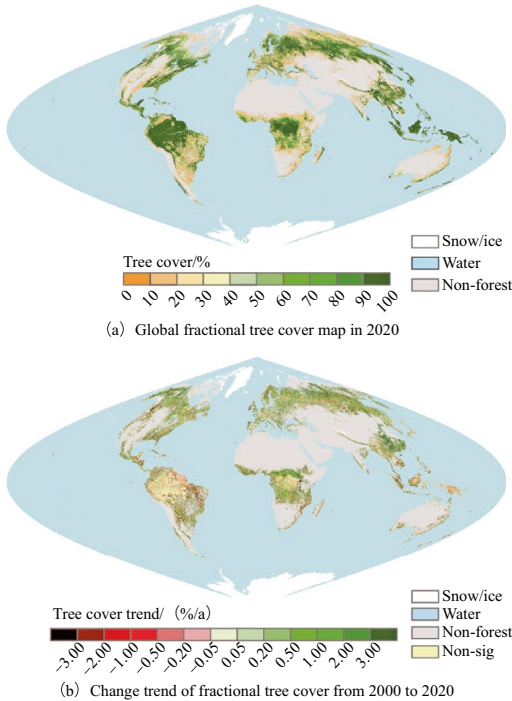


Fig. 8.1 Distribution and change trend of global fractional tree cover

region simultaneously. The expansion of the forest area may be caused by the development of plantations. The typical regions from the temperate and boreal forests demonstrated increased trends in the forest area. The area of North American temperate forests showed a pattern of first increasing and then decreasing from 2000 to 2010, followed by a fluctuating increasing trend from 2010 to 2020. The dynamics of forest areas in North American and European boreal forests were similar, showing fluctuating increasing patterns. The forest areas of East Asian temperate forests and Russian boreal forests showed notable increasing trends, which may be related to effective forest protection policies and regional temperature and precipitation changes.

8.3.1.5 Highlights

- The distributions and interannual changes of global fractional tree cover were assessed using the GLOBMAP Fractional Tree Cover dataset during 2000–2020.

- Global forest area increased by 6.73×10^9 hm^2 from 2000 to 2020. Regional discrepancies were observed in the changes of fractional tree cover. Forest gain was concentrated in the temperate forests of East Asia, the northern parts of the boreal forests, and the savannah areas of Africa. In comparison, forest loss was found in rainforests of South America, Africa, and Southeast Asia and the southern parts of boreal forests.

8.3.1.6 Discussion and Outlook

This study assesses the interannual changes of fractional tree cover in global and typical regions using the GLOBMAP Fractional Tree Cover dataset. Trees are concentrated in the tropical rainforests, mid-latitude temperate forests in the Northern Hemisphere, and high-latitude boreal forests. The highest forest density is distributed in the tropical rainforests and southern parts of boreal forests. During 2000–2020, the global forest area showed a significant increasing trend, with the rapid forest gain concentrated in the East Asian temperate forests, the northern parts of boreal forests, and the savannah areas of Africa. The hotspots of forest loss were found in the rainforest regions and the southern parts of boreal forests. This study hopes to contribute to monitoring and evaluating sustainable forest management in SDG 15.2.

The fractional tree cover dataset used in this study can support the analysis of interannual dynamics of forests at a sub-pixel level and provide a data basis for forest change detection at the global scale. The fractional tree cover represents the proportion of vegetation that shows a greenness plateau of seasonal curves at the maturity stage, including trees, shrubs, bamboo, and palm trees. It should be noted that the increase in fractional tree cover cannot fully represent an improvement in forest quality. For example, natural tropical forests were replaced by cash crops like oil palm trees and coffee beans in Southeast Asia due to the development of plantation agriculture, and tropical forests in some regions have also been restored to secondary forests after logging. Although the forest area increased in Southeast Asia, the carbon

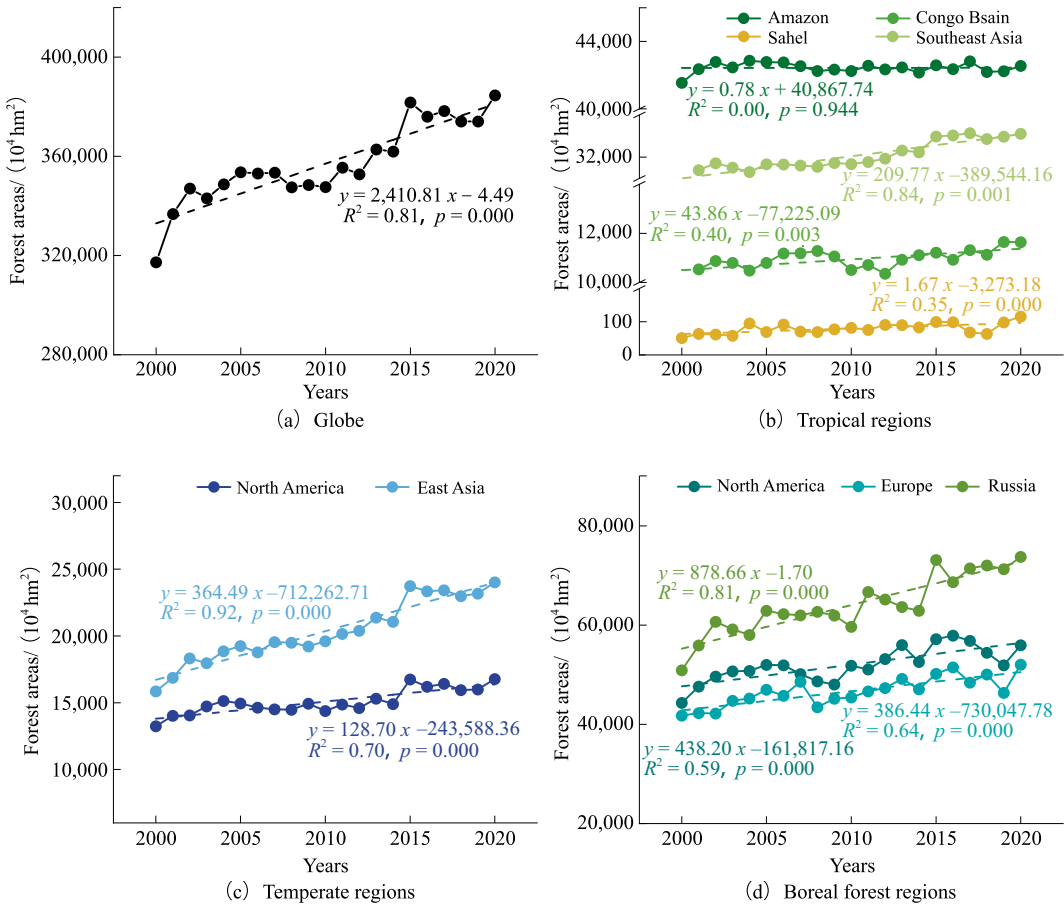


Fig. 8.2 Interannual changes in forest areas in global and representative regions from 2000 to 2020. *Note* Tropical regions include the Amazon, Congo Basin,

Sahel region, and Southeast Asia; temperate regions include North America and East Asia; boreal forest regions include North America, Europe, and Russia

sequestration capacity may decline due to the destruction of the biodiversity in natural forests. The relationship between fractional tree cover changes and ecological functions should be considered in further research.

8.3.2 Dynamic Monitoring of Global Sand Dunes/Lands

Target: SDG 15.3: By 2030, combat desertification, restore degraded land and soil, including land affected by desertification, drought, and floods, and strive to achieve a land degradation-neutral world.

8.3.2.1 Background

Sand dunes/lands cover a large area of deserts and are widely distributed in the inland and coastal areas of the global mid-latitude land (McKee 1979). Their distributions are easily influenced by climate change and human activity. Accurately identifying the different types of sand dunes/lands is essential to represent their areas, spatial distributions, and temporal changes, playing an important role in assessing a tendency toward aeolian desertification, and also contributing to assisting the evaluation of SDG 15.3.1 (“proportion of land that is degraded over total land area”). Guided by the Law of the People’s Republic of China on Desert

Prevention and Transformation and the United Nations Convention to Combat Desertification (UNCCD), the National Forestry and Grassland Administration of China has carried out desertification and sandification monitoring every five years since 1994. However, existing research still focuses on national and regional scales, resulting in a lack of consistent, comparable, and high-resolution classification maps of global sand dunes/lands (Zheng et al. 2022).

Utilizing satellite remote sensing imagery, multi-source land surface mapping products, and land cover sample sets, this study proposes a method for mapping high-resolution and global-scale sand dunes/lands and generated global 30 m sand dune/land datasets. The areas and spatial distributions of three types of sand dunes/lands were analyzed, and their changes between 2000 and 2020 were evaluated.

8.3.2.2 Data

- Global Landsat imagery during the periods of 1999–2001, 2009–2011, and 2019–2021. The image compositing method was applied to the collected images to generate 30 m Landsat imagery for the nominal years of 2000, 2010, and 2020.
- AW3D30 global digital surface model at a spatial resolution of 30 m.
- ASTER global emissivity dataset at a spatial resolution of 100 m.
- Global land cover mapping products, including GlobeLand30 (30 m), FROM-GLC (30 m), CGLS-LC100 (100 m), MCD12Q1.006 (500 m), and GLC2000 (1,000 m).
- Global terrestrial ecoregion map (RESOLVE Ecoregions), in which 846 terrestrial ecoregions were interpreted by ecologists and classified into 14 biome types.
- FROM-GLC global land cover sample set, which was obtained by expert interpretation and verification on global Landsat TM/ETM+imagery.

8.3.2.3 Methods

This study divides sand dunes/lands into shifting sand dunes/lands, semi-fixed sand dunes/

lands, and fixed sand dunes/lands and identifies them from Landsat 30 m imagery and other datasets. First, multi-source and multi-temporal feature representations, including spectrum, spectral index, multi-temporal NDVI, texture, topography, and thematic mapping features, were extracted to address the issue caused by the spatiotemporal variety of global sand dunes/lands. Second, considering that manual sample collection is labor-intensive and hardly practical for large-scale mapping, we propose a strategy to automatically obtain reliable global training samples of sand dunes/lands based on a prior sample set and a coarse-resolution land cover map. Third, due to the spatial heterogeneity of sand dunes/lands, it is difficult for a global classifier to learn the optimal parameters. Therefore, based on the multi-source and multi-temporal feature representations and the global training samples, a local random forest classifier was adopted to obtain the single-temporal classification results of global sand dunes/lands. Finally, to make the automatically obtained samples applicable to multi-temporal classification, transfer learning was introduced to remove the changed samples, and the spatiotemporal context of sand dunes/lands was modeled to improve the multi-temporal classification results. Using the above method, we generated global 30 m sand dune/land datasets for 2000, 2010, and 2020, with an overall accuracy higher than 80%.

8.3.2.4 Results and Analysis

1. Spatial Distributions of Global Sand Dunes/Lands

The spatial distributions of global sand dunes/lands in 2020 and changes in typical regions from 2000 to 2020 are shown in Fig. 8.3. The areas of global sand dunes/lands in 2000, 2010, and 2020 were 1.017×10^7 km², 1.026×10^7 km², and 1.036×10^7 km², accounting for 6.83%–6.95% of the total land area. Shifting sand dunes/lands occupied the largest area, followed by semi-fixed sand dunes/lands, while the area of fixed sand dunes/lands was the smallest. Sand dunes/lands were mainly distributed

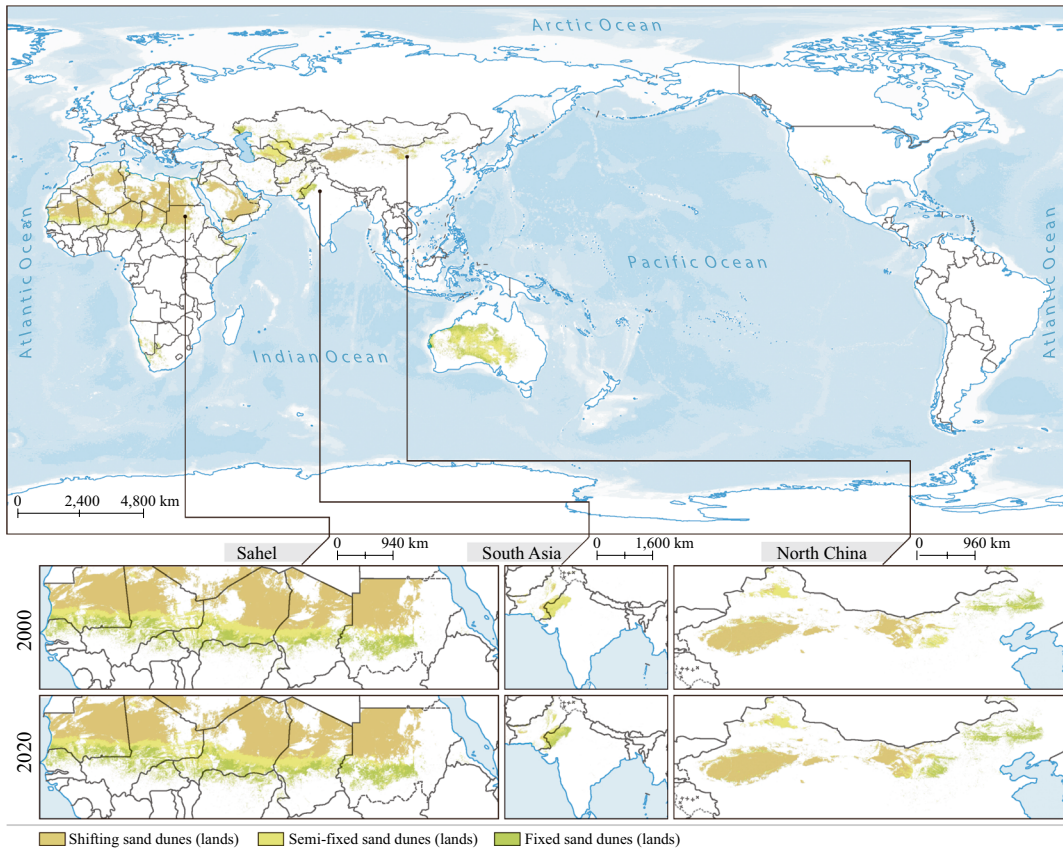


Fig. 8.3 Spatial distributions of global sand dunes (lands) in 2020 and changes in typical regions from 2000 to 2020

in 40°N – 30°S , especially in 20°N – 30°N and 20°S – 30°S , which were closely related to the mid-latitude Hadley circulation. In terms of longitude, sand dunes/lands were mainly distributed in the Eastern Hemisphere, especially in 0° – 60°E and 115°E – 145°E , while their distributions in the Western Hemisphere were relatively scattered. Among the six continents (excluding Antarctica), Africa had the largest area of sand dunes/lands, amounting to $5.567 \times 10^6 \text{ km}^2$ – $5.642 \times 10^6 \text{ km}^2$ and accounting for 18.42%–18.67% of the total land in Africa. Shifting sand dunes/lands are the predominant type in Africa. Oceania ranked third in terms of the area of sand dunes/lands ($1.776 \times 10^6 \text{ km}^2$ – $1.801 \times 10^6 \text{ km}^2$), but had the highest proportion of sand dunes/lands, reaching 19.80%–20.09%. Europe had the smallest area of sand dunes/lands (1.078×10^4

km^2 – $1.351 \times 10^4 \text{ km}^2$) and also accounted for the lowest proportion (0.11%–0.13%).

2. Temporal Change of Global Sand Dunes/Lands During 2000–2020

The global-scale changes in the area of three sand dune/land types are shown in Fig. 8.4. The area of global sand dunes/lands remained stable from 2000 to 2020, with an increase less than 1%. The area of shifting sand dunes/lands fluctuated slightly, with an increase of 0.37% ($2.166 \times 10^4 \text{ km}^2$) from 2000 to 2010 and a decrease of 0.63% ($3.709 \times 10^4 \text{ km}^2$) from 2010 to 2020; the area of semi-fixed sand dunes/lands decreased by 2.16% ($6.033 \times 10^4 \text{ km}^2$) and 1.70% ($4.644 \times 10^4 \text{ km}^2$); and the area of fixed sand dunes/lands increased by 8.39% ($1.243 \times 10^5 \text{ km}^2$) and 11.42% (1.834×10^5

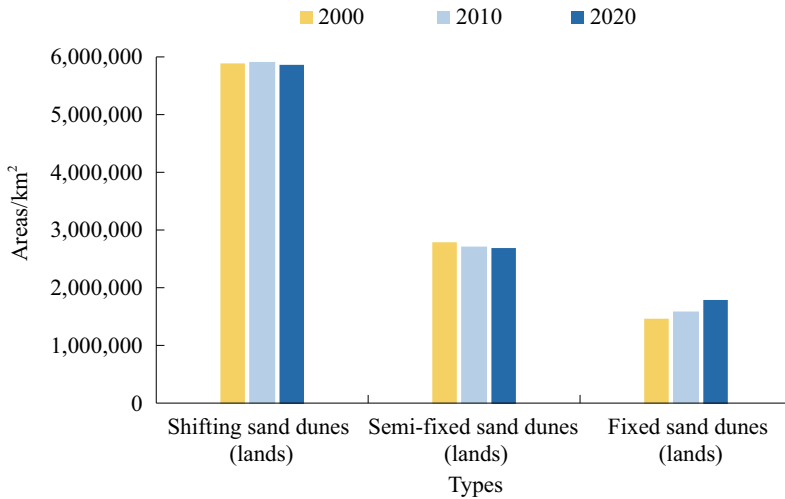


Fig. 8.4 Global-scale changes in the area of three sand dunes (lands) types

km²) in the two periods. The continental-scale analysis indicates that the area of shifting sand dunes/lands in each continent generally remained stable. Asia witnessed a significant decrease in the area of semi-fixed sand dunes/lands, and the area of fixed sand dunes/lands in Africa and Asia increased significantly (Fig. 8.5).

8.3.2.5 Highlights

- A method for high-resolution global-scale mapping of sand dunes was proposed to automatically generate global 30 m sand dune/land datasets for 2000, 2010, and 2020. The datasets include three types of sand dunes/lands—shifting sand dunes/lands, semi-fixed sand dunes/lands, and fixed sand dunes/lands—with an overall accuracy higher than 80%.
- Between 2000 and 2020, the global area of sand dunes/lands remained stable, ranging from 1.017×10^7 km² to 1.036×10^7 km². Shifting sand dunes/lands initially increased and then decreased in area, semi-fixed sand dunes/lands continuously decreased, and fixed sand dunes/lands continuously increased in area.

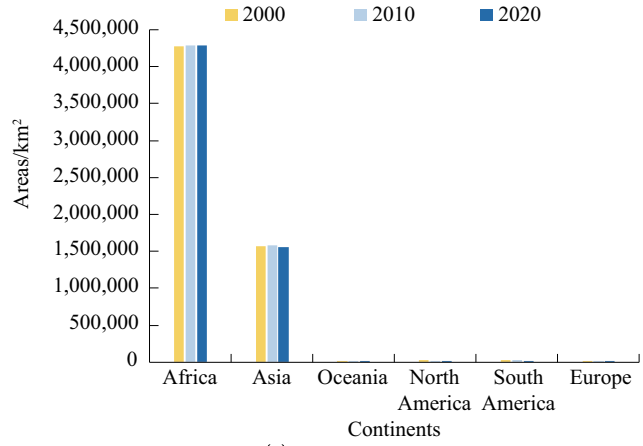
8.3.2.6 Discussion and Outlook

Using satellite remote sensing imagery, multi-source land surface mapping products, and other data, this study proposed a method for mapping sand dunes at a high resolution and global scale, generating a global 30 m sand dune/land dataset with high accuracy. The areas, spatial distributions, and temporal changes of the three sand dune/land types were analyzed, which provide important support for the assessment of SDG 15.3.1.

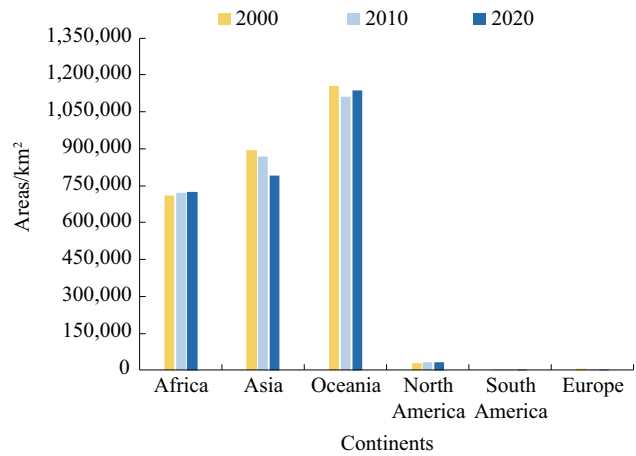
On the one hand, the expansion or shrinkage in the area of sand dunes/lands reflects whether the sand encroachment process accelerated or was controlled and reversed. Thus, the temporal changes in sand dunes/lands calculated from our datasets are an intuitive indicator for assessing SDG 15.3.1. On the other hand, the degree of desertification is another important indicator, which can be divided into extreme, severe, moderate, and low. Previous research has proved the effectiveness of determining the degree of desertification simply based on sand dune/land types. Therefore, our datasets also offer a way to extract and assess aeolian desertification degree at the global scale.

Further improvements are directed at developing sand dune/land datasets with a longer

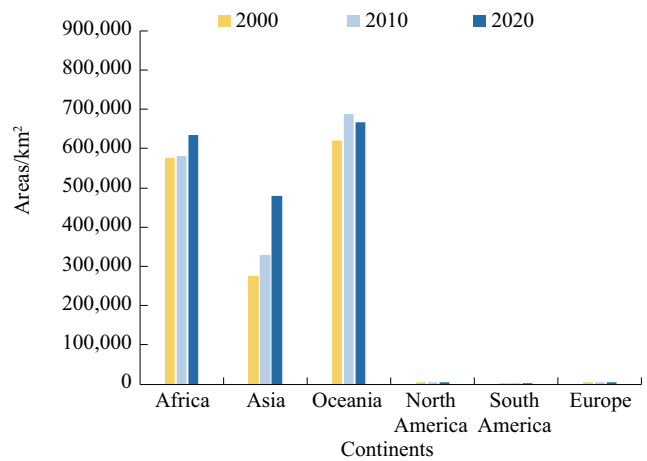
Fig. 8.5 Continental-scale changes in the area of three sand dune/land types



(a) Shifting sand dunes (lands)



(b) Semi-fixed sand dunes (lands)



(c) Fixed sand dunes (lands)

temporal coverage and exploring the impacts of climate change and human activity on their distributions.

8.3.3 Land Degradation Neutrality Process and its Attribution in Five Central Asian Countries

Target: SDG 15.3: By 2030, combat desertification, restore degraded land and soil, including land affected by desertification, drought, and floods, and strive to achieve a land degradation-neutral world.

8.3.3.1 Background

Central Asia is one of the largest arid regions in the world, with an uneven temporal and spatial distribution of water resources and extremely fragile ecological environments. In recent years, dust and sandstorms have occurred frequently in Central Asia, and land degradation has become the most significant environmental issue constraining regional socioeconomic development. The Aral Sea, formerly the fourth largest inland lake in the world, provided important ecosystem services for the basin due to its rich biodiversity. However, large-scale water and land development activities in the Aral Sea Basin have led to the rapid shrinking of the sea, which has been recognized by the UN as one of the most serious ecological disasters of the twentieth century (Micklin et al. 2016). Central Asia is a region where land degradation serves as a typical representation of such environmental issues. Therefore, monitoring the process of achieving LDN and its attribution in five Central Asian countries is crucial. It can provide a valuable reference for implementing comprehensive measures to prevent and control land degradation in arid regions. It can also provide scientific support for achieving the goal of zero net land degradation by 2030 in Central Asia.

Currently, assessing land degradation in data-deficient regions of Central Asia using the recommended NPP vegetation index by the UN and UNCCD is inaccurate. Addressing the

issues of data deficiency and localizing assessment methods for land degradation are crucial for effective monitoring in Central Asia. Land degradation is not only related to surface vegetation, but also closely linked to soil and arid conditions. Therefore, a multi-index comprehensive assessment method is more reasonable for accurately monitoring land degradation in Central Asia (Guo 2021). The case study “Monitoring and assessing land degradation in five Central Asian countries” in the 2020 edition of this report proposed a new remote sensing method for measuring and monitoring the process of land degradation in typical inland arid areas. However, the case study requires further in-depth research for the attribution analysis of land degradation. Based on the findings, recommendations for controlling land degradation can be proposed to provide decision-making references for implementing the initiative of zero net land degradation and recovery plans.

In order to achieve this, the present study utilized a constrained optimal weight algorithm to determine the weights of different monitoring indicators while considering spatial differences. This enabled the calculation of the OLDI to be a continuous sequence (Jiang et al. 2021). The analysis was performed following the SDG 15.3 calculation guidelines released by UNCCD and the recommended methods from Trends Earth. By combining data on land degradation and land use change, we identified land degradation areas in Central Asia (Sims et al. 2021). Furthermore, through the synergistic integration of climate data and human activity data, the present study was able to distinguish between areas affected by climate change and those affected by human-induced land degradation. Finally, the present study proposed governance recommendations for the areas of human-induced land degradation, providing a decision-making reference for governments to implement the LDN initiative and recovery plans.

8.3.3.2 Data

- Global land cover imagery from 2000 to 2020 at a 300 m spatial resolution provided by the ESA CCI (<https://www.esa-landcover-cci.org/>).

- The US Department of Agriculture (USDA) soil classification data at a spatial resolution of 250 m (<https://www.nrcs.usda.gov/>).
- MODIS vegetation NPP data (MOD17A3HGF), NDVI data (MOD13A1), surface albedo data (MCD43A3) at a spatial resolution of 500 m; LST data (MOD11A2) at a spatial resolution of 1 km; and evapotranspiration/latent heat flux data (MOD16A2) at a spatial resolution of 500 m are all available for the period 2000–2020 (<https://ladsweb.modaps.eosdis.nasa.gov/search/>).
- The temperature vegetation dryness index (TVDI) data from 2000 to 2020 at a spatial resolution of 500 m were provided by a Big Earth Data project launched by CAS (CASEarth).

8.3.3.3 Methods

In this case study, all the data products were resampled to a spatial resolution of 500 m. The constrained optimal weight algorithm was used to determine the weights of each monitoring indicator, and the OLDI was obtained based on the different combinations of weights, with a spatial resolution of 500 m. To obtain the optimal weight allocation scheme, NPP was taken as the reference state, and the optimal weight allocation combination for the OLDI was calculated through iterative calculations using the constrained optimal weigh algorithm. The formulas for the constrained optimal weight algorithm were calculated as follows:

$$f(\text{NPP}, \text{OLDI}_t) = \max\left(\frac{E[(\text{NPP} - \overline{\text{NPP}}) \times (\text{OLDI}_t - \overline{\text{OLDI}}_t)]}{\delta\text{NPP} \times \delta\text{OLDI}_t}\right),$$

$$\text{OLDI}_t = \alpha \times \text{NDVI} + \beta \times \text{Albedo} + \gamma \times \text{LST} + \lambda \times \text{TVDI},$$

where NPP refers to net primary productivity; OLDI_t represents the OLDI value at time t ; $f(\text{NPP}, \text{OLDI}_t)$ is the determining function based on the highest correlation coefficient between NPP and OLDI; $\overline{\text{NPP}}$ and $\overline{\text{OLDI}}_t$ indicate the mean values of NPP and OLDI_t , respectively; E refers to the expectation; δNPP and δOLDI_t represent the standard deviation of NPP and OLDI_t , respectively; NDVI, Albedo, LST, and TVDI are monitoring indicators; and α , β , γ , and λ refer to the weight of each indicator, respectively, between 0 and 1.

The OLDI data were used to monitor land degradation in Central Asia, replacing the NPP indicator recommended by the UN. The land degradation was evaluated using the trends, performances, and status methods proposed by the UNCCD, with the years 2000–2016 as the baseline period and 2017–2020 as the change period.

Water is the most sensitive and restrictive factor in arid areas, and it can be said that “water is the lifeblood”. Unreasonable utilization of water resources is a key factor in the disaster of the shrinking Aral Sea. The residual analysis method was used to identify the impacts of human activity and climate change on land degradation. Then, the water stress index (WSI) was calculated to identify areas with sufficient or insufficient water supply in typical areas affected by human-induced land degradation. The WSI value ranges between 0 and 1. The higher the WSI is, the more severe the water stress is. The WSI can be defined using the following formula:

$$\text{WSI} = 1 - \frac{\text{Actual evapotranspiration}}{\text{Potential evapotranspiration}}.$$

8.3.3.4 Results and Analysis

Long-term stable native deserts such as the Kyzylkum Desert and the Karakum Desert in Central Asia should not be considered as areas for land degradation control and were excluded from the data analysis. The results indicate that overall land degradation has worsened, but there are spatial differences. Most of the land degradation occurred in western Central Asia, while the areas of land improvement were sporadically distributed. Land degradation around the Aral Sea was more severe compared to other regions (Fig. 8.6), and land degradation in Western Kazakhstan and the Atyrau region of Central Asia should not be overlooked.

The proportion of land degradation in Central Asia as a percentage of the total area was 15.65%, while the proportion of land improvement was 6.83%. The proportion of land degradation was higher than that of land improvement in all countries, with Kazakhstan and Uzbekistan having higher proportions of land degradation at 16.49% and 14.14%, respectively.

Uzbekistan had a relatively high proportion of land improvement at 11.74%. Kyrgyzstan and Tajikistan had proportions of stable land compared to the other three countries at 83.66% and 79.86%, respectively. At the state scale, 15 regions had a larger area of land improvement compared to land degradation, achieving the goal of zero net land degradation, while other regions had a larger area of land degradation compared to land improvement. Achieving SDG 15.3, zero net land degradation, in Central Asia by 2030, still faces significant challenges, and land degradation prevention and control in Central Asia are crucial for achieving the global goal of zero net land degradation (Fig. 8.7).

Human-induced land degradation areas were clearly clustered (shown in dark red) and mainly located around the Aral Sea and the Atyrau region in Western Kazakhstan. Climate-induced land degradation areas were scattered (shown in light red), mainly in the southeastern part of Kazakhstan. Human-induced land improvement areas (shown in dark green) were mainly distributed in central Kazakhstan and the delta of Lake Balkhash wetland, while climate-induced land improvement areas (shown in light green) were relatively concentrated in the northern part of Uzbekistan. The proportion of human-induced land degradation and land improvement areas as a percentage of the total area in Central Asia was 7.25% and 5.37%, respectively, while the proportion of climate-induced land degradation and land improvement areas was 8.40% and 1.46%, respectively. Among different countries, Kazakhstan and Uzbekistan had higher proportions of human-induced land degradation at 7.74% and 7.38%, respectively, and Uzbekistan had a higher proportion of human-induced land improvement at 6.52% (Fig. 8.8).

The Aral Sea Basin was selected as a typical area to further analyze the influences of WSI on land degradation. The Aral Sea Basin was divided into 13 sub-basins based on the boundaries of irrigation districts and state boundaries to investigate the spatial differences in the WSI in the region. The WSI declined in most areas, especially in the upstream areas (with an annual change rate of $-0.008/a$) (Fig. 8.9a). However, Karakalpakstan

and Chardara showed a significant increasing trend. The WSI was positively correlated with the land degradation index (OLDI) in most areas, especially in Karakalpakstan, Khorezm, and Chardara (Fig. 8.9b).

It is worth noting that a clear boundary was found in the trend of WSI changes between the Karakalpakstan and Tashauz states. Karakalpakstan had higher WSI and land degradation intensity compared to Tashauz, and the correlation between WSI and OLDI in Karakalpakstan was significantly stronger than that in Tashauz. This is because different countries adopt different irrigation methods based on their own irrigation infrastructure and agricultural policies. On the one hand, there were significant differences in planting patterns between the two regions (Jiang et al. 2020). The impacts of water scarcity on Tashauz were relatively low because the water demand for wheat is much lower than that for cotton, and an increase in the proportion of wheat can effectively alleviate water scarcity in the downstream areas. On the other hand, Karakalpakstan is located in the most downstream area of the basin, and water scarcity has a more significant impact on agricultural fields in this region. In addition, in order to transport more water to Tashauz, a new water supply canal was constructed to connect with the Malyab Canal, which has exacerbated water scarcity in Karakalpakstan (Jiang et al. 2020).

8.3.3.5 Highlights

- A novel method was proposed for the accurate evaluation of land degradation in inland arid regions. The establishment of OLDI can provide a new data source for the evaluation of SDG 15.3.1 in arid areas.
- Defining the years from 2000 to 2016 as the baseline period and from 2017 to 2020 as the change period, land degradation in Central Asia accounted for 15.65% of the total area, while land improvement accounted for 6.83% of the total area. Land degradation around the Aral Sea and Western Kazakhstan is particularly severe. The goal of zero net land degradation has not been achieved in most of

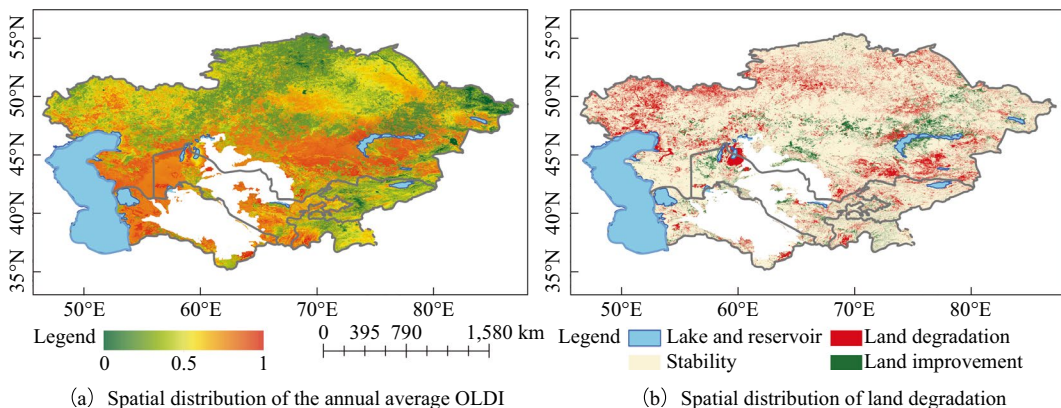


Fig. 8.6 Spatial distribution of the annual average OLDI and land degradation from 2000 to 2020

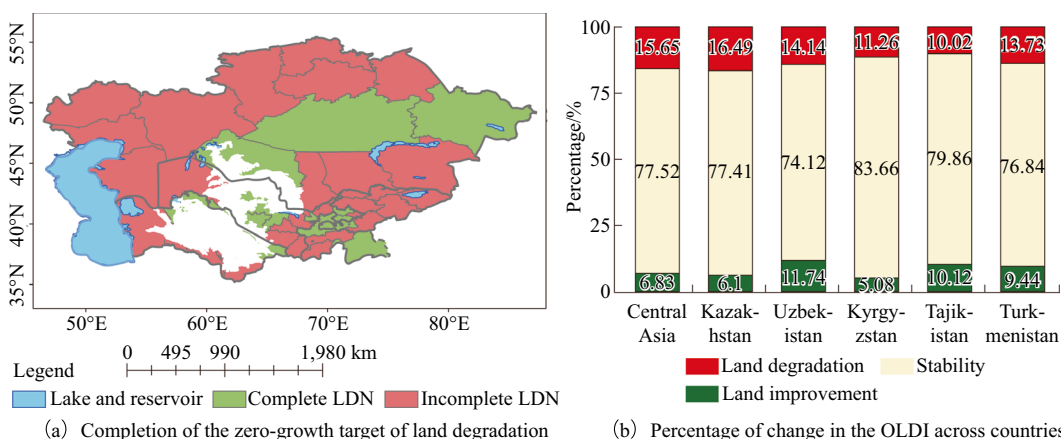


Fig. 8.7 Completion of the zero-growth target of land degradation and percentage of change in the OLDI across countries. Note for this and figures below: CA:

Central Asia; KAZ: Kazakhstan; UZB: Uzbekistan; KGZ: Kyrgyzstan; TJK: Tajikistan; TKM: Turkmenistan

Central Asia, and the realization of SDG 15.3 by 2030 still faces severe challenges.

- Land degradation caused by human activity is a significant issue in the lower reaches of the Aral Sea Basin and western Central Asia. Agricultural development in the Aral Sea Basin has led to water scarcity in the downstream areas (Karakalpakstan, Khorezm, and Chardara). It is recommended to improve irrigation infrastructure, enhance the legal framework for transboundary water management, and promote pilot water rights trading to alleviate water resource pressures in the downstream areas of the Aral Sea Basin.

8.3.3.6 Discussion and Outlook

Based on the proposed methods and models of Big Earth Data, this case optimized a novel method for accurately evaluating land degradation in inland arid areas, and it can provide a data source for the evaluation of SDG 15.3.1. Land degradation in Central Asia accounted for 15.65% of the total area, while land improvement accounted for 6.83% of the total area. Land degradation around the Aral Sea and Western Kazakhstan is particularly severe. Most regions in Central Asia had a larger area of land degradation compared to land improvement and have not achieved the goal of zero net

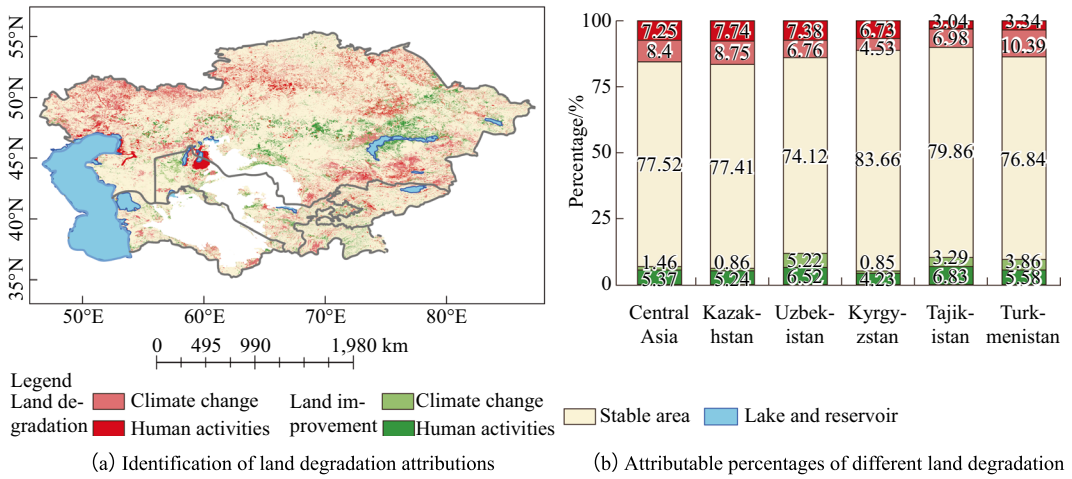


Fig. 8.8 Identification of land degradation attributions and attributable percentages of different land degradations

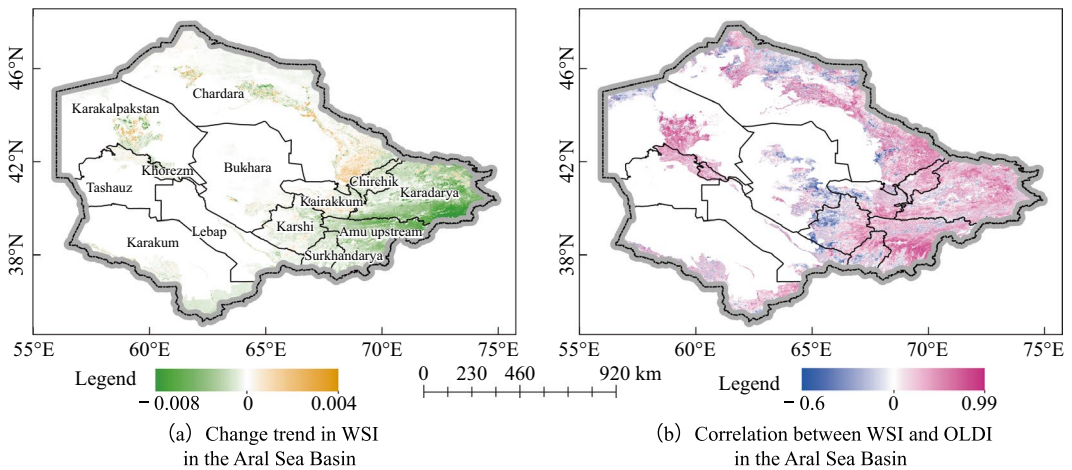


Fig. 8.9 Change trend in WSI and correlation between WSI and OLDI in the Aral Sea Basin

land degradation. The prevention and control of land degradation in Central Asia are crucial to achieving the goal of zero net land degradation.

An attribution analysis of land degradation was conducted in this case study. The results show that human-induced land degradation was mainly concentrated in the downstream areas of the Aral Sea Basin and western Central Asia. Identifying areas for human-induced land degradation can play a positive role in implementing the zero-growth initiative for land degradation.

In the future, it is suggested that the areas of human-induced land degradation can be identified as key targets for implementing restoration plans, providing a reference for governments to implement the goal of zero net land degradation.

Agricultural development in the Aral Sea Basin has led to water scarcity in the downstream areas (Karakalpakstan, Khorezm, and Chardara), resulting in severe land degradation and abandoned farmland in the areas surrounding the Aral Sea. It is recommended to improve

irrigation infrastructure, enhance the legal framework for transboundary water management, and promote pilot water rights trading to alleviate water resource pressure in the downstream areas of the Aral Sea Basin. In addition, the downstream areas can change the planting pattern and plant more low-water-consumption crops to alleviate water scarcity.

8.3.4 Assessment of the Impacts of Climate Change and Human Activity on Wild Camels and Their Habitats

Target: SDG 15.5: Take urgent and significant action to reduce the degradation of natural habitats, halt the loss of biodiversity, and by 2020, protect and prevent the extinction of threatened species.

8.3.4.1 Background

The wild camel (*Camelus ferus*), also called the wild Bactrian camel but not descended from Bactrian camels, is a separate species living in three discrete habitats in China and one in Mongolia. It is listed as critically endangered (CR) and Class I endangered by the International Union for Conservation of Nature (IUCN) and the Convention on International Trade in Endangered Species of Wild Fauna and Flora (CITES), respectively. The wild camel has an extremely important position and research value in the protection of the world's biodiversity due to its genetic characteristics. For instance, it can adapt to the extreme desert living environment and drink brackish water. It is estimated that there are only about 1000 wild camels surviving on the planet. Affected by factors such as climate change and human activity, wild camels have reached the brink of extinction.

The last 20 years' rise in temperature is eight times more than that of the last 100 years, and the rate of climate change is very rapid for most species to adapt. The ability of wildlife to adapt to climate change depends critically on the rate of change (IPCC Working Group 1992). This increasing temperature not only causes a change

in rainfall or precipitation, but also causes animals to move toward those places that are more suitable for them (Thornes 2002).

Human activity, including land use change, road traffic, and resource development, has a huge impact on animals and plants at the global and regional scales, resulting in changes in the distribution of animals and plants, and a decline in health status, or even extinction (Crooks et al. 2017). Consequently, understanding the effects of human activity on wild camels and their habitats, as well as devising strategies to cope with these effects, is an increasing challenge for scientists and policymakers.

Based on the satellite tracking data of wild camels, this case combines satellite remote sensing images and other types of data to evaluate the quality of suitable habitats for wild camels under current and future climate change conditions. The results of this case study lay a foundation for revealing the impacts of climate change and human activity on wild camels and their habitats, the estimation of the wild camel population, the assessment of habitat carrying capacity, and a scientific basis for the establishment of the China Wild Camel National Park and the China-Mongolia Cross-border Wild Camel Nature Reserve.

8.3.4.2 Data

- From 2013 to 2016, data on 12 wild camels were obtained using satellite trackers, including eight in China and four in Mongolia, with a total of 21,085 tracking points.
- Environmental data: physical environmental factors (DEM, slope, aspect), biological factors (water source, vegetation cover, vegetation type), human influence factors (roads, railways, human footprint index).
- The representative concentration pathway (RCP) 4.5 model was used with 19 current bioclimatic factors and 19 future bioclimatic factors.

8.3.4.3 Methods

Using niche models to evaluate a species' habitat suitability, including predicting changes in

suitable habitats under future climate change scenarios, is becoming a hotspot in research and applications. The maximum entropy model (MaxEnt) is an ecological niche model capable of accurate prediction. It takes into account the maximum entropy and the ecological niche, and it can construct a potential distribution model of animals based on the existing species distribution data and environmental variable data and infer the potential distribution of the population. The range and possible probability of occurrence are combined with future climate change data to predict the future distribution of the population. The model has been widely used in the assessment of habitat fragmentation, protection of endangered species, research on interspecific relationships, and prediction of the impact of climate change on species. The maximum entropy model estimates the distribution of species by finding the probability distribution of maximum entropy. The formula is as follows:

$$q\lambda(x) = \frac{e^{\lambda f(x)}}{Z_{\lambda}},$$

where λ is a vector of n real-valued coefficients or eigenweights, f is a vector of all environmental factors, and Z_{λ} is a normalization constant used to ensure that the sum of q values is 1.

The maximum entropy model reflects the habitat suitability of species through the habitat suitability index (HSI), which ranges from 0 to 1, where 0 represents the least suitable habitat and 1 represents the most suitable. It is worth noting that the model species distribution locus data are not biased, and the environmental conditions are uniformly sampled.

8.3.4.4 Results and Analysis

The spatial distribution of current suitable habitats for wild camels is shown in Fig. 8.10. In terms of the overall distribution, the potentially suitable habitats for wild camels mainly include two areas in China and Mongolia. Among them, the potentially suitable habitat in China is centered on the Kumtag Desert, including the area north of the Altun Mountains, the south of Aqike Valley, the east of Lop Nur, and the west of Dunhuang West Lake Wetland. There are also

suitable habitats in the Qaidam Basin in the southern Altun Mountains, but mainly sub-suitable habitats. The potentially suitable habitats for wild camels in Mongolia are mainly located in the Gobi Altai of Mongolia, and there are also a few sub-suitable habitats in the border region of China and Mongolia. The potential wild camel habitat patches in Mongolia have good integrity and a low degree of fragmentation, mainly with suitable habitats and less sub-suitable habitat area. There are two large patches mainly distributed in the Great Gobi A Strictly Protected Area, divided by a road.

At present, the total potential suitable habitat areas for wild camels are considerable, of which the suitable habitat area is 75,080 km² and the sub-suitable habitat area is 114,991 km². Among them, the suitable habitat area in China is 36,903 km², and the sub-suitable habitat area is 75,611 km². The suitable habitat area in Mongolia is 38,177 km², and the sub-suitable habitat area is 39,380 km².

Under the RCP 4.5 climate scenario, compared with the current potential suitable habitats for wild camels (Fig. 8.10), the area of suitable habitats for wild camels in the future will greatly decrease (Figs. 8.11 and 8.12), and the spatial distribution pattern will also change. For the entire wild camel distribution area, both suitable and sub-suitable habitats show a downward trend year after year. In 2050, the suitable habitat area will be 3519 km², and the sub-suitable habitat area will be 67,542 km², decreasing 95.3% and 41.3%, respectively, compared with the current situation. In 2070, the suitable habitat area will be 1228 km², and the sub-suitable habitat area will be 49,672 km², decreasing 65.1% and 26.5%, respectively, compared with 2050.

8.3.4.5 Highlights

- Suitable wild camel habitats were mapped under current climate conditions and future climate change scenarios in 2050 and 2070.
- The suitable habitat area for wild camels in China and Mongolia was 190,071 km² in 2016. Under the conditions of future climate

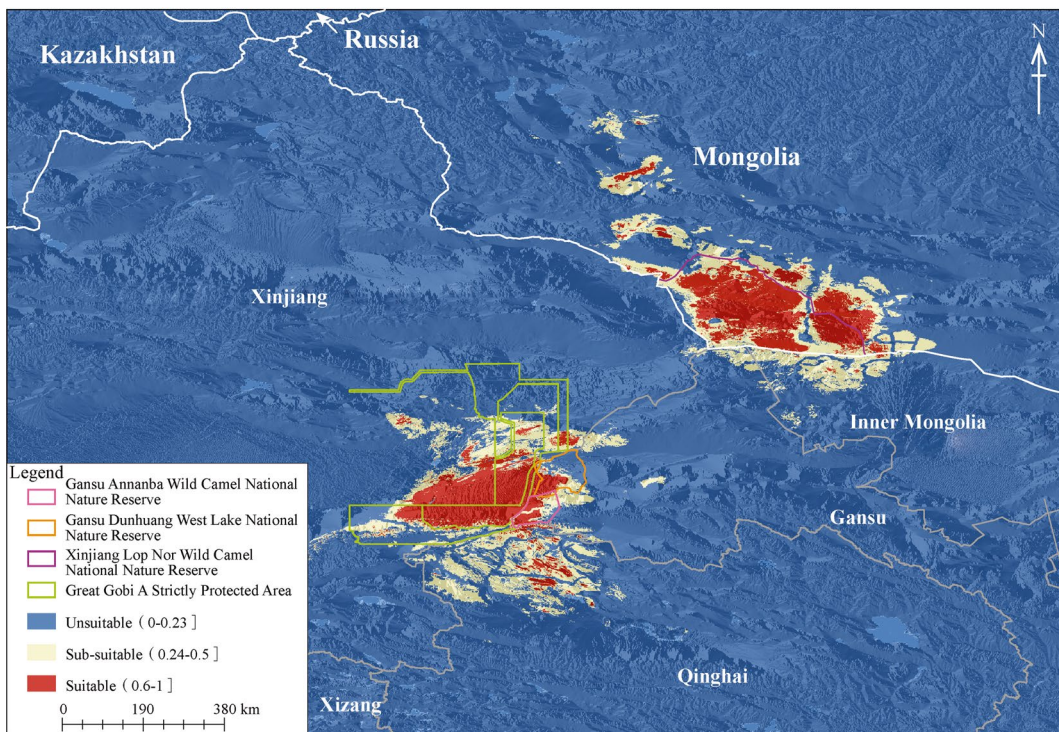


Fig. 8.10 Spatial distribution of current suitable habitats for wild camels

change, the suitable habitat areas for wild camels in 2050 and 2070 will decrease to 71,061 km² and 50,900 km², respectively, showing a rapid downward trend. In the future, the survival of wild camels will face severe challenges.

8.3.4.6 Discussion and Outlook

In this case study, spatiotemporal big data was used to statistically analyze the distribution and changes in suitable habitats for wild camels under current conditions and future climate change scenarios. It is suggested that the wild camel protection strategy should be adjusted in time according to the changing trend of suitable habitats, and the China Wild Camel National Park and the China-Mongolia Cross-border Wild Camel Nature Reserve should be established as soon as possible.

In addition to the impact of climate change and human activity, the survival of wild camels is affected by other factors such as diseases, interspecific competition, predation relationships,

hybridization of wild and domestic camels, and competition with domestic camels. In the future, in-depth research will be carried out on niche overlap or avoidance caused by predatory competition, as well as diseases and genes of wild camels. These studies are important for a better understanding of wild camels and for more effective wild camel research and conservation.

8.4 Summary

Currently, the 2030 Agenda is less than halfway to being achieved. Considering the long time it takes for ecosystems to recover and show the benefits of conservation, only urgent, concerted, and effective action to protect and restore ecosystems will make it possible to fully achieve the terrestrial biodiversity that SDG 15 brings to the 2030 Agenda.

We still have a number of challenges in assessing the indicators of SDG 15. For

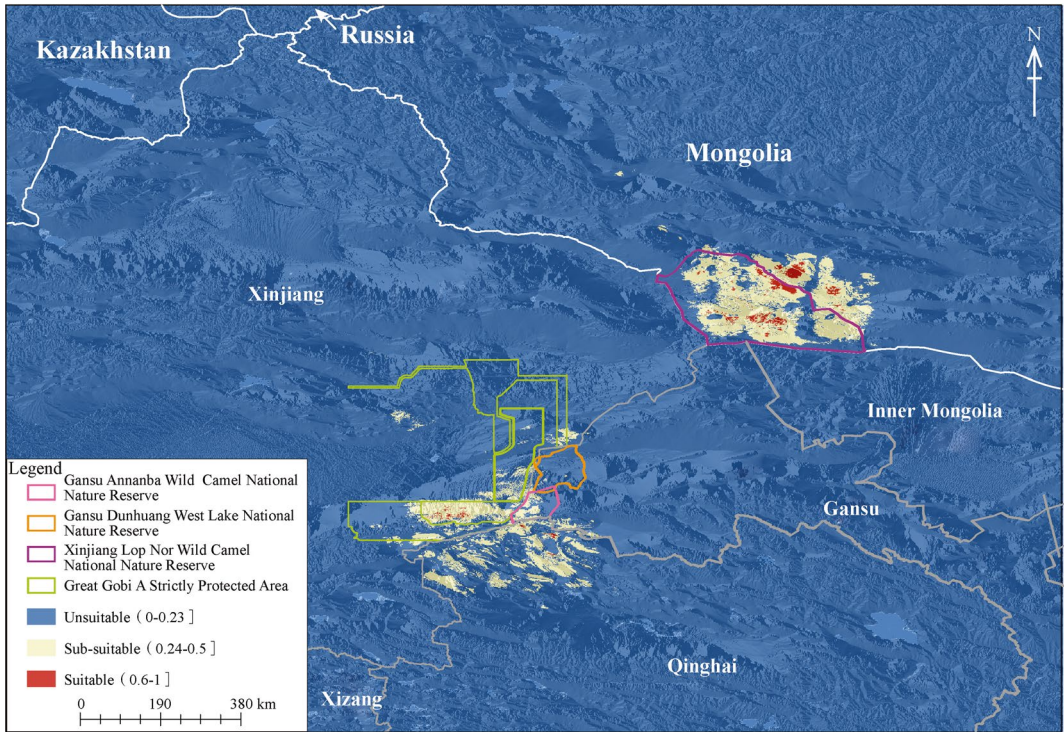


Fig. 8.11 Spatial distribution of suitable habitats for wild camels in 2050

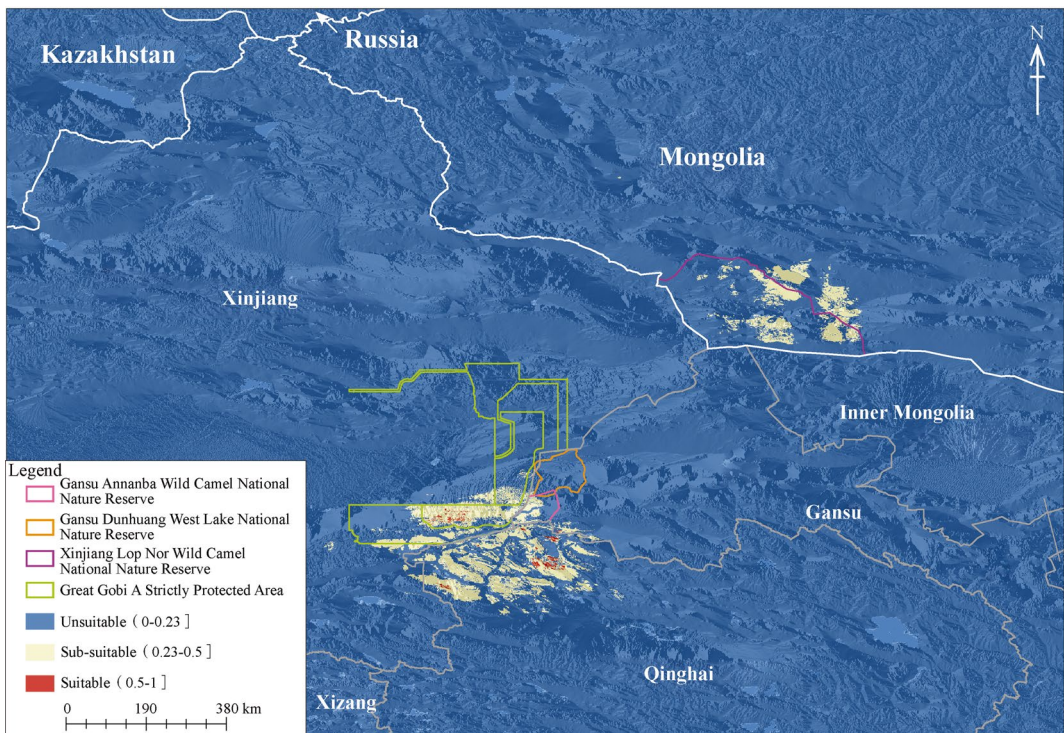


Fig. 8.12 Spatial distribution of suitable habitats for wild camels in 2070

example, biodiversity monitoring is still limited to ground survey/statistical means, and large-scale monitoring of key biodiversity variables is a big challenge; the extent of protected areas is steadily increasing, but there are still shortcomings in the effectiveness of conservation, in setting conservation targets, and in their implementation; and land degradation assessment faces a series of difficulties such as complex concepts, unclear benchmarks, and a lack of monitoring methodologies.

In the future, facing the major needs of the “UN Decade on Ecosystem Restoration” and “Post-2020 Global Biodiversity Framework”, we should give full play to the great potential of Big Earth Data in SDG 15 monitoring and assessment and strengthen the SDGSAT-1 satellite program and its applications, as well as other satellites from China and accompanying big data platforms for SDGs. This big data infrastructure can provide high-quality, easy-to-use data products, methods, models, and decision support tools to support the implementation of SDG 15.

References

- Brandt M, Hiernaux P, Rasmussen K et al (2016) Assessing woody vegetation trends in Sahelian drylands using MODIS based seasonal metrics. *Remote Sens Environ* 183:215–225
- Crooks KR, Christopher LB, David MT et al (2017) Quantification of habitat fragmentation reveals extinction risk in terrestrial mammals. *Proc Natl Acad Sci* 114(29):7635–7640. <https://doi.org/10.1073/pnas.1705769114>
- FAO (2020) Global forest resources assessment 2020 key findings. <https://www.fao.org/forest-resources-assessment/2020/en/>
- FAO, UNEP (2020) The State of the World's forests 2020: forests, biodiversity and people. Rome, FAO
- Guo H (2021) Big earth data in support of the sustainable development goals (2020): the belt and road. EDP Sciences Press, Beijing
- Hanan NP, Tredennick AT, Prihodko L et al (2014) Analysis of stable states in global savannas: Is the CART pulling the horse? *Glob Ecol Biogeogr* 23(3):259–263
- IPBES (2019) Global assessment report on biodiversity and ecosystem services of the intergovernmental science-policy platform on biodiversity and ecosystem services. Version 1. <https://doi.org/10.5281/zenodo.3831673>. (30 May 2023)
- IPCC Working Group (1992) The IPCC supplementary report. Cambridge University Press
- Jiang LL, Bao AM, Yuan Y et al (2020) The effects of water stress on croplands in the Aral Sea Basin. *J Clean Prod* 254:120114
- Jiang LL, Bao AM, Jiapaer G, et al. (2022) Monitoring land degradation and assessing its drivers to support sustainable development goal 15.3 in Central Asia. *Sci Total Environ* 807:150868
- Masiliūnas D, Tsendbazar NE, Herold M et al (2021) Global land characterisation using land cover fractions at 100 m resolution. *Remote Sens Environ* 259:112409
- McKee ED (1979) Introduction to a study of global sand seas/McKee E D. A Study of Global Sand Seas (1–20). Washington, United States Government Printing Office
- Micklin P, Aladin NV, Plotnikov I et al (2016) The Aral Sea. Springer, Berlin
- Sims NC, Newnham G, England J, et al. (2021) Good practice guidance. SDG indicator 15.3.1, proportion of land that is degraded over total land area. Version 2.0. Bonn: UNCCD. <https://www.unccd.int/resources/manuals-and-guides/good-practice-guidance-sdg-indicator-1531-proportion-land-degraded>
- Thornes JE (2002) IPCC, 2001: Climate change 2001: impacts, adaptation and vulnerability, contribution of working Group II to the third assessment report of the intergovernmental panel on climate change. In: McCarthy JJ, Canziani OF, Leary NA (eds) Cambridge, New York, Cambridge University Press
- UN (2019) The sustainable development goals report 2019. New York, UN. <https://unstats.un.org/sdgs/report/2019/The-Sustainable-Development-Goals-Report-2019.pdf>
- UNEP (2021) Measuring progress: environment and the SDGs. <https://wedocs.unep.org/bitstream/handle/20.500.11822/35968/SDGMP.pdf>. (15 June 2022)
- Yang XB, Crews K (2019) Applicability analysis of MODIS tree cover product in Texas savanna. *Int J Appl Earth Obs Geoinf* 81:186–194. <https://doi.org/10.1016/j.jag.2019.05.003>
- Zheng ZJ, Du SH, Taubenböck H et al (2022) Remote sensing techniques in the investigation of Aeolian sand dunes: a review of recent advances. *Remote Sens Environ* 271:112913

Open Access This chapter is licensed under the terms of the Creative Commons Attribution-NonCommercial-NoDerivatives 4.0 International License (<http://creativecommons.org/licenses/by-nc-nd/4.0/>), which permits any noncommercial use, sharing, distribution and reproduction in any medium or format, as long as you give appropriate credit to the original author(s) and the source, provide a link to the Creative Commons license and indicate if you modified the licensed material. You do not have permission under this license to share adapted material derived from this chapter or parts of it.

The images or other third party material in this chapter are included in the chapter's Creative Commons license, unless indicated otherwise in a credit line to the material. If material is not included in the chapter's Creative Commons license and your intended use is not permitted by statutory regulation or exceeds the permitted use, you will need to obtain permission directly from the copyright holder.





Interactions Among SDGs and Integrated Evaluations

9

9.1 Background

The assessment of a single SDG indicator can track the progress of that indicator, but judging whether the development of a certain region is sustainable requires a comprehensive consideration of the impact of different SDG indicators. Due to differences in natural resource endowment, socio-economic development levels, and development paths in different regions, there are complex interactions among SDGs and related indicators. Research on the intersection of multiple SDG indicators involves the following three aspects: (1) the synergy and trade-off relationships among multiple SDG indicators in the same time period and spatial range (the synergistic indicators promote one another, yet trade-offs emerge when achieving progress at the expense of others); (2) the spillover effects of multiple SDG indicators in different spatial ranges but in the same time period; and (3) future scenario simulation of SDGs under the interaction of multiple indicators in the same spatial range. In addition, achieving SDGs requires the integration of multiple themes, such as SDGs for agriculture, ecological environment, water resources, and urban areas, striving for balanced and sustainable development across all 17 SDGs. Understanding the intersectional

relationships between goals and indicators and conducting single-theme and regional comprehensive assessments of SDGs are of great significance for achieving the 2030 Agenda and dynamically adjusting sustainable development paths.

Research on interactions among SDGs and integrated evaluations has been carried out by organizations and the academic community at different scales since the SDGs were proposed. In terms of SDG interactions, UN-Water analyzed the six targets of SDG 6 and other targets of SDGs with potential interconnected relationships, finding 127 pairs with synergistic relationships and 29 pairs with potential trade-off relationships (UN-Water 2016). In 2021, the United Nations Environment Program (UNEP) conducted a progress report on the interaction of environmental indicators and other indicators, analyzing the relationships among the near-nature action indicators, socio-economic development indicators, and natural state indicators among the SDG indicators. Pradhan et al. (2017) used time-series data covering 122 indicators in 227 countries worldwide to quantitatively analyze the synergistic and trade-off relationships within and between all SDG targets at the global and national scales from 1983 to 2016. They concluded that at the global scale,

most countries in the world exhibit more synergistic relationships than trade-off relationships between SDG targets. Warchold et al. (2021) further analyzed the linear or nonlinear synergistic and trade-off relationships within and between SDGs at the global and national levels, using updated and higher coverage data (covering 171 indicators in 247 countries worldwide from 1991 to 2019), and reached the same conclusion. This study also found that the synergistic and trade-off relationships among SDG targets vary greatly among different populations, income groups, and regions. In terms of the comprehensive assessment of SDG themes, the UN FAO evaluated 21 indicators related to food security and found that progress in global food and agricultural production is still insufficient, making it difficult to achieve the 2030 goals (FAO 2021). The latest report from UN-Water indicates that the targets of SDG 6 are currently difficult to achieve at the global level, with 10% of the world's population still unable to access safe drinking water and sanitation facilities, and many water sources drying up or becoming more polluted (UN-Water 2023). In terms of the regional integrated evaluations of SDGs, the UN Sustainable Development Solutions Network (SDSN) and the Bertelsmann Foundation established an SDG index evaluation method and a set of SDG measurement standards for the national level, aiming to help each country identify priority issues, understand the challenges faced in the implementation process, clarify existing gaps, and support the achievement of the 2030 Agenda (Sachs et al. 2018, 2020, 2021, 2022).

However, most of the current studies on interactions among SDGs and integrated evaluations

are based on statistical data, lacking sufficient consideration of geographical spatiotemporal characteristics. The integration of Big Earth Data, which combines satellite observations, ground-based observations, and ground surveys, has massive, multi-source, and multi-temporal characteristics, providing essential data and technical support for SDG monitoring and evaluation. On the one hand, Earth observation data and geographic information data provide important supplements or replacements for traditional official statistical data. Its continuous, timely spatial, and temporal coverage can capture changes in surface features to monitor SDGs, overcoming the problems of inconsistent standards and quality of statistical data in different countries and regions. On the other hand, geographic information modeling and simulation methods based on spatial analysis and other technologies can help sort out the interactions between targets, predict future development trends, carry out comprehensive evaluations, and provide a basis for the dynamic adjustment of policy recommendations.

9.2 Main Contributions

Taking Central Asia as an example, this chapter explores the interactions and pressure transmission among water, energy, food, and ecological systems based on Big Earth Data. The sub-indexes include ecological footprint, water footprint, WSI, and crop yields, which provide a detailed evaluation of the sustainable development of the WEFE system in Central Asia and also offer decision-making support for local governments (Table 9.1).

Table 9.1 Case and its main contributions

Targets	Case	Contributions
SDG 2.1, SDG 6.4, SDG 7.2, SDG 15.3, SDG 17.16	Integrated evaluation and sustainable development of water–energy–food–ecology systems in Central Asia	Method and model: provide a detailed evaluation of the sustainable development of the WEFE system in Central Asia Decision support: provide decision support for governments and propose two mitigation strategies, i.e., “same effect trade agreement” (to replace “equivalent trade agreement”) and “power transmission from east to west” (to import electric power from China), to adjust the energy, planting, and import and export trade structure, as well as realize the sustainable development of the WEFE system in Central Asia

9.3 Case Study

9.3.1 Integrated Evaluation and Sustainable Development of Water–Energy–Food–Ecology Systems in Central Asia

Target: SDG 2.1: By 2030, end hunger and ensure access by all people, in particular the poor and people in vulnerable situations, including infants, to safe, nutritious, and sufficient food all year round.

SDG 6.4: By 2030, substantially increase water-use efficiency across all sectors and ensure sustainable withdrawals and supply of freshwater to address water scarcity and substantially reduce the number of people suffering from water scarcity.

SDG 7.2: By 2030, increase substantially the share of renewable energy in the global energy mix.

SDG 15.3: By 2030, combat desertification, restore degraded land and soil, including land affected by desertification, drought, and floods, and strive to achieve a land degradation-neutral world.

SDG 17.16: Enhance the Global Partnership for Sustainable Development, complemented by multi-stakeholder partnerships that mobilize and share knowledge, expertise, technology, and financial resources to support the achievement of the Sustainable Development Goals in all countries, in particular developing countries.

9.3.1.1 Background

SDG 2.1, SDG 6.4, SDG 7.2, and SDG 15.3 respectively correspond to food, water, energy, and ecological securities. Water, energy, and food securities are the foundations to achieve national sustainable development, and ecological security is the basic guarantee of water, energy, and food securities. Therefore, there are tight linkages between water, energy, food, and ecological systems, and changes in one sector may have unintended consequences for others. Therefore, a comprehensive indicator is needed to evaluate the overall condition of the sustainable

development of the WEF system, and measures to achieve SDGs are needed. In addition, the sharing of river basins, borders, or trade between countries will also lead to related impacts on the SDGs, which are manifested as spatial spillover. For example, the consumption of water and energy during the production of goods, along with the resulting pressure on the ecological environment, can significantly influence SDGs. Importing countries transmit the effects of these SDGs through trade to the exporting countries. According to the Sustainable Development Report 2023 (Sachs et al. 2023), GHG (greenhouse gas) emissions due to the global final demand for textiles and clothing, 59% are emitted along the supply chains of countries other than those where the final products are consumed, while 41% are emitted in the countries in which the final products are consumed.

Central Asia is located in the hinterland of Eurasia, with scarce precipitation and an arid climate. As a community with a shared future, the sustainable development of Central Asian countries is quite important to China. However, due to arid climatic conditions, a rapidly increasing population, the fallout from the collapse of the Soviet Union, and irrational human activity, the WEF system of Central Asia has become very vulnerable. In addition, the collapse of the Soviet Union broke the mechanism of complementary resource policies among countries, and the contradiction between irrigation water in upstream areas and hydropower in downstream areas became prominent. Therefore, cooperation among countries and basins is crucial to achieving WEF system security in Central Asia, corresponding to SDG 17.16, which urgently requires a comprehensive sustainable coordination mechanism.

At present, the pressure status of water, energy, food, and ecological systems in Central Asian countries is not clear, and the relationship between different sectors has not been revealed, especially whether there is pressure transmission between different sectors. Therefore, four stress indicators are constructed in this case study to reflect water, energy, food, and ecological stresses, respectively. Water stress is expressed

as the ratio of total freshwater withdrawal to the total renewable freshwater resources after deducting the environmental flow. Energy stress is expressed as the ratio of the total primary energy consumption to the total primary energy production. The hunger index (combining four factors: child malnutrition, underweight, stunting, and child mortality) is used to reflect food stress in Central Asian countries because of the difficulty in obtaining data on food consumption and production. Ecological stress is reflected by the ratio of the total ecological footprint to ecological biocapacity. These four indicators correspond to SDG 6.4.2, SDG 7.2.1, SDG 2.1.1, and SDG 15.3.1, respectively. There are tight and complex links among these four indicators, so an integrated WEFE system stress indicator is needed to reflect the synthetic security status of the WEFE system in Central Asian countries.

This case comprehensively evaluated pressure on the WEFE system through the projection pursuit model based on particle swarm optimization (PSO-PEE) and analyzed the transmission of sectoral pressure. On this basis, a cooperation framework among Central Asian countries was put forward, which provides important scientific and technological support for Central Asian countries to achieve the SDGs.

9.3.1.2 Data

- Ecological footprint and biocapacity, source: <https://data.footprintnetwork.org>.
- Total primary energy consumption and production, source: <https://knoema.com/atlas/ranks>.
- Global hunger index, source: <https://www.globalhungerindex.org/>.
- WSI, source: <https://www.fao.org/sustainable-development-goals-data-portal/data/indicators/642-water-stress/en>.
- Crop acreage, yield, energy use structure in agriculture, and population, source: <https://www.fao.org/faostat/en/#data>.
- Water footprint, source: <https://waterfootprint.org/>.
- Food trade, source: <https://data.casearth.cn/sdo/detail/5feae826819aec33049b7c57>.
- Electricity production structure, source: <https://data.worldbank.org/>.
- Water production of major crops, source: <http://wuemoca.net/app/>.
- Agriculture irrigation efficiency, source: <https://www.fao.org/aquastat/en/data-analysis/irrig-water-use/irrig-water-withdrawal/>.

9.3.1.3 Methods

1. WEFE Stress

An integrated index was constructed to quantitatively evaluate stress on the WEFE system. The integrated index has four components: the food stress index (FSI), energy stress index (EESI), WSI, and ecological stress index (ESI). We divided these four pressure indicators (FSI, EESI, WSI, and ESI) into five levels referenced in previous research and the official classification standard (Table 9.2). In order to characterize the effects of different sectors on the comprehensive stress of the WEFE system, particle swarm optimization was adopted to establish the projection pursuit model and construct the pressure index of the WEFE system.

2. Quantifying the Pressure on the WEFE System

The PSO-PEE is an emerging mathematical method for transforming high-dimensional nonlinear problems into one-dimensional ones by finding the best projection direction of the assessment indicator system. This model has been applied to the assessment of water security, ecological security, and food security. This model was constructed in three steps: (1) normalizing assessment indicators; (2) establishing the projection indicator function; and (3) optimizing the projection indicator function via particle swarm optimization.

9.3.1.4 Results and Analysis

From 1992 to 2020, the subsector of food, energy, and water experienced subtle change, while the ecological system changed greatly in Central Asian countries (Fig. 9.1). For the WSI, with the exception of Turkmenistan, the remaining countries showed a slight downward trend

Table 9.2 Classification of pressure on the WEFE system

Stress indexes	Description	Degree of pressure				
		No pressure	Low pressure	Medium pressure	High pressure	Critical pressure
ESI	The ratio of total ecological footprint to ecological biocapacity (%)	0–0.80	0.81–1.00	1.01–1.5	1.51–2.00	>2.00
EESI	The ratio of the total primary energy consumption to the total primary energy production (%)	0–45	46–78	79–108	109–150	>150
FSI	Hunger index (%)	0–4.9	5.0–9.9	10.0–19.9	20.0–29.9	>30.0
WSI	The ratio of total freshwater withdrawal to the total renewable freshwater resources after deducting the environmental flow	0–25	26–50	51–75	76–100	>100

(Fig. 9.1a). For EESI, with the exception of Turkmenistan, the remaining countries showed an overall downward trend (Fig. 9.1c). For the FSI, with the exception of Turkmenistan and Kyrgyzstan, the remaining countries showed a slight upward trend. Moreover, the FSI of five countries showed obvious fluctuations after 2003, but the trend was not significant (Fig. 9.1b). For ESI, Tajikistan, Kazakhstan, and Kyrgyzstan showed a downward trend first in the period 1992–2000 and then an upward trend in 2000–2020 (Fig. 9.1d), while for Uzbekistan and Turkmenistan, ESI showed an upward trend, and the most significant upward trend was observed in Turkmenistan. From the trend of the comprehensive pressure of WEFE system change (Fig. 9.2), the pressure level of the WEFE system in Tajikistan and Kyrgyzstan presented a relatively significant upward trend, while that of Turkmenistan presented a downward trend and that of Kazakhstan was not obvious. The stress of the WEFE system in Uzbekistan decreased first and then increased, which is consistent with the trend of WSI and ESI. From the ranking of the pressure of the WEFE system in Central Asian countries, the pressure of the WEFE system varies greatly among countries, with Kazakhstan having the lowest integrated pressure, followed by

Kyrgyzstan and Tajikistan, while Uzbekistan has the highest WEFE system pressure, followed by Turkmenistan. According to the results of the projection pursuit model, water stress plays a very critical role in the entire system pressure (weight 0.97), followed by energy stress (weight 0.22). According to the pressure situation of each subsystem in Central Asian countries in Fig. 9.1, water stress in Kazakhstan is the lowest, and energy stress has also been the lowest since 2014, which is the key factor leading to the lowest comprehensive pressure of the WEFE system in Kazakhstan.

The links between sectors are the prerequisite for the transmission of sectoral pressure, while pressure transmission requires a certain carrier. In Central Asia, virtual water trade appears to include only the transfer of physical products. This physical transfer results in simultaneous but indirect transfer among water, food, energy, and ecological pressures, which affect different SDGs. The virtual water net exports of crop products in Uzbekistan reached $10.3 \times 10^9 \text{ m}^3$, second only to Kazakhstan (Figs. 9.3 and 9.4). The largest export crop is cotton (Fig. 9.5c), which accounts for 59% of crop exports from Central Asian countries (Fig. 9.5b). It is worth noting that Kazakhstan is the main importer of cotton, mainly from Uzbekistan (Fig. 9.5b).

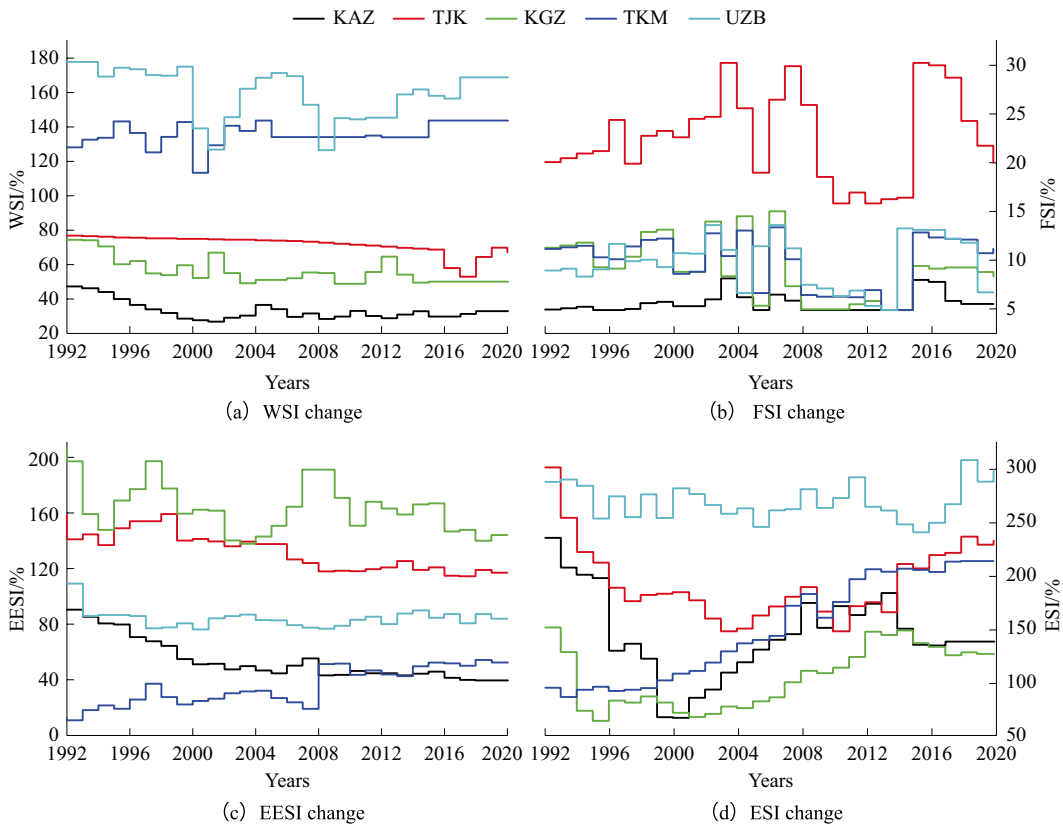


Fig. 9.1 Temporal variation in the **a** water system, **b** food system, **c** energy system, and **d** ecological system stress indexes in Central Asia during 1992–2020. Note for

this and subsequent figures: KAZ refers to Kazakhstan, TJK refers to Tajikistan, KGZ refers to Kyrgyzstan, TKM refers to Turkmenistan, UZB refers to Uzbekistan.

The water footprint of cotton in Uzbekistan is the highest, with a blue water footprint of $1.7 \times 10^8 \text{ m}^3$, constituting 63.5% of the total blue water footprint of cotton in Central Asian countries (Fig. 9.4). Although the amount of wheat exported from Kazakhstan to Uzbekistan is $1.8 \times 10^{10} \text{ kg}$ (Fig. 9.5e), the virtual water for wheat mainly comes from green water (Fig. 9.3), which may not consume a large number of surface water resources.

It can be seen that Kazakhstan has transferred water stress to Uzbekistan, while Uzbekistan has transferred food pressure to Kazakhstan. Not only that, in Uzbekistan, the electric power consumed in agriculture is 43,635 TJ, accounting for 48% of electricity consumption in agriculture in Central Asia. The pressure has

expanded from the water system to the energy and ecology systems through virtual water trade. Figure 9.1 shows that water, energy, and ecological stresses in Uzbekistan are all under high pressure. In addition, another aspect of pressure transmission is between energy stress and water stress. Kyrgyzstan and Tajikistan mainly rely on hydropower, accounting for 84 and 98% of the total power generation, respectively, resulting in insufficient water for agricultural irrigation in downstream countries. In other words, upstream countries pass water stress to downstream countries to alleviate energy stress. The dual water stress shift has caused the most severe water stress in downstream countries. Therefore, the water stress transmission starts from the upstream Tajikistan and Kyrgyzstan to

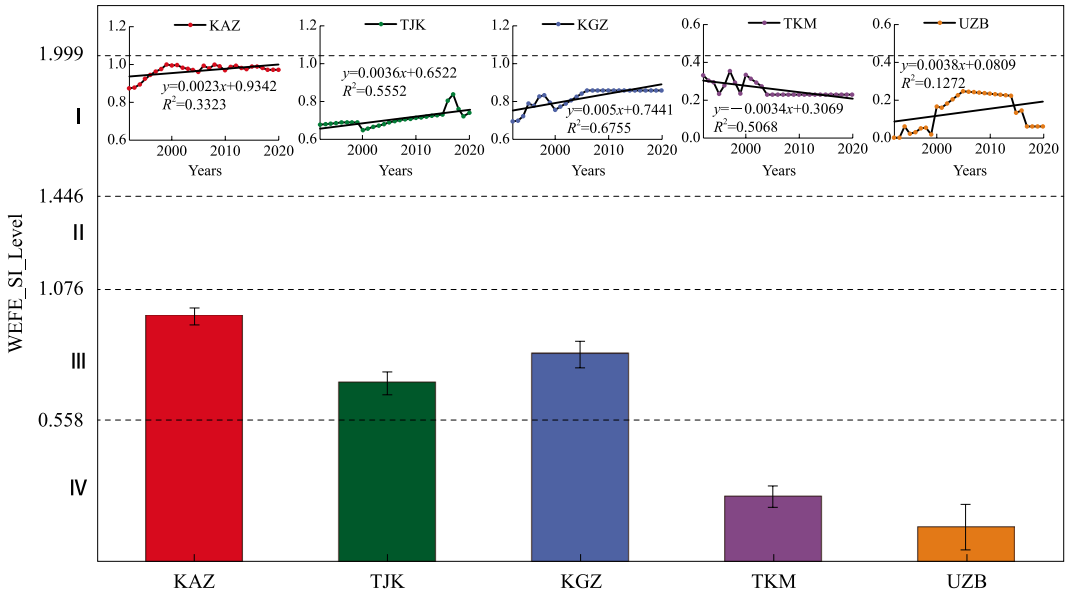


Fig. 9.2 Variations in the WEFE system pressure level (WEFE_SI_Level) in Central Asian countries during 1992–2020. Note Higher pressure level values correspond to lower WEFE system pressure

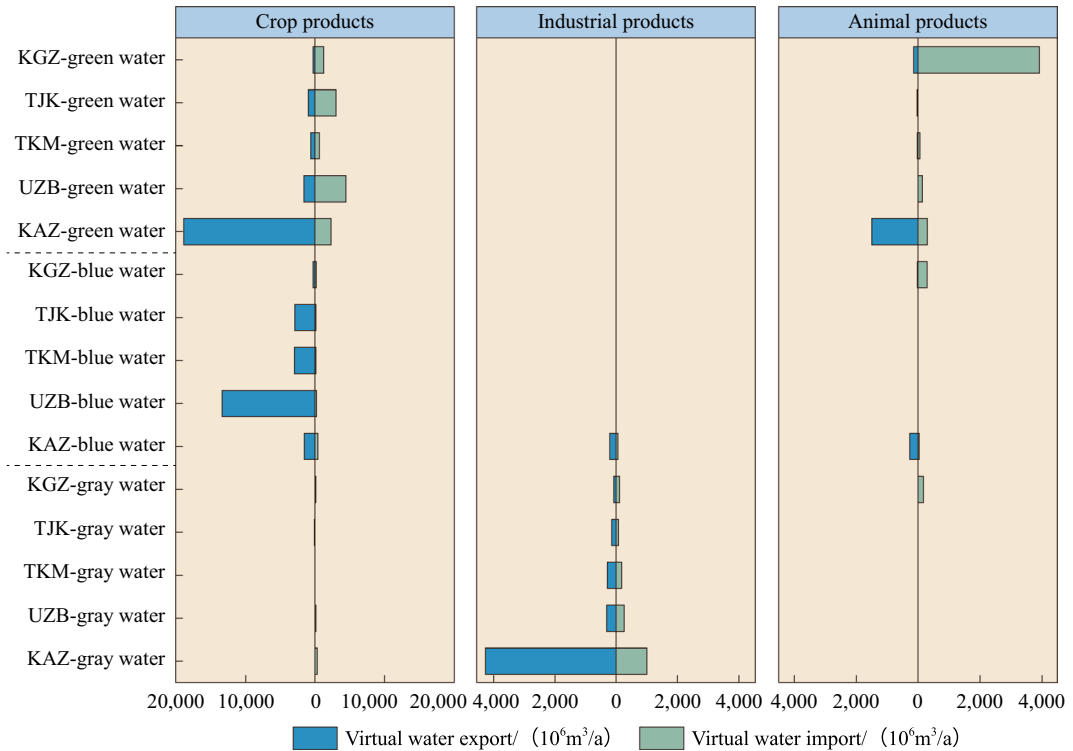


Fig. 9.3 Virtual water trade in crop, industrial, and animal products in Central Asian countries

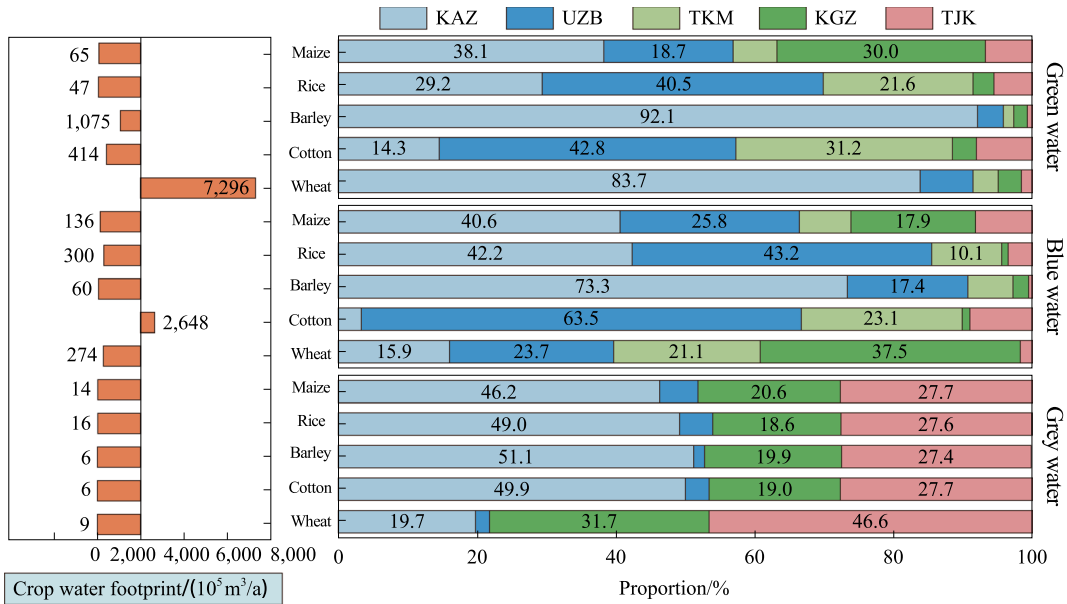


Fig. 9.4 Water footprint of the main crops in Central Asian countries

the downstream countries (Turkmenistan and Uzbekistan). The most important medium for pressure transmission is the virtual water trade of crop products, especially cotton and wheat.

Understanding the WEF nexus in Central Asian countries is the prerequisite for achieving the sustainability of the WEF system. The water–energy conflict between the upstream and downstream countries is the most critical. The Toktogul hydropower station in Kyrgyzstan and Kayrakum and Nurek hydroelectric power stations in Tajikistan are the three major hydropower stations that provide these countries with electricity and control downstream irrigation water. To meet the electricity demand in winter, the three hydropower stations usually begin to store water in summer. This leads to insufficient water for agricultural irrigation in downstream countries during the summer. Therefore, it is recommended that Kyrgyzstan establishes cross-basin cooperation agreements with Uzbekistan and Kazakhstan and reaches a “same effect trade agreement” of water–energy instead of an “equivalent trade agreement”. Additionally, Tajikistan should establish similar agreements with Uzbekistan and Turkmenistan.

For example, based on the existing water storage capacity of the three reservoirs, Tajikistan and Kyrgyzstan are suggested to reduce the water storage capacity by 5%–10% during the crop-growing season (May to July). This would increase water availability for agricultural irrigation in downstream countries.

In winter, Kazakhstan, Turkmenistan, and Uzbekistan must compensate for the same amount of electricity lost (instead of the same amount of trade or money) in the upstream countries due to the reduction in water storage. This not only meets the power demands of the upstream countries in winter, but also reduces the pressure for agricultural irrigation water in the downstream countries. In addition, given the dominant role of water power in the upstream countries and the low irrigation efficiency, the introduction of solar and wind power technology in the upstream countries and drip irrigation technology in the downstream countries can greatly improve the sustainability of the WEF system in Central Asian countries.

It is reported that from 2006 to 2018, China’s total installed capacity of wind power increased from 2.07 GW to 185 GW, and its total installed

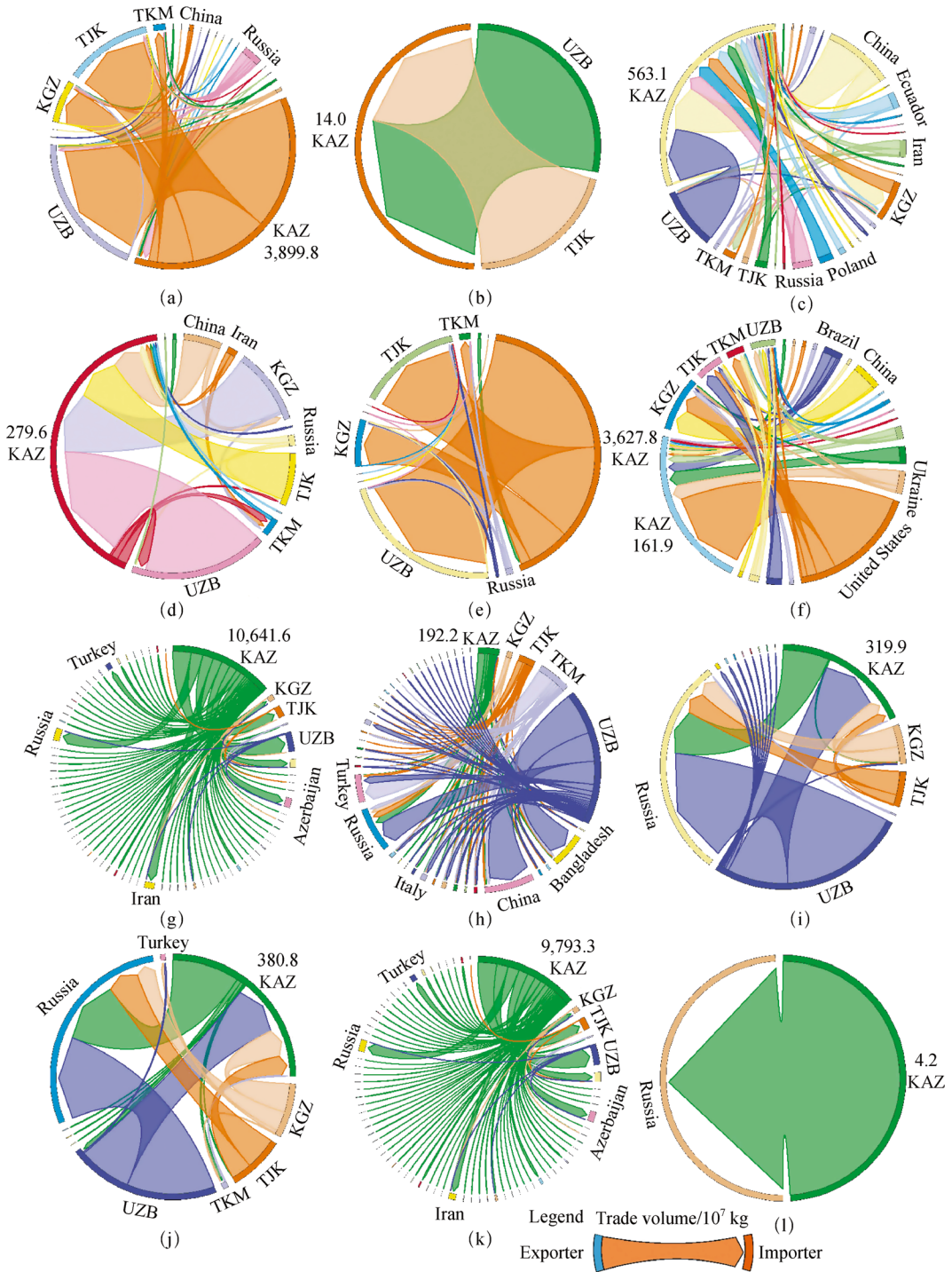


Fig. 9.5 Trade volume of the main agricultural products from the perspective of import a–f and export g–l in Central Asian countries. *Note:* The main agricultural

products are cereals (a, g), cotton (b, h), fruit (c, i), vegetables (d, j), wheat (e, k), and meat (f, l), respectively

capacity of solar photovoltaics increased from 0.16 GW to 175 GW, ranking first in the world in total solar power generation. Northwest China (Xinjiang, Gansu, Qinghai, and Inner Mongolia) plays an important role in clean energy production, accounting for 37.1% of the country's total wind power generation and 64% of the total solar power generation. The total wind and solar power generation in Northwest China is about 18 times that in Kyrgyzstan. Wind–solar technology could be improved or a power transmission network could be built from east (Northwest China) to the west (Central Asian countries). Although the current power generation costs are relatively high, solar and wind power generations can greatly alleviate the pressure of energy shortages in Central Asia, especially in Kyrgyzstan. It is also an essential step for Central Asian countries to achieve energy sustainability. In addition, to alleviate water shortages, improve the ecological environment, and increase crop yields, Central Asian countries (especially Turkmenistan and Uzbekistan) can introduce drip irrigation technology with mulching film from China. It is estimated that this technology will save 50% of water and 30% of fertilizer and increase crop yields by 50% compared to traditional irrigation methods. In addition to improving irrigation technology, the crop planting structure should also be appropriately adjusted. For example, Tajikistan, the third largest cotton producer in Central Asia, faces the most severe food pressure. To alleviate this situation, Tajikistan must make a trade-off between increasing economic income and meeting food demand. This can be achieved by appropriately reducing the cotton planting area (a 5%–10% reduction) and increasing the crop area (such as wheat, rice, and potatoes).

9.3.1.5 Highlights

- The comprehensive pressure of the WEFE system in Central Asia during 1992–2020 was analyzed. Kazakhstan had the lowest comprehensive pressure, followed by Kyrgyzstan and Tajikistan, and Uzbekistan had the highest comprehensive pressure, followed by Turkmenistan.

- The pressure transmission mechanism among the WEFE system in Central Asia was revealed, and it was found that the pressure was transmitted from the energy system of upstream Tajikistan and Kyrgyzstan to the water system of downstream Kazakhstan, Turkmenistan, and Uzbekistan, while pressure was transmitted from the water system to the food, energy, and ecological systems in the downstream countries. Wheat and cotton are the main media of pressure transmission in water systems.
- The solution to the water–energy conflict between the upstream and downstream countries is the key to realizing the sustainability of the WEFE system in Central Asia. In order to alleviate the conflict and achieve sustainable development, two mitigation strategies, i.e., “same effect trade agreement” (to replace “equivalent trade agreement”) and “power transmission from east to west” (that is, importing power from China), are put forward. Other measures are also discussed, e.g., the adjustment of energy structure, planting structure, and import–export trade structure.

9.3.1.6 Discussion and Outlook

This case study provided a synthetic understanding of the WEFE system status in Central Asia. In addition, we revealed the pressure transmission among different sectors. Thereafter, we proposed a top-down coordination mechanism to achieve the sustainability of the WEFE system and provided a framework for sustainable development for stakeholders and decision-makers (Fig. 9.6). The main conclusions of this case are as follows.

- (1) Kazakhstan has the lowest WEFE system pressure, followed by Kyrgyzstan and Tajikistan, whereas Uzbekistan and Turkmenistan have the highest pressure. The main reason behind this is the dominant role of water stress in the WEFE system.
- (2) The pressure transmission originates from the upstream countries (Tajikistan and Kyrgyzstan), whereas the downstream countries (Turkmenistan and Uzbekistan) are

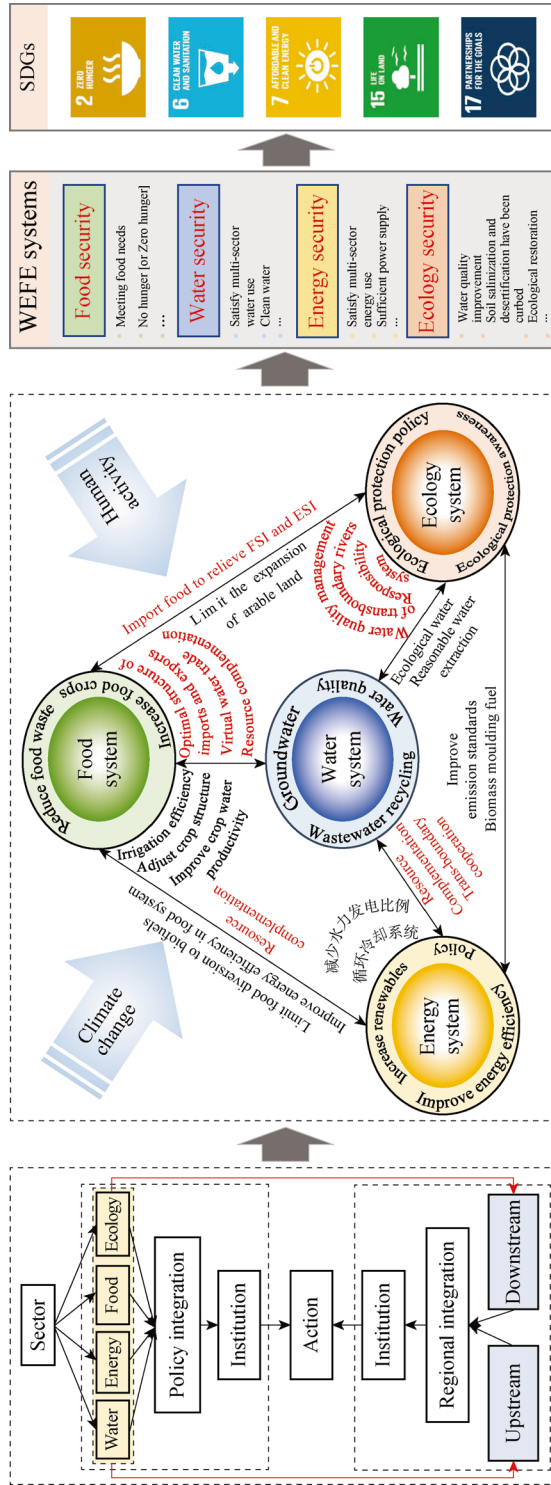


Fig. 9.6 Trade-off and synergy mechanisms of the WEF system for the SDGs

the main bearers and spreaders of the pressure. The most important medium for pressure transmission is the virtual water trade of crop products, especially cotton and wheat. Unreasonable sectoral structure (crop planting, power generation, and food import and export) and the spatial mismatch of resources and virtual water trade (especially for food trade) are important reasons for the pressure transmission within and across countries.

- (3) The proposed coordination mechanism optimizes the system structure, makes trade-offs and synergies for the interests of the sectors, and is more targeted. The integration of policies and regions is key to ensuring the smooth operation of the mechanism. Furthermore, cross-border cooperation, the adjustment of power generation, cotton planting, and food import and export trade structure are important measures to achieve the sustainable development of the WEFE system in Central Asia.

This case described the pressures on the WEFE system and their transmission processes in Central Asian countries and proposed a framework for resolving water–energy conflict, which provides basic data and theoretical support for SDG 2.1, SDG 6.4, SDG 7.2, SDG 15.3, and SDG 17.16 in Central Asia.

9.4 Summary

This chapter introduces the research direction of Big Earth Data supporting SDG interaction and integrated evaluation research. It mainly includes three aspects: the analysis of synergies and trade-offs, spatial spillover effects, and future scenario simulation. Based on these, SDG single-theme and regional integrated evaluations could be carried out to provide decision-making references for achieving the 2030 Agenda and dynamically adjusting the sustainable development paths.

In the case study section, this chapter takes an integrated evaluation of the sustainable development of the WEFE system in Central Asia

as an example. The pressures and transmission processes of water, energy, food, and ecology systems in the five Central Asian countries were studied, and a framework for resolving conflicts between water and energy was proposed. Two mitigation strategies, the “same effect trade agreement” (to replace the “equivalent trade agreement”) and “power transmission from east to west” (that is, importing power from China), were put forward to promote the sustainable development of Central Asian countries.

In the future, we will explore more themes and pay more attention to case applications of Big Earth Data in the global and regional SDG multi-indicator interactions and integrated evaluations at different scales. Specifically, we will use geographic information modeling and simulation methods based on spatial analysis technology to identify the interactions among goals, predict future development scenarios, and conduct comprehensive assessments, providing a basis for dynamic policy adjustments.

References

- FAO (2021) Tracking progress on food and agriculture-related SDG indicators 2021. <https://www.fao.org/sdg-progress-report/2021/en/>. (06 Mar 2023)
- Pradhan P, Costa L, Rybski D et al (2017) A systematic study of sustainable development goal (SDG) interactions. *Earth's Future* 5(11):1169–1179
- Sachs J, Schmidt-Traub G, Kroll C, et al. (2018) SDG index and dashboards report 2018. New York, Bertelsmann Stiftung and Sustainable Development Solutions Network (SDSN). <https://www.sdgindex.org/reports/sdg-index-and-dashboards-2018/>
- Sachs J, Schmidt-Traub G, Kroll C, et al. (2020) The sustainable development goals and COVID-19. Sustainable development report 2020. Cambridge, Cambridge University Press. <https://www.sdgindex.org/reports/sustainable-development-report-2020/>
- Sachs J, Kroll C, Lafortune G, et al. (2021) The decade of action for the sustainable development goals: sustainable development report 2021. Cambridge, Cambridge University Press. <https://www.sdgindex.org/reports/sustainable-development-report-2021/>
- Sachs JD, Lafortune G, Kroll C, et al. (2022) From crisis to sustainable development: the SDGs as roadmap to 2030 and beyond. Sustainable Development Report 2022. Cambridge, Cambridge University Press. <https://www.sustainabledevelopment.report/reports/sustainable-development-report-2022/>

- Sachs JD, Lafortune G, Fuller G, et al. (2023) Implementing the SDG stimulus: sustainable development report 2023. Cambridge, Cambridge University Press. <https://www.sustainabledevelopment.report/reports/sustainable-development-report-2023/>
- UN-Water (2016) UN World water development report 2016. <https://www.unwater.org/publications/un-world-water-development-report-2016>. (4 July 2023)
- UN-Water (2023) SDG 6 acceleration snapshots: what progress looks like. <https://www.unwater.org/publications/sdg-6-acceleration-snapshots-what-progress-looks>. (06 Mar 2023)
- Warchold A, Pradhan P, Kropp JP (2021) Variations in sustainable development goal interactions: Population, regional, and income disaggregation. *Sustain Dev* 29(2):285–299

Open Access This chapter is licensed under the terms of the Creative Commons Attribution-NonCommercial-NoDerivatives 4.0 International License (<http://creativecommons.org/licenses/by-nc-nd/4.0/>), which permits any noncommercial use, sharing, distribution and reproduction in any medium or format, as long as you give appropriate credit to the original author(s) and the source, provide a link to the Creative Commons license and indicate if you modified the licensed material. You do not have permission under this license to share adapted material derived from this chapter or parts of it.

The images or other third party material in this chapter are included in the chapter's Creative Commons license, unless indicated otherwise in a credit line to the material. If material is not included in the chapter's Creative Commons license and your intended use is not permitted by statutory regulation or exceeds the permitted use, you will need to obtain permission directly from the copyright holder.





10.1 Summary

This report presents case studies demonstrating how Big Earth Data can support the evaluation of indicators for seven SDGs (Zero Hunger, Clean Water and Sanitation, Affordable and Clean Energy, Sustainable Cities and Communities, Climate Action, Life Below Water, and Life on Land) and the interactions among SDGs. Most of the cases studied in this book have global applicability or focus on the regions involved in the Belt and Road. This is consistent with the initiative of jointly building high-quality development along the Belt and Road. To this end, experts, scholars, and decision-makers can reference the data products, methods, models, and decision support guidelines presented in this report.

Data products: Twenty-eight data products were developed at both global and Belt and Road scales. Some have narrowed the data gaps in SDG monitoring, including the dataset of global UBAs with a population above 300,000, boundary areas of World Heritage sites, global forest cover, global sand dune distribution on land, and the spatial distribution of the suitable habitats for wild camels. Some other products have improved the spatial precision of monitoring and evaluating SDG indicators, such as the global reforestation index at 30 m resolution, electrification status of BUAs at 500 m resolution, urban greenness at 250 m resolution

worldwide, worldwide assessment of eutrophication in representative lakes, spatial distribution of water transparency in large lakes worldwide, and conflictive and cooperative events related to transboundary rivers in Central Asia.

Methods and models: Twenty-two methods and models have been developed based on Big Earth Data. Some methods and models have provided optimized solutions for SDG assessment, such as a new index for the final land degradation index in arid areas, a global typical lake algae extraction method, a large-scale lake and reservoir transparency inversion model, and a global ocean carbon flux estimation method using SOMs and stepwise feedback neural networks.

Decision support: The spatial and temporal analysis of sustainable development indicators using the above data and methods has resulted in 24 decision support guidelines for sustainable development both in China and globally. Regarding SDG 2, decision support has been provided for regional food production and stable grassland utilization in Africa and Southeast Asia, as well as for the Central Asian region with a focus on animal husbandry. Regarding SDG 6, decision support has been provided for “cross-border cooperation” among Central Asian countries. Regarding SDG 7, decision support has been provided for policy formulation and investment in electrification, international energy cooperation, training, and more.

For SDG 11, the decision support guidelines in this report can help improve urban land use efficiency, reduce urban disasters, and enhance urban green space. Related to SDG 13, guidelines have been provided to reduce losses caused by floods and build disaster reduction systems. Regarding SDG 14, decision support has been provided for the prevention and control of eutrophication in coastal waters, protection of the coral reef environment, and other related efforts. Finally for SDG 15, guidelines were given to improve forest protection and restoration, monitoring and governance of land degradation, and habitat protection for endangered species, among other contributions. In addition, the pressures and transmission processes of water, energy, food, and ecosystems in the five Central Asian countries were studied using a comprehensive evaluation of sustainable development under the cross-cutting effects of WEF E multi-indicators. A framework for resolving conflicts between water and energy relationships was also proposed.

10.2 Prospects

Over the past four years, CAS has conducted exploratory research on monitoring and evaluating SDG indicators and has pinpointed that Big Earth Data has high application potential and promotional value in supporting many SDGs (Guo 2020, 2021, 2022). However, numerous challenges still exist, including the scarcity of crucial spatiotemporal data essential for SDG assessments, disjointed standards for data sharing, and inadequate safeguards for data security, especially prevalent in the regions involved in the Belt and Road. To facilitate the implementation of the 2030 Agenda, we recommend redoubling efforts in the following areas.

1. Building a Global Collaborative Observation Network for the SDGs

More and more satellites being launched into space have resulted in the rapid growth of the satellite industry and its applications. On

November 5, 2021, China successfully launched SDGSAT-1, the world's first sustainable development science satellite, and committed to sharing its data with the world. In response to the "leaving no one behind" commitment of the 2030 Agenda, we propose to speed up the construction of a global collaborative observation network for the SDGs. This initiative aims to enhance the service capacity of space-based observations, develop a standardized international space-based observation system, and provide joint data support to address unbalanced development and reduce the digital divide.

2. Improving the Spatiotemporal Dimensions of SDG Progress Assessment

Statistical surveys are among the primary methods of obtaining global SDG monitoring and evaluation data. However, due to the differences in policy and ability in the development of statistical survey systems across the world, survey data often suffer from inconsistent quality, insufficient spatiotemporal scales, and a lack of data availability in some developing countries. We, therefore, propose to make full use of Big Earth Data and other technologies to increase data acquisition methods and obtain high-quality, spatiotemporally consistent global SDG data through open access to data computing and storage facilities and adoption of advanced data processing methods. The goal is to make SDG progress evaluation timely and accurate.

3. Sharing Public Data Products for SDG Monitoring

Due to the lack of consensus in the policies on data sharing and no unified technical standards in terms of data structure and security, many users have no access to the data owned by other institutions, or the data generated by specific statistical agencies are excluded from other users. We propose to improve the new information infrastructure that combines data applications and open services and provide real-time data access, on-demand pooling, integration, open sharing and analysis services, and public data

services and products to support SDG monitoring and evaluation.

4. Promoting Exemplary Studies on Big Earth Data Supporting the SDGs

Due to differences in natural resources and socioeconomic development levels, various regions face individual difficulties in their efforts toward sustainable development. Big Earth Data, featuring multiple spatial and temporal scales, can provide important support for evaluating the implementation of the SDGs in different regions. We propose, therefore, to promote exemplary studies on Big Earth Data supporting the SDGs, to strive to build a sustainable development indicator system with different spatial scales, and to develop innovative and comprehensive demonstration systems with

regional features to inform efforts to achieve the SDGs around the world.

References

- Guo H (2020) Big earth data in support of the sustainable development goals (2019). EDP Sciences Press, Beijing
- Guo H (2021) Big earth data in support of the sustainable development goals (2020): the belt and road. EDP Sciences Press, Beijing
- Guo H (2022) Big earth data in support of the sustainable development goals (2021): the belt and road. EDP Sciences Press, Beijing

Open Access This chapter is licensed under the terms of the Creative Commons Attribution-NonCommercial-NoDerivatives 4.0 International License (<http://creativecommons.org/licenses/by-nc-nd/4.0/>), which permits any noncommercial use, sharing, distribution and reproduction in any medium or format, as long as you give appropriate credit to the original author(s) and the source, provide a link to the Creative Commons license and indicate if you modified the licensed material. You do not have permission under this license to share adapted material derived from this chapter or parts of it.

The images or other third party material in this chapter are included in the chapter's Creative Commons license, unless indicated otherwise in a credit line to the material. If material is not included in the chapter's Creative Commons license and your intended use is not permitted by statutory regulation or exceeds the permitted use, you will need to obtain permission directly from the copyright holder.



Index

A

Affordable and Clean Energy, 2, 73, 203
Algal blooms, 48–54, 69, 144, 145, 150, 158, 160

B

Big Earth Data, 2, 4–6, 15, 17, 20, 26, 40, 69, 77, 79, 85, 87, 109, 110, 112, 118, 121, 122, 125, 139, 140, 143, 163, 164, 167, 178, 180, 186, 190, 200, 203–205

C

Carbon budget, 136
Clean Water and Sanitation, 2, 203
Climate action, 2, 121, 130, 139, 140, 203
Cropland change, 8, 10
Cropping Intensity, 7, 11, 12, 15

E

Energy access, 73

G

Grassland carrying capacity, 7, 16, 22
Green house gas, 1, 121, 126, 130, 136, 140, 191

H

Harmful algal bloom species, 144, 150

I

International energy cooperation, 73, 74, 77, 78, 80, 85, 203

L

Land degradation neutrality, 2, 167, 169, 177
Life Below Water, 2, 203
Life on Land, 2, 203

M

Monitoring and early warning of coral reef bleaching, 144, 151, 152

N

Natural habitats, 169, 182

P

Phytoplankton size class, 144, 158

S

SDG integrated evaluation, 4, 189–191, 200
Sustainable cities and communities, 2, 118, 203
Sustainable Development Goals, 1, 2, 26, 93, 191

U

Urbanization, 6, 11, 87–95, 98–101, 103, 114, 117, 118

W

Water-energy-food nexus, 196
Water events, 48, 60, 62–64, 66–69
Water transparency, 48, 54–61, 69, 203

Z

Water tree cover, 168, 171
Zero Hunger, 2, 5, 6, 11, 16, 22, 26, 28, 30, 32, 36, 43, 203